UNIVERSITÀ DI PARMA

UNIVERSITÀ DEGLI STUDI DI PARMA

DOTTORATO DI RICERCA IN FISICA
XXXIV CICLO

Unconventional probes into the QCD phase diagram using Rational approximations and Lefschetz thimbles

Coordinatore:
Chiar.mo Prof. Stefano Carretta

Tutore:
Chiar.mo Prof. Francesco Di Renzo

Dottoranda:
Simran Singh

Anni Accademici 2018/2019-2021/2022

Abstract

In this thesis, we present two methods of probing quantum chromodynamics (QCD) at finite densities on a lattice. This theory studies the dynamics of the interactions between quarks and gluons. Being a strongly interacting theory, it is hard to study it using perturbative approaches. We need non-perturbative methods to study this theory. Lattice QCD, a numerical approach in which space-time is discretized and quarks and gluons are put on four dimensional space-time lattices is one such non-perturbative method which has been very successful in studying QCD at zero chemical potential. However, at finite densities we encounter the numerical sign problem, which hinders progress in simulating QCD via lattice methods. One of the main reasons we want to study QCD at finite densities is to understand its phase diagram in the temperature - chemical potential plane. Currently, most of the phase diagram is a conjecture, although some regions of the phase space are well studied both by theoretical methods and heavy-ion collision experiments. In the early stages of the Universe, the temperatures were so high that quarks and gluons existed in a de-confined phase called the quark gluon plasma (QGP). At some point in time when the temperatures dropped below a certain value (transition temperature), quarks and gluons combined to form hadrons like protons and neutrons. A particularly active field of research, currently, is the search for the transition from the de-confined to confined phases at finite densities. Through lattice methods, it has been successfully shown that at zero chemical potentials, this transition is an analytic crossover. It has also been seen that up to small chemical potentials, it continues to remain a crossover. However, at larger chemical potentials, this crossover line is expected to terminate at a critical end point. This search still remains an open problem to this day and forms a very active field of research. The goal of this thesis was to make progress towards the understanding of the QCD phase diagram at finite densities by using methods that minimise/evade the numerical sign problem to facilitate this goal. To this end we have developed a rational approximation method to study some thermodynamic variables associated with QCD simulated at imaginary chemical potentials, in the hope of finding its singularities in the complex chemical potential plane. Apart from this, some progress in the direction of studying Lefschetz thimbles within the scope of single thimble simulations and regularising non-abelian gauge theories on thimbles have also been made.

We begin by a general introduction to the importance of making progress in the QCD phase diagram in Chapter 1. This thesis is then divided into two parts. The first part describes an unconventional method of re-summation of the Taylor series expansions of thermodynamic variables simulated at zero and purely imaginary values of chemical potential to look for non-analyticities (singularities) of the partition function in the complex chemical potential plane. The scaling of these complex singularities can give very important hints about the phase diagram. In Chapter 2

of this thesis we describe in detail the method of re-summation used by us. This is followed by Chapter 3 where we give a general overview of phase transitions in QCD. Chapter 4 contains an introduction to the complex singularities mentioned above, called Lee Yang edge singularities, with a section containing a case study on the 2D Ising model performed by us recently to demonstrate the validity of our analysis. In Chapter 5 we discuss the most significant work of this thesis, i.e., studying the phase diagram of 2+1 flavour QCD at imaginary values of chemical potential using the rational-function re-summation techniques to find the Lee-Yang edge singularities. We then study the scaling of these singularities in the vicinity of the Roberge-Weiss transition and show the consistency of our results. We also briefly mention another singularity that we found in the vicinity of a chiral transition.
We then move on to the second part of the thesis that is more directly focused on the numerical sign problem and the current status of its possible solution using Lefschetz thimbles. In Chapter 6 we describe the numerical sign problem and introduce the Lefschetz thimble approach and a method to do single thimble simulations. In Chapter 7 we formulate a method of applying Lefschetz thimbles to non-abelian gauge theories which is currently an unsolved problem. We further discuss the problem of having extra zero modes when regularising gauge theories and how they can be removed by using different boundary conditions. We end the discussion on non-abelian gauge theories by introducing some ideas as to why studying the topological charge using Lefschetz thimble regularisation can be a good idea. We finally conclude and provide a summary of our results and perspective on future directions in Chapter 8.

Acknowledgements

This thesis is the result of continued guidance and support, both academically and on a personal level, of my thesis supervisor - Prof. Francesco Di Renzo. Justice cannot be done to my gratitude toward Prof. Di Renzo in the small section of acknowledgements of this thesis. I am grateful to him for having taken me on as a PhD student and for going beyond in helping a foreign student like me navigate the barriers of administration in Italy. As for the academic part of my PhD, this thesis would not have been possible without the long discussions of physics and mathematics both online and offline, due to Francesco always being available, even despite the pandemic.

I further thank the EuroPLEx network for selecting me and funding this PhD.

I would also like to extend my thanks to all the staff and professors I had the opportunity of interacting with at Parma. I would like to thank Prof. Stefano Carretta for taking out time in helping me with the bureaucracy needed during my PhD studies. A special thanks to Prof. Luca Griguolo and Prof. Marissa Bonnini for including me in all of their group's activities. I would like to thank Alberto and Claudia for being ever so kind in helping me with general problems in the department despite the language barrier.

I would also take this opportunity to thank Dr. Christian Schmidt at Bielefeld University for his support during my PhD. I am very grateful for all the discussions we had on phase transitions and Lee Yang edge singularities. I greatly appreciate having had the opportunity to spend a few weeks at the Physics department at Bielefeld University. I would also like to thank David at Bielefeld University for including me in all the activities both on campus and off.

I thank Kevin, Petros and Itamar for having very helpful discussions in relation to the work presented in this thesis.

I am immensely grateful to my parents for never questioning and fully supporting all the life altering decisions I have made, even though they may not have agreed with all of them. I am also grateful to them for providing a safe environment for learning for me all through my life.

I also take this opportunity to thank my friends, both back home and here, in Europe. My officemates - Emil, Paolo, Luigi and Sophie - in Parma seem more like childhood friends than colleagues. I also thank Maria for being there for me in Parma, even during the dark lockdown times. I hope the friendships made here remain for a lifetime. Although we haven't had the opportunity to meet very much due to the pandemic, I would not have been able to make it without the immense emotional support offered to me by my closest friends Ishita and Mallika back home.

I would lastly like to thank Jerome and his mother for "adopting" me as a family member in every respect. It is impossible for me to imagine what my life would have looked like today if I had not met Jerome in Mainz three years ago.

Contents

List of Figures

List of Tables

Chapter 1

Introduction

1.1 Part I

One of the most active fields of research in the high energy physics community today is making progress toward the phase diagram of quantum chromodynamics (QCD). QCD is a strongly interacting theory describing the dynamics of the interactions between quarks and gluons. Being strongly interacting it is best studied using non-perturbative tools. Lattice QCD is one of those tools which has been very successful in studying QCD at zero densities or zero chemical potential[1]. However, at finite densities, lattice simulations which rely on the concept of importance sampling, fail due to not having a well-defined probability measure. This is a numerical problem and is known commonly as the sign problem. The origin of this problem, in lattice QCD, can be traced back to the Grassmann odd nature of fermions and how they enter into the QCD partition function. Being Grassmann odd[2], fermions are integrated out of the partition function, leaving us with an object called the fermion determinant which is a part of the probability measure and has the following property (details are left for Chapter 6):

$$[\det\, M(\mu)]^* = \det\, M(-\mu)$$

where M is the fermion matrix operator and μ represents the chemical potential. It can be seen that for real values of μ, this determinant is complex. This is the reason finite (real) μ simulations are hindered. However, simulations at zero and imaginary chemical potentials are still possible using the standard lattice QCD techniques and in fact have been successful in gaining some knowledge about the phase diagram, from extrapolation, to finite μ. Studies in the direction of Taylor expansions about zero chemical potential were pioneered in [1]. This was followed by imaginary chemical potential simulations and analytic continuations to real chemical potentials [2, 3]. But these two methods certainly don't exhaust all the research directions. One of the first (μ, T) phase diagrams presented for the (2+1) flavour QCD was in [4] utilising the technique of *re-weighting* (See Chapter 6) on direct simulations at zero chemical potential predicted some values for the critical end-point. Based on universality arguments (relating to chiral symmetry breaking and restoration), QCD is

[1] A system with zero chemical potential for a particular species of particles indicates an equal abundance of particles and anti-particles of that species. At finite densities, we have an excess of particles to anti-particles (conventionally).

[2] Grassmann odd numbers anti-commute. Ordinary numbers cannot represent them. We need operator-valued objects to represent them.

expected to undergo a first order phase transition at very high densities, whereas, at zero chemical potential lattice QCD simulations have shown that the transition from quark-gluon plasma to the hadronic phase is a crossover [5]. We want to emphasize that methods of analytic continuation from either zero chemical potential or imaginary μ are only possible because the transition at zero chemical potential is a crossover - a smooth transition. Since a second order transition interpolates between a crossover and a first transition, there is an expectation of a second order critical end-point somewhere in the QCD $\mu - T$ phase diagram between these two regions. This is a field of active research and not enough can be said about it in an introduction. The reader is referred to the following reviews, which are ordered according to the publication year and are definitely not exhaustive : [6, 7, 8, 9].

The transition that we will be focused on in this thesis is the Roberge-Weiss (RW) transition [10]. This is a transition that occurs for imaginary values of the chemical potential, i.e., this is a transition that occurs in the $\mathrm{Im}[\mu] - T$ plane. This transition has been studied for many years and remains an active area of research. We will discuss this in detail in Chapter 3. We have proposed a new method of re-summing the Taylor series coefficients of the net-baryon density measured at zero and purely imaginary chemical potential using multi-point Padé approximants (Chapter 2). The goal of the analysis was to extract stable singularities closest to the imaginary μ axis (axis of expansion) and determine whether they were related to the Lee-Yang edge [11, 12, 13] singularities expected in the vicinity of the RW transition. An introduction to Lee Yang edge singularities is presented in Chapter 4. Chapter 5 should be seen as the main focus of this thesis as it shows our findings regarding the nature of the RW transition. We further discuss another stable pole obtained from the Padé analysis, in the context of simulations performed away from the RW transition. We will discuss the scaling of this point with respect to the chiral transition. Further, we have recently performed simulations on the 2D Ising model to test our claim about the Padé approximant extracting the relevant Lee-Yang edge singularities. To this end, we can safely conclude that our re-summation technique did indeed extract the relevant singularities. We present our findings in Chapter 4.

The content presented in the first part of this thesis is based on the following publications and conference proceedings that the author of this thesis, was a part of :

- Net Baryon number fluctuations, **Acta Physica Polonica B Proc. Supl. No 2 Vol. 14(2021)**,[arXiv:2101.02254].
- Contribution to understanding the phase structure of strong interaction matter: Lee-Yang edge singularities from lattice QCD - Dimopoulos, P. and Dini, L. and Di Renzo, F. and Goswami, J. and Nicotra, G. and Schmidt, C. and Singh, S. and Zambello, K. and Ziesché, F. Published in **Physical Review D 105,034513** on 26th February 2021, [arXiv:2110.15933]. In particular, for this paper, the author of this thesis was the **corresponding author**.
- Lee-Yang edge singularities in lattice QCD : A systematic study of singularities in the complex μ_B plane using rational approximations - Simran Singh, Petros Dimopoulos, Lorenzo Dini, Franceso Di Renzo, Jishnu Goswami, Guido

Nicotra, Christian Schmidt, Kevin Zambello, Felix Ziesché, Bielefeld-Parma Collaboration - **PoS LATTICE2021 (2022) 544**. In particular, this proceeding was a result of the talk given by the author at the International Lattice conference organized by MIT in 2021 via Zoom.

- Lee-Yang edge singularities in 2+1 flavor QCD with imaginary chemical potential - Guido Nicotra(Bielefeld U.), Petros Dimopoulos(Parma U.), Lorenzo Dini(Parma U.), Francesco Di Renzo(Parma U.), Jishnu Goswami(Bielefeld U.), Christian Schmidt(Bielefeld U.), Simran Singh(Parma U.), Kevin Zambello(Parma U.), Felix Ziesche(Bielefeld U.) - **PoS LATTICE2021 (2022) 260**

- Taylor expansions and Padé approximations for Lefschetz thimbles and beyond - Kevin Zambello, Franceco Di Renzo and Simran Singh - **PoS LATTICE2021 (2022) 336**

In addition, the author had the opportunity to be a speaker at the following seminars :

1. Invited talk at Massachusetts Institute of Technology MIT (USA) as part of the Virtual Lattice Field Theory Colloquium Series held via ZOOM on 07.10.2021 (link to recording : [14]).

2. Invited talk at University of Bielefeld on 25.10.2021, held in person, to talk about Padé approximations in the context of imaginary μ simulations of lattice QCD.

Furthermore, the work presented on using the 2D Ising model to demonstrate the feasibility of using Padé approximants to study the Lee-Yang edge singularities related to its phase transitions was done outside of the collaboration, between the author and Prof. Francesco Di Renzo at University of Parma.

1.2 Part II

The second part of the thesis is focused on thimble regularisation as a solution to the sign problem. The first half of this part discusses the origins of the sign problem in general, and a possible solution by the method of Lefshetz Thimbles. We also discuss our published results on the thimble regularisation of the Thirring model. The next half is focused on attempting to regularise non-abelian gauge theories using the technique of Lefschetz thimbles. Although this part does not contain any published material, we will show a few results relating to thimble regularisation SU(2) theories in 2 dimensions. Non-abelian gauge theories are not easy to study via thimble regularisation due to the presence of certain zero modes arising due to gauge symmetry called Torons. It will be described how these Torons cause problems in constructing a stable Lefschetz thimble and how this can be resolved by changing boundary conditions from periodic to twisted. We will then discuss the non triviality of finding saddle point solutions for non-abelian gauge theories and discuss preliminary results from our recently completed code. The discussion on thimble regularisation should be seen as a pedagogical discussion aimed as an

invitation to further study this subject. We will also briefly present our motivations for studying the theta term on the lattice using Lefschetz thimbles.

Starting from Chapter 6 we will explain the sign problem and the Lefschetz thimble [15] approach to solve it. We then again discuss Padé approximants in the context of multi-thimble simulations performed on the 1D Thirring model. We will then move on to applying Lefschetz thimbles to non-abelian gauge theories in the final Chapter 7 of this thesis. There we will discuss the non-trivialities of regularizing non-abelian gauge theories with thimbles and end with some numerical results. We finally end the chapter with an illustrative discussion on the scope of using thimble regularisation of Yang-Mills theory in the presence of a θ-term.

The content presented in the second part of this thesis is based on the following publications and conference proceedings that the author was a part of :

- One thimble regularisation of lattice field theories - Francesco Di Renzo, Kevin Zambello, Simran Singh - **PoS LATTICE2019 (2020) 105**, [arXiv:2002.00472v1]
- Taylor expansions on Lefschetz thimbles - Francesco Di Renzo, Kevin Zambello, Simran Singh published in **Physical Review D 103,034513** on 26th February 2021, [arXiv:2008.01622].

Part I

Insights on the QCD phase diagram a la Padé

Chapter 2

Rational approximations à la Padé

The concept of using rational functions to approximate arbitrary functions of matrices is not new in lattice studies of QCD. *Remez* type algorithms have been and are currently being used to calculate the roots of the Dirac operator for use in lattice QCD simulations. There are at least two well known types of Remez algorithms - the 1^{st} and the 2^{nd} Remez algorithm [1]. The first one is based on using polynomials as the approximating function and the second one using rational functions as approximants. The algorithm is based on Chebyshev's theorem which states that for any order of a polynomial (rational function), there is a unique polynomial (rational function) that minimises the error between the approximation data and the approximant (For a very nice introduction to Chebyshev's theorem and rational approximations see [17]). These algorithms are iterative in nature and require a continuous function as an input to be approximated. See [18] and references therein for extensive discussions on Remez type algorithms [2].

However, our first choice in constructing a rational approximation is not Remez, but rather based on *Padé Approximants* (See [21] for a thorough introduction to the topic.). One of the reasons for this is that the construction of a Padé approximant uses the input Taylor series coefficients in a direct manner, whereas the construction of a Remez type rational function first needs the construction of a good interpolating function followed by an iterative procedure needed to find the best rational function that approximates the interpolating function. Hence, the study of the propagation of errors from the errors on the input Taylor coefficients to the final rational function becomes more straightforward for the Padé as compared to the Remez. Padé approximants have been used and studied in the context of phase transitions as early as 1965 by M.E Fisher (see [22]). Moreover, it is well known that rational functions are much better at approximating certain kinds of functions than simple Taylor series. This is because a large class of functions contain non-analyticities that cannot be represented by an analytic series.
Our goal in this chapter is to convince the reader that not only should rational

[1] The reason we introduce Remez algorithms (although very briefly) is because we have implemented a version of this algorithm as a cross check to our lattice QCD results presented in [16].

[2] Unfortunately, the original work on Remez algorithms is not in English but can be found in [19, 20]

functions be preferred over Taylor series when approximating thermodynamic quantities, which become non-analytic at phase boundaries, but also to highlight the credibility of these approximations in identifying singularities of certain functions. We begin this chapter, by motivating the choice for using the mulit-Padé methods for studying lattice QCD data, taking inspiration from the already existing methods of Taylor series expansions and imaginary μ simulations in QCD, in Section 2.1. In Section 2.2 we describe the construction of the Padé approximations used. We then describe a few functions for which rational approximations out-perform Taylor series approximations in Section 2.3. In Section 2.4, we describe how the Padé re-summation of the same Taylor series can lead to a faster convergence to the true radius of convergence of the function (defined by the nearest singularity of the function). In Section 2.5 we discuss the scope of validity of our Padé approximation by means of numerical experiments performed on toy models like the 1D Thirring model. We then discuss in Section 2.6 the occurrence and consequences of *spurious* singularities. We will finally end the Chapter by discussing some convergence theorems, currently known about Padé approximations, in Section 2.8.

2.1 Numerically motivating the choice of Multi-Point Padé

One of the biggest challenges in lattice QCD simulations at finite chemical potential today is generating higher-order Taylor coefficients at $\mu = 0$ and purely imaginary $\mu_I = i\mu$. This is a computational cost problem - it gets very expensive to generate enough statistics to get reliable estimates for higher Taylor coefficients. But as we know, and will see in the up-coming sections, even for simple functions we need a high number of Taylor coefficients to extract the radius of convergence. In order to motivate our choice for multi-point Padé approximations, we will briefly describe the two main, current state of the art, methods used in lattice studies of QCD to probe the phase diagram at finite densities ($\mu \neq 0$).

I **Taylor expansion** about $\mu = 0$: Pioneered in [1], this method relies on Taylor expansions of the conserved charges in terms of their fluctuations simulated at zero chemical potential ($\mu = 0$). This is because at $\mu = 0$, lattice QCD does not suffer from a sign problem, hence it is possible to perform numerical simulations based on Monte Carlo methods. More precisely, the pressure of QCD is written in terms of an expansion about zero chemical potential as follows [3]

$$\frac{p(T,\mu)}{T^4} = \frac{p(T,0)}{T^4} + \frac{\partial(p/T^4)}{\partial(\mu/T)}|_{\mu=0} \left(\frac{\mu}{T}\right) + ... + \frac{1}{n!}\frac{\partial^n(p/T^4)}{\partial(\mu/T)^n}|_{\mu=0} \left(\frac{\mu}{T}\right)^n + ...$$
$$\chi_i^f = \frac{\partial^i(p/T^4)}{\partial(\mu_f/T)^i} \ , \ c_n^f = \frac{1}{n!}\chi_n^f \tag{2.1}$$

with χ_i^f the conserved charge fluctuations or *cumulant*, related to the quark flavor f, that we measure in standard lattice QCD simulations and c_n^f the

[3] At this stage we are not distinguishing between the quark and baryonic chemical potential as our goal is only to illustrate the method. The proper expansion variables will be discussed in Chapter 5.

respective Taylor coefficients. The goal of this method is to compute Taylor coefficients of high enough order to study the ratios of coefficients to estimate the radius of convergence. Such an estimate would give us hints for a possible transition point in the finite T , μ plane. The main drawback of this method lies in computing higher order Taylor coefficients. The statistics needed to compute higher derivatives of pressure increase with the order of derivative computed. Even today only a few Taylor coefficients are known with reasonable precision (see [9] for a recent review). And as we saw from Fig. 2.4, we need a large number of Taylor coefficients in general to estimate the radius of convergence.

II **Imaginary** μ simulations : Because the fermion determinant is real at purely imaginary values of chemical potential ($\mu_I = i\mu$, with $\mu \in \mathbb{R}$), another type of simulation is possible in lattice QCD. Here, simulations are first performed at purely imaginary values of μ which are then analytically continued back to real values of μ (see [2, 23] for the pioneering work). An important point to be noted is that since the partition function is an even power of μ_B/T, the Taylor expansions about $\mu_B/T = 0$ are related when we compute them from real or purely imaginary μ_B/T. Alternate coefficients will appear with negative signs of one Taylor series with respect to another. For example, if we consider the Taylor series expansion of the Pressure, we get :

$$\begin{aligned}
\frac{p(T,\mu)}{T^4} &= \frac{p(T,0)}{T^4} + \frac{\partial^2(p/T^4)}{\partial(\mu/T)^2}|_{\mu=0} \left(\frac{\mu}{T}\right)^2 + \frac{\partial^4(p/T^4)}{\partial(\mu/T)^4}|_{\mu=0} \left(\frac{\mu}{T}\right)^4 + ... \\
\frac{p(T,i\mu)}{T^4} &= \frac{p(T,0)}{T^4} - \frac{\partial^2(p/T^4)}{\partial(\mu/T)^2}|_{\mu=0} \left(\frac{\mu}{T}\right)^2 + \frac{\partial^4(p/T^4)}{\partial(\mu/T)^4}|_{\mu=0} \left(\frac{\mu}{T}\right)^4 + ...
\end{aligned} \tag{2.2}$$

The main drawback of this method lies in the limits of analytic continuation. This is because QCD can have non trivial singularities in the complex chemical potential plane. The will limit the values of real μ, upto which the series can be continued. A famous example of this is the Roberge-Weiss phase transition (discussed in Chapter 3) that occurs for QCD at imaginary quark chemical potential. This limits the analytic continuation using the method above to $\mu_B = \pi$.

This motivates us to go beyond Taylor expansions, and our method uses the information from both simulations at zero and imaginary chemical potentials to construct a rational approximation called *multi-point* Padé. In order to implement the multi-point Padé we still have to perform the standard lattice QCD simulations at imaginary μ_B and extract the relevant Taylor coefficients. This in-itself is an involved procedure and we show, in the form of a "dictionary", the relation between code output (traces of the fermion determinant) and the final cumulants used in Appendix A. All the simulations for the construction of Padé approximants shown in this thesis were exclusively performed in MATLAB [24] and JupyterLAb [25] was used for the plots.

2.2 Construction of Padé

Our goal in this section is to demonstrate how to build Padé approximants from given Taylor series data of a function[4]. For clarity of notation we mention that a [m,n] Padé is a rational function with the numerator being a polynomial of $\mathcal{O}(n)$ and denominator a polynomial of $\mathcal{O}(m)$. Hence, the number of undetermined coefficients in an [m,n] Padé will be $(m+1)+(n+1)$. However, because it is a ratio of polynomials, one coefficient can be set to unity and therefore, we have $m+n+1$ undetermined coefficients. Also, an $\mathcal{O}(p)$ polynomial has $p+1$ coefficients. This means to build a Padé of order [m,n] we need at least $\mathcal{O}(m+n)$ input Taylor coefficients.

Let us begin by considering a function $f(x)$ which is only known up to $\mathcal{O}(L)$ about a single expansion point (which in the example below is the origin):

$$f(x) = \sum_{i=0}^{L} c_i\, x^i + \mathcal{O}(x^{L+1}) \tag{2.3}$$

Using the Taylor coefficients we would like to construct a rational function $R_n^m(x)$ of order [m,n] given by the ratio of two polynomials as:

$$R_n^m(x) = \frac{P_m(x)}{\tilde{Q}_n(x)} = \frac{P_m(x)}{1+Q_n(x)} = \frac{\sum\limits_{i=0}^{m} a_i\, x^i}{1+\sum\limits_{j=1}^{n} b_j\, x^j}\,, \tag{2.4}$$

The simplest way to obtain the coefficients a_i & b_i in terms of c_i is to equate Eq. 2.3 with Eq. 2.4 and solve for coefficients at each order of x (making use of the functional independence of x^n for different n) as follows

$$\begin{aligned}\sum_{i=0}^{m} a_i\, x^i = P_m(x) &= f(x)\,(1+Q_n(x)) \\ &= (\sum_{i=0}^{L} c_i\, x^i)\,(1+\sum_{j=1}^{n} b_j\, x^j)\,,\end{aligned}$$

We then obtain the following (Eq. 2.5) system of simultaneous, linear equations to be solved. This method of building a Padé in literature is known as *approximation through order*.

$$\begin{aligned} a_0 &= c_0 \\ a_1 &= c_1 + b_1 c_0 \\ a_2 &= c_2 + b_1 c_1 + b_2 c_0 \\ &\dots \end{aligned} \tag{2.5}$$

The set of equations presented in Eq. 2.5 can be obtained from Eq. 2.6 by setting $x = 0$ when equation Eq. 2.3 with Eq 2.5 and utilising the following tower of equations built from differentiating order by order.

[4]We would like to point out a very comprehensive reference book on Padé approximants that discusses the existence, uniqueness, convergence and beyond of Padé approximations: [21]

$$\begin{aligned} P_m(x) - f(x)Q_n(x) &= f(x) \\ P'_m(x) - f'(x)Q_n(x) - f(x)Q'_n(x) &= f'(x) \\ P''_m(x) - f''(x)Q_n(x) - f(x)Q''_n(x) & \\ - 2f'(x)Q'_n(x) &= f''(x) \\ &\dots \end{aligned} \tag{2.6}$$

We would also like to mention another equivalent method of solving for the coefficients a_i & b_i in terms of c_i, but this time simultaneously solving the following (Eq. 2.7) set of non-linear equations. This tower of equations is obtained by extracting Taylor coefficients of R_n^m about an expansion point (we again choose $x = 0$ for the following) and equating them with the corresponding coefficients of $f(x)$ as follows : $\frac{d^k}{dx^k} R_n^m(x) = f^{(k)}(x)$, i.e. [5],

$$\begin{aligned} a_0 &= f(0) \\ a_1 - a_0 b_1 &= f'(0) \\ 2a_2 - 2a_1 b_1 + a_0(2b_1^2 - 2b_2) &= f''(0) \\ &\dots \end{aligned} \tag{2.7}$$

This was actually the first method we attempted to solve with, but it turns out to be very inconvenient and one can only solve for relatively small orders. Hence, we switched to the linear solver whose obvious disadvantage was that the systems to be solved were at many times ill-conditioned. But in those situations, care was taken to ensure that the resulting set of solutions was stable.

Until now we have only been focused on building Padé approximants from Taylor series about single expansion points. Notice that a very practical problem with *single* point Padé approximants is that in order to build even a small order rational function, around double the number of Taylor coefficients are needed. And this is usually the roadblock we face in studying QCD at finite density - computing higher-order Taylor coefficients is very hard and expensive. This small amount of Taylor series data might still work well for meromorphic functions but would completely fail for guessing the presence of, for example, a branch cut (see Fig. 2.3 for the zero-pole structure of a branch cut), since we need a series of poles on a line to understand the presence of a cut. For this reason, we will now focus our attention on multi-expansion-point Padé approximants (from now on we will refer to these simply as "multi-Padé" approximants.). We will implement this very easily by looking at Eq. 2.6

[5] Again, we assume we know the derivatives in $x = 0$

$$
\begin{aligned}
P_m(x_1) - f(x_1)Q_n(x_1) &= f(x_1) \\
P'_m(x_1) - f'(x_1)Q_n(x_1) - f(x_1)Q'_n(x_1) &= f'(x_1) \\
&\dots \\
P_m(x_2) - f(x_2)Q_n(x_2) &= f(x_2) \\
P'_m(x_2) - f'(x_2)Q_n(x_2) - f(x_2)Q'_n(x_2) &= f'(x_2) \\
&\dots \\
P_m(x_N) - f(x_N)Q_n(x_N) &= f(x_N) \\
P'_m(x_N) - f'(x_N)Q_n(x_N) - f(x_N)Q'_n(x_N) &= f'(x_N) \\
&\dots ,
\end{aligned}
\tag{2.8}
$$

which is once again a linear system in $n+m+1$ unknowns where now $n+m+1 = \sum_{i=1}^{N}(L_i+1)$. In the previous formula, the highest order of derivative which we know (i.e., L_i) can be different for different points. To illustrate what we mean, consider a function $f(x)$, known about three points : $\{f(x_1), f(x_2), f(x_3)\}$. Further, consider that we know its first derivatives about two points : $\{f'(x_1), f'(x_3)\}$. With the given Taylor coefficients about the three points, our goal is to construct the coefficients of the polynomials $P_m(x)$ and $Q_n(x)$, such that, when expanded about the origin, the rational function has the form as the first line in Eq. 2.5. Since we are only given five Taylor coefficients, we can only construct rational functions of the order [m,n] = [2,2],[1,3],[3,1]. By choosing to construct [2,2], the linear system to be solved would become :

$$
\begin{aligned}
a_0 + a_1(x_1) + a_2(x_1)^2 - f(x_1)\left(b_1(x_1) + b_2(x_1)^2\right) &= f(x_1) \\
a_1 + 2*a_2(x_1) - \left(f'(x_1)(x_1) + f(x_1)\right)b_1 - \left(f'(x_1)(x_1)^2 + 2*f(x_1)(x_1)\right)b_2 &= f'(x_1) \\
a_0 + a_1(x_2) + a_2(x_2)^2 - f(x_2)\left(b_1(x_2) + b_2(x_2)^2\right) &= f(x_2) \\
a_0 + a_1(x_3) + a_2(x_3)^2 - f(x_3)\left(b_1(x_3) + b_2(x_3)^2\right) &= f(x_3) \\
a_1 + 2*a_2(x_3) - \left(f'(x_3)(x_3) + f(x_3)\right)b_1 - \left(f'(x_3)(x_3)^2 + 2*f(x_3)(x_3)\right)b_2 &= f'(x_3)
\end{aligned}
\tag{2.9}
$$

Multi-points Padé approximations set up in the above form will be our choice for the analysis of this work. To see how this is implemented in a MATLAB script, see section 5.2.2.

2.3 Taylor vs Rational approximations

In this section, we will demonstrate the effectiveness of rational functions to approximate functions with simple poles and branch cuts over their Taylor series counterparts. We focus on functions with poles and branch cuts because of their relevance in the study of Lee Yang edge singularities which will be discussed in detail in Chapter 4. We will first consider a function with isolated poles, i.e, analytic everywhere is the complex plane except for a finite number of poles - also known as *meromorphic* functions.

$$
\frac{z}{(z-c_1)(z-c_2)} \tag{2.10}
$$

with c_1 and c_2 can be arbitrary complex numbers (but for the purposes of Figs. 2.1 & 2.2 have been chosen to be $c_1 = 1+2i$ and $c_2 = 3-4i$.). As already seen in

section 2.2, in order to determine a [m,n] Padé, a Taylor series of at least $\mathcal{O}(m+n)$ is required. In Fig. 2.1(Left), we display how the Padé approximation (constructed at the origin) compares with the corresponding Taylor series using the same Taylor series expansion with even less number of coefficients (a [2,3] Padé uses six Taylor coefficients, hence an $\mathcal{O}(5)$ Taylor series, which is less information than the $\mathcal{O}(7)$ series plotted in Fig. 2.1). In Fig. 2.1, we show both the real and imaginary restrictions of the complex rational function obtained from the analysis. Moving onto Fig. 2.2, we display the results for the *singularity structure*[6] for two different orders of the approximant, i.e., a [2,3] and a [3,4] Padé to show the stability of the genuine poles of the function. Notice the extra structure in addition to the expected poles c_1 & c_2 : this extra structure made up of zero-pole pairings is harmless since these can be factored out of the rational function (More on this in Section 2.6).

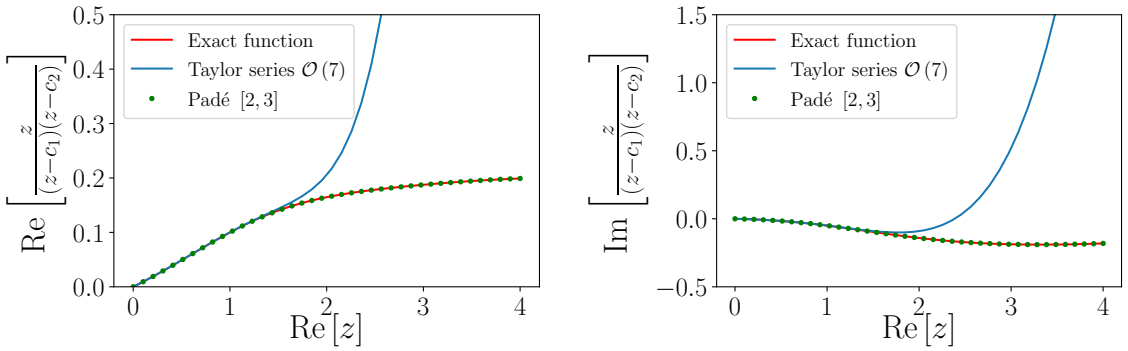

Figure 2.1: A function with complex poles $\frac{z}{(z-c_1)(z-c_2)}$ and its approximation by Taylor vs Padé using the same information

The next function to consider is a function with a branch cut:

$$\sqrt{\frac{2z+1}{z+6}} \tag{2.11}$$

A very reasonable question to ask at this point will be : How can we expect a Padé approximant, which is rational by definition and hence only able to produce poles, to approximate an irrational branch cut? The answer is that it clusters poles along the cut (for details, see [21], Chapter 10). This can be seen via the following integration formula

$$(1+x)^{-1/2} = \frac{1}{\pi}\int_1^\infty \frac{dz}{(x+z)(z-1)^{1/2}}$$

In Fig. 2.3(Left) we display the approximation itself for the function shown in Eq. 2.11. As can be seen, even in the region where there aren't any non-analyticities, the Taylor expansion fails, which is to be expected because the expansion is about $z=0$ and the branch point at $z=-0.5$ limits the radius of convergence. But the remarkable feature is that the Padé approximant built from the same Taylor series (about $z=0$ and at a lower order), is able to approximate the function far beyond the radius of convergence of the Taylor series it was built from. Moving on to the singular structure in Fig. 2.3 (Right), we display the zero-pole structure found by the Padé, lying along the branch cut between $x=-0.5$ to $x=-6$ with both zeros

[6]We will use the term singularity structure repeatedly in this thesis to mean the zero-pole structure found by the Padé approximant.

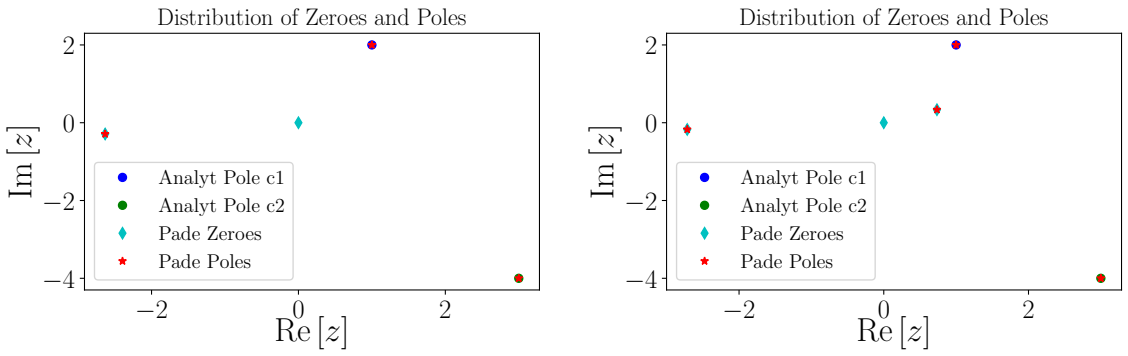

Figure 2.2: Recovery of poles of the function $\frac{z}{(z-c_1)(z-c_2)}$ from Padé at [2,3] and [3,4] order

and poles lying on the branch cut and not canceling with each other. This is a genuine feature of the manifestation of a branch cut by a rational function. As we increase the order of the Padé, the zeros and poles become denser and denser along the cut.

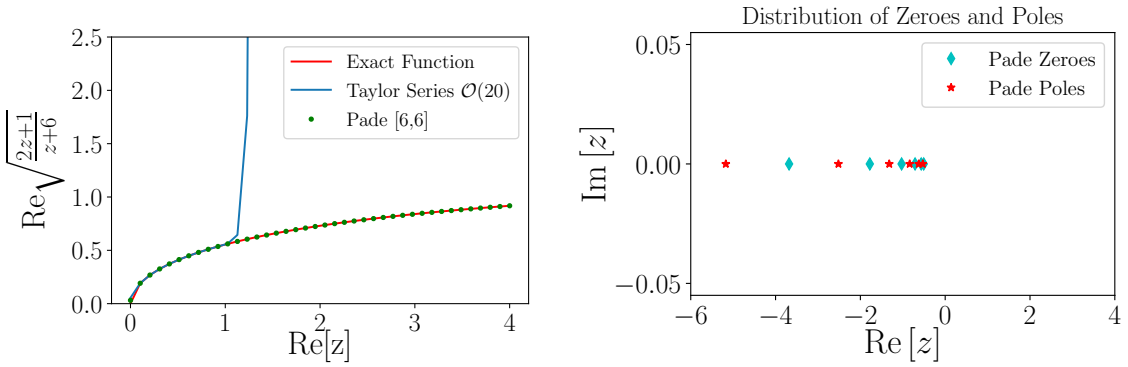

Figure 2.3: A function with branch cut (Eq. 2.11) and its approximation (left) and singular structure (right) by a Padé.

2.4 Comments on Radii of convergence from Taylor vs Padé

It is hard to overstate the importance of extracting the radius of convergence of a given series, reliably, in lattice QCD simulations. Most lattice simulations are currently based on extracting higher-order Taylor coefficients at finite μ_B in order to determine radii of convergence from those series. In the absence of a very large number of Taylor coefficients, the ratio tests, however precise, cannot help us much more than just giving bounds. As can be seen from the plots above, a rational function built from even a small number of Taylor coefficients can give the precise location of the poles of the function - getting rid of the need for having very high Taylor coefficients.
Basically, the question that one would like to try to answer is whether the closest pole found by the Padé approximation is related in a straightforward way to the

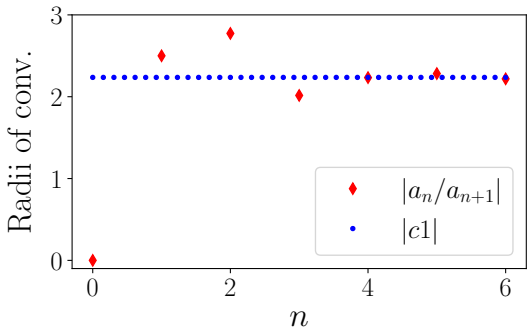

Figure 2.4: This plot shows the ineffectiveness of the Taylor expansion to estimate the radius of convergence even for a function with a simple pole.

radius of convergence. Of course, this will depend on the type of the function as will be described below.

- **Case I** : *Meromorphic functions*
  This class of functions is defined by having a finite number of poles in any given disc. In this case, the Padé approximant gives the radius of convergence exactly by finding the closest pole to the point or axis of expansion, whereas higher-order Taylor coefficients are needed to estimate a faithful bound on the radius of convergence. We refer to reader to look at Fig. 2.2 to see how even a low order Padé ($\mathcal{O}[2,3]$) gives us the exact location of the closest pole (labelled c_1 in the plot). However, if we try to estimate this pole by the ratio test, using only Taylor coefficients, we get the following Fig. 2.4. Using the same Taylor coefficients as used to build the Padé (which gave the exact pole) - we get an error of ~ 2 %

- **Case II** : *Functions with branch points*
  Let us now consider a more interesting class of functions : those with with branch points/cuts. Since a Padé approximation is, by definition, a rational function, we will show via Fig. 2.5 the rate of convergence of the closest pole (zero) to the true radius of convergence of the function vs. the rate of convergence via the ratio test using simple Taylor coefficients. We will consider the distance to end point of a branch cut closest to the point (axis) of expansion to be the relevant radius of convergence. We define the *rate of convergence* to the true radius of convergence as the relative distance between the closest pole found from the Padé approximation multiplied by 100. We will consider two functions with branch cuts, one of them being the function already plotted in Fig 2.3. It has a branch cut starting at $z = -0.5$ and ending at $z = -6$. Note that this function is zero at $z = -0.5$, hence if we Taylor expand around $z = 0$, then we need to, strictly speaking, look at the closest zero and not the pole of our Padé approximation to determine the radius of convergence (since this zero is a branch point and not a simple zero of the function under consideration). The other function that we choose is $1.0/\sqrt{2z+1}$. This has been chosen to contrast with the previous function in having a singularity at the closest branch point to the origin. In this case, we will look at the closest pole of the Padé. Again the rates of convergence of the poles toward the true radius of convergence are plotted in Fig. 2.5.

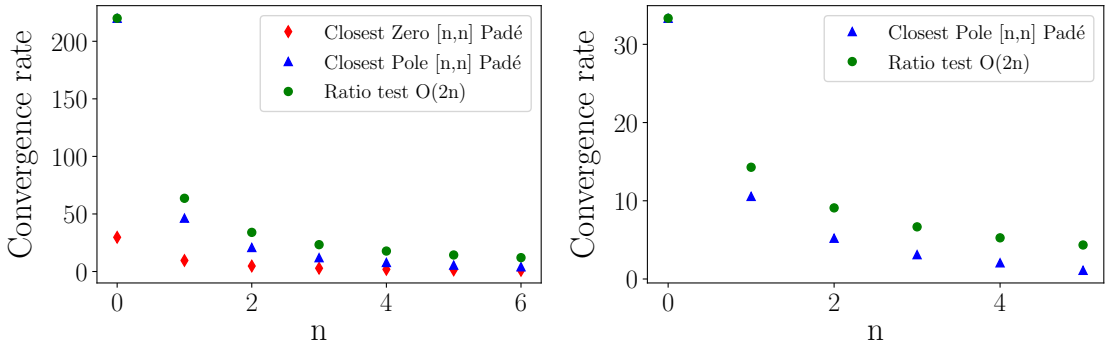

Figure 2.5: Rate of convergence of ratio test vs Padé with increasing order.

2.5 Scope of validity using 0+1 D Thirring model

Many of our results shown in the following sections will be based on numerical experiments performed on an exactly solvable (0+1) dimensional fermionic model that was initially studied as a toy model for the sign problem in [26, 27]. This model can also be seen as a (0+1) D version of the Thirring model[28] (which was originally defined in (1+1) D as a fermionic model with quartic interaction). We will briefly comment below on why the fermionic model that we will study is be called a 1D or a (0+1)D Thirring model in literature ([29, 30, 31, 32]) and we will use this terminology for the rest of the thesis.

The model that we will use (discussion adapted from [33]) describes two fermion flavours sitting at a single spatial site, with a continuum Lagrangian density given by :

$$L_{TH} = \bar{\chi}\left(\gamma_0 \frac{d}{dt} + m + \mu\gamma_0\right)\chi + \frac{g^2}{2}\left(\bar{\chi}\gamma_0\chi\right)^2 \ , \tag{2.12}$$

where χ is the two-component, time-dependent spinor, and hence γ_0 is a Pauli matrix. The reason we will call this the (0+1) D Thirring model should now be apparent : the interaction term in Eq. 2.12 is the (0+1) version of current-current interaction term in the original (1+1) D Thirring model [28]. In order to reach the version of the model we will use in this thesis a few more steps are needed to be performed on the partition function associated to the Lagrangian mentioned in Eq. 2.12. First, the quartic interaction is eliminated by introducing an auxiliary field, and then the resulting action is discretized (in the time coordinate). Using a staggered fermion formulation we reach the following partition function [27] :

$$S = \beta \sum_n \left(1 - \cos\left(x_n\right)\right) - \log\left(\det D\right) \ , \tag{2.13}$$

with

$$\det D = \frac{1}{2^{L-1}}\left(\cosh\left(L\hat{\mu} + i\sum_n x_n\right) + \cosh\left(L\sinh^{-1}\left(\hat{m}\right)\right)\right) \ , \tag{2.14}$$

where x_n denotes the (rendered dimensionless by multiplying with lattice spacing), discretized auxiliary field, L stands for the number of lattice sites, and $\hat{m} = am$

,$\hat{\mu} = a\mu$ are the mass and number density in lattice units respectively.
This model has been studied in [31] using multi-point Padé and happens to be the work where the idea of applying Padé to QCD at imaginary μ ([16]) was born. We will again come back to this model in the framework of Lefschetz thimbles in Chapter 6.
This model is chosen by us to perform numerical experiments with Padé approximants because its partition function has a known analytical solution and hence is a good testing ground for building approximations. Also, there exists closed-form expressions for the chiral condensate and the fermionic number density for this model and both these observables can be seen to have a string of poles at a certain value of μ, parallel to the imaginary μ axis and a string of zeros at $\mathrm{Re}[\hat{\mu}] = 0$. For the purposes of these experiments we will simulate the number density of the 1D Thirring model:

$$N_{\beta,L,\hat{m}}(\hat{\mu}) = \frac{I_1(\beta)^L \sinh(L\hat{\mu})}{I_1(\beta)^L \cosh(L\hat{\mu}) + I_0(\beta)^L cosh(Lsinh^{-1}(\hat{m}))} \ , \tag{2.15}$$

where I_1 and I_0 denote the first two modified Bessel functions of the first kind. We perform our analysis of the singularity structure of the number density simulated at $\beta = 1$, $L = 8$, and $\hat{m} = 2$. Because we know the location of the exact poles and zeroes of the 1D Thirring model, this model is well suited to either validate or invalidate our Padé ansatz.

2.5.1 Interval Dependence

We will first demonstrate a feature of the multi-point Padé which may seem obvious *aposteriori* but will be essential to our analysis. As has been seen, when we perform a multi-point Padé analysis, our input Taylor coefficients are spread over an interval of choice. We found a high sensitivity of the poles of the Padé found, on the interval chosen for the multi-point. Specifically, we found that to get the best estimate when looking for genuine poles, an interval centered around that pole should be chosen. We agree that this may not be the best observation in support of the multi-point Padé since for most systems of interest we don't where the singularity lies to begin with. In that case, our suggestion would be to *slide* the interval of sampling in order to probe singular structure. We will demonstrate this interval dependence using the 1D Thirring model with the parameters listed above. Before proceeding, it is important to mention that for the above-stated parameters the number density of the 1D Thirring model has an infinity of poles separated by a fixed amount, parallel to the imaginary $\hat{\mu}$ axis, at real value of $\hat{\mu} \sim 2.25$ and $\hat{\mu} \sim -2.25$ and an infinite set of zeros at along the imaginary $\hat{\mu}$ axis. What we will demonstrate below is taking three intervals on the $\hat{\mu}$ axis, each centered about a different set of poles/zeros and using the same number and order of Taylor coefficients in each interval, therefore studying the sensitivity of the approximation to the different sets of exact poles/zeros of the number density.

First consider the top plot in Fig. 2.6 : The interval chosen is $\hat{\mu} \in \{-2, 2\}$. This interval is centered about $\hat{\mu} = 0$. It can be seen that the Padé is able to locate up to five zeros of the function correctly (see blue diamonds and green circles). As far as poles are concerned, the approximant fails at reproducing any of the pole.
Next, consider the center plot in Fig. 2.6 : The interval chosen is $\hat{\mu} \in \{0, 4\}$. This

interval is centered about $\hat{\mu}_R \sim 2$. It can be seen that the Padé is able to locate roughly six poles (four exactly and two almost completely) located in the right half of the complex $\hat{\mu}$ plane (see red stars and black dots). It is also seen that the Padé has missed the information concerning the zeros located along the imaginary $\hat{\mu}$ axis and placed the zeros incorrectly.

Lastly, consider the bottom plot in Fig. 2.6 : The interval chosen is $\hat{\mu} \in \{-4, 4\}$. This interval is centered about $\hat{\mu} = 0$, but also the left half of the interval covers the poles in the left half of the plane and the right one covers the right line of poles. Before proceeding, let us reiterate that the order of the Padé here is fixed, so this extended interval can only do so much. It is readily seen that the Padé is able to locate two poles in the left half of the plane and two poles on the right as well as one zero. An interesting point to note is that the Padé has distributed the poles more accurately than the zeros.

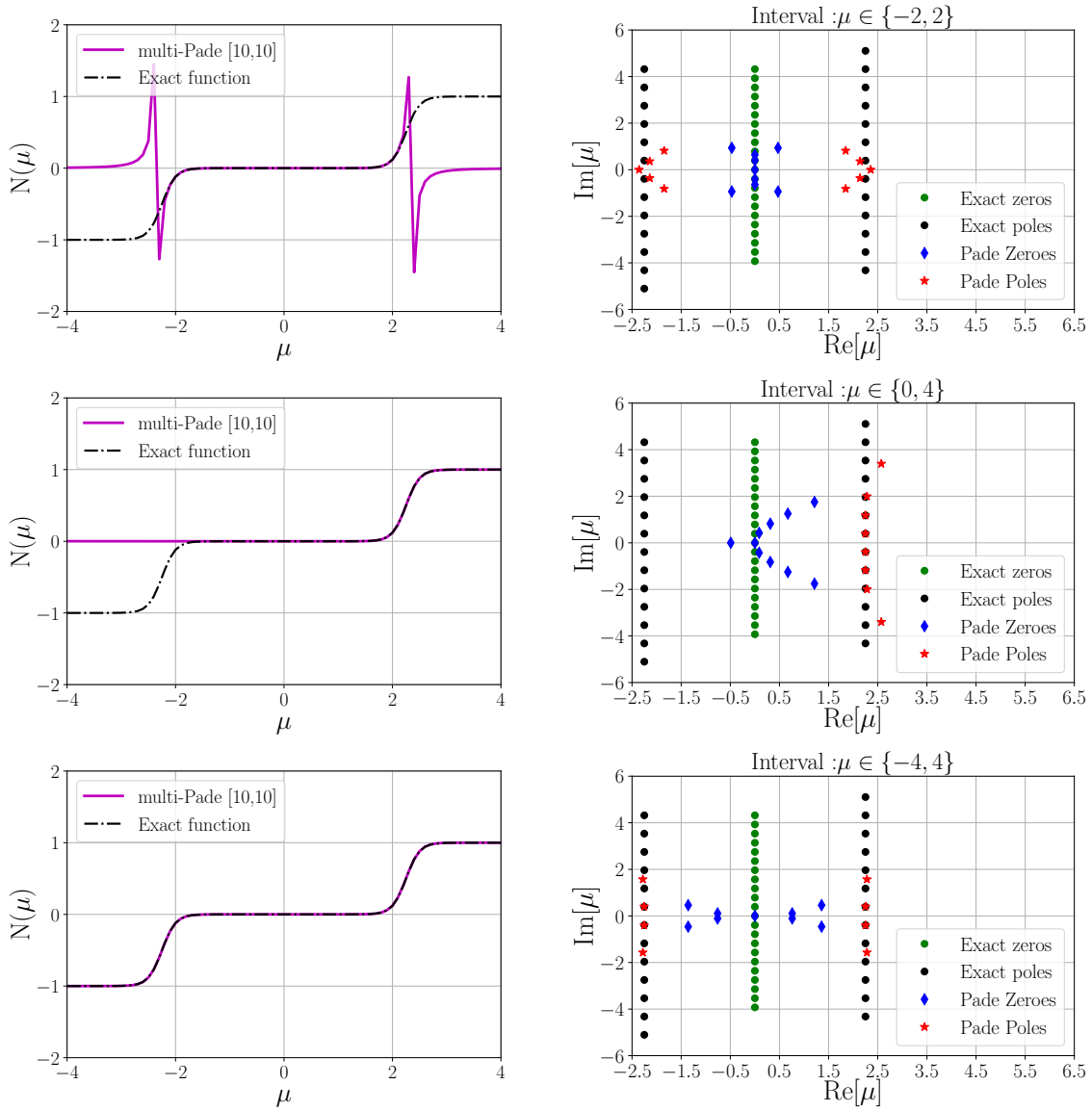

Figure 2.6: Interval sensitivity of the Padé approximant to the zeros/poles of the function (left) approximant (right) singular structure. (Top) : Interval $\hat{\mu} \in \{-2, 2\}$, (center) : Interval $\hat{\mu} \in \{0, 4\}$, (bottom) : Interval $\hat{\mu} \in \{-4, 4\}$

2.5.2 Distinguishing between different types of singularity

Here we wish to demonstrate how a rational function approximates different types of singularities. An important point to notice will be the ability of the rational function to faithfully distinguish between different kinds of singularities. This will be useful in understanding and classifying unknown functions through their singularity structure.

The first function that we consider in Fig. 2.7 is a corner function. Technically it is the super set of the well known cusp functions. This type of function is continuous but its derivative is not. Notice the cluster of zero-pole pairs along the axis where the cusp is located.

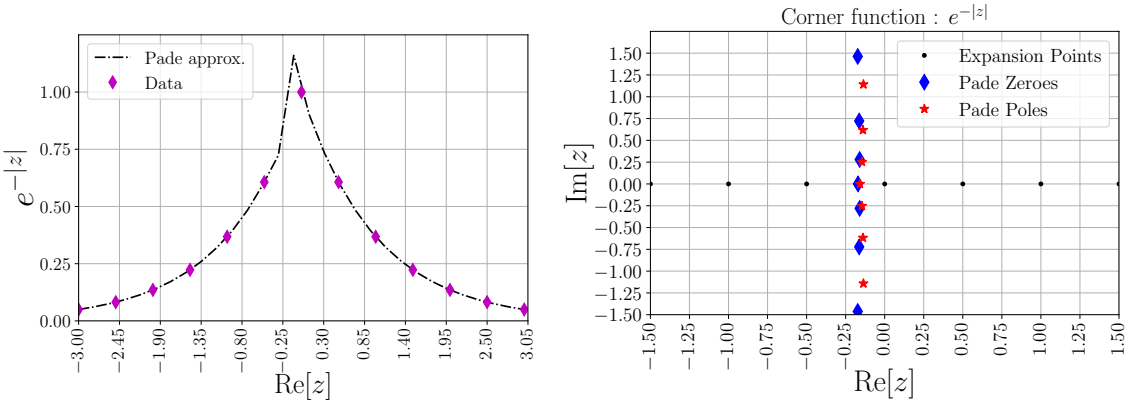

Figure 2.7: Padé approximation of a corner function : (left) Approximation (right) Zero Pole structure

The next function in Fig. 2.8 is of great importance, since it is a function with a discontinuity. We will encounter these in systems with first order phase transitions. The Padé has put a structure which should remind us of a branch cut (discussed in Section 2.3) crossing the axis at the position of the cut, and is distinct from the singularity structure of the function studied in Fig. 2.7.

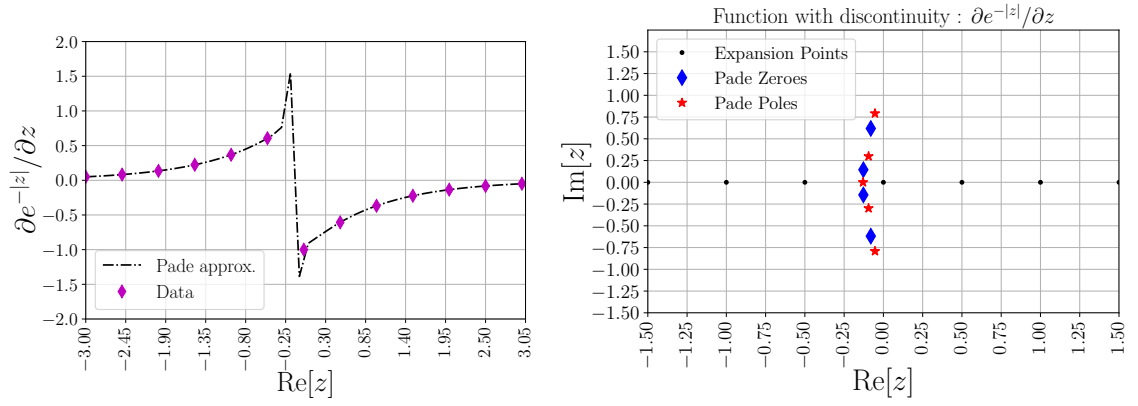

Figure 2.8: Padé approximation of a discontinuous function (a function that is continuous but its derivative is not) : (left) Approximation (right) Zero Pole structure

The next example is of a function with two cusps (a cusp (or a spinode) is a point where two branches of a curve meet and have equal tangents). A very interesting point to notice about this singular structure is the two branch-cuts that originate

at $x = \pm 2$ making angles corresponding to their powers. The (sign) modulus causes the branches cuts to spilt at the cusps.

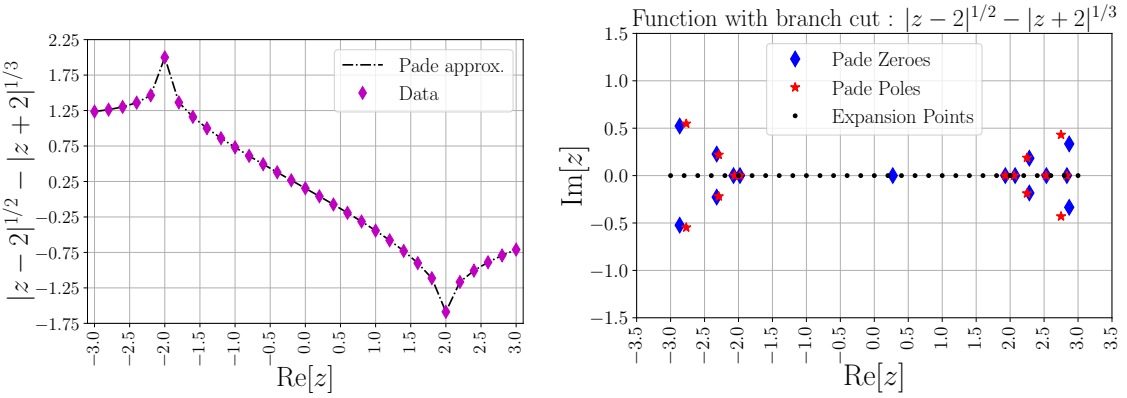

Figure 2.9: Padé approximation of a cusp function : (Left) Approximation ; (Right) Zero Pole structure

The function considered in Fig. 2.10 is $e^{-z/(z+1)}$. This function has an essential singularity at $z = -1$. The structure found by the Padé has been seen to be pretty consistent with this particular kind of an essential singularity.

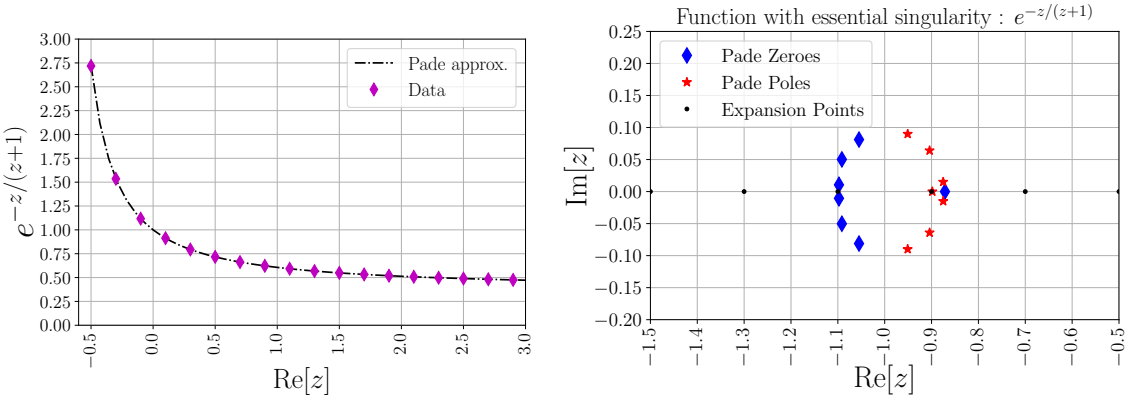

Figure 2.10: Padé approximation of function with essential singularity : (left) Approximation (right) Zero Pole structure

The last function that we consider is a branch cut (we have already seen two examples of functions with branch cuts in Section 2.3). However, we would like to demonstrate it again for two reasons. The first is the approximation itself in Fig. 2.11 (left) and its analytic continuation. In this example, we used an interval on the imaginary z axis. We then continue it to real z and study the restriction of the complex function on the real axis. For the zero poles structure, we already know what to expect for a branch cut and see it in Fig. 2.12. We also see more zeros and poles accumulating along the branch cut as we increase the order of the Padé.

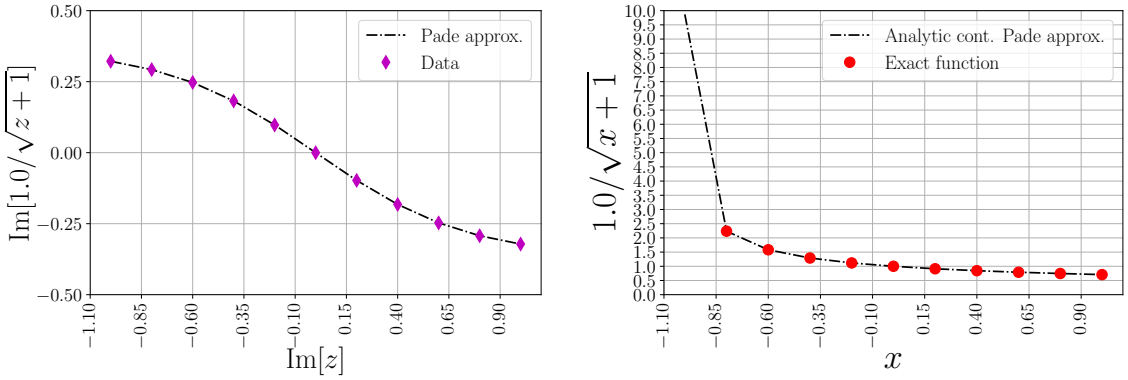

Figure 2.11: Padé approximation of a function with branch cut : (left) Approximation with respect to the original data (right) Analytic continuation to the real axis as compared with exact data.

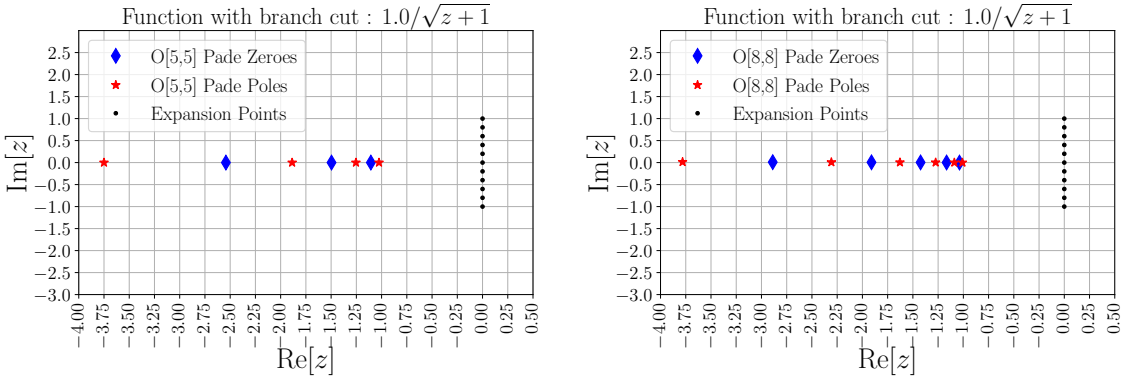

Figure 2.12: Singularity structure from the Padé approximation : (left) $\mathcal{O}[5,5]$ Padé (right) $\mathcal{O}[8,8]$ Padé

2.6 Comments on the occurrence of spurious singularities

More often than not, the singularities obtained from Padé, or any other rational approximation, are not accepted as being *genuine* features of the unknown function being approximated. In order to begin addressing this issue we would first like to list the types of spurious poles known in literature and then argue how we are safe from them :

1. *Exactly cancelling pairs of zeroes and poles* : As the name suggests - it is not just sufficient to calculate the poles of a rational function. One should either list the zeroes as well or calculate the residue of each pole and discard the poles corresponding to vanishing residue. We are safe from these in our analyses since we plot both the zeroes and poles of the approximation and discard the cancelling pairs. Examples for the exactly cancelling zero-pole pairs can be seen in Fig. 2.2, when we try to demand a higher order (in this case more than two in the denominator) of the rational function which only has two genuine poles.

2. *Unstable isolated poles* : After discarding the poles arising in zero-pole pairs, we have to deal with the isolated poles which can, at first glance, be mistaken

for genuine singularities. But based on the theory of Padé approximations [21], genuine poles remain stable under changing the order of the approximation. This means it is not sufficient to look at a single rational approximation of the data. Different orders of the rational function have to be built using different sets of data and stability of the singularity structure needs to be established before estimating error bars due to statistical errors. In our analysis we have checked against this type of spurious pole by constructing many variations of the rational functions. A very nice visualisation of this will be seen in a later chapter (Chapter 5), in Fig. 5.13, where the only genuine information in the imaginary plane of the expansion variable - remains fixed.

3. *Zero-pole pairs and Isolated poles in the presence of Noisy data* : In the presence of noise the above described points get modified in the following ways - zero-pole pairs may not cancel exactly but may have some "distance" between them depending on the magnitude of the noise present. But even in this case it is sufficient to calculate the residue and discard poles with nearly vanishing residues. On the other hand, *isolated* poles don't exactly stay stable, but in this case they are found to move around in *ellipses* of standard deviation consistent with the amount of noise present in the data. A numerical example to demonstrate this effect is shown in Fig. 2.13. Here we approximate the number density of the 1D Thirring model using Padé approximation, with the same parameters used as in Section 2.5.1. The experiment was to add noise to the Taylor coefficient data for the 1D Thirring model with two combinations of errors : the first with 1% and 10% noise on the first and second Taylor coefficients and the second with 5% and 15% percent noise on the first and second Taylor coefficient respectively. Each figure represents and average of 5000 samples drawn each for the two different error values shown taken in bins of 50 to show the 100 points in Fig. 2.13. It can be seen clearly how increasing the noise on clean data affects the sensitivity to the closest pole. Though we can argue that we checked for the stability of the poles before estimating statistical errors - strictly speaking the systematical (arising from changing orders) and statistical (arising from noisy data) errors are correlated. But as seen from our numerical experiments and based on observations within [21], it is safe to say that as long as we only focus on the singularity closest to the axis of expansion we are doing fine.

2.7 Axes of expansion

Until now all of our tests and applications of Padé approximations have been based on using Taylor series coefficients along a single axis in the complex plane of the expansion variable. The goal of this section is to determine if we benefit from *mixing* Taylor coefficients along different axes. Mathematically, this seems obvious, because when we only use expansion points along a single axis in the complex plane of the expansion variable, any information we obtain by from the restriction of the resulting complex function along the other axis is completely unconstrained. Therefore, adding a few points along the orthogonal axis can only be beneficial in constraining the rational approximation in the complex plane of the expansion variable. However, our primary focus lies in determining the singularity structure

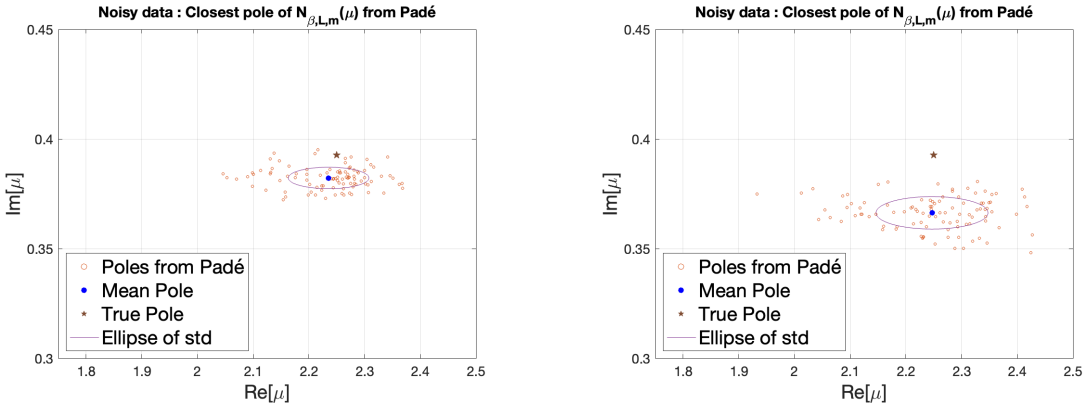

Figure 2.13: Sensitivity of the Padé approximant in the presence of noise : (Left) The input Taylor coefficients of have 1% noise on the first coefficient and 10% noise on the second; (Right) : The input Taylor coefficients of have 5% noise on the first coefficient and 15% noise on the second. Increasing error decreases the sensitivity to the true pole in proportion to the magnitude of the noise present.

of a given thermodynamic function, so this is a direction worth exploring. The physical motivation for doing this in our lattice QCD simulations, which are as of now done completely along the imaginary μ axis, comes from adding (a few) Taylor coefficients obtained along the *real* μ axis either by re-weighting or some other techniques for very small values of μ such that the sign problem is not significant. A direct implementation of this is algorithmically challenging, so once again we will numerically test this idea on a toy model first.

The most useful toy-model for us is the 1D Thirring model because of its rich singularity structure and an exact functional form available to us to compare the approximation with. We will consider (again) as our function to be approximated the number density in the 1D Thirring model (Shown in eqn. 2.15). The simulation parameters for the model are chosen to enhance the imaginary signal of the number density on the imaginary axis in order to make the signal clear. The parameters we will be working with, in this section, are : $\beta = 2, L = 2, \mu, m = 0.5$.

The first experiment formed was using completely either the imaginary axis or the real axis with exactly the same input points for comparison. The next step is to select half the coefficients from the real and half from the imaginary μ axis. From these coefficients we will construct the three rational functions and compare their respective restrictions on both the imaginary and the real μ axis. As can be seen from Fig. 2.14, the Padé constructed from the purely real data (blue dashed curve), does better on the real μ axis and fails quite quickly on the imaginary μ axis. On the other hand, the approximation constructed from purely imaginary data (dashed green curve) does better on the imaginary μ axis and fails on the real μ axis. However, the approximation constructed from the mixed data (dashed magenta) does quite well on both the axes. Next we will consider the singularity structure of these three Padé approximants. Presented in Fig. 2.15 are the respective singularity structures compared with the analytic known results for the three cases mentioned above : (Top Left) : Padé approximation obtained from considering Taylor coefficients only on the real μ axis; (Top Right) : Padé approximation obtained from considering Taylor coefficients only on the imaginary μ axis; (Bottom) : Padé approximation obtained from considering Taylor coefficients on both the real and imaginary μ axis.

As can be seen, the Padé approximant in the case of mixed coefficients is sensitive to three genuine poles of the function as opposed to only two in the other two cases. This can also be attributed to the interval dependence of the multi-point Padé approximations seen in Section 2.5.1.

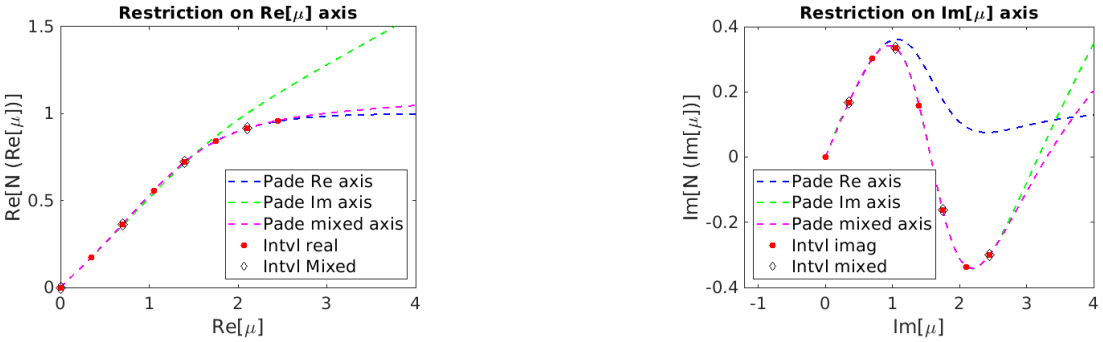

Figure 2.14: Plotted are the restrictions of the number density for the 1D Thirring model with parameters $\beta = 2, L = 2, \mu, m = 0.5$ on (Left) the real μ axis and (Right) the imaginary μ axis. The blue dashed lines represent the Padé approximation obtained by considering Taylor coefficients (red, filled dots, Left plot) on the real μ axis; the green dashed lines represent the Padé approximation obtained by considering Taylor coefficients along the imaginary μ (red, filled dots, Right plot) axis and the magenta dashed lines are obtained from taking Taylor coefficients (half each in number) from both the imaginary and real μ axis (black, empty diamonds).

2.8 Notes on rates of convergence

From our experience, it has been quite hard to find literature on the convergence theorems relating to multi-point Padé. Even for single point Padé, most of the literature is based around two theorems concerned with two kinds of functions : the first type being the Stieltjes functions[7] and the second being meromorphic ones (see Section 2.4). In this thesis we will not be dealing with Stieltjes type functions, but often with meromorphic functions. Hence we will only mention the theorems relating to meromorphic functions.
The first theorem is due to Montessus de Ballore [35] and talks about uniform convergence of a Padé approximant to a meromorphic function in a disk with a fixed number of simple poles at distinct points. The theorem then states that in such a disk, with a radius defined by the pole with maximum modulus, a Padé approximant will uniformly converge to the correct function in the limit of infinite order. This theorem further states that no spurious poles will be found within this disc. This theorem can also be extended to poles of higher multiplicity than one. A further extension of this theorem exists and is known as the Nuttal-Pommerenke theorem [36, 37]. It states that for meromorphic functions, uniform convergence can be shown

[7] A (non-negative) *Stieltjes* function is a function $f : (0, \infty) \to [0, \infty)$ which can be written as

$$f(\lambda) = \frac{a}{\lambda} + b + \int_{(0,\infty)} \frac{\sigma(dt)}{\lambda + t}$$

where $a, b \geq 0$ are constants and σ is a measure on $(0, \infty)$ such that $\int_{(0,\infty)}(1 + t)^{-1}\sigma(dt) < \infty$. Definition taken from [34]

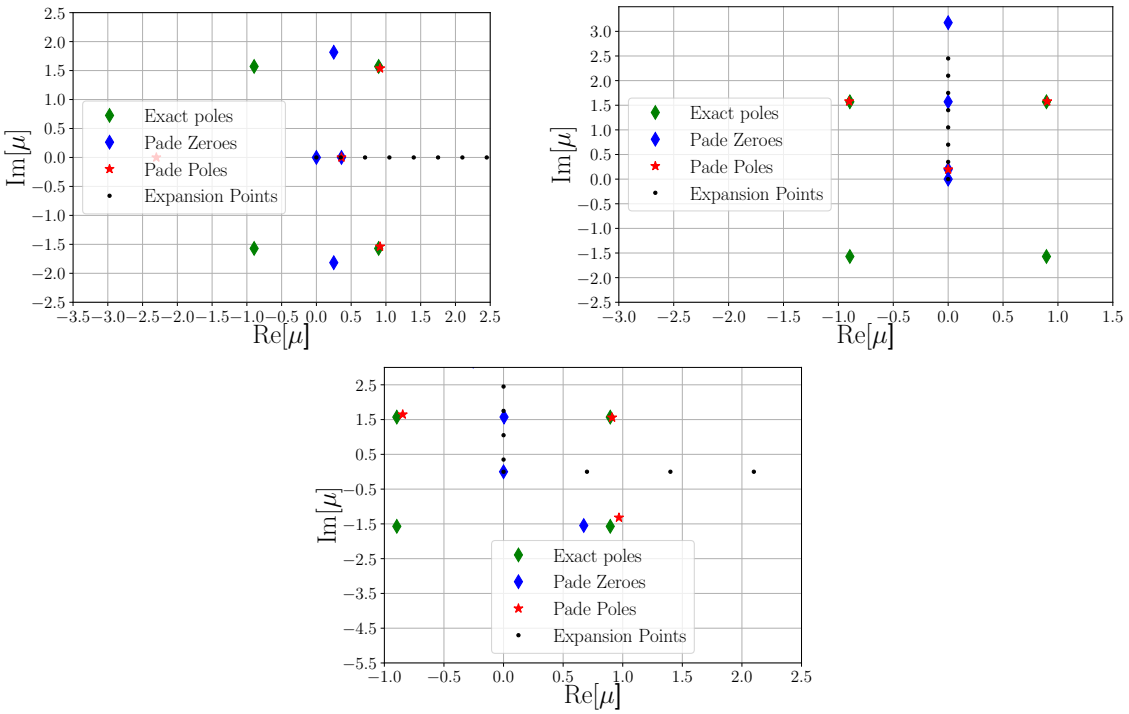

Figure 2.15: Presented in this figure are the respective singularity structures compared with the analytic known results for the three cases mentioned above (see main text and Fig. 2.14) : (Top Left) : Padé approximation obtained from considering Taylor coefficients only on the real μ axis; (Top Right) : Padé approximation obtained from considering Taylor coefficients only on the imaginary μ axis; (Bottom) : Padé approximation obtained from considering Taylor coefficients on both the real and imaginary μ axis

not only within the disk mentioned above but everywhere except a set of measures composed of the isolated poles of the function. It is this statement that one encounters most often in literature when talking about Padé approximants. Some further references relating to the Nuttal-Pommerenke theorem can be found here [38, 39] and references within. Unfortunately, none of the theorems stated above mention the *rate of convergence* of the Padé approximant to the function to be approximated. However, this can be checked case by case, for various functions, by increasing the order of the Padé.

However, a lot of empirical evidence, based on performing numerical experiments on functions both with and without the presence of noise, exists, see [29, 40, 41] and references therein. The results that we present in this thesis are also based on numerical experiments constructed and performed by us.

Chapter 3

Overview of phase transitions with focus on QCD

Thermodynamic systems are characterized by physical observables which can take different values in different regions of *phase space*. A phase space can be characterized by sets of variables like pressure (P), temperature (T), and chemical potential (μ), otherwise known as control parameters. Physical observables like number density, magnetization, and their respective susceptibilities can be studied as functions of these control parameters. A phase transition is set to occur at those values of the control parameters where one or more of these physical observables and/or their derivatives become discontinuous or singular or in other words non-analytic. The knowledge of phase transitions is essential in understanding the equation of state of a thermodynamic system.

The focus of this chapter is to introduce, very briefly, the most general classes of phase transitions in Section 3.1, followed by mentioning the importance of symmetries while looking for phase transitions in Section 3.2. The main goal of the current chapter is to describe the current status of our knowledge of the QCD phase diagram in the two corners of the Columbia plot (also described) in Section 3.3. This is followed by Section 3.4 describing in some detail the main theme of this thesis i.e, hunting for the Roberge Weiss critical point in QCD at imaginary μ using Padé approximants. The last section of this chapter (Section 3.5) outlines the expectations of the QCD phase diagram at real chemical potentials.

3.1 Classification of Phase transitions

A common method to classify phase transitions is by using the Ehrenfest classification. The basic statement of this classification is to relate the order of the phase transition to the first discontinuity obtained in the derivatives of $\log Z$. Further, since the derivatives of $\log Z$ are related to the expectation value of various thermodynamic quantities, these discontinuities represent non-analyticities in those physical observables. When studying a thermodynamic system, a quantity of fundamental importance is the *order parameter*. This observable has the property that it is *qualitatively* able to distinguish between the phases of interest. This observable is usually chosen based on the symmetries of the lagrangian of a physical system.

The most common phase transitions found in nature are the first order, second

order, and crossover in decreasing order of *being violent*. Basically, a second order transition interpolates a first order transition and a crossover transition.

- **First order**: This type of transition is characterised by a discontinuity in the first derivative of $\log Z$. Being the most "violent" transition, it is marked by the formation of "bubbles" at the phase boundary. Some examples include boiling of water or the 2D Ising model (magnetization as a function of external magnetic field below T_c)

- **Second order**: This type of transition is marked by a discontinuity in the *second* derivative of $\log Z$. The system state evolves continuously into the new state. Some examples are opalescence, the 2D Ising model when considering magnetization as a function of temperature at zero external magnetic field.

- **Crossover** : This is an analytic crossover, there is no discontinuity in any of the derivatives of $\log Z$. The system changes smoothly from one state to another. A very relevant example for the purpose of this thesis is the transition from quark-gluon plasma to the Hadronic state at $\mu_B = 0$, finite T [42]. Another relevant example is the transition from the $SU(2)_L$ symmetric phase of Standard Model of particle physics to the broken phase, for a Higgs mass above 72 GeV.

3.2 Symmetry breaking and Phase transitions

Symmetries of a physical system are one of the most important handles one has in the study/classification of phase transitions. The reason for this is simple : since a phase transition indicates a transition from one thermodynamic phase to another of a physical system, it is very likely that in this process either a symmetry of the system was broken or restored.

As an example, we will consider the 2D Ising model [43]. The Hamiltonian for the Ising model in the absence of an external field can be written as

$$\mathcal{H}_{2D} = -J \sum_{\langle i,j \rangle} \mathbf{s}_i . \mathbf{s}_j \ , \tag{3.1}$$

where J is the coupling constant and measures the strength of interaction between nearest neighbours. Notice that $J > 0$ implies ferromagnetic interaction (*aligning spins* lower the energy of the system) and $J < 0$ implies anti-ferromagnetic coupling (*anti-aligning spins* lower the energy of the system). Further notice that this system has a Z_2 symmetry in the spin variable, since, if all the spins are flipped at the same time, the total energy of the system remains unchanged. This symmetry is spontaneously broken when the temperature falls below a characteristic transition temperature T_c and is restored above it.
On the other hand, the same model in the presence of an external magnetic field is given by :

$$\mathcal{H}_{2D} = -J \sum_{\langle i,j \rangle} \mathbf{s}_i . \mathbf{s}_j - \mathbf{h} . \sum_i \mathbf{s}_i \tag{3.2}$$

Hence, adding an external magnetic field, in the form above, *explicitly* breaks the Z_2 symmetry of the Ising model. Depending on the sign of the external magnetic

field, a certain direction of spins will get preferred at low values of temperature. But notice that the system still has a symmetry under spin reversal at all sites if, in addition, even the sign of the external magnetic field is flipped.

3.3 Phase transitions in QCD : Columbia plot

The "Columbia" plot first introduced in [44], is a schematic description of the QCD phase diagram in quark "mass" and "flavour" space at zero chemical potential. This is because the QCD phase diagram is expected to undergo different types of phase transitions for different values of quark masses and number of flavours. The reason for this is again manifest in the symmetries the action has for different masses of the quarks - the Chiral symmetry at $m_q = 0$ and centre symmetry at $m_q \to \infty$. The non-trivial observation about the Columbia plot is that the transitions remain first order even for finite values of quark masses. The first order regions are bounded by second order transition lines. The region in the middle is a crossover. A point to emphasize about the Columbia plot is that *only a single point*, marked by the purple point, in Fig. 3.1, represents a point in the QCD phase diagram and has been determined to be a crossover in [5], everything else is un-physical but important to make progress toward the conjectured QCD critical end-point. We will discuss below the two extreme regions of the Columbia plot Fig. 3.1 , (with $m_q \to 0$ and $m_q \to \infty$). Most of the following discussion and notation used below is based on [45, 46, 47, 8].

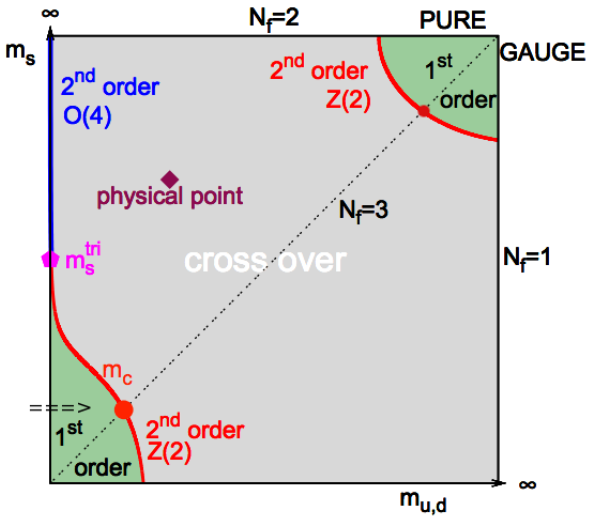

Figure 3.1: Columbia plot for QCD 2+1. Figure taken from [48]

3.3.1 Case I : Infinite (quark) mass limit of QCD

In this case, QCD reduces to a purely gluonic theory and is governed by the SU(3) Yang-Mills action. We already know that the action of an SU(N) theory is invariant under local gauge transformations. The Euclidean SU(N) action can be shown to have an additional Z_N symmetry [49]. This is a very important symmetry in the discussion of the *de-confinement* transition in pure SU(N). The Polyakov loop is an order parameter for this transition. We will show why this is the case below.

The Polyakov loop, in the continuum, is defined as :

$$\phi(\vec{x}) = \frac{1}{3}\,\mathrm{Tr}\,\mathcal{P}\exp\Big\{-\int_0^\beta dx_4\, G_4(\vec{x}, x_4)\Big\} \tag{3.3}$$

where $\mathcal{P}$ denotes the path ordering operator, $\mathrm{G}_4(\vec{x}, x_0)$ is the time-like gauge field at position $\vec{x}$.

The equivalent loop on the lattice at the point m, is given by

$$P(m) = \mathrm{Tr}\left[\Pi_{j=0}^{N_\tau - 1}\, U_4(m, j)\right] \tag{3.4}$$

where $U_4(m, j)$ is the temporal link (actually the *imaginary* time-like link, since we are in Euclidean space). This loop is invariant under the usual SU(N) gauge transformations given periodic boundary conditions.

Apart from the usual periodic boundary conditions there exist topologically inequivalent class of solutions to the Yang-Mills equations of motion given by the *twisted* boundary conditions (see Chapter 7 for details on twist transformations). A class of these transformations consists of multiplying the temporal links ($\mathrm{U}_4(n)$) by a phase factor z^k given by :

$$U_4(n) \to z^k U_4(n), \;\; z^k = e^{2\pi i k/N} \;\; (k = 0, .., N-1) \tag{3.5}$$

where these $z^k \in \mathbb{Z}_N$ (center of SU(N)). Since these transformations preserve the pure gauge action, the Yang-Mills action is said to have a *center symmetry*.
Gauge transformations on the lattice live at the lattice sites and are independent of the directions, denoted as $\Omega(n)$, whereas gauge fields or links live between the lattice sites and are as many as there are directions and sites, denoted as $U_\mu(n)$. Then a gauge transformation on a link is defined as :

$$U_\mu(n) \to U'_\mu(n) = \Omega(n) U_\mu(n) \Omega(n+\mu)^\dagger \tag{3.6}$$

Since we are considering a periodic lattice (equivalently a Torus in the continuum), points separated by the length of the lattice in every direction are identified as : $n_0 + L_{\hat{\mu}}\hat{\mu} \equiv n_0$. Hence, the gauge fields at these points must be physically equivalent, i.e, equal up to gauge transformations. We will first consider the case of strictly periodic gauge configurations :

$$U_\nu(n + L_\mu \mu) = U_\nu(n) \tag{3.7}$$

It can be easily shown that for the above periodicity to hold under arbitrary gauge transformations, the gauge transformations must satisfy exact periodicity,

$$\Omega(n + L_\mu \mu) = \Omega(n) \tag{3.8}$$

for the periodic boundary conditions to hold :

$$\begin{aligned} U_\nu(n + L_\mu\mu) \to U'_\nu(n + L_\mu\mu) &= \Omega(n + L_\mu\mu) U_\nu(n + L_\mu\mu) \Omega(n + L_\mu\mu + \nu) \\ &= \Omega(n) U_\nu(n + L_\mu\mu) \Omega(n+\nu)^\dagger = U'_\nu(n) \end{aligned} \tag{3.9}$$

Additionally, under the above periodic boundary conditions, the Polyakov loop transforms remains invariant.

Next we consider the twisted boundary conditions, with $\Gamma_\mu \in$ SU(N) (where these Γ_μ's can be seen as a generalisation of z^k in Eq. 3.5) :

$$U_\nu(n + L_\mu\mu) = \Gamma^\mu U_\nu(n) \tag{3.10}$$

The relevant question to answer now would be *What kinds of the gauge transformations preserve these twisted boundary conditions on the gauge fields?*

$$\begin{aligned} U_\nu(n + L_\mu\mu) \to U'_\nu(n + L_\mu\mu) &= \Omega(n + L_\mu\mu)U_\nu(n + L_\mu\mu)\Omega(n + L_\mu\mu + \nu) \\ &= \Omega(n + L_\mu\mu)\Gamma^\mu U_\nu(n)\Omega(n + L_\mu\mu + \nu)^\dagger \end{aligned} \tag{3.11}$$

It should be apparent that there are two different conditions under which the gauge transformations preserve the twisted boundary conditions - we will only consider one of them in this chapter and the other will be discussed in detail in Chapter 7. We will assume strict periodicity of the gauge transformation matrices $\Omega(n)$ and this will force the allowed Γ_μ's to belong in the centre of the group SU(N) (as they must commute with arbitrary SU(N) matrices):

$$\begin{aligned} U'_\nu(n + L_\mu\mu) &= \Omega(n + L_\mu\mu)\Gamma^\mu U_\nu(n)\Omega(n + L_\mu\mu + \nu)^\dagger \\ &= \Omega(n)\Gamma^\mu U_\nu(n)\Omega(n + \nu)^\dagger \\ &= \Gamma^\mu\Omega(n)U_\nu(n)\Omega(n + \nu)^\dagger = \Gamma^\mu U'_\nu(n) \end{aligned} \tag{3.12}$$

Although these transformations are still the symmetry of the Yang-Mills action, the Polyakov loop transforms non-trivially under twist :

$$\begin{aligned} P(m) \to P'(m) &= \mathrm{Tr}\left[\Pi_{j=0}^{N_\tau-1}\, U'_4(m, j)\right] \\ &= \mathrm{Tr}\left[U'_4(m, 0)\, U'_4(m, 1) \,....\, U'_4(m, N_\tau - 1)\right] \\ &= \mathrm{Tr}\left[\Omega(m, 0)U_4(m, 0)\Omega^\dagger(m, 1)\Omega(m, 1)U_4(m, 1)\Omega^\dagger(m, 2)\right. \\ &\quad \left.\,....\,\Omega(m, N_\tau - 1)U_4(m, N_\tau - 1)\Omega^\dagger(m, N_\tau)\right] \\ &= \mathrm{Tr}\left[\Omega(m, 0)U_4(m, 0)U_4(m, 1) \,....\, U_4(m, N_\tau - 1)\Omega^\dagger(m, N_\tau)\right] \\ &= \mathrm{Tr}\left[\Omega(m, 0)U_4(m, 0)U_4(m, 1) \,....\, U_4(m, N_\tau - 1)\Omega^\dagger(m, 0)z_4^\dagger\right] \end{aligned} \tag{3.13}$$

Considering the fact that z_4 is a *constant* matrix belonging to the centre of SU(3), making it a constant phase times and identity matrix, it can be commuted past $\Omega^\dagger(m, 0)$ and taken out of the trace to get :

$$P(m) = z_4^\dagger\, \mathrm{Tr}\left[U_4(m, 0)U_4(m, 1) \,....\, U_4(m, N_\tau - 1)\right] \tag{3.14}$$

This is an important result. It shows that the Polyakov loop transforms non-trivially under the twist transformations. This further implies that a non-zero value of the Poyakov loops breaks the centre symmetry. The zero to non-zero transition of the expectation of the Polyakov loop therefore marks the spontaneous breaking of the centre symmetry. The corresponding transition marks the confinement/deconfinement phase transition in pure gauge theories. We now come the question of the order of the phase transition, which depend upon the number of colour charges N in SU(N). For $N = 2$, the transition is 2^{nd} order, for $N = 3$ it is weakly first order and for $N \geq 4$, it is strictly first order (see [50, 51]). For SU(2), the second order transition was confirmed on the lattice in [52].

3.3.2 Case II : Mass(-less) limit of quarks

The QCD lagrangian density, in the mass-less quark limit, can be written as (note that explicit dependence on space-time has been omitted):

$$L_{QCD} = -\frac{1}{4}F^a_{\mu\nu}F^{a\mu\nu} + i\bar{\psi}\gamma_\mu D^\mu\psi \ , \tag{3.15}$$

where the first term is the usual gauge action and the second term is the kinetic term for the quarks. Spinors (here denoted by ψ) can be decomposed into left and right components using the following projectors involving the γ_5 matrix:

$$\begin{aligned} P_L &= \frac{1}{2}\left[\mathbb{I} - \gamma_5\right] \\ P_R &= \frac{1}{2}\left[\mathbb{I} + \gamma_5\right] \ , \end{aligned} \tag{3.16}$$

where $\mathbb{I}$ is the identity matrix, and the projectors having the properties that : $P_L + P_R = \mathbb{I}$ and $P_L P_R = P_R P_L = 0$. This operation decomposes the fermion kinetic term into two parts that do not mix (and hence form two invariant sub-spaces which means rotations in one sub-space will not affect the other sub-space):

$$i\bar{\psi}\gamma_\mu D^\mu\psi = i\bar{\psi}_R\gamma_\mu D^\mu\psi_R + i\bar{\psi}_L\gamma_\mu D^\mu\psi_L$$

Mathematically, a *chiral* transformation is defined as:

$$\begin{aligned} U(1)_A &: e^{i\alpha\gamma_5} \\ SU(N_f)_A &: e^{i\theta_a T^a\gamma_5} \ , \end{aligned} \tag{3.17}$$

with α, θ_a being real and constant and T^a being generators of SU(N_f), N_f being the number of fermion flavors. These chiral transformations leave the mass-less QCD action given Eq. 3.15 invariant.
However, for QCD with two mass-less quark flavours (up and down quarks), the vacuum spontaneously breaks the $SU(2)_A$ symmetry resulting in three Goldstone bosons – pions. This symmetry is restored at high temperatures. The transition temperature is denoted by T_c^0, and the order parameter is the vacuum expectation value of the chiral condensate given by :

$$\left\langle\bar{\psi}\psi\right\rangle = \left\langle\bar{\psi}_L\psi_R\right\rangle + \left\langle\bar{\psi}_R\psi_L\right\rangle \ , \tag{3.18}$$

This is a good order parameter for the mass-less limit of QCD in the same spirit the expectation value of the Polyakov loop in the previous section was, i.e., the operator $\bar{\psi}\psi$ is not invariant under chiral transformations mentioned above in Eq. 3.17. Hence, any non-zero value of $\bar{\psi}\psi \neq 0$ indicates a broken symmetry. Moreover, in the high temperature ($T > T_c^0$) symmetric phase this expectation value is exactly zero : $\left\langle\bar{\psi}\psi\right\rangle = 0$. A function that is non-zero in a certain region and exactly zero in another region must be non-analytic at the point of transition. Hence, the temperature at which $\left\langle\bar{\psi}\psi\right\rangle$ becomes zero denotes a phase transition.

Since we have already introduced the operator $\bar{\psi}\psi$, it is not hard to understand why the QCD action in the presence of massive quarks breaks the chiral symmetry.

Indeed, the quark mass term, given by $m\bar{\psi}\psi$, transforms under the operation by the projectors defined in Eq. 3.16 as:

$$m\bar{\psi}\psi = m\bar{\psi}_L\psi_R + m\bar{\psi}_R\psi_L \ ,$$

thereby explicitly mixing the left and right components (hence, no invariant subspaces). From a phenomenological point of view, one can ask if is there a phase transition even when quarks are massive, since the physical quarks are light? The answer is actually based on experimental evidence.

Experimental evidence: [46] If we only had the explicit chiral symmetry breaking due to the light quarks, then we would observe a non-degeneracy between the nucleon and its partner with negative parity, the N^*, commensurate with the amount of explicit symmetry breaking caused by the light quarks. However, the observed mass difference between the nucleon and N^* is around 600 MeV, too large to be explained by the small masses of the quarks. Hence, a spontaneous breaking of the chiral symmetry must be taking place. This would also explain the small but finite masses of the pions.

Remarks on the order of the transition:
As seen from the Columbia plot in Fig. 3.1, the transition is heavily influenced by the masses of the quarks and the number of flavours. We will state below what is currently known about the order of this transition:

- For three massless flavours ($N_f = 3$), the transition cannot be second order [53].
- For two massless quarks, this transition is supposed to be second order in the continuum limit and to belong to the universality class of $3d - O(4)$.
- the staggered formulation in lattice QCD away from the continuum limit, there is only one Goldstone boson, and the universality class is expected to be $3d - O(2)$.
- For the physical light quark masses, the order of this transition has been shown to be a crossover [5].

Moreover, some determinations of T_c^0 exist by extrapolating to light quark masses (zero quark mass simulations in lattice QCD are not possible). One such estimate is for $T_c^0 = 136^{+3}_{-6}$ MeV by [54]. The order of transition for the left boundary in the Columbia plot (Fig. 3.1) is still under investigation.

3.4 Phase diagram of QCD at imaginary μ (RW transition)

Quarks are introduced in the QCD action by a term proportional to $\bar{\psi}_n U_4(n)\psi_{n+\hat{4}}$. Hence, in the presence of quarks, the centre symmetry of pure gauge theory, as given by Eq 3.5, is explicitly broken. However, a remarkable feature for the case of imaginary chemical potential was discovered by Roberge and Weiss in their seminal paper [10]. In the presence of an imaginary chemical potential, the QCD partition

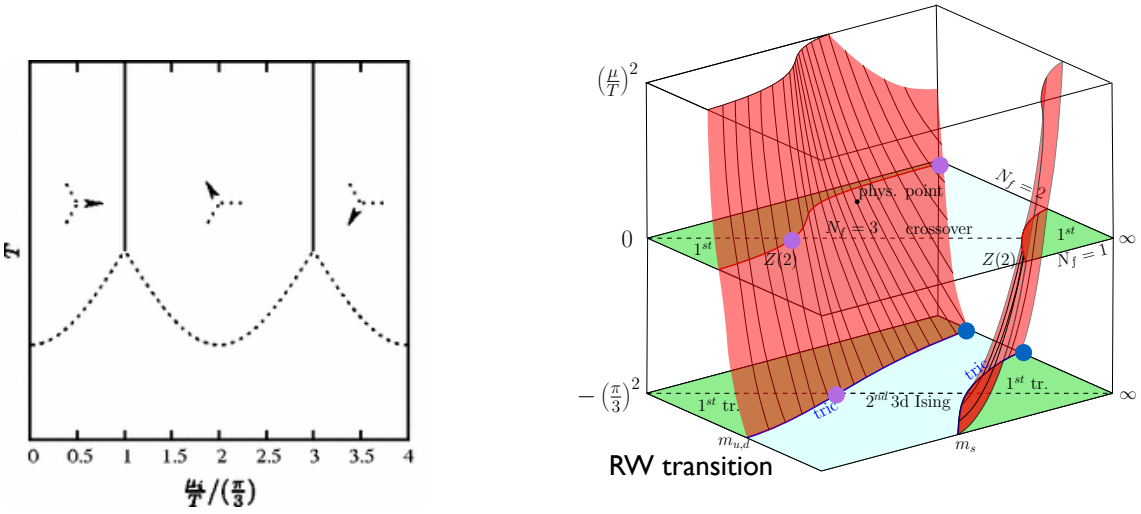

Figure 3.2: (Left) Phase structure in the T - μ_I plane, showing the three sectors with their respective directions of symmetry breaking. Figure taken from [48], (Right) 3D realisation of the Columbia plot. Figure taken from [56]

function inherits a non-trivial periodicity, which is a remnant of the centre symmetry of the Yang-Mills action[1]:

$$Z_{QCD}(\mu_B + i2\pi T) = Z_{QCD}(\mu_B) \tag{3.19}$$

To see why this is the case, it is important to consider how the chemical potential term enters the partition function. In the staggered fermion formulation, the chemical potential is added to the temporal links in the following way [55] [2] :

$$U_4(n) \rightarrow e^{a\mu N_\tau} U_4(n) \tag{3.20}$$

with $aN_\tau = 1/T$, a being the lattice spacing and N_τ the temporal lattice extent. It is easy to see that if $\mu = i\mu_I$, with $\mu_I \in \mathbb{R}$, the chemical potential term just becomes a phase given by $e^{i\mu_I}$. Since, the center transformation, given by $z^k = e^{2i\pi k/N}$, is also a phase, the centre transformation can be undone by a shift in μ_I. This is the reason for the non-trivial Roberge-Weiss symmetry in the QCD partition function in the presence of an imaginary chemical potential. However, there are further consequences of this Roberge-Weiss symmetry relating to phase transitions of QCD at imaginary μ in the presence of quarks. It was shown in [48] that the phase-space points given by $\mu_I = \pi/3$ and $\mu_I = 2\pi/3$ mark two first order phase boundaries (see Fig. 3.2 [Left]), even in the presence of quarks, using Polyakov loop as the order parameter. This can be seen by noting that at purely imaginary values of the chemical potential, the term multiplying the temporal link is just a phase - exactly like the centre elements. Therefore, increasing μ_I is commensurate with a centre transformation. Hence, in the de-confined phase, where $\langle P \rangle \neq 0$, the vacuum preferred by the fermions will change.

As seen from the Columbia plot (Fig. 3.1), number of flavours of quarks and their masses influence the details of the phase structure heavily. Now we will briefly describe the situation at non-zero chemical potentials - also known as the 3D Columbia

[1] In the following, μ and μ_B are the chemical potentials for the quark number (Q) and the baryon number (B) respectively

[2] For a detailed discussion on why the chemical potential is added this way, see [46, 47]

Plot (see Fig. 3.2 [Right]). The 3D Columbia plot can be described depending on quark masses. For very light or heavy quarks, that transition which was first order at zero chemical potential remains first order for all values of imaginary μ_B/T. For quarks with intermediate masses, the smoother crossover at $\mu_B/T = 0$, becomes a first order transition at some value of imaginary μ_B/T. Hence in this case the first order line ends in a second order critical end point at some value of imaginary μ_B/T. For some specific value of quark masses, the critical end point mentioned above coincides with the RW point. In this case the transition is a crossover for all values of $\mu_B/T \leq \pi$. Roberge Weiss transition remains an important research direction today. Some interesting references for further reading include [10, 57, 58, 47, 59, 45, 60]

3.5 Phase transitions relevant to QCD at real μ

To conclude this chapter on an introduction to phase transitions in QCD, we will briefly sketch the phase transitions expected in QCD at real values of chemical potential. For this we will first discuss the left plot in Fig. 3.3, which sketches the conjectured phase diagram of QCD at real chemical potentials. Beginning at $\mu = 0$, lattice QCD simulations have shown that the transition from quark-gluon plasma (QGP) at high temperatures to the hadronic phase at lower temperatures is a crossover [5]. Despite the sign problem, lattice simulations at very small values of μ_B have been performed combined with various methods to circumvent the sign problem with the result that the transition remains a crossover. This has led to the need for determining the *pseudo-critical* line that separates the low-T phase characterized by color confinement and chiral symmetry breaking, from the high-T phase which is made up of the QGP [61]. Many lattice studies have been performed to determine the curvature of this line, as that would help in narrowing down the search for the conjectured QCD critical end-point (CEP). The CEP is a well defined singularity in the QCD phase diagram at least from theoretical arguments. To understand why, we consider the low T, high μ_B region of the phase diagram. This μ_B driven transition at low T is believd to be a first order phase transition. Although this conclusion is not very robust, because of the sign problem, various model predictions in this region indicate that the transition from nuclear to quark matter is strongly first order [62, 63, 64]. For these two regions (crossover at low μ_B and high T and first order phase transition at high μ_B and low T) to exist in the phase diagram of QCD, there must be a second order critical point in the intermediate region which interpolates between these two regions. This is the conjectured CEP of QCD. However, to locate the point in the phase diagram, we must be able to perform exact simulations or calculate the partition function exactly to understand its singular structure - which is currently out of reach. Another region of interest to theorists is the one marked by a line separating the quark matter and the colour superconductor phase (or the Colour Flavour Locked (CFL) phase) [65]. Because of the asymptotic freedom of QCD, analytic calculations are possible in this region. Moving onto the right plot in Fig. 3.3, we first want to comment that the plot on the left is but just a slice of the 3D plot on the right, taken at a fixed value of physical quark masses. In different regions of the (T, μ_B) plane of QCD, it can be described by different effective theories, each determining the behaviour of the relevant transitions. At high temperature, far above the QCD phase transition, a free Fermi gas model can

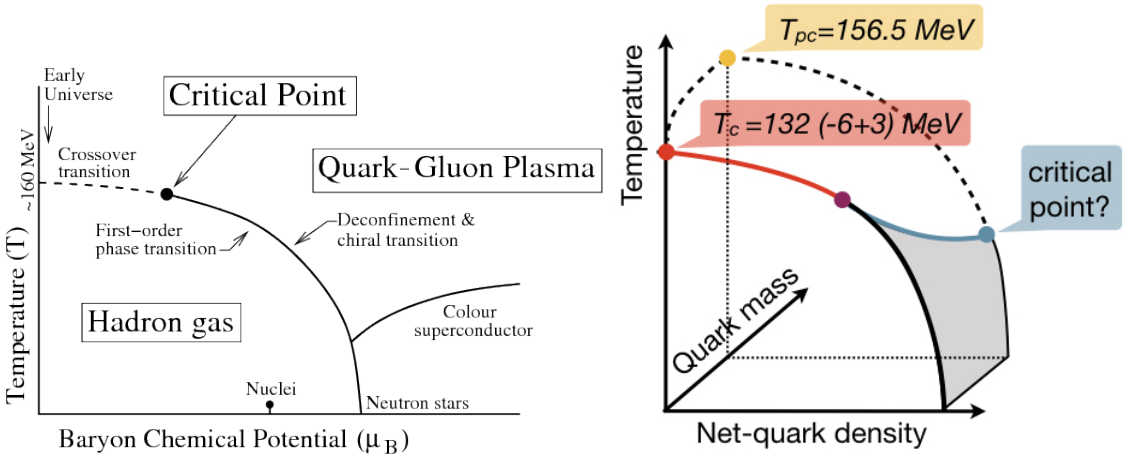

Figure 3.3: (Right) Conjectured QCD phase diagram for physics quark masses [68]. (Left)[Image credit : Christian Schmidt] Schematic picture of the phase diagram of QCD in three dimensions, including an axis for Quark mass. Indicated are pseudo-critical transition temperature of QCD (T_{pc}) with massive quarks and the chiral transition temperature (T_c) of QCD with two mass-less quarks and one heavy strange quark. Dashed lines indicate the crossover transition and solid lines represent a second ordder transition. The grey region represents a first order transition.

be expected to approximate the behaviour of quarks. The relevant singularities to look for in this region of phase space are the poles of the Fermi-Dirac distribution function, also known as the *thermal singularities*. Then, moving to the region of the RW transition, $(T, \mu_B) = (T_{RW}, i\pi T)$, we expect universal behaviour in accordance with the Z(2) symmetric scaling function, if the RW point is an end point of the first order transition line. The Z(2) scaling behaviour close to the physical point has been verified by us (in addition to others) and forms the main result of this thesis. Close to the chiral limit, we expect universal behavior in accordance with the O(4)-symmetric scaling function. The O(4) universal behavior has been demonstrated and used in many instances, recently for the determination of the chiral transition temperature [66]. In the vicinity of the QCD critical point, we expect again critical scaling with respect to Z(2)- symmetric scaling function. The position of the critical point is unknown, not even its existence has been verified. Nevertheless, a mapping to its critical region is frequently used to check for signals of critical behavior in experimental data [67].

Chapter 4

Lee Yang zeros and edge singularities

In 1952, Lee and Yang [11, 12] provided a novel alternative mechanism to look for phase transitions in a system. Their idea was to extend the grand-canonical partition function (Z_{GC}^{N}) of a system in a finite volume to a function of complex values of the parameter space (phase space). As is well-known, in a finite volume, the partition function can be expressed as a finite polynomial in the fugacity variable ($z = e^{(\beta\mu)}$)

$$\mathrm{Z}_{GC}^{N} = \sum_{n}^{N} C_n z^n, \tag{4.1}$$

where C_n's are coefficients that can be interpreted as the canonical partition function of the system, but in any case represent the statistical weights associated to the particular canonical ensemble. For real values of $\hat{\mu}$ ($\equiv \mu/\mathrm{T}$), the fugacity variable is strictly positive. Therefore, for $z > 0$, Z_{GC}^{N} is strictly positive, and cannot have any zeros along the real axis. We are interested in the zeros of the partition function because thermodynamic quantities can be expressed as functions of $\log(\mathcal{Z}_{GC})$[1]. Hence, one expects the appearance of divergences of the partition function at these points, signaling the onset of a phase transition. Terminology-wise, we will call the complex zeroes of Z_{GC}^{N}, **Lee-Yang zeroes** (LYs) but reiterate that a phase transition is realized only at real LYs, which is only possible in the thermodynamic limit (i.e. when $N \to \infty$). Apart from the study of LYs which deals with the zeros in the complex plane of the external fields, there exist studies on complex zeros of the partition function in the complex β (inverse temperature) plane. These are called **Fisher zeros** and were first studied in [13]. In the same paper, M.E. Fisher coined the term **Lee-Yang edge singularities** (LYEs), referring to the closest Lee-Yang zero to the real axis of z. Also in the same paper, he showed that these LYEs define a universality class of their own and for theories like the Ising model and O(N) models, this universality class happens to be that of the ϕ^3 theory with purely imaginary coupling. In this thesis, we only focus on the LYs and LYEs.

In this Chapter, we will first introduce the Lee-Yang zeroes in the fugacity (z) plane in Section 4.1 and see how the complex zeros of Z_{GC}^{N} relate to real zeros of

[1]Notice the change in notation : we will denote $\mathcal{Z}_{GC}$ as the grand canonical partition function of the system in the thermodynamic limit

$\mathcal{Z}_{GC}$. In Section 4.2 we will illustrate a plausible picture of the Lee-Yang zeros in the $\hat{\mu}$ plane. In Section 4.3, we will briefly discuss the symmetry properties of these zeros. We will end this chapter by studying the staple model of statistical physics, the 2D Ising model, and its phase transition using the Lee-Yang analysis in Section 4.5.

4.1 Lee-Yang zeroes & Edge singularities

Having already introduced the idea of Lee-Yang zeroes and why they should be studied, we now make concrete statements starting with the original Lee Yang theorems (to be found in their original paper [11] along with the proofs).

Theorem 1 *For all positive real values of z, the quantity*

$$f(z) = \lim_{V\to\infty} \frac{1}{V} \log Z^V_{GC}(z) \tag{4.2}$$

approaches a limit that is independent of the shape of V[2]. Moreover, this limit is a continuous, monotonically increasing function of z.

Since Z^V_{GC} is a finite polynomial in V, increasing the volume will increase the number of complex roots of Z^V_{GC}. Lee-Yang showed that the distribution of these roots in the V$\to\infty$ limit gives the complete analytic behaviour of the thermodynamic functions in the z plane. This leads us to their next theorem:

Theorem 2 *If in the complex z plane a region $\boldsymbol{R}$ containing a segment of the positive real axis is always free of roots, then in this region as V$\to\infty$ all the quantities :*

$$\frac{1}{V}\log Z^V_{GC},\quad \left(\frac{\partial}{\partial \log z}\right)\frac{1}{V}\log Z^V_{GC},\quad \left(\frac{\partial}{\partial \log z}\right)^2\frac{1}{V}\log Z^V_{GC},\quad ...$$

approach limits which are analytic with respect to z. Furthermore, the operations $\left(\frac{\partial}{\partial \log z}\right)$ and $\lim_{V\to\infty}$ commute in $\boldsymbol{R}$.

In the following, we will explain how the theorems mentioned above relate to phase transitions and the associated non-analyticities of the partition function. It is not hard to see that ultimately it is the form of the region $\mathbf{R}$ that decides whether a phase transition occurs in a system. If there exists a region $\mathbf{R}$ that includes the entire positive real axis (in z) such that it is free of any roots of $\mathcal{Z}_{GC}$, then all the quantities depending on $\log \mathcal{Z}_{GC}$ will be analytic at all real values of $\log z$ (or in our case $\hat{\mu}$) and we conclude that our system exhibits no phase transitions (our system exists in a single phase throughout $\mathbf{R}$). If, on the other hand, the zeros of the partition function, with increasing volume of the system, close-in on the real axis at, say, at a point z_1, then this point divides the real axis into two parts $\mathbf{R_1}$ and $\mathbf{R_2}$ separated by the point z_1. At this point, the quantities depending on $\mathcal{Z}_{GC}$ will display non-analyticities (in the form of discontinuity or multi-valuedness). The conclusion in this situation is that the system undergoes a phase transition at z_1 and divides the phase space into two regions $\mathbf{R_1}$ and $\mathbf{R_2}$ both of which are single

[2] An assumption is made about the surface area to volume ratio of the shape of V. The surface surface area cannot increase faster than $V^{2/3}$.

phases.

The nature of the phase transition is further decided by the manner in which the zeroes of the partition function close-in on (or approach the real positive z axis). A first order transition occurs when the Lee-Yang zeros cross the positive real z axis at the phase transition point. Whereas, a second order transition occurs when complex conjugate pairs of poles "pinch" the axis in the V$\rightarrow \infty$ limit.
In this thesis we will only study systems that exhibit a second order phase transition. Hence we will be on the lookout for the "pinching" effect. Another feature to notice about the Lee-Yang zeros in the finite volume case is that Z^V_{GC} is a finite polynomial in V, hence we have :

$$\left(\mathrm{Z}^V_{GC}(z)\right)^* = \mathrm{Z}^V_{GC}(z^*)$$

This condition (satisfied by all finite polynomials with real coefficients) ensures that the roots of Z^V_{GC} either come in complex conjugate pairs or lie on the $z < 0$ axis. However, depending on whether the partition function has additional symmetries, a richer structure of roots can be expected. For example, the QCD partition function has a charge conjugation symmetry :

$$\begin{aligned} & Z_{QCD}(\hat{\mu}) = Z_{QCD}(-\hat{\mu}) \\ \implies & Z_{QCD}(z) = Z_{QCD}(z^{-1}) \end{aligned} \tag{4.3}$$

This means that in addition to complex conjugate roots, we will also observe the corresponding inverse roots and their complex conjugates.

4.2 Analysis of LY theorems in the μ plane

Now that we have discussed the LY theorems in the plane of the fugacity variable ($z = e^{\beta\mu}$), it would be useful to see how they translate to the plane of the chemical potential (μ). This is because μ (or the external magnetic field h) are usually the control variables when performing simulations and not the fugacity, which means that most of our results on the position of the complex zeroes of the partition function are in the μ plane. This can seem a little concerning in the beginning since the partition function as a function of μ is not a finite polynomial. But we will show in this section that the LY theorems easily translate to the μ plane. Discussions along the same lines can also be found [69].

All zeros of the partition function in terms of μ are related to z by the exponential map (and inversely by the logarithm map). The important point for our purposes is whether we can encounter spurious poles in the μ plane which are not LY zeroes, i.e, zeroes of the partition function in the fugacity plane. But this will never be a problem because the exponential map is a well-defined single-valued map

$$\begin{aligned} f(z) &= a_0 + a_1\, z + a_2\, z^2 \\ f(z) &= a_2 * (z - z_1) * (z - z_2) \\ f(z(\hat{\mu})) &= (e^{\hat{\mu}} - z_1) * (e^{\hat{\mu}} - z_2) \end{aligned} \tag{4.4}$$

There can never be a situation in which we get zeroes on the real line in the $\hat{\mu}$ plane which will not lie on the $z > 0$ axis because of the exponential map. Conversely, the logarithm of a *complex number* can never lie on the Im$\hat{\mu} = 0$ line.

This translates into statements in the $\hat{\mu}$ plane :

- o If the quantity $f(z)$ exists for all $z > 0$, then does also $g(\hat{\mu})$ for all $\hat{\mu} \in \mathbb{R}$ (since the region $z > 0$ corresponds to $\hat{\mu} \in \mathbb{R}$).
- o The region **R'** in the $\hat{\mu}$ plane that corresponds to **R** above can contain *any part* of the Im$\hat{\mu}$=0 axis.
- o Since for the finite polynomial in z the zeroes come in complex conjugate pairs – and the complex conjugation of a exponential is straightforward – the corresponding zeroes in the $\hat{\mu}$ plane will also come in complex conjugate pairs modulo a factor of 2π.

4.3 Symmetry properties :

i) What do complex conjugate pairs in the fugacity plane ($z = e^{\hat{\mu}}$) translate into in the $\hat{\mu}$ plane? Assume F(z) is a finite polynomial.

$$F^*(z) = F(z^*)$$
$$z = e^{\hat{\mu}} \rightarrow z^* = e^{\hat{\mu}^*}$$

ii) Charge conjugation symmetry of the partition function $Z(\hat{\mu}) = Z(-\hat{\mu})$.

$$F(z(\hat{\mu})) = F(z(-\hat{\mu}))$$
$$z(-\hat{\mu}) = e^{-\hat{\mu}} = z^{-1}(\hat{\mu})$$

4.4 Zeroes of the Partition function

Let us assume that the partition function $\mathcal{Z}_{GC}$ admits a finite-dimensional polynomial in the fugacity variable. Then

$$\mathcal{Z}_{GC} = \kappa(V)\Pi_i \ (e^{\Lambda\hat{\mu}} - z_i)^{n_i} \tag{4.5}$$

where κ can be some volume, model-dependent parameter and n_i is the multiplicity of each zero.
Thermodynamic variables like pressure and number density is related to the

$$P = \left(\frac{T}{V}\right) \log(\mathcal{Z}_{GC}) \tag{4.6}$$

$$\chi_B^1 = \frac{1}{(VT)^3} \frac{\partial \log \mathcal{Z}_{GC}(\hat{\mu})}{\partial \hat{\mu}}$$
$$= \frac{1}{(VT)^3} \left(\log \kappa(V) + \sum_i \frac{n_i \, \Lambda z}{(z - z_i)} \right) \tag{4.7}$$

Since we are measuring the baryon number density, and we are approximating via Padé the baryon number density - the residue should be $\frac{1}{(VT)^3} \times n_i \Lambda z_i$

4.5 Test Case : The Ising Model

Ising model is one of the most studied systems in statistical physics and its role in understanding phase transitions cannot be overstated. Listing even a fraction of the work done on the model would take up many sheets of paper. However, we point the reader to a very nice review of critical phenomena in 2D Ising model [70], done the conventional way of studying the scaling of the magnetic susceptibility with lattice volume and extracting the critical exponents from this data. In this section, we will try to understand the critical phenomena of the Ising model using the technique of Yang-Lee to determine the existence (2D Ising) or non-existence (1D Ising) of a phase transition.
The goal of this section is two-fold : 1) To use the Padé approach to obtain the singularity structure of the 2D Ising model in the complex **H** (external magnetic field) plane. 2) To study the scaling of the edge singularity obtained. A very exhaustive reference on equilibrium and non-equilibrium phase transitions in terms of the Yang-Lee formalism can be found in [71].

4.5.1 1D Ising

It is well known that the 1D Ising model does not exhibit a phase transition at any finite values of temperature. Nonetheless, it is a very good starting point for discussing the Lee-Yang theorems. This is because it has an exact solution for the partition function at all values of system size which makes it possible to see exactly where the Lee-Yang zeros are located for this model. It also serves as a good example for seeing via the Lee-Yang analysis, when there *isn't* a phase transition in a system. If we consider again the Hamiltonian of Eq. 3.2, it can be shown (see [72]) that the partition function (using the method of transfer matrices [73]), can be written as a sum of its eigenvalues ($\lambda_\pm$) raised to the power of volume (number of lattice sites in this case):

$$Z_N = \lambda_+^N + \lambda_-^N; \;\; \lambda_\pm = e^{\beta J}\cosh(\beta h) \pm \sqrt{e^{2\beta J}\sinh^2(\beta h) + e^{-2\beta J}} \;\; , \tag{4.8}$$

where N is the number of lattice sites, J and h the ferromagnetic coupling and the external magnetic field (as defined in Eq 3.2) and β is the inverse temperature. The partition function then has zeros when

$$\begin{aligned} &\lambda_+^N + \lambda_-^N = 0 \\ &\implies \lambda_+ = e^{i(2n-1)\pi/N}\lambda_- \;\; , \;\; n \in \{1, ...N-1\} \\ &\rightarrow \cosh(\beta h) = \pm\sqrt{1-e^{-\beta J}}\cos\frac{(2n-1)\pi}{2N} \end{aligned} \tag{4.9}$$

It should be clear from the last equation (Eq. 4.9) above, that the partition function will only have zeros at purely imaginary values of the external field : $\beta h = i h_I$ with $h_I \in \mathbb{R}$. Further, at any finite temperature, βJ is finite, which implies that $\left|\sqrt{1-e^{-\beta J}}\right| < 1$ and $\left|\cos\frac{(2n-1)\pi}{2N}\right| < 1$ for all $n = \{1, ..., N-1\}$, for any N. This means that for no finite value of βJ, and for no lattice volume N, the zeros of the partition function will touch the real h axis, i.e , $h_I \neq 0$. Hence, using the distribution of the Lee-Yang zeros, in the thermodynamic limit, we have recovered the

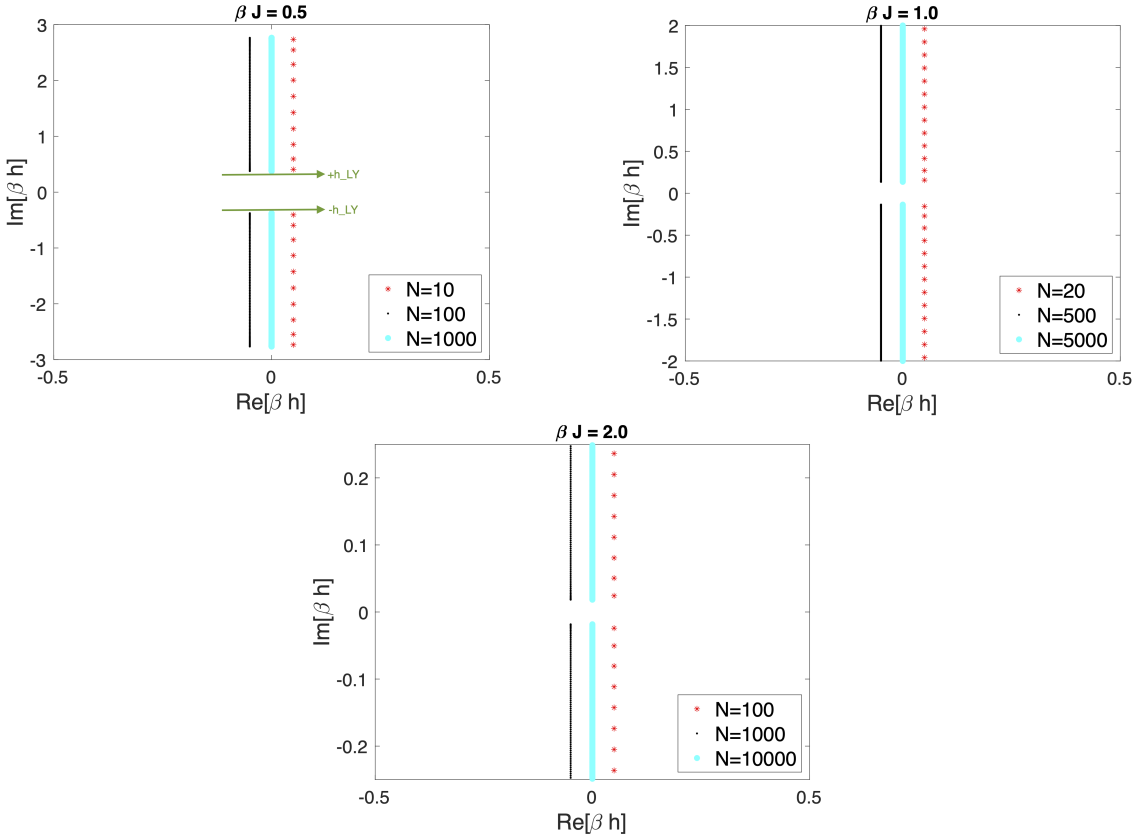

Figure 4.1: Lee Yang zeroes for 1D Ising model. Notice that the zeros given by red stars and black dots are shifted with respect to the cyan circles to display with clarity the string of zeros in for the three lattices. But they all lie on $\mathrm{Re}[\beta h] = 0$ axis.

result that the 1D Ising model does not have a phase transition.

Now we will visualise how these zeros look in the plane of the external magnetic field h. In Fig 4.1 we have chosen three different values of the temperature, and shown the distribution of zeros in the thermodynamic limit [3]. Notice that at each value of βJ chosen there is a definite gap between $+h_{LY}$ and $-h_{LY}$, which does not go close-in even after taking a very large number of lattice sites (equivalent to $V \to \infty$). Not surprisingly, the gap reduces when we change βJ, indicating only that the term $\sqrt{1 - e^{-\beta J}}$ gets closer to unity as $T \to 0$. If there truly was a phase transition of this model at any $T = T_c$, then the closest LY zeros, $\pm h_{LY}$ would approach the real axis as $V \to \infty$.

4.5.2 2D Ising

The 2D Ising model is a particularly well-suited model to test our analysis of the QCD Lee Yang edge singularities (LYEs) in the complex chemical potential plane which is based on extracting the genuine LYEs using poles of the Padé interpolant. There are a number of reasons for studying this model, the primary one being that the distribution of the LYEs of Ising model, in all dimensions, is known (they lie on

[3]Here the thermodynamic limit means taking large enough volumes beyond which the position of the closest LY zero does not change.

the imaginary h axis). Furthermore, a very wide literature on these LY zeros for the Ising model exists [74, 75, 76] (many using the functional re-normalisation group approach [77, 78]).The other reason for studying the 2D Ising model using Padé analysis to extract the LYEs is that the order parameter for this model is obtained as a result of numerical Monte Carlo simulations, hence the type of statistical noise present in the data would be similar to the one appearing in the QCD analysis at imaginary μ (see Chapter 5).

In this section, we want to numerically verify a few theorems based on the LYEs for the Ising model. In order to do this, we will study two types of scaling using the LYEs obtained by our Padé analysis. The first scaling is a fixed-volume temperature scaling and the second one is a fixed (reduced) temperature volume scaling. Before showing the LYEs data we would like to give a few comments on the order parameter studied in this work. Details of simulations along with relevant plots of magnetisation and susceptibility can be found in Appendix C

We remind again that the Hamiltonian used is the same as in Eq 3.2, with ferromagnetic couplings and only nearest neighbour interactions. This theory exhibits a second order phase transition from an ordered (broken symmetry phase) to a disordered Z_2 symmetric phase. Due to Onsager [79], the 2D Ising model is solved and all its critical exponents along with the transition temperature ($T_c = 2J/\log(1+\sqrt{2}) \approx 2.269J$) are known. We consider the order parameters for our Lee Yang edge singularity scaling analysis - the mean magnetization per site ($\langle m \rangle = \frac{1}{N}\langle M \rangle$) and the first cumulant of the order parameter, i.e., magnetic susceptibility (per site) χ_M defined as the following :

$$
\begin{aligned}
M &= \sum_i s_i \\
\chi_M &= \frac{1}{N}\frac{\partial \langle M \rangle}{\partial h} = \frac{1}{N}\beta\left(\langle M^2 \rangle - \langle M \rangle^2\right) \\
\chi_M &= \beta N \left(\langle m^2 \rangle - \langle m \rangle^2\right)
\end{aligned}
\tag{4.10}
$$

We consider χ_M as our function to be approximated by the Padé analysis, along with its first derivatives. The signals we obtain for the singularity structure (or the poles and zeroes of the function) from the approximant are shown in Fig. 4.2). Notice that our order parameter does not involve the modulus on the spins as usually done when analysing the Ising data. The reason for this is that our analysis for the LYEs is only performed at $T > T_c$, hence we are not faced with the situation (at $T < T_c$) when the spins are either all aligned along $+1$ or -1 spin directions and averaging gives the wrong results. Also, what we are studying is the behaviour of the magnetisation and its susceptibility around $h = 0$, when we move from negative values of h to positive values. Introducing a modulus would then artificially force discontinuities in the order parameter causing the Padé approximant to pick up *spurious* singularities.

Since our analysis to extract the relevant Lee-Yang edge singularities completely relies on our method of re-summing the Taylor coefficients, we would like to digress from our discussion on the Lee-Yang zeros to display the "raw" outcome of our Padé analysis with respect to the singularity structure found for the 2D Ising model.

Padé approximants applied to 2D Ising :

The goal of this digression is to display the zero-pole structure found by Padé and also display the pinching of the branch cut associated to the Lee-Yang singularity as one approaches the transition temperature (T_c). It is well known that the Lee-Yang zeroes display a gap in the density of zeroes at all $T>T_c$ (see previously mentioned references in this Chapter). This gap becomes smaller as one approaches the transition temperature from above finally pinching the real axis at T_c. Our Padé approximation was able to capture this behaviour for the 2D Ising model and we display the results for the 50×50 Ising model when solved numerically. A snapshot of the distribution of zeroes and poles will be displayed below, and lastly, the stability of the LY zeroes will be discussed by including error estimates. In Fig. 4.2 and Fig. 4.3, we display the zero pole structure taken from a [17,17] order Padé approximation at twelve different values of the temperature shown on the title of each sub-figure. We would like to draw the attention of the reader to the two complex conjugate poles found closest to the real $H = \beta h$ axis. We want to emphasize that no symmetries were imposed on the functional form of the approximating function and hence the complex conjugate found is a genuine effect of the data. Further, every other pole has been cancelled by an associated zero and hence can be completely disregarded. Perhaps the most important feature of this singularity structure is that as we move closer to the transition temperature, the closest complex conjugate pairs of poles also move closer to the real H axis. Further, notice the appearance of a branch cut structure as we approach the transition. This is a characteristic feature of Lee-Yang edge singularities. Also note, that for the 50×50, from the peak of the susceptibility (shown in Fig. C.1 (left)), it can be seen to have a transition at $T_c = 2.3J$). The very last plot in Fig. 4.3 is exactly at that value of temperature. The point being that there are still a complex conjugate pairs not touching the real axis. Note that this conforms to the expectation that there is no phase transitions in a finite volume. One might argue that this is due to just the fact that the function to be approximated (χ_M in this case) becomes sharper near the transition, i.e., it may not signify the presence of LYEs. Of course to argue with that we will have to perform the scaling analysis of the poles found by the Padé, which we will do below.

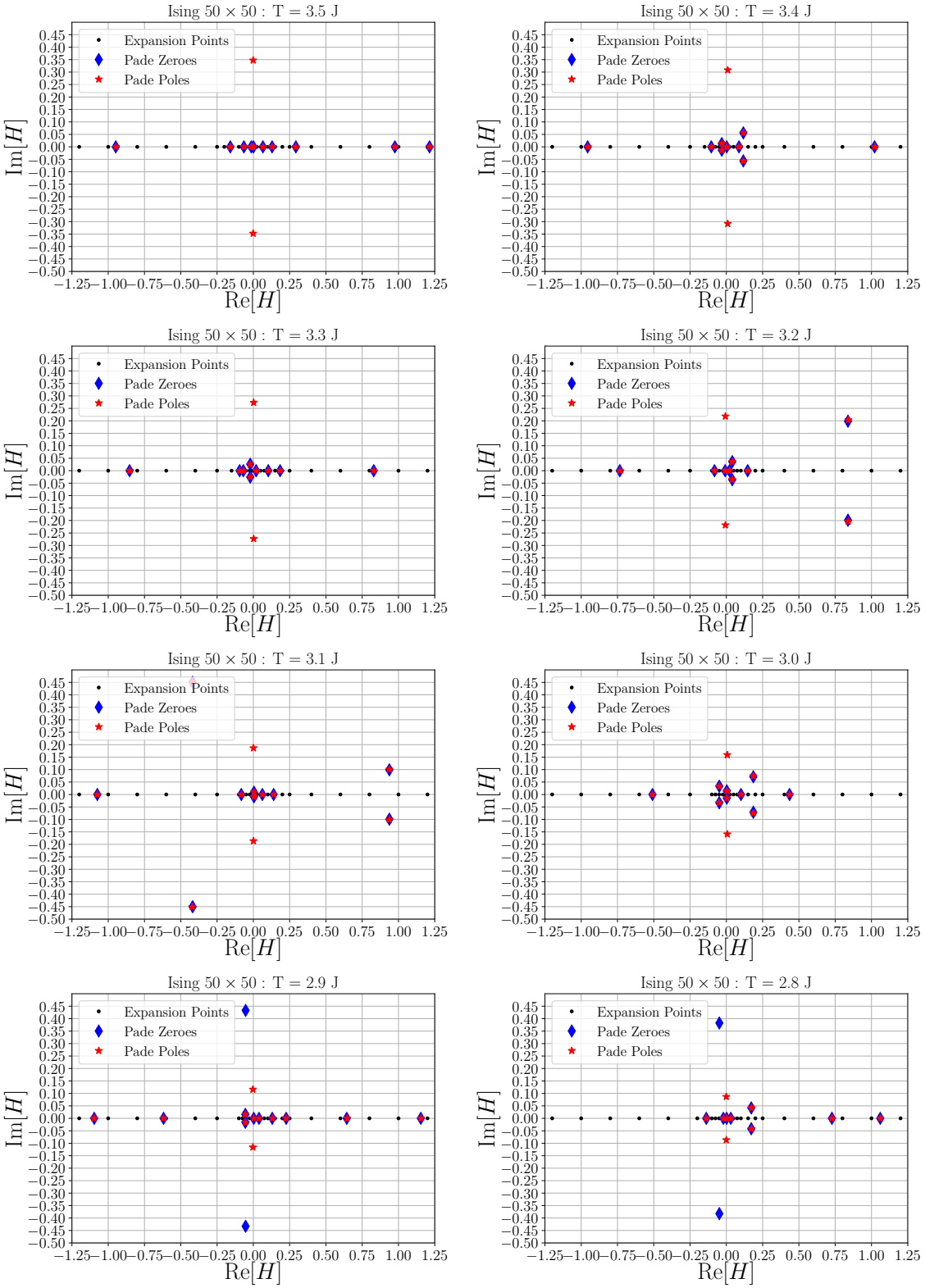

Figure 4.2: Case Study - 2D Ising model: Displayed are snapshots of the singularity structure of the magnetic susceptibility approximated by a Padé function simulated at Temperatures starting from T=3.5 J (Top left) to T = 2.8 J (Bottom right). Note on the units - the temperatures are taken relative to the transition temperature of 2D Ising, i.e $T_c = 2.269J$, with k_B set to unity. Further, H is a short hand for βh.

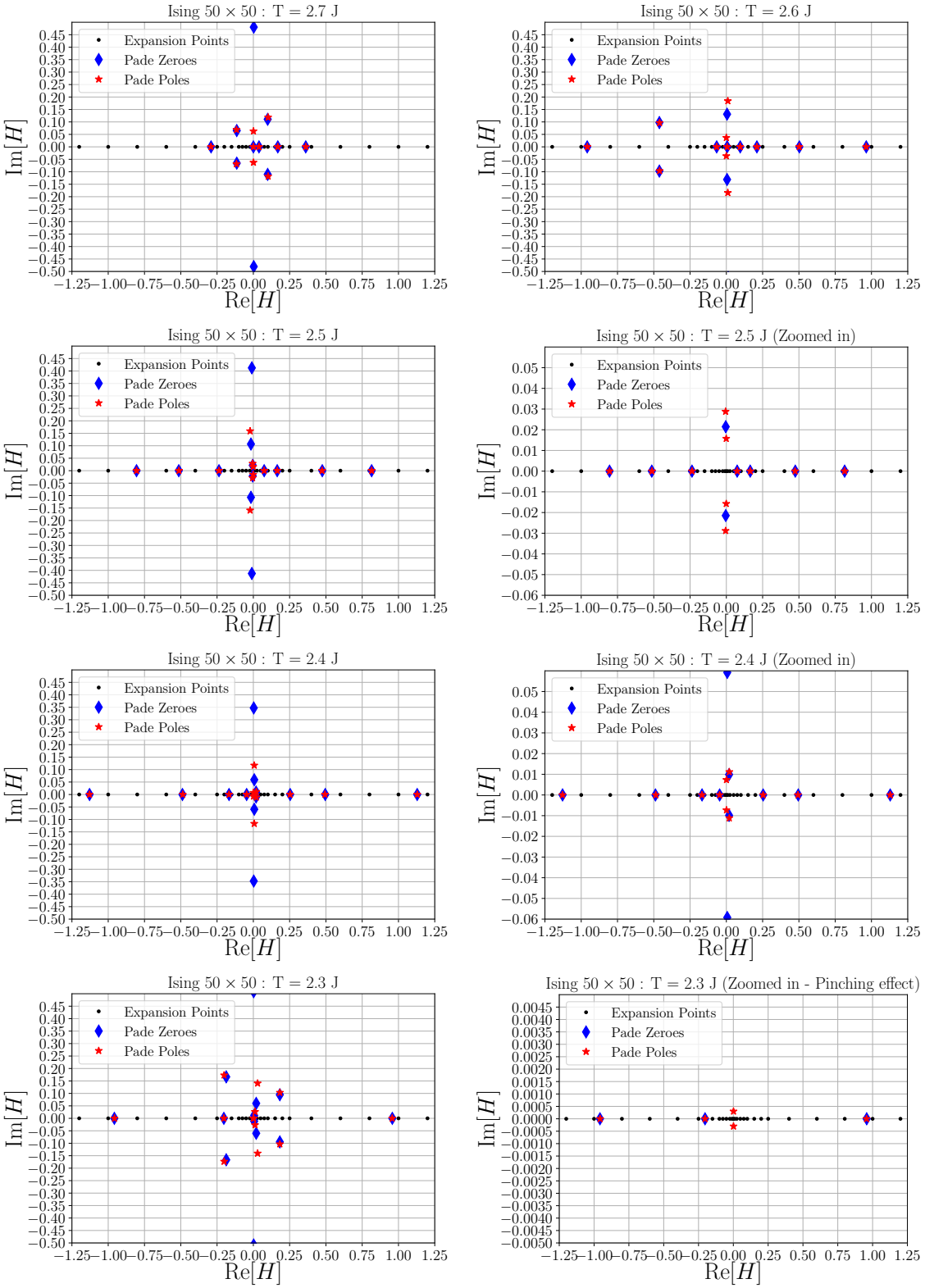

Figure 4.3: Case Study - 2D Ising model: Displayed are snapshots of the singularity structure of the magnetic susceptibility approximated by a Padé function simulated at Temperatures starting from T=2.7 J (Top left) to T = 2.3 J (Bottom right). Note on the units - the temperatures are taken relative to the transition temperature of 2D Ising, i.e $T_c = 2.269J$, with k_B set to unity. Further, H is a short hand for βh.

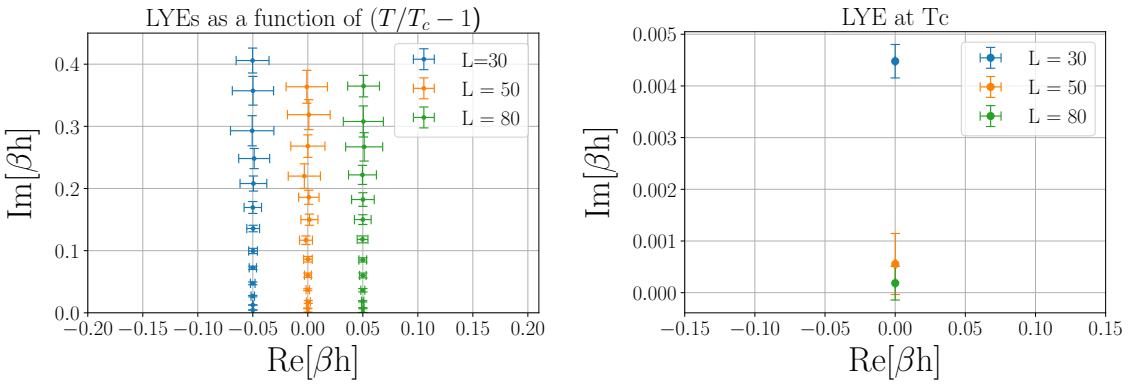

Figure 4.4: (Left) Displaying the LY edge singularities for an array of temperatures $T > Tc$ for three lattice sizes. Notice that the LYEs for L=30 and L=80 are artificially shifted to depict the scaling clearly. (Right) The closest LYE to the real h axis for the three lattice sizes considered.

Shown in Fig. 4.4 are the two types of scaling mentioned above. In Fig. 4.4(Left) is the scaling for the closest poles extracted by the Padé interpolant for a set of temperatures ($T > T_c$) for all the three lattice volumes shown. Simulations for the three lattices were done at the same set of reduced temperatures ($t = (T - T_C)/T_C$), where T_C was the value of the peak of the susceptibility for each lattice size (see Appendix C). The values of the reduced temperature used in the plot : $t \in$ { 0.0022,0.0458,0.0893,0.1329,0.1765,0.2200,0.2636,0.3072,0.3508 ,0.3943,0.4379,0.4815,0.5251 }. We claim that these poles are the relevant LYEs for the 2D Ising model simulated by us. This is because the poles extracted always lie on the imaginary h axis, come in complex conjugate pairs and moreover obey the expected scaling with temperature, i.e, come closer to the real h axis as one approaches T_c from above, finally "pinching" the real h axis as we hit T_c. Although as of now we only have simulation results for three lattice sizes, we would also like to claim that, looking at Fig. 4.4(Right), we see the onset of a phase transition. As we have seen throughout this Chapter, the "smoking gun" evidence of a phase transition using the LY zeros is that the LYE at T_c, goes closer to the real h axis by increasing volume. This behaviour (which was not observed in Fig. 4.1) can be seen in Fig. 4.4. Further, in Fig. 4.4(Left) we have tried to stay at the same reduced temperature (or relative distance from the respective peaks of susceptibility for the three lattice sizes) to compare the position of the LYEs.

Temperature scaling of LYEs :
Here we want to study the temperature scaling of the LYEs shown in Fig. 4.4(Left) to see if it is consistent with the Universality class of the 2D Ising model (within errors) [4]. We want to do this in the same spirit as described in [80, 81]. Following [80], we note that the branch cuts associated to LYEs in the presence of an external magnetic field h, are located at positions given by functions of reduced temperature $t \propto (T - T_c)/T_c$ (for $T > T_c$) as:

$$h_* = \left(\frac{t}{x_*}\right)^{\beta\delta} \tag{4.11}$$

[4] We do a similar analysis for the Roberge-Weiss transition done in the paper [16], which will be described in Section 5.5.1.

where x_* is a complex constant and h_* denotes the position of the singularity closest to the real h axis. The fact that h_* is purely imaginary at $t > 0$, fixes the argument of the complex constant to be : $\arg x_* = \frac{\pi}{2\beta\delta}$ (this value is universal and can be found in the two references mentioned above. Also, the universal location of LYE in O(N) models has recently been found in [78].)

We will fit two types of equation to the poles of the Padé shown in Fig. 4.4 (Left) in accordance with Eq. 4.11.

$$\textbf{Fit I :}\ h_{LY}(t) = a * (T/T_c - 1)^{\beta\delta} + b \tag{4.12}$$

where we fix the the critical exponent $\beta\delta = 1.875$ in accordance with the known values from Onsager's solution [79]. We fit for a, T_c and b. Notice the extra fit parameter b in Eq. 4.12 as compared to Eq. 4.11. This is added to incorporate the fact that there are no phase transitions at finite volume - hence, $h_{LY}(t = 0) \neq 0$ at finite V.

The other fit we perform is :

$$\textbf{Fit II :}\ h_{LY}(t) = a * (T/T_c - 1)^{c} + b \tag{4.13}$$

where now the critical exponent is also a parameter to be fitted. We display our results both in tabular (4.1 and 4.2) form and as plots in Fig. 4.5. The results from the first fit analysis, where we fixed the Universality class ($\beta\delta = 1.875$) of the Ising model model to 2D Z_2, despite being consistent with the University class, the values of T_c returned from the fits are not accurate. However, when we do not fix the Universality class (allow $\beta\delta$ to be a fit parameter), then we observe expected results. We see that with increasing volume, the values of T_c and $\beta\delta$ approach the known values in the thermodynamic limit.

Volume	T_c	a	b	χ^2
L = 30	2.2567 (75)	1.183 (34)	0.00186(55)	0.55
L = 50	2.2316 (94)	1.105 (36)	-0.00134 (65)	0.36
L = 80	2.2221 (90)	1.079 (34)	-0.00163 (47)	0.38

Table 4.1: Results for **Fit I** : Closest poles obtained from the Padé along with their errors were fit to Eq. 4.12 with fixed critical exponent $\beta\delta = 1.875$ for the 2D Ising Universality class and fit parameters a,b,T_c were determined. Reduced χ^2 is also shown. Fit degrees of freedom are 10.

Volume	T_c	$\beta\delta$	a	b	χ^2
L = 30	2.3166 (59)	1.671 (23)	1.129 (15)	0.00396 (23)	0.09
L = 50	2.2848 (93)	1.699 (34)	1.071 (23)	0.00038 (36)	0.14
L = 80	2.278 (15)	1.705 (51)	1.068 (25)	-0.00004 (37)	0.22

Table 4.2: Results for **Fit II** : Closest poles obtained from the Padé along with their errors were fit to Eq. 4.13 with the critical exponent as a fit parameter along with a,b,T_c were determined. Reduced χ^2 is also shown. Fit degrees of freedom are 9.

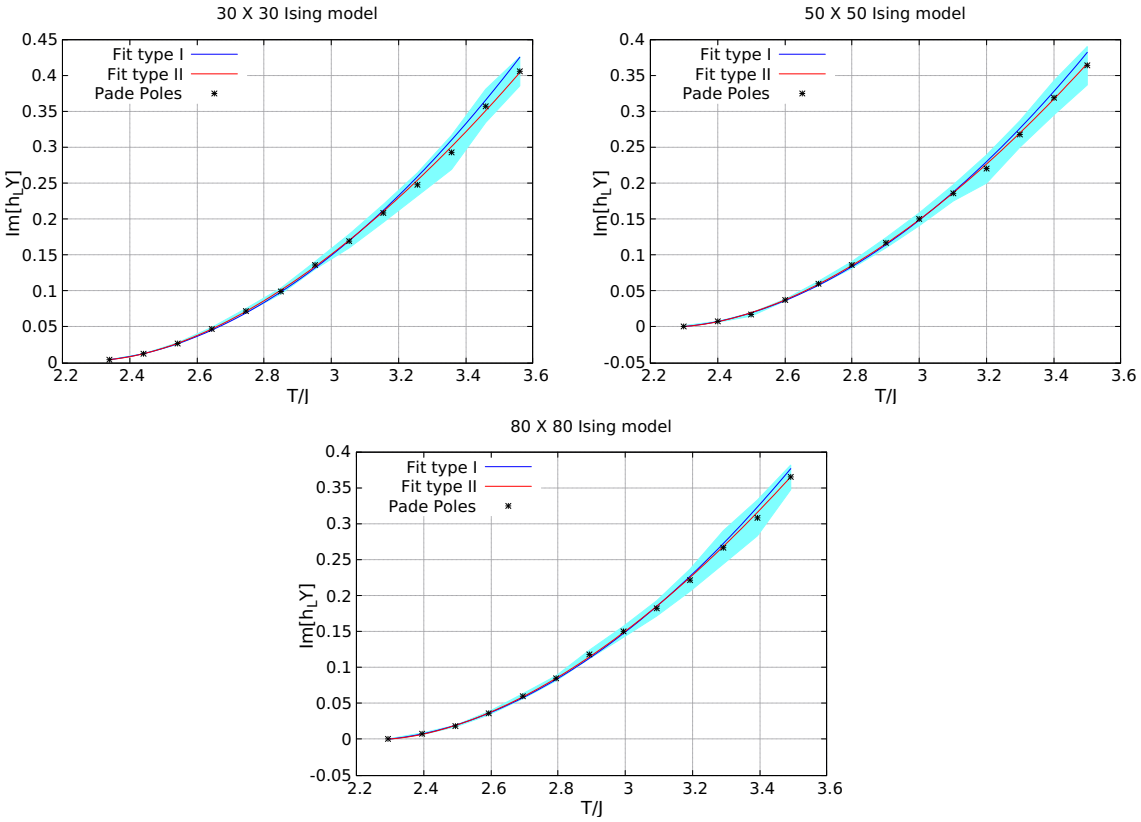

Figure 4.5: Comparison of **Fit I** & **Fit II** with errors on data (shown as a cyan band) for : (Top Left) : 30 × 30 Ising model, (Top Right) : 50 × 50 Ising model and (Bottom center) : 80 × 80 Ising model.

4.6 Outlook and conclusions

We would like to conclude this chapter by first reminding the reader that the primary reason for the above shown temperature scaling analysis of the LYEs of the 2D Ising model was to mimic the analysis done by us for the Roberge-Weiss (RW) analysis (section 5.5.1) and to compare our findings. In one way the comparison is meaningful because (as stated previously), both are a result of numerical Monte-Carlo simulations and have the same type of statistical errors and they both undergo a discontinuous phase transition (2D Ising below and the RW transition above a certain transition temperature). So the goal was to see if the Padé analysis would return to us the genuine Lee-Yang zeros also for the 2D Ising model when the analysis was performed for the temperature scaling exactly the same way as for RW transition. From a numerical point of view, we do find that the closest poles of the Padé analysis obtained for the 2D Ising model satisfy all the properties expected of Lee-Yang edge singularities of the Ising model to have (lie on imaginary H axis, come in complex conjugate pairs and follow the expected temperature scaling). But from a physical point of view, such a comparison can be misleading. The Ising model is a discrete model and the thermodynamic limit for it only means taking infinite lattice size. Although we see from fit II a trend, that supports the statement that with increasing lattice size, we are moving toward the expected critical exponents, the analysis uses only small lattices. For QCD, the thermodynamic limit also means taking infinite volume, but the theory has an inherent length scale. Because of this the discretiza-

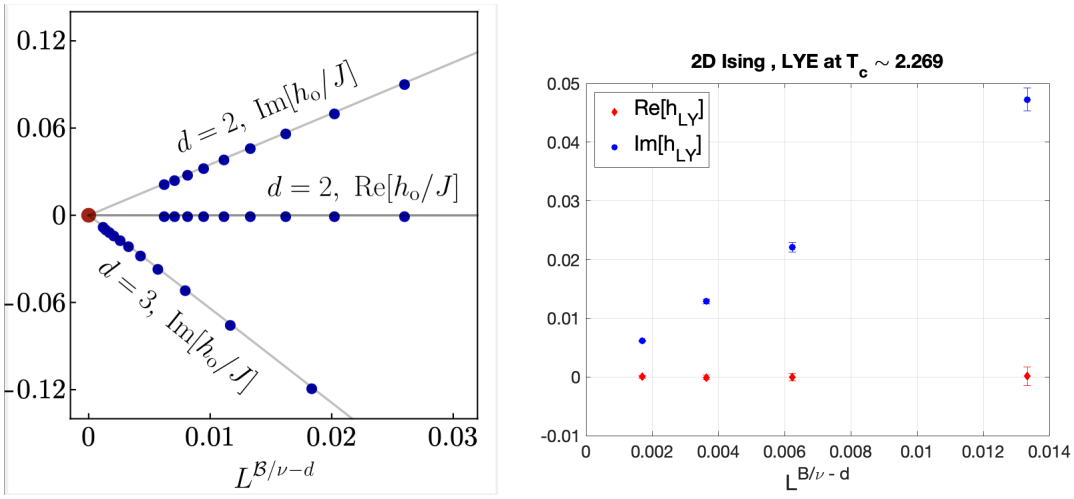

Figure 4.6: (Left) : [75]Determination of the convergence points of the Lee-Yang zeros (red circle) for d = 2, 3. For d = 3, the real-part also vanishes (not shown). (Right) : Scaling of LYEs from our analysis for 2D Ising model done at $L \in \{10, 15, 20, 30\}$ for $T = T_c \approx 2.269J$, to be compared with the $d = 2$ plot on the left.

tion is also extremely important, and a scaling analysis of the Lee-Yang zeros can have a very different meaning. We say this to emphasize that the volume scaling done for the 2D Ising model should not be compared to the analysis done later in Chapter 5.

Further studies on the 2D Ising model in relation to the extracting the LYEs from Padé analysis were done. These were done following an analysis done in [75, 76]. The authors of [75] have come up with a method of extracting critical exponents using the Lee Yang formalism, even for systems away from phase transition. A detailed analysis of both the Fischer and Lee Yang zeros have been done in the paper. For the purposes of this thesis, we will discuss only the Lee Yang zero study along with our results [5]. They briefly describe the analysis we want to reproduce. Using a method we will not describe here (makes use of higher order cumulants), LYEs were obatined for $d = 2, 3$ Ising model, at different lattice volumes. The finite size scaling hypothesis was applied to the LYEs found :

$$|h_0 - h_c| \propto L^{B/\nu - d} \implies \mathrm{Im}[h_0] \propto L^{B/\nu - d} \tag{4.14}$$

with h_0 represent the LYE for a lattice volume, denoted by L, h_c represents the value for the external magnetic field for which the transition occurs and B/ν represents the ratio of critical exponents, which for the 2D Ising model is $B/\nu \sim 0.125$. From Eq. 4.14 it can be seen that we can either fit for B/ν or input it and verify the scaling law. The results from the paper are shown in Fig. 4.6(Left).

Our goal was to obtain the LYEs via the Padé analysis to check (again) if the closest Padé poles are the genuine LYEs. For this simulations were performed for the 2D Ising model for the lattice sizes $L \in \{10, 15, 20, 30\}$ at an array of values of the external magnetic field (similar to the analysis above) at temperature fixed at the critical temperature ($T = T_c \approx 2.269J$). A Padé approximation is constructed using

[5]We have also performed the Fischer zero studies which will form the content of a future publication.

the multi-point Padé method. The closest pole for each of the lattices was obtained and fitted according to Eq. 4.14. The results are shown as below in Fig. 4.6 (Right). It can be seen from the plot that the poles lie very nicely on the expected scaling curves. As a last comment we would like to mention that a detailed study following the analysis in [75] was performed by us after submitting the first version of this thesis. The results of that study will appear in a future publication.

Chapter 5

Probing QCD at imaginary μ using Padé

As already seen in Chapter 3, QCD displays a very rich phase structure at imaginary values of the chemical potential. In this chapter, we will study complex singularities of 2+1 flavour lattice QCD with physical quark masses[1]. One of its most important features being the Roberge Weiss (RW) transition. We will first present our findings relating to the RW transition and then briefly discuss the other transitions that we might be sensitive to, for example the chiral transition.
The QCD partition function at imaginary values of the quark chemical potential (μ_q) is free of the sign problem and hence suitable for integration using Monte Carlo methods. Being free of the sign problem, QCD simulations in the imaginary μ_q (in this chapter we will use μ_q for the quark chemical potential and μ_B for the baryon chemical potential) plane in order to constrain the phase diagram at real μ_q, via analytic continuation remains one of the most popular choices to hunt for the QCD critical point [57, 58, 82]. This research direction mainly relies on obtaining Taylor series coefficients for cumulants of various conserved charges at either $\mu = 0$ or purely imaginary. Recently, many methods of re-summation of these Taylor series have appeared - [83, 84, 81, 85] to name a few.

In this Chapter, we will first discuss in Section 5.1 our simulation details for both generation and measurement of gauge configurations followed by a description of the cumulants measured. We will then describe the three methods used for our Padé analysis of the cumulants in Section 5.2. This will be followed by a discussion on the approximations obtained and their analytic continuation to real μ_B in Section 5.3. We will then describe the singularity structure found by our Padé functions and the stability of those results in Section 5.4. We will finally discuss the scaling of the stable poles found by the Padé approximation in Section 5.5.1 found in the vicinity of the RW transition and show that they are indeed the expected Lee Yang edge singularities. We will also discuss an additional stable pole found by the Padé analysis not in the vicinity of the RW transition in 5.5.2. We will discuss the scaling of this point with respect to the Chiral transition. Finally, in Section 5.6 we discuss the implications of the LYEs found in the context of the QCD phase diagram.

[1]This chapter is heavily based on our recent publication [16], although results from our new analysis for $N_\tau = 6$ are presented

5.1 Simulation details

The theory that we will be studying is the (2+1) flavor of QCD using highly improved staggered quarks (HISQ) with imaginary chemical potential with the partition function given by:

$$Z = \int \mathcal{D}U \, \det[M(m_l, i\mu_l^I)]^{2/4} \times \det[M(m_s, i\mu_s^I)]^{1/4} \, e^{-S_G(U)} \,, \tag{5.1}$$

where $M(m, i\mu^I)$ represents the fermion matrix of a HISQ flavor with mass m and chemical potential $\mu = i\mu^I$. The first determinant represents the two degenerate light flavors (up and down quarks). For the gauge part $S_G(U)$, we are using the Symanzik improved Wilson action, which is correct to $\mathcal{O}(a^2)$ in the lattice spacing. For the gauge field generation, we were using the SIMULATeQCD package [86] with an implementation of the rational hybrid Monte Carlo algorithm (RHMC) [87]. The lattice bare parameters are used from various publications of HotQCD. The lattice bare quark masses are varied with the lattice coupling such that for each coupling physical meson masses are obtained; i.e., we stay on the line of constant physics (LCP). Here, we make use of the parametrization of the LCP (for the physical value of the pion mass, $m_l/m_s^{\rm phys} = 1/27$) obtained and refined in previous works [88, 89, 90]. The same holds true for the scale setting, where the parametrization of the β function based on the kaon decay constant has been used. For simplicity, we fix the ratio of the explored chemical potential in this study to $\mu_l/\mu_s = 1$. The initial goal during the commencement of this project was to see whether Padé approximants were sensitive to the RW singularity (the end-point of the RW phase transition). To study this transition we chose the net baryon number density (χ_{1B}) as the function to be approximated and to this end we have measured its cumulants to the 4^{th} order:

$$\chi_n^B(T, V, \mu_B) = \left(\frac{\partial}{\partial \hat{\mu}_B}\right)^n \frac{\ln Z(T, V, \mu_l, \mu_s)}{VT^3} = \left(\frac{1}{3}\frac{\partial}{\partial \hat{\mu}_l} + \frac{1}{3}\frac{\partial}{\partial \hat{\mu}_s}\right)^n \frac{\ln Z(T, V, \mu_l, \mu_s)}{VT^3} \,, \tag{5.2}$$

To motivate our choice for studying this function in order to look for the RW singularity, we again mention the two very important properties of the QCD partition function at imaginary μ_B :

$$Z_{QCD}(\mu_B + i2\pi T) = Z_{QCD}(\mu_B) \;\; \& \;\; Z_{QCD}(-\mu_B) = Z_{QCD}(\mu_B)$$

Based on the above and the fact that χ_{1B} is a derivative of the logarithm of the QCD partition function[2], it is easy to see that χ_{1B} is an odd and periodic function of μ_B/T. Moreover, since the order of the transition is expected to be first order at physical masses of quarks at $\mu_B/T = i\pi$, $\chi_{1B}(\mu_B/T)$ is expected to become discontinuous at the transition point. This periodicity also limits the interval (in μ_B/T)

[2]The logarithm of an even function is itself an even function. This statement is not true for logarithm of odd functions, but we are not concerned with those.

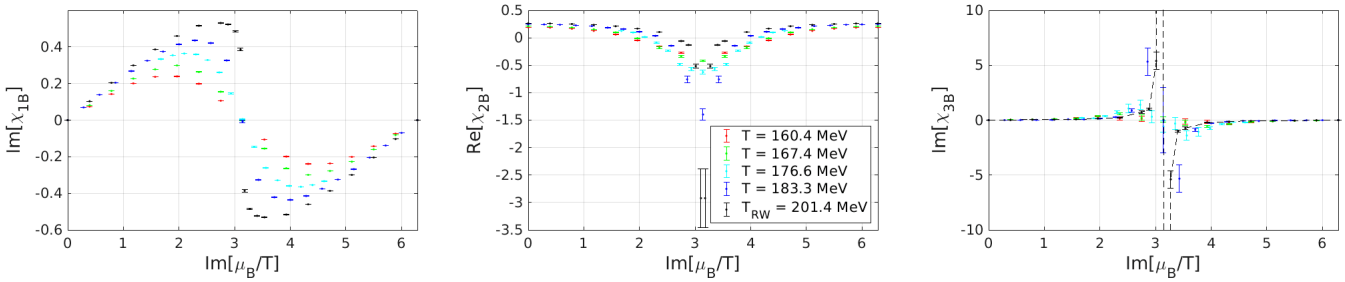

Figure 5.1: Cumulants measured for $24^3 \times 4$ lattices. (Left): net baryon number density, (Center): its first cumulant χ_{2B}, (Right) : second cumulant χ_{3B} simulated at temperatures $T \in \{160.4, 167.4, 176.6, 183.3, 201.4\}$ MeV

where we can gain genuine information about the partition function and the observables derived from it. Also, because of this periodicity, we only need to simulate the net baryon number cumulants in the interval $\mu_B/T \in \{0, \pi\}$. Our hope is that the rational function will be able to encode this discontinuity [3] as a singularity as we approached the RW transition point. Our primary analysis was done for lattices with spatial extent $N_\sigma = 24$ and temporal extent $N_\tau = 4$. The reason for choosing this lattice volume was that an independent analysis in [91] had already been performed to determine the RW transition temperature for this lattice volume, using the HISQ action and for the same quark masses (throughout this work we use physical quark masses $m_l/m_s = 1/27$). Hence, this was a good testing ground to check whether our approach would work. A summary of the simulations in the forms of plots of the cumulants of the net baryon number density measured is shown in Fig. 5.1. More details of the simulations including the μ_B/T values sampled and number of configurations generated at each temperature are available in Table B.1 for the $N_\tau = 4$ simulations.

Also within the same work, simulations on finer lattices ($N_\sigma = 36$ and $N_\tau = 6$) were performed at lower temperatures $T \in \{120, 145\}$ MeV. The goal there was to stay away from the RW transition in hope of being sensitive to other singularities like the Chiral transition. The net baryon number cumulants for this simulation can be found in Table B.2.

Recently we have been simulating net baryon number density cumulants along with other observables like chiral condensate and charge density for $36^3 \times 6$ lattices (using the same action as above) at higher temperatures ($T \in \{166, 179.5, 185, 190, 196\}$ MeV). The goal of this analysis was to predict the RW transition temperature for this discretization of the lattice. At this moment we only have completed simulations for four temperatures $T \in \{145, 179.5, 185, 190\}$ MeV. Again, a summary of the first two cumulants measured is shown in Fig. 5.2 & 5.3. Note that we only show the first two cumulants for the new simulations because only those have been used to produce the results presented in the next section. More details of simulations are to be found in Appendix B.

Lastly, we have also been running simulations around the crossover temperature $T = 156.5$ MeV for $32^3 \times 8$ lattices. The goal here is not exactly the same as for

[3] We of course realise that a lattice discretization regularises a discontinuity, so what we strictly mean here is the *tendency* of a discontinuity.

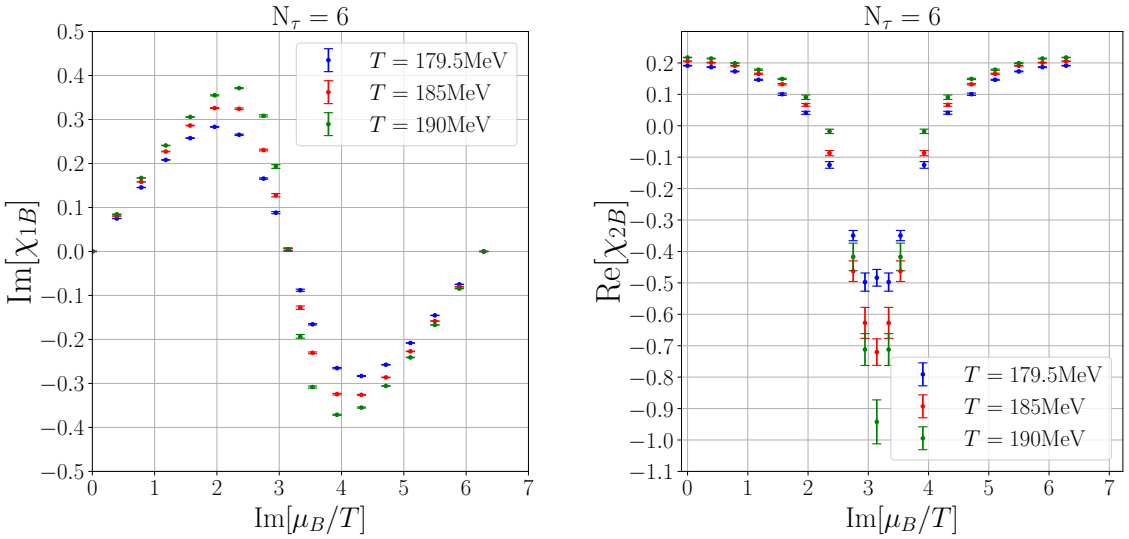

Figure 5.2: **[New simulations]** Net baryon number density (χ_{1B}) (Left) and its first cumulant (χ^2_B) (right) for $36^3 \times 6$ lattices simulated at temperatures $T \in \{179.5, 186, 190\}$ MeV

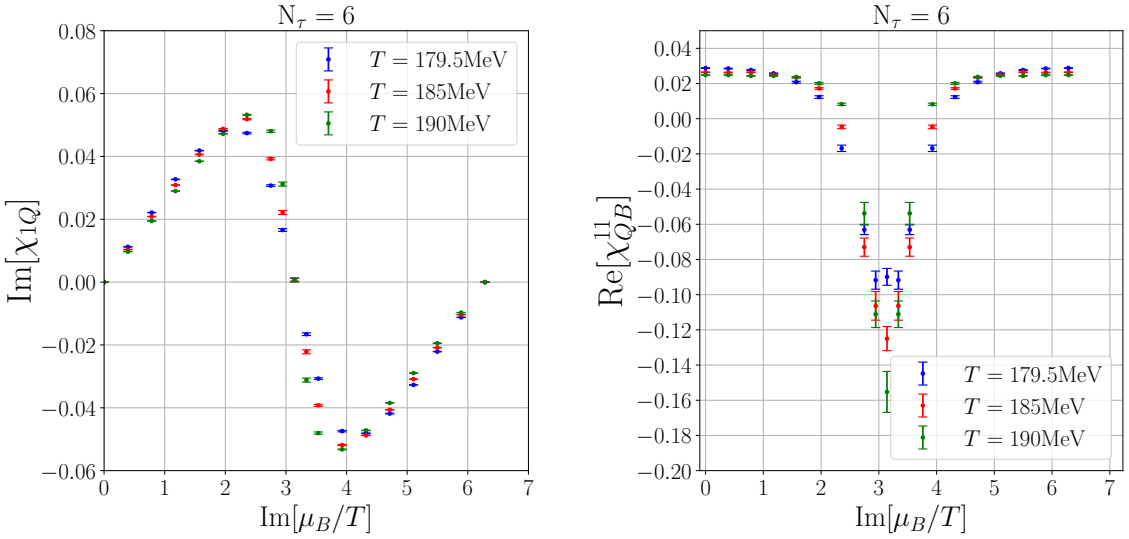

Figure 5.3: **[New simulations]** Net charge density (χ_{1Q}) (Left) and its first cumulant w.r.t. μ_B (χ^{11}_{QB}) (right) for $36^3 \times 6$ lattices simulated at temperatures $T \in \{179.5, 186, 190\}$ MeV

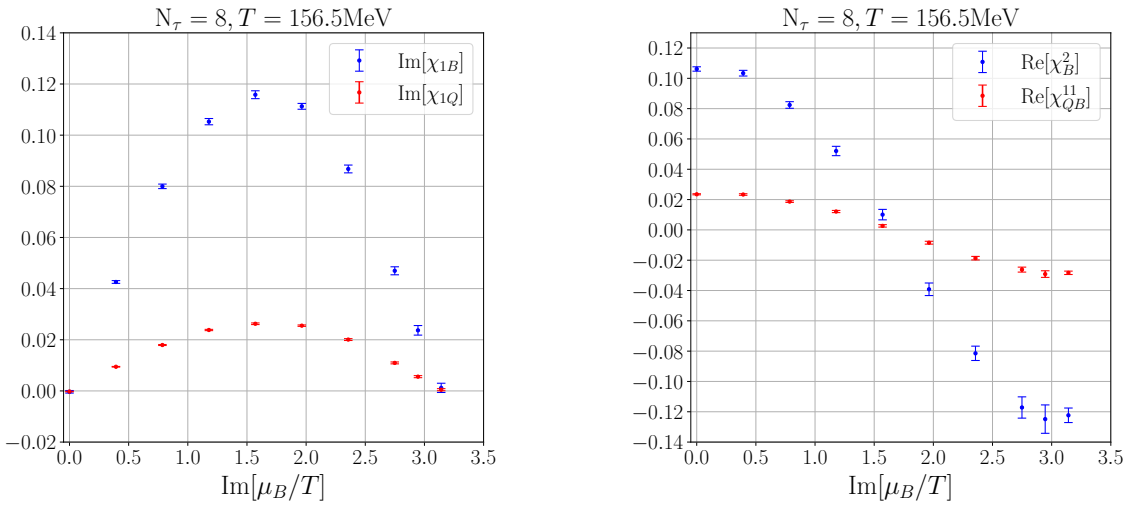

Figure 5.4: [New simulations] (Left) Net charge and baryon number density for $32^3 \times 8$ lattices simulated at $T = 156.5$ MeV

the above experiments mentioned above, i.e., we are not really looking for complex singularities here. The goal here is more phenomenological. We would like to see how our analytic continuation of the net baryon number density and other observables (chiral condensate and charge density) compares with the current state-of-the-art results.

5.2 Padé analysis

In this section we would like to describe in greater detail the main approaches used by us to build the Multi-Point Padé approximations. In the first subsection 5.2.1, the general structure of the equations used in the three implementations of the Padé construction is described. In the second subsection 5.2.2, we explain the actual implementation of the Multi-Point Padé solver with the help of MATLAB scripts. We also discuss the inclusion of errors on Taylor coefficients in our construction.

5.2.1 Description of methods used

We present here the list of approaches used by us to build Padé approximants. This was partly motivated by needing consistency checks and partly by observing certain patterns occuring in our approximations.

I The solution of the linear system (2.8) has been worked out in two different ways, namely,

  i One can build the system by writing the most general form for $R^m_n(x)$, i.e., that of (2.4).

ii One can instead impose the form

$$R_n^m(x) = \frac{\sum_{i=0}^{m'} a_{2i+1}\, x^{2i+1}}{1 + \sum_{j=1}^{n/2} b_{2j}\, x^{2j}}\,, \qquad (5.3)$$
$$(\; m = 2m' + 1,\;\; a_1 = \chi_2^B(T, V, 0)\;)\,,$$

with the coefficients $\{a_i\}$ and $\{b_j\}$ that turn out to be real. This form ensures the following: (a) The function $\chi_1^B(T, V, \mu_B)$ has the right parity (it is an odd function). (b) As a consequence of the coefficients being real-valued, for imaginary $\mu_B = \mu_B^I$, the odd cumulants $\chi_{2n+1}^B(T, V, \mu_B^I)$ are imaginary valued, while the even $\chi_{2n}^B(T, V, \mu_B^I)$ are real-valued, as it must be. (c) When Eq. (5.3) is computed for real $\mu_B = \mu_B^R$, the cumulants are real; i.e., the analytic continuation one is typically interested in is guaranteed to be meaningful.

Notice that taking into account different functional forms for R_n^m is not the end of the story. Another alternative which can (and actually was) taken into account is whether one :

i performs the Padé analysis in the (original) complex-μ_B plane or

ii goes through a *conformal map* $\mu_B = \phi(\nu)$ and performs the Padé analysis in the complex-ν plane (where ν would be the relevant variable after mapping. Details of the map used for this work in Section 5.4.2).

This is in the spirit of [92, 93, 81].

II Because of the cumulants being known to finite precision, the minimization of a generalized χ^2 is an obvious alternative to the solution of (2.8). Suppose we want $R_n^m(x)$ to be a Padé approximant for the function $f(x)$ whose values and derivatives we know at given points $\{x_j \,|\, j = 1 \ldots N\}$, *i.e.* $c_j^{(k)} \equiv \frac{\partial^j f}{\partial x^j}(x_k) \simeq \frac{\partial^j R_n^m}{\partial x^j}(x_k)$, with the $c_j^{(k)}$ known with errors $\Delta c_j^{(k)}$. Then, the coefficients $\{a_i, b_j\}$ the R_n^m depends on can be fixed minimizing the generalized χ^2,

$$\tilde{\chi}^2 = \sum_{j,k} \frac{|\frac{\partial^j R_n^m}{\partial x^j}(x_k) - c_j^{(k)}|^2}{|\Delta c_j^{(k)}|^2}. \qquad (5.4)$$

Of course, all the alternatives that we commented on in 1 (namely, different functional forms for R_n^m, use of conformal maps) can be also implemented in this approach.

III Both 1 and 2 make use of the knowledge of $f(x)$ (and its derivatives) at given points; i.e., the only information on $f(x)$ we have is at a finite (possibly small) number of points. One could instead compute a smooth interpolation of $f(x)$ before entering the Padé analysis.

5.2.2 Simulation details : Padé analysis

Solving for the Rational function :

The first function that we will describe is the linear solver for building multi-point Padé approximation. We will do this with the help of the MATLAB script shown below. The function named **NSLinPadeGen** takes as input a matrix **MyDD** consisting of Taylor coefficients (in this implementation only the value and its first derivative are used) as columns simulated at multiple values of the chemical potential with each row representing a different chemical potential value. The first column is given by the value of the chemical potential followed by the value of the function in the second column. The third column is always assumed to be the statistical error associated to the given Taylor coefficient. The fourth column contains the first derivative of the function followed in the fifth column by the statistical error associated to it. The next input to the function is another matrix labelled **idx** consisting of two columns, the first one labelling the rows corresponding to the matrix **MyDD** and the second column contains any number up to the number of Taylor coefficients to be considered for the evaluation. In our case it can only take values $\in \{0, 1, 2\}$ because we only consider two Taylor coefficients in the current implementation. Making the value zero excludes that particular row from the Padé construction, as can be seen in line number 3 in the script below. Based on the total number of Taylor coefficients available, the next step is to decide on the order of the Padé approximant. This is done between lines 7 and 13. At line 7, the total number of coefficients available is obtained by summing the second column of the input matrix labelled **idx**. Then depending on whether this number is even or odd, the order of the polynomials in the numerator and denominator is constructed. For odd number of Taylor coefficients, a rational function with same order in numerator (On) and denominator (Od) will be constructed (lines 8 to 10). For even number of Taylor coefficients available, a rational function with order one less in numerator than denominator ([On,On+1]) will be constructed (lines 12 and 13) [4]. After this the first column of the input matrix **MyDD** will be copied into a new vector called **mu** in line 16 and the value of the first Taylor coefficient from the first row will be copied to a variable **ff** in line 18. We now proceed to construct the matrix **A** and the column vector **b** with an aim to solve the linear system $Ax = b$, with **x** the column vector made up of the required coefficients of the rational function we want. We want to remind the reader that the system of equation we are trying to solve is given in Eq. 2.8, while the matrices **A** and b are set up according to Eq. 2.9. Between lines 20 to 27, we set up the first row of the system of Eqs. 2.9, because we always include the Taylor coefficients at $\mu_B = 0$, and assume that to be our first row. We set up this row separately because, the number density is always zero for zero chemical potential. It is straightforward to remove this assumption, in order to solve for arbitrary functions, but we implement this assumption below since we are dealing with the number density here. Between lines 29 and 41 we set up the remaining rows of our system of equations and solve them for the vector **b**. Between lines 47 and 52, the vector **b**, which contains the coefficients of the polynomials of the numerator (denoted in the script by P) and the denominator

[4]Other combinations of the difference in degrees between numerator and denominator have also been tried. However no new non-trivial information was gained regarding the singularity structure or the functional form of the approximation, because of which we are making a choice

(denoted in the script by QQ), is split according to the values of [On,Od] requested to build the respective polynomials. Finally, using the inbuilt multi-root solver of MATLAB, called **roots**, the entire set of roots for the numerator (denoted by **zz** in the script) and denominator (denoted by **pp** in the script) of the rational function are constructed.

```
function [P, QQ, zz, pp] = NSLinPadeGen(MYdd,idx)

idx(idx(:,2)==0,:)=[];

dd = MYdd(idx(:,1),:);

lll = sum(idx(:,2));
if mod(lll,2)
    On = (lll-1)/2;
    Od = On;
else
    On = lll/2-1;
    Od = On+1;
end

mu = dd(:,1);

ff = dd(1,2);

A = [mu(1).^(0:1:On) (-ff*mu(1).^(1:1:Od))];
b = ff;
if idx(1,2)>1
    ddd = dd(1,4);
    A(end+1,:) = [0 (1:1:On).*mu(1).^(0:1:On-1) (-ddd*mu(1).^(1:1:
    Od)-
    ff*(1:1:Od).*mu(1).^(0:1:Od-1))];
    b(end+1) = ddd;
end

for ii=2:length(dd(:,1))

    ff = dd(ii,2);
    A(end+1,:) = [mu(ii).^(0:1:On) (-ff*mu(ii).^(1:1:Od))];
    b(end+1) = ff;
    if idx(ii,2)>1
        ddd = dd(ii,4);
        A(end+1,:) = [0 (1:1:On).*mu(ii).^(0:1:On-1)
        (-ddd*mu(ii).^(1:1:Od)-ff*(1:1:Od).*mu(ii).^(0:1:Od-1))];
        b(end+1) = ddd;
    end

end

b = transpose(b);

aux = A\b;

P = zeros(1,On+1);
P(1:1:end) = [aux(1:On+1)];
P = flip(P);
QQ = zeros(1,Od+1);
QQ(1:1:end) = [1; aux(On+2:end)];
```

```
52 QQ = flip(QQ);
53
54 zz = roots(P);
55 pp = roots(QQ);
56
57 end
```

Including errors :

An immediate observation from the script above is that the analysis does not take into account errors present on the simulated Taylor coefficients, even though they are present in the input matrix constructed. A straightforward way to include errors is vary the input Taylor coefficients over a randomly generated spread determined by a Gaussian centered around the central values of the Taylor coefficients obtained and having a standard deviation proportional to the error on that coefficient (see the section above for the placement of error in the input matrix **MyDD**). The lines of code necessary to implement one instance (is run in a loop to generate error estimates and check for the stability of poles of the Padé approximant) of this error on the coefficients is shown below. Here, the inbuilt function of MATLAB called **randn** is used, whose most basic function is the generate a random number drawn from a normal distribution. The most natural way to construct a random number drawn from a different Gaussian distribution, say with mean m and standard deviation d, is $r = m + d * randn(M, N)$, where M, N are dimensions of the matrix needed. The use of the imaginary value in line 3 and 5, is to indicate that the number density and its second derivative are imaginary when simulated at imaginary μ_B.

```
1
2     DD = MYdd;
3     DD(:,2) = DD(:,2) + 1i*randn(size(DD(:,2))).*DD(:,3);
4     DD(:,4) = DD(:,4) + randn(size(DD(:,4))).*DD(:,5);
5     DD(:,6) = DD(:,6) + 1i*randn(size(DD(:,6))).*DD(:,7);
6
7     [~,~,zz,pp]=NSLinPadeGen(DD,idx);
```

The procedure described above takes into account *statistical errors*. The stable poles found in our analysis are always reported along with statistical errors obtained from generating stable poles from about 500-2000 random generations of Taylor coefficients. The magnitude of errors can be viewed in Table 5.4.
To inspect how the stable pole moves *systematical errors*, one varies the input matrix **idx**. This can be done by deleting certain rows and including or dis-including higher order Taylor coefficients for some rows and their various permutations. We have also ascertained the stability of the poles found under this test. As an example, see Fig. 5.13 and Fig. 5.14. The green dots are results from the analysis of varying the second column of **idx** matrix, with the number of permutations used indicated in the caption of the figures.

5.3 Results : Approximation and analytic continuation

In this section we will describe how the Padé function obtained approximates our data. We will display results from both the approximation in the imaginary μ_B/T

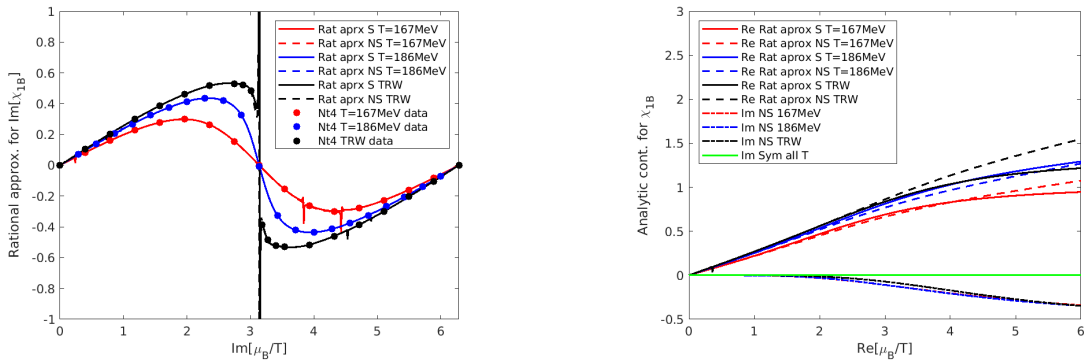

Figure 5.5: (Left) : Rational approximation of the baryon number density for the $24^3 \times 4$ lattices simulated at temperatures $T \in \{167.4, 186.3, 201.4\}$ MeV. (Right) : Analytic continuation of the rational functions shown in the left plot to real μ_B/T for the same temperatures.

plane and the analytic continuation of the results to the real μ_B/T plane. We will also display results obtained both from our symmetric and general ansatz.

Results for the $N_\tau = 4$ data: Here we display the net baryon number density and its analytic continuation. On the left plot in Fig. 5.5 are displayed the results from the two ansatz : one using the symmetric Padé solver (labelled S in the plot) and the other by using no symmetries imposed (labelled NS in the plot). As can be seen, they lie on top of each other and approximate the data very well. The spikes that one can see in Fig. 5.5 (Left) are due to zero-pole pairs on the imaginary μ_B/T axis, which are supposed to exactly cancel each other (as explained in Section 2.6), but due to the presence of noise are slightly different (difference is in the 3^{rd} or 4^{th} digit.) Now we move onto Fig. 5.5 (Right) - the analytic continuation of the rational approximations to the real μ_B/T plane. As for the analytic continuation, it can be seen that the curves corresponding to a given temperature from both the ansatz agree up to $\mu_B/T \sim 2$. Another feature to notice is that we have also plotted the *imaginary* part of the number density as a function of real μ_B/T (which of course should be zero). We can see that for the ansatz with no symmetry imposed, this curve starts as zero, but soon deviates from it, around $\mu_B/T \sim 1.5 - 2.0$. We claim that we should be able to trust the analytic continuation up until the point where the imaginary part of the number density at real μ_B/T deviates from zero. As for the symmetric ansatz, the imaginary part of the number density at real μ_B/T is zero by construction such that it cannot give an indication about when the analytic continuation fails.

Results for the $N_\tau = 6$ data at T = 145 MeV: Now we discuss the rational approximation and analytic continuation for the case for $36^3 \times 6$ lattice. We would like to remind the reader that this lattice size and temperature were chosen in order to probe other singularities like the chiral transition. To this end we did find a signature of a pole in the complex μ_B/T which was not a thermal singularity - only when we restricted our input interval to $\mu_B/T \in \{0, \pi\}$. We will display this singular structure in the next section (Section 5.4). Here we will discuss the approximation itself and its analytic continuation. Displayed in Fig. 5.6 (Left) are the rational approximation (top) and analytic continuation (bottom) obtained from the

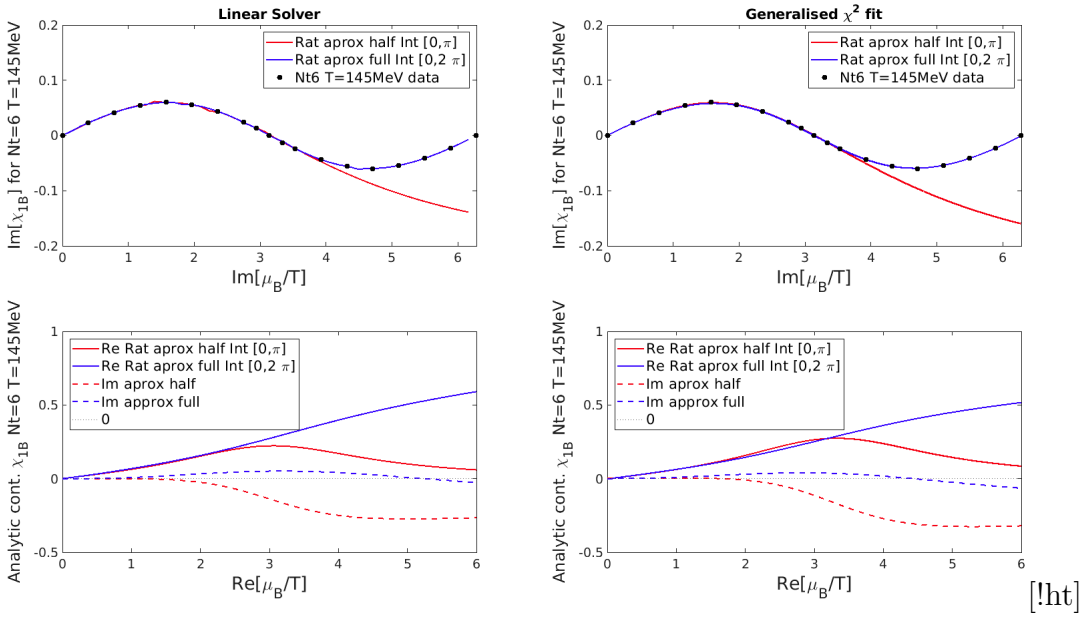

[!ht]

Figure 5.6: $36^3 \times 6$ lattice data at $T = 145$ MeV : Rational approximation (Top Left) and Analytic continuation (Bottom Left) using the Linear solver described in Eq. 2.8 and Rational approximation (Top Right) and Analytic continuation (Bottom Right) from the generalised χ^2 fit method described in Eq. 5.4.

linear solver (Eq. 2.8) using both the half interval as input ($\mu_B/T \in \{0, \pi\}$) and full interval ($\mu_B/T \in \{0, 2 * \pi\}$). It is not surprising that the approximant built from the full interval does a better job at approximating the number density on the full interval. As for the analytic continuation, the real part of the number density at real μ_B/T for both the half and full interval inputs starts deviating around $\mu_B/T \sim 2.5$ while their imaginary parts start deviating from zero at around the same value of $\mu_B/T \sim 1.5$. The situation on the right plot of Fig. 5.6 is qualitatively the same as the one on the Left, but was obtained using the generalised χ^2 procedure mentioned in Eq. 5.4.

Results for the $N_\tau = 6$ data at $T \in \{179.5, 186, 190\}$ MeV: These are results from our most recent simulations. We have approximated here also the charge density and its cumulants, in addition to the net baryon number density. We display below only the rational approximations for this data. In Fig. 5.7 the reader will find both the rational approximation for the charge and baryon number densities displayed in the same plot.

Results for $N_\tau = 8$ data at T = 156.5 MeV : $32^3 \times 8$ lattices were simulated at $T = 156.5$ MeV for the purposes of comparing how the Padé approximant and its analytical continuation perform with respect to the state of the art methods currently used in lattice QCD simulations. But for the moment we only display preliminary results for $N_\tau = 8$. Below we display a new variable simulated - the chiral condensate. Since the chiral condensate is a mass derivative of the partition function, we would expect it to inherit the even behaviour of the partition function across $\mu_B/T = \pi$, but for the moment we only display results for the first half of the interval in Fig. 5.8.

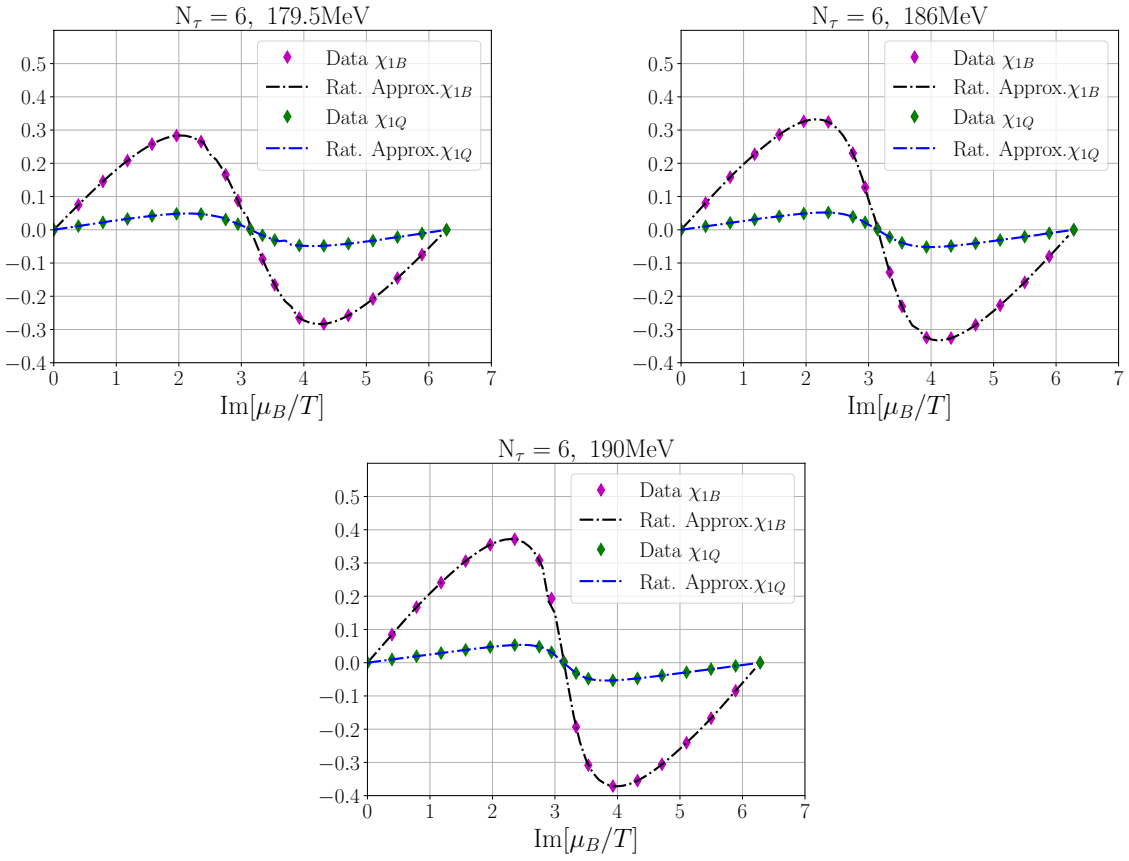

Figure 5.7: Rational approximations for net baryon number density and net charge density for $36^3 \times 6$ lattices simulated at: (Top left) : T = 179.5 MeV,(Top right) : T = 185 MeV, (Bottom) : T = 190 MeV

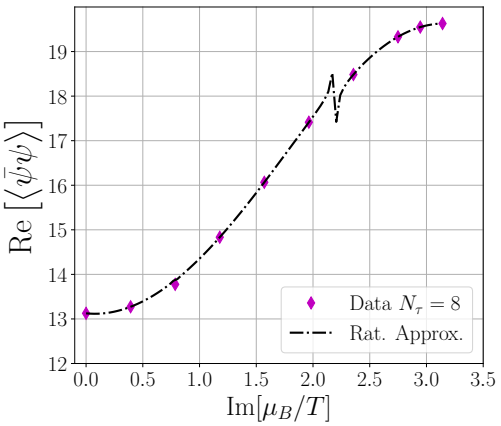

Figure 5.8: Rational approximation vs simulated data for the chiral condensate obtained for $32^3 \times 8$ lattices at $T = 156.5$ MeV

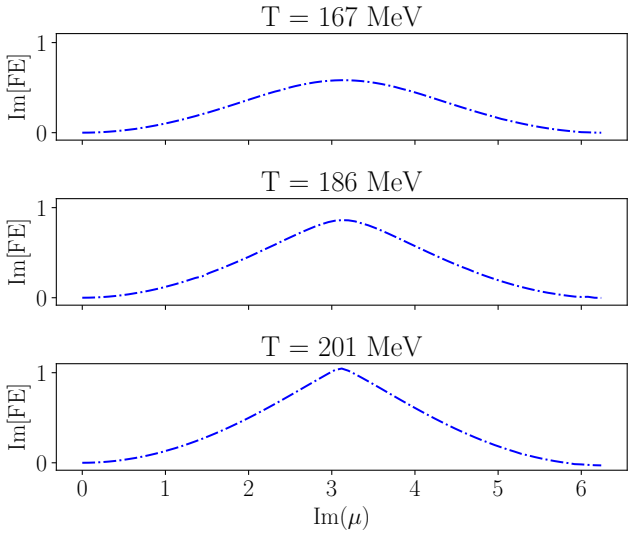

Figure 5.9: Free energy for the $N_\tau = 4$ data near the RW transition obtained by integration of the corresponding Padé approximation of net baryon density.

Free energy for the $N_\tau = 4$ data near the RW transition : Since we have the rational function at for the number density at our disposal, we decided to numerically integrate it to obtain the free energy profiles for temperatures near the RW transition. Shown in Fig. 5.9 are the free energy profiles constructed for three temperatures for the $24^3 \times 4$ lattices : (Top) at T = 167.4 MeV, (center) : T = 183.6 MeV; (bottom) : T = 201.4 MeV (expected RW transition). More details about the RW transition can be found in the following section, but we however would like to point out that a signature cusp is developing around Im[μ]= π as T approaches the expected RW transition temperature.

5.4 Results for the singularity structure

In this section we will begin by displaying our final results for the stable poles obtained by the Padé approximation of the net baryon number density in Tables 5.1 & 5.2. The results of Table 5.1 can also be found in our recent publication [16]. The poles that are displayed in Tables are the only stable poles found by the Padé approximant. The stability has been checked for every single pole by repeating the analysis at various order (more on this in the following subsection). After determining the stable poles an error estimation was proposed on each of them. The errors are computed out of a bootstrap in which our Padé analysis is repeated by letting the input Taylor coefficients vary within their errors. A note on the type of errors is due. There are two effects which we believe are correlated. One of them is statistical which originates from the nature of Monte Carlo methods and we have taken them into account for the current error estimates on the poles in the tables. The other is more systematic in nature and has to do with the choice of order we make for generating our Padé approximant. This effect has also been studied by us qualitatively in [16]. But the main message is that these systematic effects grow proportionally with the noise present in the data, and with the given magnitude of noise on our input coefficients (for the $24^3 \times 6$ lattices), our statistical error bars are larger than the systematic ones. But of course a more careful analysis will have to be done in the future taking into account both effects.

The main message we want to convey from Table 5.1 is that the poles from the three different methods described to construct the rational approximation are consistent within errors. Method III in the table indicates the analysis performed in the fugacity plane and Method III* the values mapped back to the original plane (being a logarithmic map there are infinitely many relatives of the pole found, but we pick the one in the first quadrant since they are all physically equivalent.)

T (MeV)	Method I		Method II		Method III*		Method III	
	$\hat{\mu}^R_{LY}$	$\hat{\mu}^I_{LY}$	$\hat{\mu}^R_{LY}$	$\hat{\mu}^I_{LY}$	$\hat{\mu}^R_{LY}$	$\hat{\mu}^I_{LY}$	z^R	z^I
201.4	0.11(11)	3.142(10)	0.077(45)	3.133(15)	0.0541(15)	3.1294(63)	-0.9472(14)	-0.0116(60)
186.3	0.48(14)	3.118(54)	0.53(13)	3.112(66)	0.397(51)	3.127(34)	-0.672(34)	0.010(21)
176.6	1.03(10)	3.112(72)	1.022(80)	3.18(12)	1.040(94)	3.115(65)	-0.353(33)	-0.010(20)
167.4	1.82(11)	3.125(79)	1.79(13)	3.164(95)	1.694(55)	3.12(13)	-0.184(12)	0.004(22)
160.4	2.097(90)	3.147(11)	2.14(12)	3.150(70)	2.07(76)	3.14(24)	-0.126(70)	0.000(14)

Table 5.1: Method I : Linear Solver. Method II : χ^2 fit approach. Method III : Linear solver in fugacity plane. (Note* : Mapped back values from fugacity plane. We are picking the value in first quadrant given the symmetries of the partition function)

We now focus on the poles found from the recent analysis on $36^3 \times 6$ data with temperatures in the vicinity of the RW transition. We used two different observables to approximate via our Padé analysis here : the net baryon density and the net charge density since they have the same symmetry properties across the RW transition. The results from the same type of bootstrap analysis are presented in Table 5.2. This is again a positive result for us, that the two agree very well within errors.

Lastly, we would like to display results for the $36^3 \times 6$ lattice data simulated at $T = 145$ MeV. This was only error-analysed using method II described in Section 2.2. This point is special because it only shows up when we consider half the input interval (the full interval gives a thermal type singularity as shown). But there is

T (MeV)	χ_{1B}		χ_{1Q}	
	$\hat{\mu}^R_{LY}$	$\hat{\mu}^I_{LY}$	$\hat{\mu}^R_{LY}$	$\hat{\mu}^I_{LY}$
190	0.532(82)	3.160(66)	0.539(85)	3.153(91)
186	0.91(12)	3.154(91)	0.869(95)	3.151(76)
179.5	1.33(17)	3.14(14)	1.25(12)	3.136(95)
145	2.99(39)	3.15(96)	2.89(59)	3.58(99)

Table 5.2: Comparison of thermal singularities obtained from the analysis of two cumulants for the $N_\tau = 6$ data: χ_{1B} and χ_{1Q}

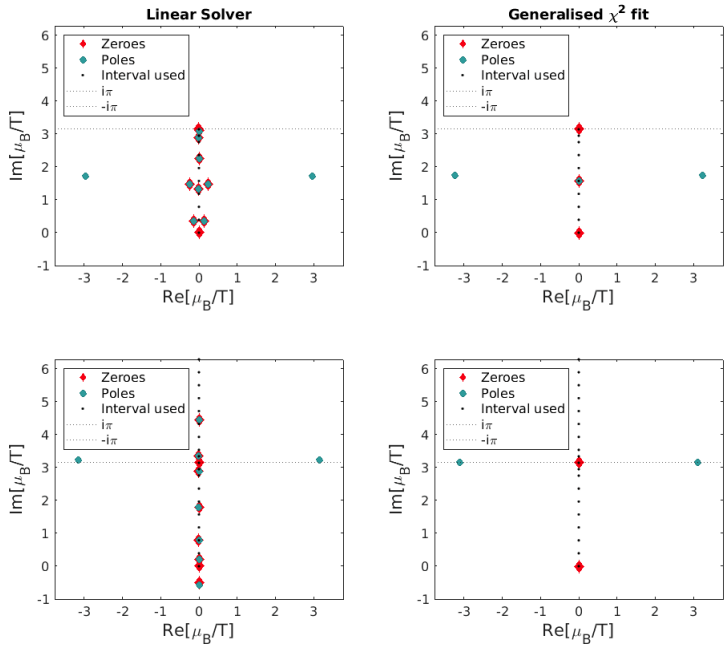

Figure 5.10: Singularity structure in the $\hat{\mu}_B$ plane on $N_\tau = 6$ at $T = 145$ MeV. As in Fig. 5.6, the method for obtaining the rational approximants can be the solution of the linear system (left) or the minimization of the generalized-χ^2 (right); the input interval for the analysis can be $\hat{\mu}^I_B \in [0, \pi]$ (top) or $\hat{\mu}^I_B \in [0, 2\pi]$ (bottom).

still the stability of this pole across methods as shown in Fig. 5.10. The pole with its statistical error bars is presented in Section 5.5.2.

5.4.1 Stability of the singularity structure under choice of coefficients

In this sub-section we will comment more on the systematic effects of changing the order of the Padé to display the stability of the pole found. This is important because the only true signature of a genuine pole is stability under changing order of the Padé. Of course this stability is subject to noise as explained in Section 2.6. We display this stability in two ways. The first one can be seen in Figs. 5.11 & 5.12, and the second can be seen in Figs. 5.14 & 5.13.

In Fig. 5.11 we explicitly display the singularity structure obtained from the Padé at three different order for the $24^3 \times 4$ lattices simulated at 160 MeV. As can be seen, the stable poles only move within the statistical error bars quoted. The same holds of the data shown in Fig. 5.12.

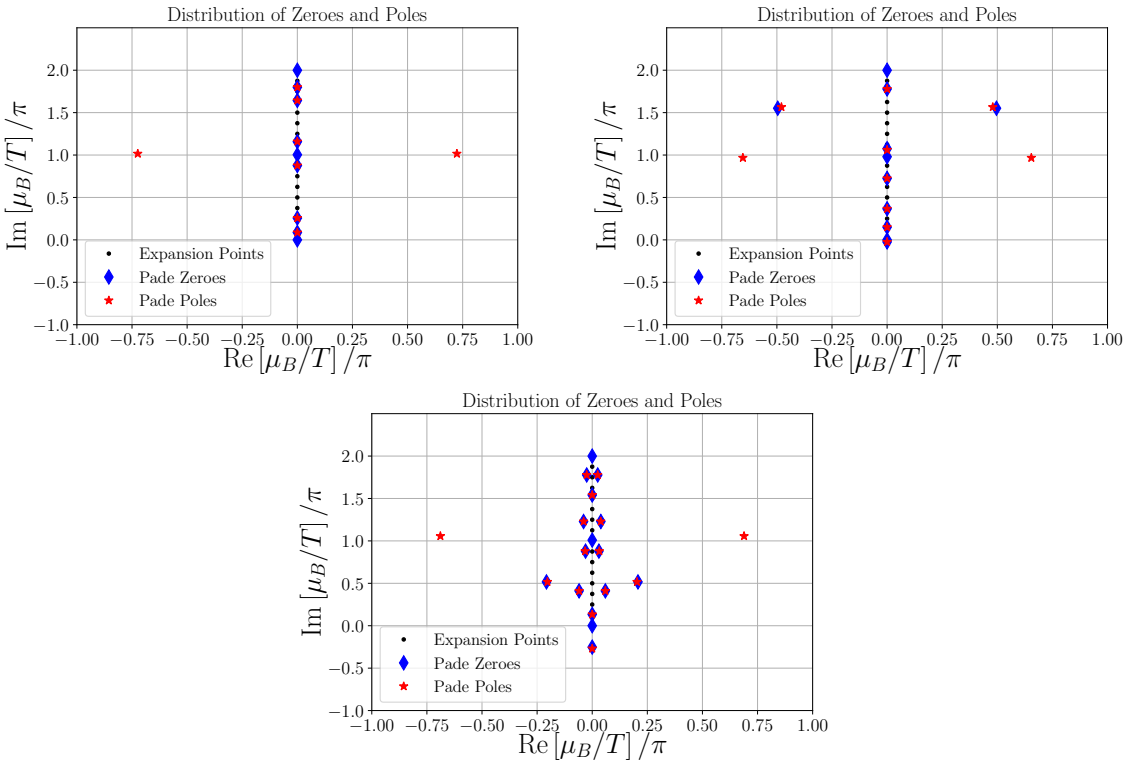

Figure 5.11: Zero pole structure for N$\tau = 4$, T=160MeV at different orders of the Padé interpolant

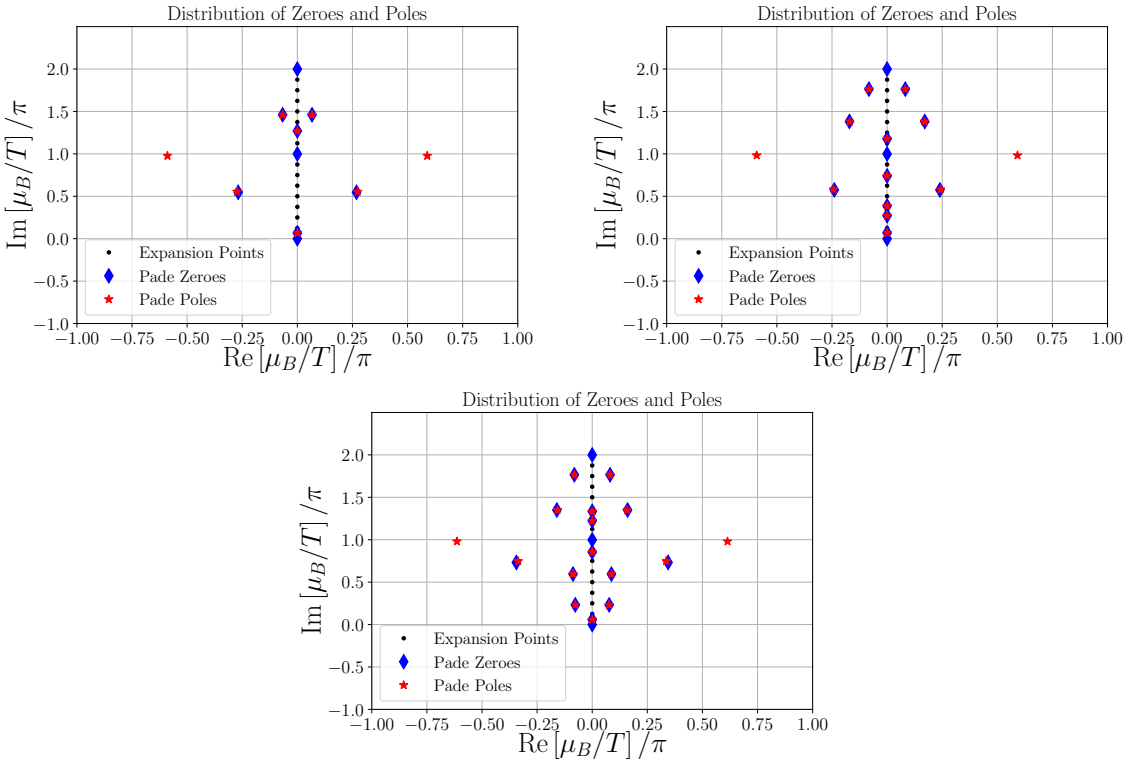

Figure 5.12: Zero pole structure for N$\tau = 4$, T=167MeV at different orders of the Padé interpolant

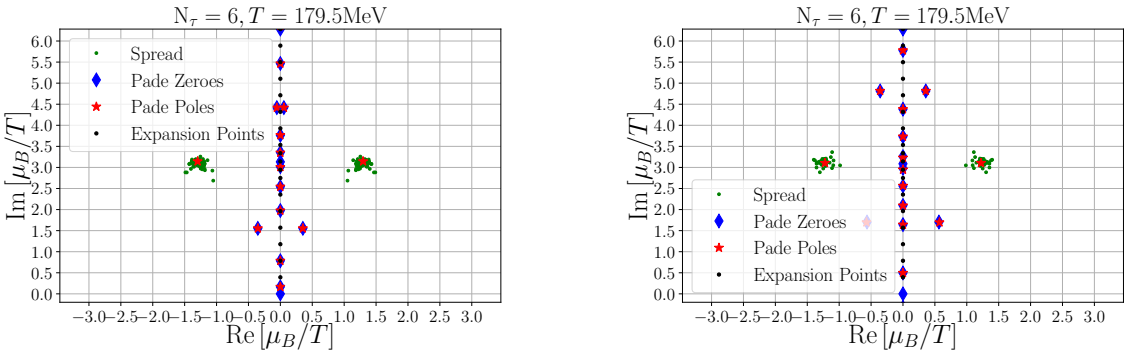

Figure 5.13: Stability of poles using fifty permutations of the input Taylor coefficients (marked Spread) for $36^3 \times 6$ lattice simulated at $T = 179.5$ MeV : (Left) net baryon density and (Right) net charge density

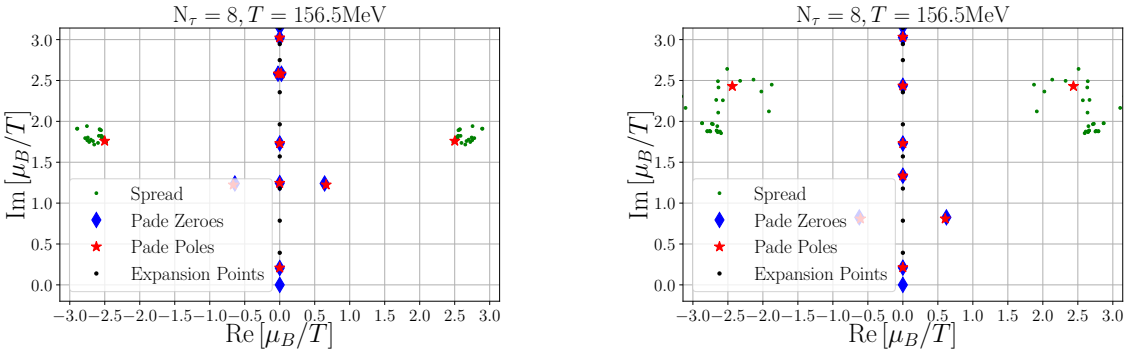

Figure 5.14: Stability of poles using thirty five permutations of the input Taylor coefficients (marked Spread) for $32^3 \times 8$ lattice simulated at $T = 156$ MeV : (Left) net baryon density and (Right) net charge density

In Fig. 5.13 we demonstrate stability of the closest pole found by the Padé by using fifty permutations of the input Taylor coefficients. These are marked by green dots. The spread of the poles in indeed very small within statistical error bars shown in Table 5.2.

However, the situation in the $32^3 \times 8$ lattice is less promising at the moment. But irrespective of that there is definitely the signature of a pole which will be investigated in the future.

5.4.2 Stability of results under conformal maps

Taking inspiration from [92, 81], we repeated our analysis in a different variable obtained via a conformal map of our data. The primary reason for doing this was to determine whether the poles obtained in the μ plane are artifacts of the variable of expansion or invariant under the choice of variable which can confirm the genuineness of the stable poles we find. Another reason (which became apparent to us after doing the analysis in the conformal plane) was that when we choose a map that shrinks our input interval for the multi-point Padé analysis, the linear system we solve becomes well-conditioned. To be specific, the map we chose was the fugacity map : $z = e^{\hat{\mu}_B}$. Before we display the results of this map, we would like to comment on the expected singularity structure from this map.

i Our interval of expansion $\hat{\mu}_B = i\hat{\mu}_I$ with $\hat{\mu}_I \in \mathbb{R}$ will be mapped to a unit circle in the fugacity plane because of the exponential map.

ii The signal for the Roberge-Weiss transition observed in the $\hat{\mu}_B$ plane was either poles or branch-cuts all lying on the line $\hat{\mu}_B = i\pi$. Hence, these will be mapped to the real z axis.

iii Even though one of the motivations for the conformal map was to get rid of the spurious poles (if any) in the original plane, we still find some poles of residue zero (poles accompanied by zeros). But this is to be expected since they are both an artifact of noise and of the order we demand from our Padé as explained in Section 2.6.

In Fig. 5.15, we display results for the singularity structure in the conformal (fugacity) plane for the thermal singularities for the $N_\tau = 4$ data for three temperatures: $T = \{201.4, 186.3, 167.4\}$ MeV. As can be seen, all the relevant singularities we found in the μ plane have survived including the branch cut structure for T_{RW} ($T = 201.4$MeV).

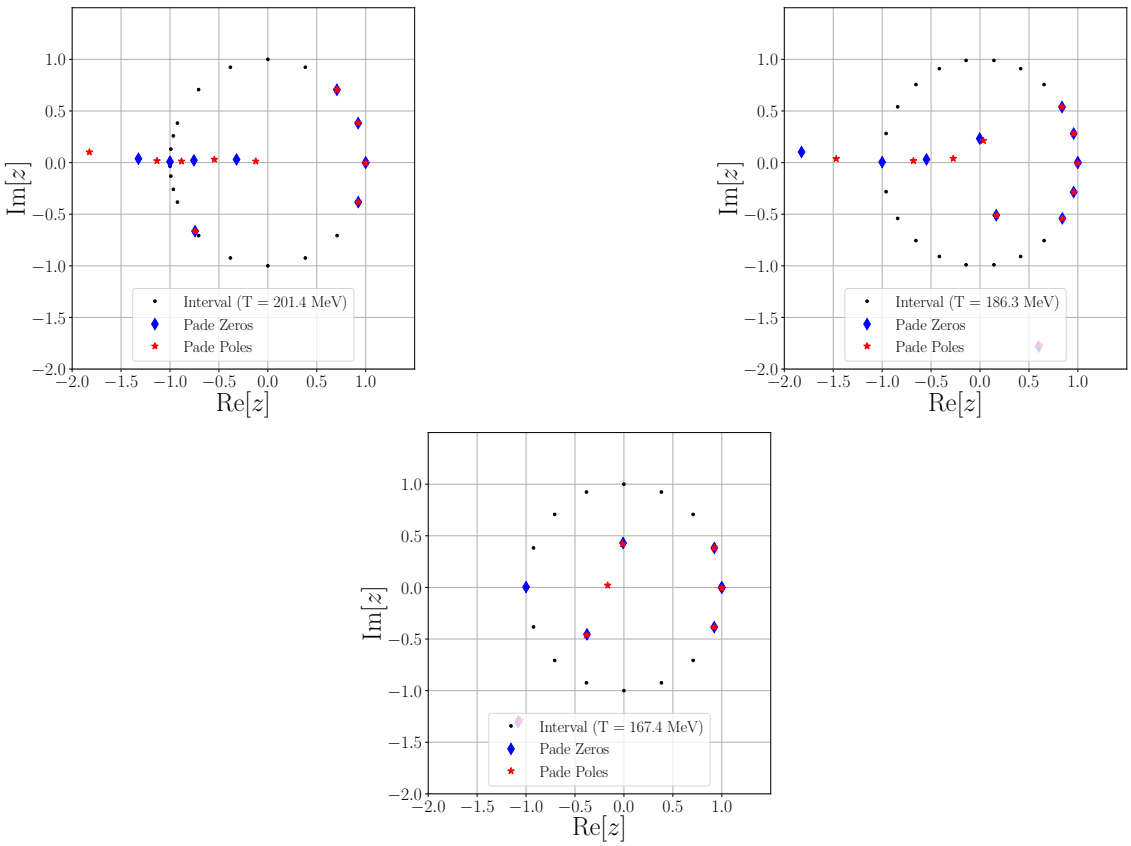

Figure 5.15: Singularity structure in the fugacity ($z = e^{\hat{\mu}_B}$) plane for the RW transition (N_τ) data. (Top left): T = 201.4 MeV ,(Top right): T = 186.3 MeV, (Bottom center): 167.4 MeV

5.5 Scaling analysis

After having extracted the stable singularities from the Padé analysis we now have to discuss the physical relevance (if any) of our poles. The most natural test is to check whether these are Lee-Yang edge singularities because if they are, they will follow a particular scaling law. In the following, we make extensive use of the fact that the scaling function of the order parameter $f_G(z)$ exhibits a branch cut singularity at $z = z_c$, where the scaling variable z is expressed in terms of the reduced temperature t and symmetry breaking field h as $z = t/|h|^{1/\beta\delta}$. The universal position z_c of the universal singularity, known as the Lee-Yang edge singularity, has been recently determined for different universality classes [78]. To this end, we will show that the poles we obtained relating to the RW transition indeed follow a scaling consistent with the 3d Ising Z_2 universality class for both the $N_\tau = 4$ and $N_\tau = 6$ high temperature data. We will also briefly discuss the physical relevance of the single-pole found in the low temperature simulation ($T = 145$ MeV) of the $36^3 \times 6$ lattice in the context of chiral transitions.

5.5.1 Roberge-Weiss scaling

As has already been seen in Section 3.4, the RW critical point is a remnant of the Z_3 symmetry in the $m_q \to \infty$ limit of QCD. The nature of the RW end-point depends on the masses of the quarks as well as the scheme of lattice discretization chosen. In 2+1 flavour QCD with physical value of quark masses and improved lattice discretizations, the RW end-point has been shown to belong to the Z_2 critical end-point [94, 91, 59]. Using the poles for $N_\tau = 4$ data from Table 5.1 and for $N_\tau = 6$ data from Table 5.2, we will fit them to a scaling equation which describes a Z_2 symmetric second order phase transition in the scaling region of the RW transition. We will then show the consistency of these fits.

The order parameter in the vicinity of a second order transition can be written as the sum of a universal and a regular part,

$$M = h^{1/\delta} f_G(z) + M_{\text{reg}} \; ; \; z \equiv t/|h|^{1/\beta\delta}, \tag{5.5}$$

where, t, h are scaling fields and β, δ are critical exponents. Also, f_G is the universal scaling function for the order parameter, whereas M_{reg} accounts for regular contributions. The relevant scaling fields for a Z_2 symmetric second order transition can be defined as

$$t = t_0^{-1} \left(\frac{T_{RW} - T}{T_{RW}} \right), \tag{5.6}$$

$$h = h_0^{-1} \left(\frac{\hat{\mu}_B - i\pi}{i\pi} \right) \; , \tag{5.7}$$

where t is now our reduced temperature with respect to the RW transition, $\hat{\mu}_B = \mu_B/T$, and h_0, t_0 and T_{RW} are the non-universal parameters. Notice that this reduced temperature is defined in the negative sense to the one used for the 2D Ising model in Section 4.5. The reason for that is that for the 2D Ising model we approach the transition T_c form above, i.e., from the symmetric to the non-symmetric phase.

For the RW transition, we do the same, but here the low temperature phase is the symmetric phase, and hence we approach it from below. Also, in the RW transition, the chemical potential plays the role of the symmetry-breaking field ($h = 0$ corresponds to $\hat{\mu}_B = i\pi$ which marks the position of the RW transition in the $\mu_B - T$ plane). We now can solve $t/h^{1/\beta\delta} \equiv z_c = |z_c|e^{i\frac{\pi}{2\beta\delta}}$ for $\hat{\mu}_B$ to obtain,

$$\hat{\mu}^R_{LY} = \pm\pi \left(\frac{z_0}{|z_c|}\right)^{\beta\delta} \left(\frac{T_{RW} - T}{T_{RW}}\right)^{\beta\delta}, \tag{5.8}$$

$$\hat{\mu}^I_{LY} = \pm\pi\,, \tag{5.9}$$

where the normalization constant z_0 is defined as $z_0 = h_0^{1/\beta\delta}/t_0$. Equations (5.8) and (5.9) thus define the temperature scaling of the Lee-Yang edge singularity, associated with the Roberge-Weiss critical point.

Now we move on to the actual fitting equation that has been used by us to fit the $N_\tau = 4$ pole data. We will actually implement two fitting ansatz : the first one will only be used for the $N_\tau = 4$ data, using the known values for $T_{RW} = 201.4$ MeV which was obtained for our particular $24^3 \times 4$ lattice set up in [91]. In the second fit we fit both the $N_\tau = 4, 6$ results and allow T_{RW} to be fitted.

The first fit method for $N_\tau = 4$: In order to show that the real part scales in accordance with Eq. (5.8) we perform fits to the data listed in Table 5.1 with the ansatz

$$\hat{\mu}^R_{LY} = a\left(\frac{T_{RW} - T}{T_{RW}}\right)^{\beta\delta} + b\,, \tag{5.10}$$

with fit-parameter a, b. We fixed the critical exponents to that of the Ising universality class; i.e., we have $\beta\delta \approx 1.5635$. The parameter b is added to capture the leading order finite-size effects. Since our calculations are done in a finite volume, we expect that the Lee-Yang edge singularities will not reach the real h axis, which is here the $\hat{\mu}^I_B$ axis. Or with other words, there is no phase transition in a finite volume. A more elaborate finite-size analysis is ongoing. We will display the results of our fit in Fig. 5.16 (Left)[5]. The results for the fit parameters are shown in Table 5.3:

Method	a	b	χ^2	z_0
I	24.77 (2.68)	0.1192(80)	1.14	9.18(99)
II	25.54 (79)	0.0806(9)	0.49	9.37(29)
III	26.08 (63)	0.0541(1)	0.96	9.49(23)

Table 5.3: Fit parameter a, b, obtained from a scaling fit to the Lee-Yang edge singularities in the vicinity of the Roberge-Weiss transition. Also given are the reduced χ^2 and the deduced values for the nonuniversal constant z_0 for the data sets obtained from methods I-III, respectively.

The second fit method for $N_\tau = 4$ & $N_\tau = 6$: The fit ansatz used is

$$\hat{\mu}^R_{LY} = a\left(\frac{T_C - T}{T_C}\right)^{\beta\delta}, \tag{5.11}$$

[5]The scaling has been performed in Bielefeld and checked in Parma (by the author). Here we would like to acknowledge this and present the original plot.

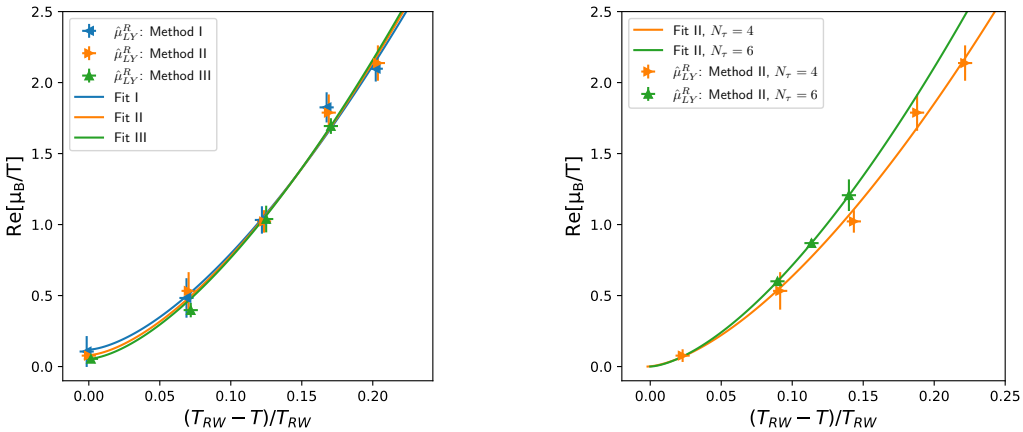

Figure 5.16: [Image credit : Christian Schmidt] RW scaling plots : (Left) Scaling of the real part of the poles (from Table 5.1) with the fit equation Eq. 5.8. (Right) : Scaling of the real part of the equation for χ_{1B} data from both $N_\tau = 4$ & $N_\tau = 6$ using the Padé procedure Method II., the fit equation used is 5.11

with fit-parameter a, T_C (we fit for T_{RW}). We again fixed the critical exponents to that of the 3d Z_2 Ising universality class. The results for the parameters of the fit obtained are (note that z_0 is not a fit parameter but calculated from a, T_C) :

N_τ	T_C	a	χ^2	z_0
4	22.66 (2.18)	206.12 (2.67)	0.61	8.68 (84)
6	26.085 (5)	208.704 (2)	0.000324	8.696 (2)

Table 5.4: Fit results for the fit shown in Fig. 5.16 (Right). [Fit data obtained from Christian Schmidt]

We have demonstrated that our Padé poles scale in accordance with the expected 3d Z_2 scaling in the Ising universality class. Besides the demonstration for scaling, we have calculated a non-universal constant z_0. To our knowledge, this is the first such estimation for z_0 for the RW transition.

5.5.2 Chiral Scaling:

Following the discussion from Section 3.3.2, chiral transition with staggered fermions on coarse lattices falls in the $3d-O(2)$ universality class. However, the full $3d-O(4)$ symmetry is expected to be restored in the continuum limit. The chiral transition in QCD has been subject to many lattice studies, and the scaling equation in the vicinity of the chiral transition is given by :

$$t = \frac{1}{t_0}\left[\frac{T - T_c}{T_c} + \kappa_2^B \left(\frac{\mu_B}{T}\right)^2\right], \tag{5.12}$$

$$h = \frac{1}{h_0}\frac{m_l}{m_s^{\text{phys}}}. \tag{5.13}$$

Here the light quark mass m_l in units of the physical strange quark mass m_s^{phys} takes the role of the symmetry breaking field ($m_l/m_s^{\text{phys}} \propto h$). In addition, this relation

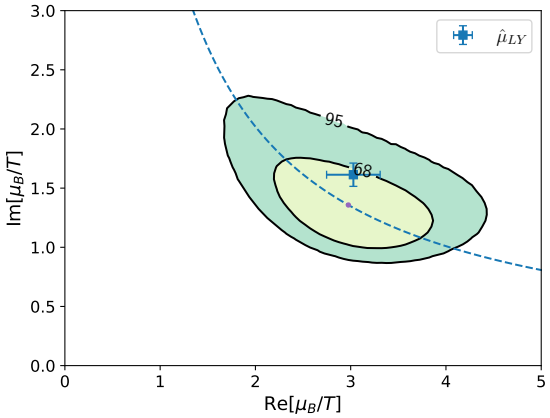

Figure 5.17: Pole obtained from $36^3 \times 6$ lattice when only half interval taken into account is compared with the expected LYE singularity for the $O(2)$ universality class with previously estimated non-universal parameters (68% and 98% confidence areas). Dashed line indicates the expected temperature scaling of the LYE.

involves three non-universal parameters z_0, T_c, κ_2^B. The latter two are prominent numbers that quantify the QCD phase diagram and have been determined to quite some precision [95, 96, 97]. We can now proceed as we did in Eq. 5.8 5.9, but finding a solution for $z = z_c$ to obtain the trajectory of the LYEs :

$$\hat{\mu}_{LY} = \left[\frac{1}{\kappa_2^B} \left(\frac{z_c}{z_0} \left(\frac{m_l}{m_s^{\rm phys}} \right)^{1/\beta\delta} - \frac{T - T_c}{T_c} \right) \right]^{1/2} , \tag{5.14}$$

This solution has also been used in [98] to derive an estimate of the radius of convergence.

However, since we cannot study the LYE scaling with only one data point, the goal in this section is to compare the position of the stable pole of the Padé observed by us when taking the half interval data for the $36^3 \times 6$ lattice: $(\hat{\mu}_B^R, \hat{\mu}_B^R) = (3.03(28), 1.61(10))$ shown in Fig. 5.10, to the expected position of the Lee-Yang edge singularity in the $O(2)$ universality class[6]. In Fig. 5.17, we show the 68% & 96% confidence areas of the expected Lee Yang edge singularity of the $O(2)$ universality class when the non-universal parameters are varied, under the assumption of Gaussian distributed errors. In particular, for $N_\tau = 6$, specific values and errors are chosen :

$$\begin{aligned} T_c &= (147 \pm 6)\ \text{MeV}\,, \\ z_0 &= 2.35 \pm 0.2\,, \\ \kappa_2^B &= 0.012 \pm 0.002\,, \end{aligned} \tag{5.15}$$

and in addition, we take $|z_c| = 2.032$ [78]. As can be seen from Fig. 5.17, the results from the rational approximation to our data (method II), $(\hat{\mu}_B^R, \hat{\mu}_B^I) = (3.03(28), 1.61(10))$, lie within the 68% confidence area of this prediction.

[6]The study on the Chiral scaling is based on scaling studies of the HotQCD collaboration and is presented in more detail in [16]

5.6 Conclusions and Outlook : Scaling analysis

To conclude this chapter, it is important to see how the two different scaling analyses tie together in the context of the conjectured QCD phase diagram. For this we will refer again to the RW transition described in Section 5.5.1 and the 3D QCD phase diagram described in Section 3.5. All the stable LY edge singularities found, in the context of both the RW and the Chiral transition can be summarised in a single plot (bottom right corner in Fig. 5.18) shown. The RW region (yellow line) can be easily seen as the LY edge trajectory with varying temperature as a straight line in the (μ_{LY}^R, μ_{LY}^I) plane according to Eq. 5.8 and Eq. 5.9. As can be seen, the stable poles from the Padé agree, even with errors, with this scaling. Moreover, from the scaling of these poles (now seen to be the relevant LYEs for the RW transition), it was shown to be in the 3d Z_2 universality class of the Ising model. This is indicated by the plot on the bottom left in Fig. 5.18, where the first order RW transition line ends at a 2_{nd} order critical point, turning into a cross over line that extends into the real μ_B plane. Equation (5.14) is visualized in Fig. 5.18 as green band, where we chose $m_l/m_s^{\text{phys}} = 1/27$ (physical mass ratio) and $T_c = 147$ MeV which is our knowledge the best estimate for the Chiral transition temperature for $N_\tau = 6$. It is however obvious that T_c does not alter the line of constant $z = z_c$ much; it mainly alters the normalization of the temperature behavior. The curvature κ_2^B is chosen as $\kappa_2^B = 0.012$. The construction of the red band is discussed in [16] and is based on [99]. We vary z_0 from 1.5 to 2.5 which generates the width of the green band. Our best estimate for $N_\tau = 6$ is $z_0 = 2.35$, which stems from scaling fits to the magnetic equation of state. It is fair to say that not much can be concluded from a single point that we have for the low temperature ($N_\tau = 6$,$T = 145MeV$) data. Currently, more data is being generated at low temperature and thus more LY edge singularities are expected. Once a number of points will be available, one can be in a position to inspect whether what we start seeing is indeed the signature of the Chiral transition. Notice that in principle one could even find that the scaling of the singularities points to the red band (thus being a signature for the CEP).

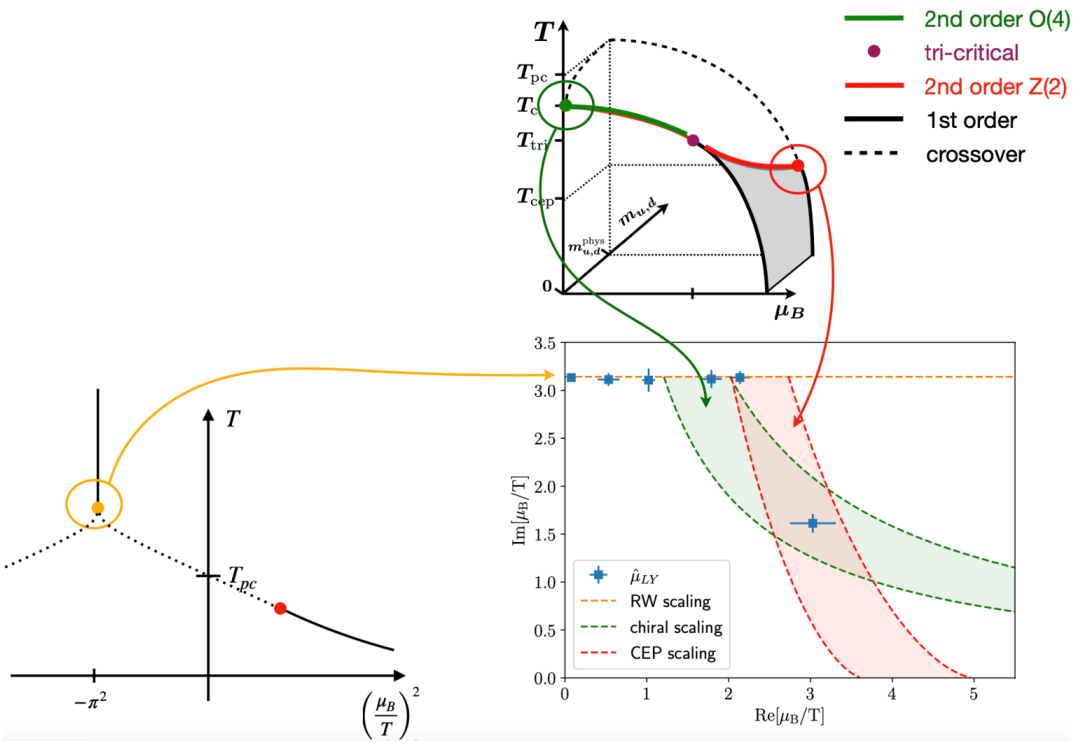

Figure 5.18: This figure displays our main findings (Bottom right corner, see [16]) along with the relevant scaling regions we are sensitive to in our analysis. The region marked by yellow corresponds to the RW transition. The LY edge singularities corresponding to this are indicated by a yellow arrow. The other stable singularity found, which is consistent with the Chiral scaling is shown in the red and green shaded regions. The green shaded region corresponds to the Chiral scaling while the red corresponds to a possible CEP scaling. The width of the bands indicate uncertainties in the non-universal parameters. See main text for details of construction of the bands.

Part II

Lefschetz Thimbles : Focus on Non-abelian gauge theories

Chapter 6

Sign problem & Lefschetz Thimbles

6.1 The *complex action* problem

The complex action problem occurs in many physical systems of interest – mostly fermionic. In this section, we will show how and why it occurs in lattice quantum chromodynamics simulations.

Since fermions are *Grassman-odd* objects, it is not straightforward to represent them using plain numbers - at best they can be understood using matrix representations which is dimensionally not very feasible when it comes to lattice simulations. Hence, in order to perform lattice simulations, we need to integrate fermions out of the path integral. This leads us to the following equation for the QCD partition function :

$$\mathrm{Z}_{QCD} = \int \mathcal{D}U \, \det \mathbf{M}(\mathbf{U}) \, e^{-S_G} \tag{6.1}$$

The fermion matrix $\mathbf{M}$ is γ_5 hermitian in the absence of the baryon chemical potential which leads to a real fermion determinant :

$$\begin{aligned} (\gamma_5 M) &= (\gamma_5 M)^\dagger \\ \rightarrow M^\dagger &= (\gamma_5 M \gamma_5) \\ \implies \det\big(M^\dagger\big) &= \det\left(\gamma_5 M \gamma_5\right) \\ \rightarrow \det(M)^* &= \det(M) \end{aligned} \tag{6.2}$$

However in the presence of a chemical potential, the γ_5 hermiticity condition mentioned above becomes :

$$\begin{aligned} \rightarrow M^\dagger(\mu) &= (\gamma_5 M(-\mu^*)\gamma_5) \\ \implies [\det M(\mu)]^* &= [\det M(-\mu^*)] \end{aligned} \tag{6.3}$$

This means we are faced with a complex fermion determinant at finite μ lattice QCD simulations - this makes direct Monte Carlo simulations impossible as we lose the notion of a positive definite measure in the partition function. There are certain workarounds listed below which however come with their own set of problems, as shown in the next sections.

6.1.1 Re-weighting and the overlap problem

A natural way to try to avoid simulating at any finite value of μ (where we cannot perform direct Monte Carlo simulations) is to perform the simulation at $\mu = 0$ and *re-weight* those configurations to obtain results at some finite value of μ. This method was first introduced in [100, 4] to estimate the QCD end-point at finite T and μ for relatively small lattices. However, their estimate was shown to be only correct for the lattice size and discretization they had chosen in [101]. A simple illustration of the idea of re-weighting is shown below. Starting with a simulation at $\mu = 0$ (assume that the finite μ term in the action occurs as an additive term, namely, $S(\mu) = S(\mu = 0) + S_{int}(\mu)$) :

$$\begin{aligned} Z|_{\mu=0} &= \int \mathcal{D}U \; e^{-S} \\ \langle O \rangle \, |_{\mu=0} &= \frac{1}{Z|_{\mu=0}} \int \mathcal{D}U \; O \; e^{-S} \end{aligned} \tag{6.4}$$

we can mimic the result at $\mu \neq 0$ by re-writing the $\mu = 0$ configurations as :

$$\begin{aligned} \langle O \rangle \, |_{\mu} &= \frac{1}{Z|_{\mu}} \int \mathcal{D}U \; O \; e^{-S(\mu)} \\ &= \frac{1}{Z} \int \mathcal{D}U \; O \; e^{-S - S_{int}(\mu)} \\ &= \left(\frac{Z|_{\mu=0}}{Z|_{\mu}} \right) \frac{1}{Z|_{\mu=0}} \int \mathcal{D}U \; \left[O e^{-S_{int}(\mu)} \right] \; e^{-S} \\ &= \left(\frac{Z|_{\mu=0}}{Z|_{\mu}} \right) \left\langle O e^{-S_{int}(\mu)} \right\rangle |_{\mu=0} \end{aligned} \tag{6.5}$$

The ratio of the two partition functions can also readily seen to be $\left(\frac{Z|_{\mu=0}}{Z|_{\mu}} \right) = \frac{1}{\left\langle e^{-S_{int}(\mu)} \right\rangle |_{\mu=0}}$, leading us to the final result :

$$\langle O \rangle_{Re-weighted} \, |_{\mu} = \frac{\left\langle O e^{-S_{int}(\mu)} \right\rangle |_{\mu=0}}{\left\langle e^{-S_{int}(\mu)} \right\rangle |_{\mu=0}} \tag{6.6}$$

One should immediately raise the question about the range of validity of this re-weighting procedure. Since, when we perform a Monte Carlo simulation at some given values of parameters – we are in essence approximating an integral with random configurations given by the Boltzmann-weights around those parameters. The assumption (or hope) of the re-weighting procedure relies on the fact that there are enough configurations sampled during the simulation *that are also relevant in the domain of integration* for the observable at the parameters we want the re-weighting. This means that we should have enough overlap between the configurations at the re-weighted values of μ and $\mu = 0$. Hence, there are two ways in which this can fail. The first is the obvious one - we should not expect re-weighting to work for configurations separated by large values of the parameter in which we want to re-weight. The second one is less obvious and is displayed in Fig. 6.1. There it can be seen that

by increasing the volume (going to the continuum limit), the distributions become narrower and the overlap between configurations decreases and increasing statistics would not lead to a better result in this situation!

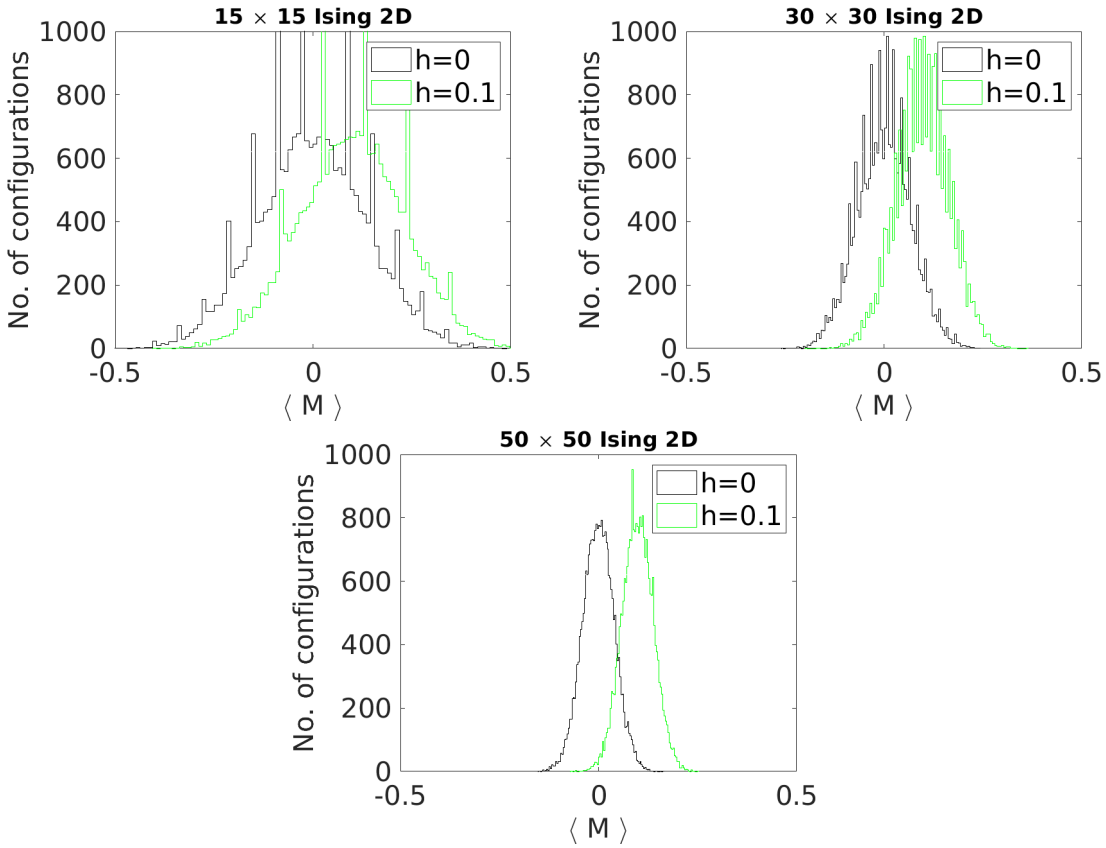

Figure 6.1: Overlap problem : Reduction in the "shared" configurations between two values of the external magnetic field for the cae of the 2D Ising Model while increasing the volume (Left to Right)

6.1.2 The Sign problem

The above-explained complex action problem can be reduced to the (in-)famous *Sign Problem* [102, 103]. Apart from re-weighting, another method of indirect Monte Carlo sampling can be applied to the partition function with the complex fermion determinant. It can be seen from the charge conjugation symmetry of the partition function that the partition function is real at finite μ. And also since e^{-s_G} is real, this means that we can use the real part of the integrand as weight to perform our Monte Carlo simulations :

$$Z_{QCD} = \int \mathcal{D}U \;\; \mathrm{Re}[\det M(U)] e^{-S_G(U)} \tag{6.7}$$

Now, we have that the probability weight is real but it is however still not positive. This is what causes the sign problem. Regions of integration now differ in sign and in order the get the precise cancellations correctly very high statistics are needed, for which the computational cost explodes exponentially with volume. This can be seen using a simple toy partition function ($Z_{toy} = \int_{-\infty}^{\infty} dx \exp\{(-x^2 + i\lambda x)\}$) below :

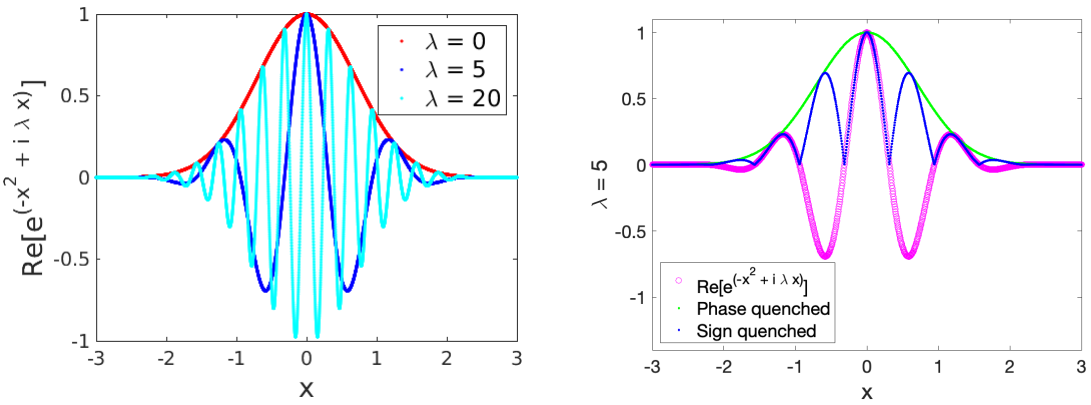

Figure 6.2: (left) : Illustration of the sign problem. (right) : Illustration of Sign quenched vs Phase quenched action.

There are two possible ways to tackle the above-mentioned sign problem (See Fig. 6.2) :

- **Phase quenching** : Instead of simulating with the real part of $\det M(U)$, simulations are performed with $|\det M(U)|$. As is apparent, if we simulate with this measure, we are actually simulating a *different* partition function. In order to get the original one back, we must re-weight the phases. This re-weighting has *overlap* problems in the same spirit as listed above (configurations not overlapping enough between the two partition functions). Further, this type of re-weighting has additional problems as the average phases can become zero. A nice overview can be found in [104]. Lattice QCD studies using this phase re-weighting method can be found in [1, 105, 106] and references therein.

- **Sign quenching** : Simulations are performed with $|\mathrm{Re}[\det M(U)]|$. Here, only the sign of the real part of the fermion is being *quenched*. This means (as seen in Fig. 6.2 (left)), by a *sign re-weighting* technique, the original integral can be recovered. This re-weighting has no configuration overlap problem as the Monte Carlo simulations generate the relevant configurations from the beginning. Only the sign of various integration regions has to be corrected. A recent application of this technique in lattice QCD can be found in [107]. Other references include [108, 109, 110].

The above two have an obvious drawback that we are simulating a different problem. This can be easily corrected by *sign re-weighting*. And there is no overlap problem as we are basically re-weighting from the same distribution. In any case, the finite-size effects are very bad for the direct simulations even today as can be seen in [107]

6.2 Lefschetz Thimbles : A possible way out?

Lefschetz thimble was developed as a technique to avoid the sign problem [111, 3]. The idea is to deform the original domain of integration into a suitable subspace of a complex domain while maintaining the same homology class, such that the imaginary part of the action remains constant on this new domain. Such paths exist and are shown to be solutions of the *steepest descent* equations originating at the *saddle points* of the action.

6.2.1 Defining a thimble

Thimbles are defined as solutions of the steepest ascent equations

$$\frac{d}{dt}z_i = \frac{\partial S_R}{\partial z_i} \tag{6.8}$$

originating from saddle points of the action $\left(\frac{\partial S}{\partial z_i} = 0\right)$ (here $i \in \{1, 2...d\}$, with d being the dimension in field space). The following properties of Lefschetz thimbles should be noted below (shown in $d = 2$ for simplicity).

1. Imaginary part of the action remains constant on a thimble (due to holomorphicity of the action). This can be seen as:

$$\frac{dS_I}{d\tau} = \frac{\partial S_I}{\partial x}\frac{dx}{d\tau} + \frac{\partial S_I}{\partial y}\frac{dy}{d\tau} \rightarrow \frac{\partial S_I}{\partial x}\frac{\partial S_R}{\partial x} + \frac{\partial S_I}{\partial y}\frac{\partial S_R}{\partial y} \rightarrow 0 \tag{6.9}$$

2. Convergence of the integral is ensured because the real part of the integral increases along a thimble :

$$\frac{dS_R}{d\tau} = \frac{\partial S_R}{\partial x}\frac{dx}{d\tau} + \frac{\partial S_R}{\partial y}\frac{dy}{d\tau} \rightarrow \frac{\partial S_R}{\partial x}\frac{\partial S_R}{\partial x} + \frac{\partial S_R}{\partial y}\frac{\partial S_R}{\partial y} \rightarrow ||\nabla S_R|\,|^2 \tag{6.10}$$

3. And lastly, thimbles form a basis for all integration contours. This will be made explicit in the next section.

An implicit assumption has gone into defining a Lefschetz thimble and that has to do with the fact that thimble formulation comes from a theory (Morse theory) that is only defined for *isolated* critical/saddle points of the action. This is because a thimble is defined as the union of all steepest ascent curves originating from a saddle point. The eigenvectors of the *Hessian* matrix, $H(S; p_\sigma)$ defined as

$$H(S; p_\sigma) = \frac{\partial^2 S}{\partial\phi_i \partial\phi_j}\ , \tag{6.11}$$

with positive eigenvalues span the tangent space of the stable thimble at the saddle point. And for isolated saddle points, this matrix has no null eigenvalues, this means it has exactly the number of positive eigenvalues as the dimensionality of the original field space (recall that we doubled the degrees of freedom when we complexified the field space.). We will see in the next chapter (Chapter 7) that gauge symmetry introduces null eigenvectors into this Hessian thus messing up the dimension of the thimble.

6.2.2 Single thimble vs Multi-thimble simulations

The quantities of interest in any Monte Carlo simulation are the expectation values of certain observables. When using the thimble approach, prior to computing this expectation value, we must determine the thimbles that contribute to the partition function and perform the Monte Carlo simulation on each of the contributing thimbles. This will lead us to the correct value of the expectation value of the observable as expected from the original action:

$$\langle O \rangle \ = \ \frac{\sum_\sigma \ n_\sigma \, e^{-i\,S_I(p_\sigma)} \ Z_\sigma \, \langle O \, e^{i\,\omega} \rangle_\sigma}{\sum_\sigma \ n_\sigma \, e^{-i\,S_I(p_\sigma)} \ Z_\sigma \, \langle e^{i\,\omega} \rangle_\sigma} \tag{6.12}$$

where the summation is over all contributing thimbles which are attached to critical points labelled by σ, S_I is the (constant) imaginary part of the action on each contributing thimble, n_σ is an integer known as the intersection number and represents the intersection of the unstable thimble with the original domain of integration. Whenever the unstable thimble (see next section) attached to a given critical point does not intersect the original domain of integration, that critical point does not contribute to the expectation value mentioned above. Notice that although we have factored out the constant imaginary part of the thimble outside the integral, there is a *residual phase*, denoted by $e^{i\omega}$, that accounts for the orientation of the thimble with respect to the original manifold. In principle, Eq. 6.12 is all we need to perform Lefschetz thimble simulations. However, in practice, it turns out to be quite hard to determine which thimbles contribute. This is because of two reasons : the first one being that it is not straightforward to calculate all the critical points of the action, in many cases this has to be done numerically (see Chapter 7 for an example of this), the second reason being that thimble decomposition may not stay the same when varying parameters of the theory. This means that even if one has determined the contributing thimbles in one region of parameter space, this may be the same thimble decomposition in another region of space. Points in the parameter space where thimble decomposition fails are called *Stokes points*, which we will discuss next. Nevertheless, multi-thimble simulations are still not easy to simulate even if one did have the knowledge of the contributing thimbles as has been shown in many works [30, 33, 112, 113, 32].

6.2.3 Stokes phenomena

As seen from Eq. 6.8,a union of steepest ascent (SA) curves originating from saddle points constitutes stable thimbles whereas solutions of steepest descent (SD) contribute to the unstable thimbles (anti-thimbles). Since these curves are solutions to first order differential equations with different boundary conditions (starting from different saddle points), thimbles (or anti-thimbles) can never cross each other. And the only way in which two such curves can cross each other is if they completely lie on top of each other. In the thimbles decomposition scenario this can only happen in one way : when there is SA/SD curve connecting two saddle points (see [31]), i.e, a SA curve lies on top of a SD curve. This is called a Stokes phenomenon. Across a Stokes point, there is a discontinuity in the number of contributing thimbles. However, this discontinuity is not harmful since it does not imply a discontinuity in the physical observables defined on the original thimble. In fact, we can use this discontinuity to our advantage in circumventing the problem of multi-thimble simulations. The idea is that instead of computing an observable $\mathcal{O}(\mu)$ as a weighted sum of contributions over many thimbles, we identify regions of parameter space where only a single thimble contributes, and then using the fact that the physical observable is defined and continuous [1] across a Stokes point we can circumvent simulating on many thimbles. This is done by bridging Taylor series of a physical observable across the Stokes points covering the region where more than one thimble contributes. We

[1] We are only claiming here that a discontinuity in the number of contributing thimbles does not imply a discontinuity in the physical observables in the original manifold. Of course, it is possible that in some situations Stokes phenomena can be accompanied by a discontinuity in the physical observable. In that case, we cannot apply this bridging solution and must look for other points in parameter space where only one thimble contributes.

can improve this bridging mechanism by using Padé series instead of Taylor series as will be seen in the next section.

6.2.4 Examples of success in Toy models

We applied the idea mentioned above to two toy models for which analytical results are known, in [31]. In both these models, regions of parameter space were identified where only single thimbles contribute, and then these regions were bridged first using Taylor series and finally using Padé approximants. In this section, we will only discuss the Thirring model in 0+1 dimensions and the second model which is heavy dense QCD (a 3d effective field theory) can be found explained in detail in the paper mentioned above [2]. We will summarize the main results of our work using Fig. 6.3 shown below.

1 D Thirring model : We begin by very briefly reminding the reader of this model in the context of the sign problem. The theory of this model has already been discussed in section 2.5. This is a model of staggered fermions coupled to U(1) gauge fields. The sign problem in this model is caused by the terms containing the chemical potential (μ). The action that we consider is given by Eq. 2.13, which we display again for convenience (the 1D Thirring has been introduced in Chapter 2, Section 2.5),

$$S = \beta \sum_n \left(1 - \cos\left(x_n\right)\right) - \log\left(\det D\right) \ ,$$

with

$$\det D = \frac{1}{2^{L-1}} \left(\cosh\left(L\hat{\mu} + i \sum_n x_n \right) + \cosh\left(L \sinh^{-1}\left(\hat{m}\right)\right) \right)$$

where all the dimension-full quantities are in lattice units. Moreover, we only consider expansions of our Taylor series in dimensionless quantities by taking ratios, i.e., in $\hat{\mu}/\hat{m}$ (The parameters chosen for our discussion are : $L = 8$, $\beta = 1$ and $m = 2$). It was shown in [30, 112] that contributions from multiple thimbles were required to account for the correct analytical result (which is known as seen in Eq.2.13), especially in the region with moderate values of the chemical potential $\hat{\mu}/\hat{m} \sim 1$. As shown in Fig. 6.3 (centre plot), we pick four points (marked by triangles at $\hat{\mu}/\hat{m} = \{0.15, 0.4, 1.4, 1.95\}$) where we determine (based on arguments presented in the paper [31]) that only a single thimble contribution matters and then we compute Taylor coefficients of the chiral condensate ($\langle\bar{\chi}\chi\rangle$) up-to various orders. We use those Taylor coefficients to build a multi-point Padé whose ability to approximate $\langle\bar{\chi}\chi\rangle$ can be seen in the middle plot of Fig. 6.3. The right-most plot of Fig. 6.3 shows the validity of our Taylor expansions. The circles represent the radii of convergence about two expansion points and have an overlap, which justifies joining the Taylor expansions in that region. Also shown as a red dot is the analytical pole of $\langle\bar{\chi}\chi\rangle$, which seems to be in very good agreement with the only stable poles found by our Padé approximant in that region. Lastly, for the sake of clarity, we explain the left-most plot in Fig. 6.3. The plot shows the various saddle points of the action for the specific values of the parameters mentioned above at $\hat{\mu}/\hat{m} = 1.4$ (marked at green dots) and zeros of the fermion determinant (marked with red points) where thimbles

[2] Only the Thirring model has been described here since this was the model the author contributed to. Details of the heavy dense QCD can be found in [31]

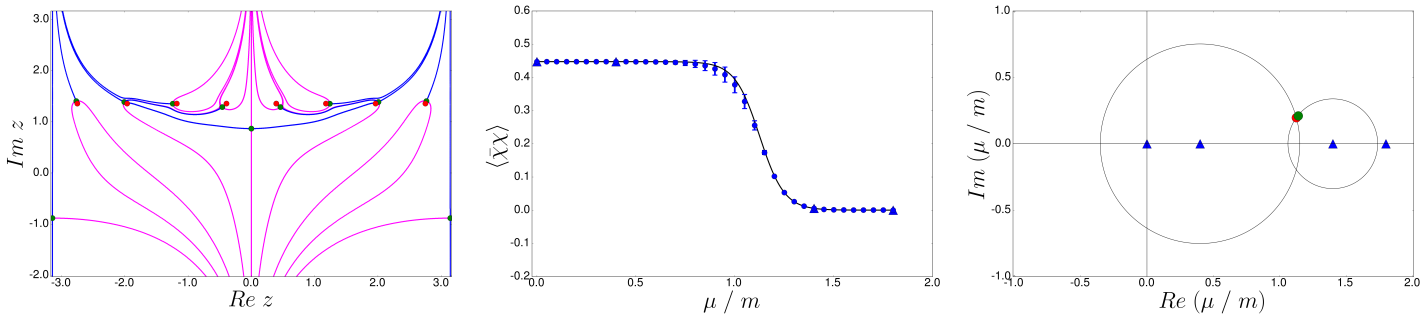

Figure 6.3: 1D Thirring model (see main text for explanation). (Left) : Thimble structure for a particular expansion point ($\hat{\mu}/\hat{m} = 1.4$). Anti-thimbles are marked in magenta and thimbles in blue. (Centre) : Bridging regions in parameter space using Padé. Note for moderate values of $\hat{\mu}/\hat{m} \sim 1$, multiple thimbles contribute to the partition function and the single thimble approximation fails, but using our approach we can get around multi-thimble simulations. (Right) Validity of our approximation using poles of the Padé to determine radii of convergence around our expansion points.

end, along with the thimbles (in blue) and anti-thimbles (in magenta) originating from those points. The dominant thimble at this region in parameter space is the one at $Re[z] = 0$.

6.2.5 Outlook : What have we learnt from the 1D Thirring model ?

The reader has certainly noticed that in Section 2.5 many numerical experiments on multi-Padé were performed on the 1D Thirring model. Here we saw that there was a good reason for that. We first want to draw the attention of the reader to the Fig. 6.3 (middle), where we show how the Taylor expansions about the four points (represented by filled triangles) mentioned above (section 6.2.4) bridge the regions described by different composition of thimbles. The solid line (analytic solution of the Chiral condensate) is faithfully represented by the joining of the four Taylor expansions. The obvious question to ask here is : When is such a analytic continuation allowed ? This question is answered in the next Fig. 6.3 (right most). The two circles represent the radii of convergence about two points (filled triangles at $\hat{\mu}/\hat{m} \in \{0.4, 1.95\}$) shown in the plot before. The validity of the analytic continuation can be seen by the overlapping of the two circles about the region of bridging ($\hat{\mu}/\hat{m} \sim 1.4$). Furthermore, the pole of the analytic function that represents the Chiral condensate (red dot) is captured by the pole of the multi-point Padé (green dot) and its position marks the radii of convergence of the two Taylor expansions mentioned above. Seeing the success of the multi-point Padé approximant in capturing the pole of the Chiral condensate, further numerical experiments were conducted on understanding the various aspects of validity of this approximation primarily using the 1D Thirring model. Many of the results of these studies have been shown in section 2.

This was the result that prompted our further studies of using the multi-point Padé approach in studying QCD. But the most important point, beyond the reconstruction of the functions, is that the singularity structure was correctly identified. Since, also in QCD, we can simulate to low orders (because of computational costs associ-

ated with precision needed) at zero and imaginary chemical potentials, we wanted to see if the multi-point Padé can be sensitive to the singularities of the thermodynamic functions of QCD.

Chapter 7

Lefschetz thimble regularisation of Yang Mills

Until now, Lefschetz thimble as a solution to the sign problem has only been successful in studying toy models, like the ones we mention in Chapter 6. However, the original motivation was to study QCD at high densities [114]. In order to make progress in that direction we first need a mechanism to regularize Yang-Mills theories using Lefschetz thimbles. This is because the gauge fields form the basis of integration in any lattice QCD simulation[1]. However, as we will discuss in this chapter, regularising non-abelian gauge theories using Lefschetz thimbles is a hard problem both conceptually and computationally. There is yet another motivation to study non-abelian gauge theories using Lefschetz thimbles, and that is in the presence of a θ-term. This is because the Euclidean Yang Mills action with the θ-term present has a genuine sign problem.

The layout of this chapter is as follows : In Section 7.1 we will briefly mention the notation used. In Section 7.2, we will show the steps for complexifying the gauge fields and constructing the Steepest ascent equation. In Section 7.3 we will show a problem with the naive thimble construction for the gauge field and in Section 7.4 we will try to resolve this problem using twisted boundary conditions. In that section we will also display results from our new code which has the thimble regularisation of non-abelian gauge fields implemented. Following this, in Section 7.6 we will discuss another problem native to non-abelian gauge theories - that is of identifying all the relevant saddle points and discuss a few well known results for the case of 2D SU(2) partition functions. In Section 7.7 we will display a few results from our "numerical hunt" for saddle points using the steepest ascent equations and finally as an outlook we describe the possible motivation to study the topological θ-term on Lefschetz thimbles.

7.1 Notation used

Since this chapter can seem dense in equations, we will introduce in this section some useful notation.

Our discussion in the following sections will be based on Non-Abelian gauge fields living on a Torus in Euclidean space. We will for the most part also restrict our

[1]Fermions are integrated out in lieu of being Grassmann odd objects.

analysis to 2D SU(N) theories , finally restricting further to SU(2) on a 2D Torus.

7.1.1 In the continuum :

The gauge fields are represented by the vector potential $\mathbf{A}_\mu(x) = A^a_\mu(x)\mathbf{T}^a$, with $\mathbf{T}^a$'s being the generators of the SU(N) Lie algebra in the fundamental representation. They satisfy the following algebra (summation over repeated indices is implied unless stated otherwise):

$$\begin{aligned} \mathrm{Tr}\{\mathbf{T}^a\mathbf{T}^b\} &= \frac{\delta_{ab}}{2} \\ [\mathbf{T}^a, \mathbf{T}^b] &= if^{abc}\mathbf{T}^c \end{aligned} \tag{7.1}$$

The field tensor is given by :

$$\begin{aligned} \mathbf{F}_{\mu\nu}(x) &= \partial_\mu \mathbf{A}_\nu(x) - \partial_\nu \mathbf{A}_\mu(x) - i[\mathbf{A}_\mu(x), \mathbf{A}_\nu(x)] \\ \mathbf{F}_{\mu\nu}(x) &= F^a_{\mu\nu}(x)\mathbf{T}^a \end{aligned} \tag{7.2}$$

Gauge transformations (Ω(x)) on the vector potentials act as usual :

$$\mathbf{A}_\mu(x) \to \Omega(x)\mathbf{A}_\mu(x)\Omega^{-1}(x) + i\Omega(x)\partial_\mu\Omega^{-1}(x) \tag{7.3}$$

Under these transformations the field tensor transforms as $\mathbf{F}_{\mu\nu}(x) \to \Omega(x)\mathbf{F}_{\mu\nu}(x)\Omega^{-1}(x)$. Finally, the Yang Mills action is given by :

$$S_{YM} = \frac{1}{2}\int_{T^4} d^4x\, \mathrm{Tr}\{\mathbf{F}_{\mu\nu}\mathbf{F}_{\mu\nu}\}$$

7.1.2 On the lattice :

Gauge fields are represented by *links* which live on the edges connecting lattice sites (Fig. 7.1). The lattice equivalent of the field strength tensor $F_{\mu\nu}$ is given by the *Plaquette*, shown in Fig. 7.1. The plaquette is the simplest gauge invariant term on the lattice. The main point of difference between the continuum and the lattice representations of the gauge fields to notice is that in the vector potentials in the continuum are elements of the Lie algebra whereas the gauge links on the lattice belong in the Lie group.

The lattice Yang Mills action can be written in terms of the plaquette as follows.

$$\begin{aligned} U_{\mathbb{P}} &= U_{\hat{\mu}}(n)U_{\hat{\nu}}(n+\hat{\mu})U^\dagger_{\hat{\mu}}(\hat{\nu})U^\dagger_{\hat{\nu}}(n) \\ S_{LYM} &= \frac{\beta}{N}\sum_{\mathbb{P}}\left(\mathrm{Tr}\left[\mathbb{I}_N - \frac{1}{2}\left(U_{\mathbb{P}} + U^\dagger_{\mathbb{P}}\right)\right]\right) \end{aligned} \tag{7.4}$$

Gauge transformations are given by (as already seen in Chapter 2):

$$U_{\hat{\mu}}(n) \to U'_{\hat{\mu}}(n) = \Omega(n)U_{\hat{\mu}}(n)\Omega^\dagger(n+\hat{\mu}) \tag{7.5}$$

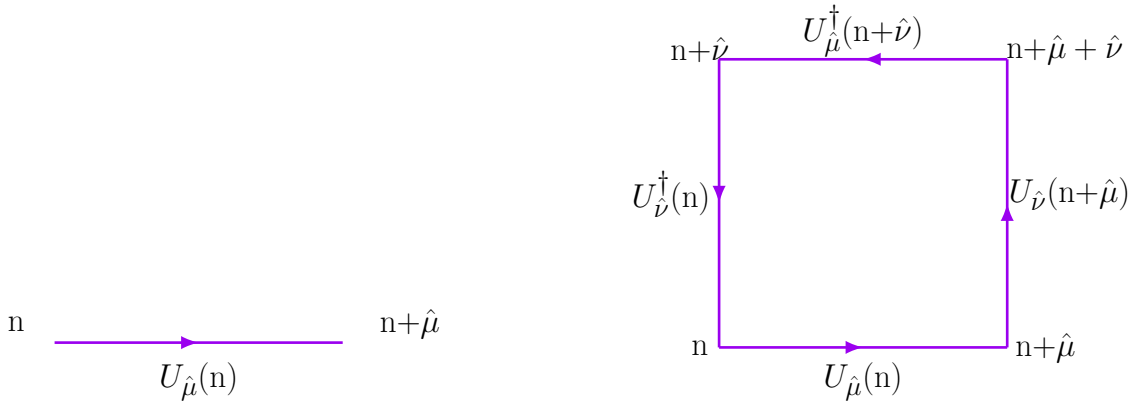

Figure 7.1: (Left): Directed gauge link connecting the sites n and $n+\mu$, (Right) : A plaquette in the $\mu\nu$ plane.

7.2 Thimble construction for Yang Mills

Consider a pure-YM, SU(N) theory. This means considering a set of fields $\{U_k\}$ on a manifold (in field space) of real dimension $dim_{\mathbb{R}} = n$. A suitable complexification of this manifold will take us to another manifold of real dimension $dim_{\mathbb{R}} = 2n$. We complexify in the algebra as follows

$$\mathrm{SU}\left(N\right) \ni U = e^{ix_a T^a} \rightarrow e^{iz_a T^a} = e^{i(x_a + iy_a)T^a} \in \mathrm{SL}\left(N, \mathbb{C}\right). \tag{7.6}$$

Notice that the transpose conjugation operation becomes,

$$\mathrm{SU}\left(N\right) \ni U^{\dagger} = e^{-ix_a T^a} \rightarrow e^{-iz_a T^a} = e^{-i(x_a + iy_a)T^a} = U^{-1} \in \mathrm{SL}\left(N, \mathbb{C}\right).$$

We finally proceed to write down a suitable Steepest Ascent (SA) equation. A natural way of writing down the SA equations follows from [115, 116]

$$\frac{\mathrm{d}}{\mathrm{d}\tau} U_{\hat{\mu}}\left(n;\tau\right) = \left(i\, T^a \bar{\nabla}^a_{n,\hat{\mu}} \overline{S\left[U\left(\tau\right)\right]}\right) U_{\hat{\mu}}\left(n;\tau\right) \tag{7.7}$$

written in terms of the Lie derivative given by,

$$\nabla^a f\left(U\right) = \lim_{\alpha \to 0} \frac{1}{\alpha}\left[f\left(e^{i\alpha T^a} U\right) - f\left(U\right)\right] = \frac{\delta}{\delta \alpha} f\left(e^{i\alpha T^a} U\right)\Big|_{\alpha=0}.$$

Notice that, since $\frac{\mathrm{d}}{\mathrm{d}\tau} = \bar{\nabla}^a_{n,\hat{\mu}} \bar{S}\, \nabla^a_{n,\hat{\mu}} + \nabla^a_{n,\hat{\mu}} S\, \bar{\nabla}^a_{n,\hat{\mu}}$ we proceed to show that Eq. 6.9 and Eq. 6.10 are satisfied,

$$\frac{\mathrm{d}S^R}{\mathrm{d}\tau} = \frac{1}{2}\frac{\mathrm{d}}{\mathrm{d}\tau}\left(S + \bar{S}\right) = \frac{1}{2}\left(\bar{\nabla}^a_{n,\hat{\mu}} \bar{S}\, \nabla^a_{n,\hat{\mu}} S + \nabla^a_{n,\hat{\mu}} S\, \bar{\nabla}^a_{n,\hat{\mu}} \bar{S}\right) = \left\|\nabla S\right\|^2 \geq 0$$

and

$$\frac{\mathrm{d}S^I}{\mathrm{d}\tau} = \frac{1}{2i}\frac{\mathrm{d}}{d\tau}\left(S - \bar{S}\right) = \frac{1}{2i}\left(\bar{\nabla}^a_{n,\hat{\mu}} \bar{S}\, \nabla^a_{n,\hat{\mu}} S - \nabla^a_{n,\hat{\mu}} S\, \bar{\nabla}^a_{n,\hat{\mu}} \bar{S}\right) = 0,$$

Among all the solutions of Eq. (7.7), we have to look for the ones whose union defines the thimble. We will see in the next section why this is not straightforward for gauge theories in the next section.

7.3 Generalised Thimbles and the need for *Twisting*

In general we would proceed by identifying the critical points and building Lefschetz Thimbles from the union of all steepest ascent curves arising from the points saddle points of the Yang Mills action. However, we immediately hit two roadblocks, one of them is discussed in this section has to do with the fact that we violate the criteria for having isolated critical points for Yang Mills (YM) because of gauge symmetry. The other problem has to do with hunting for the saddle point of the Yang Mills action which we discuss in the next section.

When we consider YM theories, because gauge transformations are a symmetry of the action, instead of getting isolated critical points we get a manifold of critical points given by:

$$\mathcal{M}_\sigma = \{U \in \chi | \exists G \in \mathcal{G} : {U_\sigma}^G = U\} \tag{7.8}$$

Where $\mathcal{G}$ is a complexification of the original gauge group $\mathcal{H}$ (of dimensionality $dim_{\mathbb{R}} = n_G$) and the dimensionality of this manifold is $\dim_{\mathbb{R}} \mathcal{M}_\sigma = 2n_G$.

Consequently the Hessian $H(S_R; U)$ for $U \in \mathcal{M}_\sigma$ is degenerate, with $\mathbf{n - n_G}$ positive, $\mathbf{2n_G}$ zero and $\mathbf{n - n_G}$ negative eigenvalues. These zero eigenmodes cause problems with the dimensionality of the thimbles as explained below.

A thimble by definition has dimensions equal to the dimension of the original manifold (before complexification). In our case, because of the zero modes, the naive thimble will have the dimension $\mathbf{n - n_G}$. Therefore we can't use the Lefschetz thimble formulation as it stands for regularising gauge theories. Witten pointed out in [111], a way to construct a thimble decomposition for degenerate critical points is to first generalize to a *non-degenerate critical manifold* $\mathcal{M}_\sigma$ and then consider the normal bundle associated to it, which has the dimensions $\mathbf{n - n_G}$ (positive eigenmodes og the Hessian at the gauge orbit). Now the way to construct a n-cycle $\mathcal{J}_\sigma$ attached to U_σ (critical gauge orbit), is by considering all the SA curves attached to a *middle dimensional* manifold $\mathcal{N}_\sigma \subset \mathcal{M}_\sigma$ (such that it has dimension $\mathbf{n_G}$). Then we have the required n-cycle $\mathbf{n - n_G + n_G = n}$. Where the middle dimensional manifold $\mathcal{N}_\sigma$ is given by,

$$\mathcal{N}_\sigma = \{U \in \chi | \exists H \in \mathcal{H} : {U_\sigma}^H = U\}$$

In principle our problem should be solved as we now know how to construct the stable thimble attached to a degenerate critical manifold. Unfortunately, this is again not the end of the story. When we consider the the critical manifold as seen above, attached to classical vaccuum of the YM equations of motion, i.e , $U_k = \mathbb{I}_N$ (this corresponds to the choice $A_k = 0$), we run into a problem of additional zero-modes. These correspond to zeros of the Hessian, not given by gauge modes. The Hessian[2],

$$\begin{aligned} H(S, U_\sigma) &= \nabla^b_{m,\hat{\rho}} \nabla^a_{n,\hat{\mu}} S[U]|_{U_\sigma = \mathbb{I}} \\ &= \frac{\beta}{2N} \delta^{ab} \{2d\delta_{n,m}\delta_{\hat{\mu},\hat{\rho}} - \delta_{n,m} + \delta_{n+\hat{\mu},m} + \delta_{n-\hat{\rho},m} - \delta_{n+\hat{\mu}-\hat{\rho},m} - \end{aligned}$$

[2]the general form of the Hessian for SU(N) is a very large formula, hence we only write the version evaluated at the classical vacuum.

$$\delta_{\hat{\mu},\hat{\rho}} \sum_{\hat{\nu}} (\delta_{n+\hat{\nu},m} + \delta_{n-\hat{\nu},m}) \Bigg\} \tag{7.9}$$

can be seen to have not only the required n_G zero modes due to the gauge directions, but additional zero modes arising because of the periodic boundary conditions named **Torons**. Gauge oriented zero modes are given by the discrete equivalent of the infinitesimal gauge transformations

$$V^a_{\hat{\mu}}(n) = \Lambda^a(n+\hat{\mu}) - \Lambda^a(n) \tag{7.10}$$

and the number of these modes are $(V-1)(N^2-1)$ [3]. The *toronic* zero modes given by space-time independent vectors of the form : $V^a_{\hat{\mu}}$, the number of these are $d(N^2-1)$. So clearly, the classical vacuum has the incorrect dimensionality for the zero-mode manifold to construct the middle dimensional manifold: We have $dim_{CV} = (V-1)(N^2-1) + d(N^2-1) \neq n_{\mathcal{G}}$. (Where $n_{\mathcal{G}} = V(N^2-1)$.)

One possible way out of this problem is to make use of *twisted* boundary conditions. How this corrects the dimensionality will be shown in the next section.

7.4 Twisting and zero modes

As mentioned in Chapter 2, pure Yang Mills SU(N) theories have an additional *center symmetry* given by invariance under the center group Z_N. Twisting refers to changing the boundary conditions from strictly periodic (for the gauge fields) to periodic up to a twist transformation. G. 't Hooft in [118] showed that group elements defining a twist are restricted to the centre of the group. Further, if the group has a trivial center there can be no non-trivial twists. Twisting in lattice gauge theories is usually used in the context of describing the phase structure of non-abelian gauge theories.

In this section we will try to illuminate the need for having twisted boundary conditions in the framework for studying Yang Mills theories using Lefschetz thimbles regularisation and what they correspond to on a lattice. Most of the following discussion is based on [119]. Below we briefly remind the reader what twist transformations we consider and what algebra they must follow. The boundary conditions we want to consider are (square lattices with extent L are considered) :

$$U_{\hat{\nu}}(n + L\hat{\mu}) = \Gamma_{\hat{\mu}} U_{\hat{\nu}}(n) \Gamma^{\dagger}_{\hat{\mu}} \tag{7.11}$$

To preserve these under gauge transformations :

$$\begin{aligned} U_{\hat{\nu}}(n + L\hat{\mu}) \to U'_{\hat{\nu}}(n + L\hat{\mu}) &= \Omega(n + L\hat{\mu}) U_{\hat{\nu}}(n + L\hat{\mu}) \Omega(n + L\hat{\mu} + \hat{\nu}) \\ &= \Omega(n + L\hat{\mu}) \Gamma_{\hat{\mu}} U_{\hat{\nu}}(n) \Gamma^{\dagger}_{\hat{\mu}} \Omega(n + L\hat{\mu} + \hat{\nu}) \end{aligned} \tag{7.12}$$

Hence, as seen in Chapter 2, either we demand strict periodicity in the gauge transformation matrices and force $\Gamma_{\hat{\mu}}$'s to lie in the centre Z_N. Or the gauge transformation matrices must satisfy:

$$\Omega(n + L\hat{\mu}) = \Gamma_{\hat{\mu}} \Omega(n) \Gamma^{\dagger}_{\hat{\mu}} \tag{7.13}$$

[3] Strictly speaking these zero modes have dimensionality $V(N^2-1)$, but the mode corresponding to zero momentum must be discarded as it amounts to a null eigenvector [117]

to give,

$$\begin{aligned} U'_{\hat{\nu}}(n+L\hat{\mu}) &= \Omega(n+L\hat{\mu})\Gamma_{\hat{\mu}}U_{\hat{\nu}}(n)\Gamma^{\dagger}_{\hat{\mu}}\Omega(n+L\hat{\mu}) \\ &= \Gamma_{\hat{\mu}}\Omega(n)\Gamma^{\dagger}_{\hat{\mu}}\Gamma_{\hat{\mu}}U_{\hat{\nu}}(n)\Gamma^{\dagger}_{\hat{\mu}}\Gamma_{\hat{\mu}}\Omega(n+\hat{\nu})\Gamma^{\dagger}_{\hat{\mu}} \\ &= \Gamma_{\hat{\mu}}U'_{\hat{\nu}}(n)\Gamma^{\dagger}_{\hat{\mu}} \end{aligned} \tag{7.14}$$

Further, as a consequence of physical arguments (on a 2D torus it should not matter in what order one reaches a point identified with another point when we have periodic boundary conditions.) these twist matrices are shown to obey the twist algebra shown below :

$$\begin{aligned} U_{\hat{\nu}}(n+L\hat{\mu}+L\hat{\rho}) &= \Gamma_{\hat{\mu}}\Gamma_{\hat{\rho}}U_{\hat{\nu}}(n)\Gamma^{\dagger}_{\hat{\rho}}\Gamma^{\dagger}_{\hat{\mu}} \\ &= \Gamma_{\hat{\rho}}\Gamma_{\hat{\mu}}U_{\hat{\nu}}(n)\Gamma^{\dagger}_{\hat{\mu}}\Gamma^{\dagger}_{\hat{\rho}} \end{aligned} \tag{7.15}$$

To not reach a physical contradiction we must have :

$$\Gamma_{\hat{\mu}}\Gamma_{\hat{\rho}} = z_{\hat{\rho}\hat{\mu}}\Gamma_{\hat{\rho}}\Gamma_{\hat{\mu}} \tag{7.16}$$

with $z_{\hat{\rho}\hat{\mu}} = e^{2\pi i n_{\hat{\rho}\hat{\mu}}/N}$ are elements of the centre of SU(N). Here, $n_{\hat{\rho}\hat{\mu}}$ is an anti-symmetric tensor and hence has dimension $\frac{1}{2}d(d-1)$.

It can further be shown [120] that the twisted boundary conditions with the original Wilson gauge action is equivalent to a modified action with periodic boundary conditions. One then proceeds to find the classical vacuum of this twisted action and investigate its dimensionality. Moreover, this twisted action admits a class of zero-action solutions called *twist eaters*. The existence and class of configurations of these twist eaters can be proved using the following theorem [4]. Before writing out the theorem we will list a few conditions which the action (Wilson in our case) must satisfy for the theorem to hold (which are all satisfied!) :

A : Let $f_{\mathbb{P}}(U)$ denote the plaquette action function. Then it must satisfy $\Omega f_{\mathbb{P}(U)}\Omega^{-1} = f_{\mathbb{P}}(U)$, with U and $\Omega \in \mathcal{H}$.

B : $f_{\mathbb{P}}(U) \geq 0$, for all plaquettes and U $\in \mathcal{H}$.

C : For each $\mathbb{P}$, $f_{\mathbb{P}} = 0$, iff $U = 1$.

Theorem 3 *If the plaquette action functions* $\mathbf{f}_{\mathbb{P}}$ *satisfy conditions (A) - (C) listed above, then a lattice gauge system (defined originally with periodic boundary conditions), on a d-dimensional hyper-torus with a gauge group* $\mathcal{G}$ *and twist tensor* $\mathbf{z} = \{z_{\mu\nu}\}$*, admits a zero action configuration if and only if also the following condition is satisfied : There exist, in* $\mathcal{G}$*, d elements* $G_1, ...G_d$ *such that*

$$G_\nu G_\mu = z_{\mu\nu}G_\mu G_\nu \quad (1 \leq \mu < \nu \leq d) \tag{7.17}$$

Following this, all the zero action solutions of the twisted action can be shown to be the "ladder" or twist-eater configurations whose construction (Fig. 7.2) can also be found in [121]. The important point here is the dimensionality structure of those solutions:

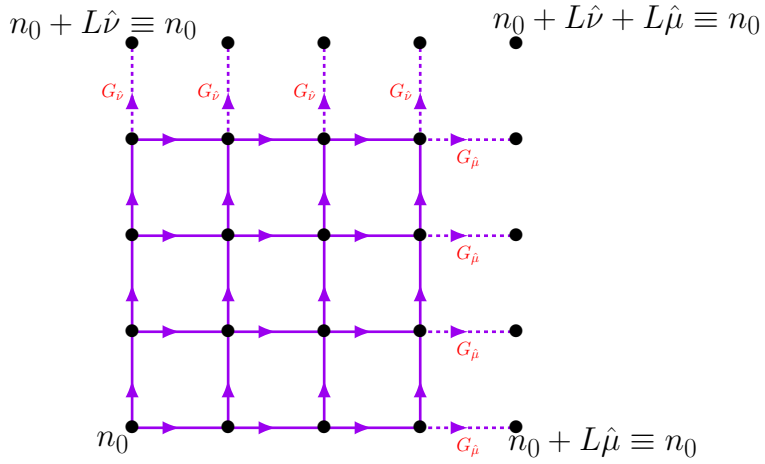

Figure 7.2: Twist Eater solution (along with all the conventions for links)

The twist-eater solutions are maximal gauge trees, with links everywhere unity except for the two ladders given by (say) $G_{\hat{\mu}}$ and $G_{\hat{\nu}}$ obeying the relation:

$G_{\hat{\nu}\hat{\mu}} = z_{\hat{\mu}\hat{\nu}} G_{\hat{\mu}\hat{\nu}}$ with $z_{\hat{\mu}\hat{\nu}} = e^{2\pi i n_{\hat{\mu}\hat{\nu}}/N}$ for SU(N). Since these twist-eater solutions exhaust the set of solutions for zero action solutions of EOM for the twisted action, we can now proceed to fnd the dimensionality of the manifold of such solutions.

It can be shown (Appendix A in [119]) that the zero-action configuration manifold is diffeomorphic to $\otimes^{V-1} SU(N) \otimes \mathcal{M}_{\hat{\mu}\hat{\nu}}$, where $\mathcal{M}_{\hat{\mu}\hat{\nu}}$ is the twist dependent manifold given by:

$$\mathcal{M}_{\hat{\mu}\hat{\nu}} = \{G_1, ...G_d | G_{\hat{\mu}} \in SU(N), G_{\hat{\nu}\hat{\mu}} = z_{\hat{\mu}\hat{\nu}} G_{\hat{\mu}\hat{\nu}}\}$$

For the case of no twist ($z_{\hat{\mu}\hat{\nu}} = 1$), i.e, the original Wilson action, the dimension of $\mathcal{M}_{\hat{\mu}\hat{\nu}}$ is (N - 1)(N + d). So the total dimension of the zero action configuration manifold is : $(V-1)(N^2-1) + (N-1)(N+d)$. This is clearly not equal to $n_G = V(N^2-1)$.

Next consider the case of a simple twist, i.e, $z_{\hat{\mu}\hat{\nu}} = e^{2\pi i k/N}$, with k and N coprime. It is shown (Appendix D & E in [119]) that the dimension of $\mathcal{M}_{\hat{\mu}\hat{\nu}}$ in this case is given by N^{d-2} connected components, each with dimension $\mathbf{N^2 - 1}$. Moreover, any two points in the same connected component are related to each other by a gauge transformation.

This gives us the dimension for the zero action configuration to be : $(V-1)(N^2-1) + (N^2-1) = n_G$, which is precisely the dimension we need to build Lefschetz thimbles of the correct dimensionality. Therefore, we have got rid of the toronic degrees of freedom and can proceed with Witten's prescription to build the stable thimble and proceed with steepest ascent and parallel transport simulations.

7.5 Numerical Results

Before proceeding to the next problem of looking for the saddle points of the lattice YM action, we briefly describe the steps in our code which implement Lefschetz

[4]The theorem and its proof can be found in [119]

thimble regularisation for SU(2) Yang-Mills in any number of dimensions [5]. Monte Carlo sampling on Lefschetz thimbles is a hard subject. The Parma group put forward one approach [122] which is conceptually clean and can be implemented for YM fields, provided one is able to construct steepest ascents. The idea is that of writing the functional integral on a single thimble as a sum over ascent paths:

$$\langle O \rangle_\sigma = \frac{\int \mathcal{D}\hat{n}\ \mathcal{Z}_{\hat{n}}^{(\sigma)} \left(\mathcal{Z}_{\hat{n}}^{(\sigma)-1} \quad \int dt\ \Delta_{\hat{n}}(t)\ \mathrm{e}^{-S_R(\hat{n},t)}\ e^{i\omega(\hat{n},t)}\ O(\hat{n},t) \right)}{\int \mathcal{D}\hat{n}\ \mathcal{Z}_{\hat{n}}^{(\sigma)} \left(\mathcal{Z}_{\hat{n}}^{(\sigma)-1} \quad \int dt\ \Delta_{\hat{n}}(t)\ \mathrm{e}^{-S_R(\hat{n},t)}\ e^{i\omega(\hat{n},t)} \right)} \equiv \frac{\int \mathcal{D}\hat{n}\ \mathcal{Z}_{\hat{n}}^{(\sigma)} \langle e^{i\omega}\, O \rangle_{\hat{n}}}{\int \mathcal{D}\hat{n}\ \ \mathcal{Z}_{\hat{n}}^{(\sigma)} \langle e^{i\omega} \rangle_{\hat{n}}}$$

All in all, the thimble manifold is parameterised in a simple way: in order to reach a given point on the thimble, we must specify the direction ($\hat{n}$) along which we leave the critical point and the value of the "time" (t) at which one stops integrating the steepest ascent (see Eq. 6.8). In order to implement this algorithm, one must be able to construct the steepest ascents that sit on the thimble. Notice that this means that, having chosen an initial condition (which is built in $\hat{n}$) we will integrate all the way up to fully reconstruct the contribution $\langle O\, e^{i\omega} \rangle_{\hat{n}}$. Next, we briefly summarise the basic building blocks. The fist step is to build the *twist-eating* configuration described above. In order to begin integrating the SA equations along the stable thimble, we first need to find the tangent space around the critical point (twist-eater in this case) to prepare the initial conditions. The basis needed for this tangent space is obtained by diagonalising the Hessian matrix (defined for the classical vacuum in Eq. 7.9) keeping only the eigenvectors corresponding to the positive eigenvalues. The choice of coefficients will not be discussed here, as it is described in detail in [117]. The tangent basis has to be parallelly transported along the thimble. Solving the parallel transport equations is the most computing-time intensive part of the code. To perform the integration of the SA and PT equations, a 4th-order Runge-Kutta-Munthe-Kaas integrator was used, following [123]. Such a numerical integrator preserves exactly the geometric structure of the differential equation to be integrated, like the group manifold of SU(2) in our case. In our code, the SA and PT equations are *inter-woven* with each other, i.e, first the field is integrated by one step followed by the basis vectors and so on. The output of our code is precisely computing averages using the procedure described above - but only on a single dominant thimble. The thimble that we start from is the twist-eating configuration. The average plaqutte computed from our code can be seen as blue dots along with the respective error bars, in Fig. 7.3 [6]. To show what the red dots in the Fig. 7.3 represent and how they compare with the results of the code will be seen in Section 7.6.3.

7.6 Hunting for saddle points

In order to proceed with thimble regularisation, we need to identify all the contributing saddle points of the action to Eq. 6.12. As we have already seen in the previous

[5] The code base is a part of a private repository on GITHUB which was meant to be made public this year, but there have been delays.

[6] The code based for simulating non-abelian gauge on lefschetz thimbles was already developed to a large extent by a student of the Parma group. The author of this thesis in collaboration with Kevin Zambello, completed the code to perform the Steepest ascent integration while building the necessary routines needed for the same.

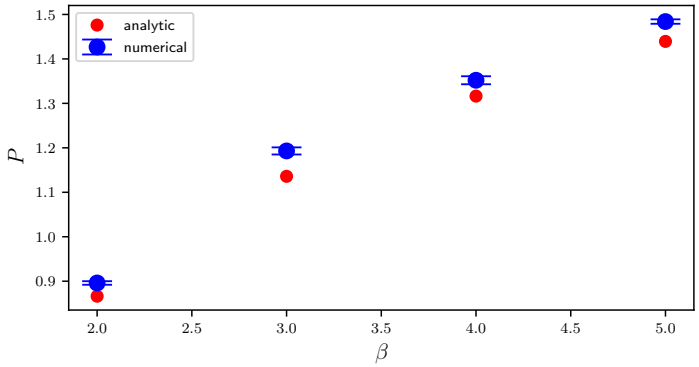

Figure 7.3: [Image credit : Kevin Zambello] This figure shows the comparison of the analytical expression for the 2D SU(2) results for the average plaquette with results fro our code at real values of β.

chapter (Section 6.2.4), even for simple models, single thimble decomposition is not enough. But at least in the model studied in the previous chapter we knew all the saddle points of the action since we had a closed for expression for it. For the case of Yang Mills theory, it is still a conjecture. The closest theory we have to testing this conjecture is for 2D SU(2) gauge theory, for which Witten in [124] has given us a closed form expression in the continuum, for the partition function as a sum over saddle points. This is exactly the result we would like to have *on the lattice*.

Below we will try to motivate and list all the forms of the partition function for the 2D SU(2) YM theory currently known. We will start with Witten's famous solution.

7.6.1 Witten's 2D Yang Mills partition function

Based on [124] : Starting with the Lagrangian of non-abelian YM theory, Witten arrives at the sum over representations formula on a Riemann surface with genus g:

$$Z(\Sigma,\epsilon) = \frac{1}{(2\pi^2)^{(g-1)}} \sum_{n=1}^{\infty} \frac{\exp\left(-\epsilon\pi^2 n^2\right)}{n^{2g-2}} \tag{7.18}$$

which for g=1 becomes:

$$Z(\Sigma,\epsilon) = \sum_{n=1}^{\infty} \exp\left(-\epsilon\pi^2 n^2\right) \tag{7.19}$$

This is the formula which can now be changed into sum over saddle points using the Poisson summation formula:

Let $f : \mathbb{R} \to \mathbb{C}$ be a Schwartz function, then

$$\sum_{n\in\mathbb{Z}} f(n) = \sum_{m\in\mathbb{Z}} \hat{f}(m) \tag{7.20}$$

where $\hat{f}$ is the Fourier transform of f. All we need to do now is to compute the Fourier transform of $\exp\left(-\epsilon\pi^2 n^2\right)$. This is easily seen to be $\exp\frac{\left(-\pi n^2\right)}{\epsilon\pi}$. But $\epsilon' =$

$4\pi^2\epsilon$, giving us:

$$\sum_{n\in\mathbb{Z}} \exp\left(-\epsilon\pi^2 n^2\right) = \sum_{m\in\mathbb{Z}} \exp\frac{(-(2\pi m)^2)}{\epsilon'} \tag{7.21}$$

Hence, the 2D partition in the continuum can be expressed both as a sum over representations and as a sum over saddle points. We will see below that we can also write down a closed form for the partition function as a sum over representations on the lattice.

7.6.2 Migdal's 2D SU(2) lattice partition function

Migdal in [125] gave a set of recursion relations which allow us to write down a closed form expression of the lattice gauge action (Wilson) in terms of a sum of over representation formula. We briefly sketch his procedure here: Starting with a 2d lattice and integrating out the internal lines to get a boundary Γ enclosing an area S:

$$Z_S(v_\Gamma) = \sum_p (Z_{a,p})^{S/a^2} d_p \chi_p(v_\Gamma) \ , \tag{7.22}$$

where v_Γ are the path ordered links on the boundary, p denotes a particular representation, d_p is the dimension of that representation and $\chi_p(v_\Gamma)$ the character of the representation and $(Z_{a,p})$ are the coefficients of the expansion. Here, a denotes the lattice spacing , so S/a^2 denotes the number of plaquettes. Taking the local limit $a \to \infty$, one must take the limit $Z_{a,p} \to 1 - a^2\epsilon_p$, so that

$$Z_S(v_\Gamma) = \sum_P \exp\{(-S\epsilon_p)\} d_p \chi(v_\Gamma) \tag{7.23}$$

Deleting the vacuum energy, $\epsilon_p \to \epsilon_p - \epsilon_0$ and demanding that these differences must be positive: $\epsilon_p - \epsilon_0 = g_p^2$, one gets:

$$Z_S(v_\Gamma) = \sum_P \exp\left\{\left(-S g_p^2\right)\right\} d_p \chi(v_\Gamma) \tag{7.24}$$

If you require the bare action to go over into Yang Mills in the local limit, g_p^2 is replaced by $g^2(T)_p^2$, where T^2 is the Casimir operator.

7.6.3 Exact lattice result from Wilson's YM action

In this section we sketch the derivation of the exact sum over representations formula on the lattice for SU(2) YM, to which we compared the numerical results from our code shown in Fig. 7.3. The original derivation can be found in Appendix F of [117]. We begin by writing a formula exactly analogous to Migdal's recursion formula (Eq. 7.22), with S/a^2 replaced by the lattice volume V, and the coefficients replaced by λ_R:

$$Z_S(v_\Gamma) = \sum_P (\lambda_P)^V d_p \chi(v_\Gamma) \tag{7.25}$$

Using periodic boundary conditions, taking into account the overall additive constant βV in the action, which we had ignored since the being, he arrives at:

$$Z^{(pbc)}(\beta) = e^{-\beta V} \sum_p [\lambda_p]^V \tag{7.26}$$

Then he calculates λ_p as:

$$\lambda_p = \frac{1}{d_p} \int dU \chi_p(U) e^{\beta f(U)} \tag{7.27}$$

Using the Wilson action in the fundamental representation, he arrive at:

$$\lambda_p = \frac{2}{\beta} I_{2j+1}(\beta) \tag{7.28}$$

$$Z^{(pbc)}(\beta) = e^{-\beta V} \sum_p \left[\frac{2}{\beta} I_{2j+1}(\beta) \right]^V \tag{7.29}$$

Recall that for SU(2) , all the representations are labelled by $j = 0, \frac{1}{2}, 1, \frac{3}{2}, ...$, so that the formula becomes:

$$Z^{(pbc)}(\beta) = e^{-\beta V} \sum_{n=1}^{\infty} \left[\frac{2}{\beta} I_n(\beta) \right]^V \tag{7.30}$$

This is the formula we used to compute (up to a trivial sign factor that has to do with using twisted boundary conditions instead of the periodic one) the partition function for comparison with our code [7]. In Fig 7.3 we depict the comparison of the known result and the result we got by taking only the dominant thimble into account (single-thimble simulation). The red dots are the average plaquette obtained from the partition given in Eq. 7.30 by the following :

$$\langle S_p \rangle / N_p = \frac{d \log Z^{(pbc)}}{d\beta} / N_p + 1 \tag{7.31}$$

where S_p is the value of the average plaquette for a lattice with N_p plaquettes and coupling β. Referring again to the Fig. 7.3, we see that the results from the single thimble simulation are not consistent with the analytic results. Hence, we have a partial result (and a negative one). However, this has been the first attempt at a Lefschetz thimble simulation of a Yang-Mills theory and in that forms a new result.

7.7 Finite action solutions

We would like to end the discussion on thimble regularisation of Yang Mills theories with some numerically obtained saddle points of the lattice Yang Mills action, which have zero value of the action, along with their modification to obtain finite action solutions. We numerically solved Eq. 7.7 starting from a random SU(2) matrix and flowed to a solution of the equation of motion. We also constructed a maximal gauge

[7] The continuum limit of this action can be shown to result in the correct action given by Witten (Eq. 7.19).

tree of the solution obtained, in order to compare easily to the ladder solutions. To our surprise we always converged to a ladder solution - even for the un-twisted action as shown in Fig. 7.4 (Right). The left plot in Fig. 7.4 shows the expected solution. However, note that this ladder solution obtained by the simulation is special because it always results in a ladder solution with *commuting* SU(2) matrices.

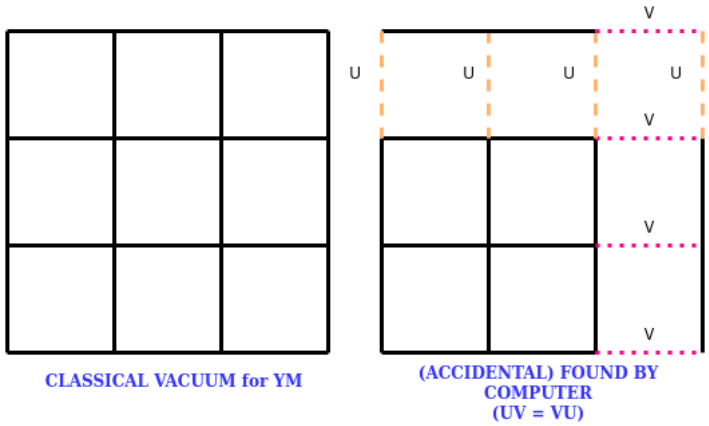

Figure 7.4: Untwisted cases : (Left): Classical vacuum, (Right) : Solutions found by steepest ascenting from a random SU(2) matrix.

For the twisted Wilson action, the simulation always converged on the expected solution : a zero action solution given by a maximal gauge tree with *anti-commuting* ladder matrices (shown in Fig. 7.5 (Left)). What we display in Fig. 7.5(Right) is a modification of the twist eater shown in the left plot. In this we instead of choosing the same matrix in every step of the ladder, we use (-1) times the matrix (Note this only works for even dimensional lattices to preserve the correct boundary conditions). This way we get a non-zero action solution to the equation of motion - a non-trivial candidate saddle point.

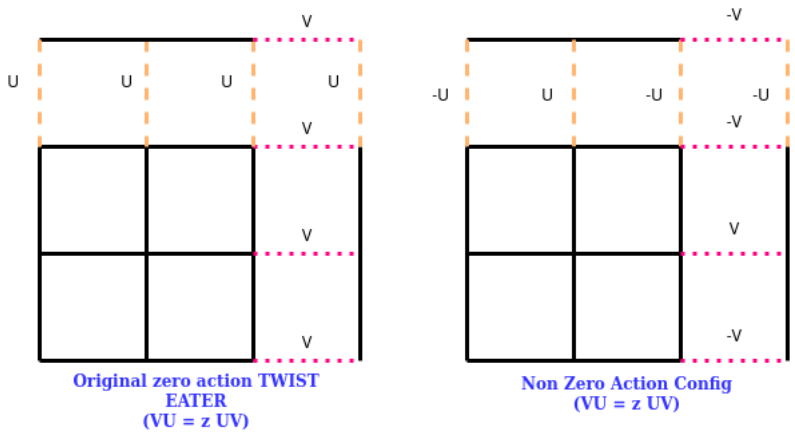

Figure 7.5: Twisted case : (Left) : Twist eater solution found by the simulation (expected result). (Right) A modification to the twist eater to get a finite action solution.

7.8 Outlook : Yang Mills in presence of θ term

For Yang-Mills theories, in addition to the usual Kinetic term for gauge theories we are allowed to write another term referred to, in literature, as the θ - *term*. The reason behind writing a θ term is the fact that apart from the usual quadratic $\mathrm{F}^{\mu\nu}\,\mathrm{F}_{\mu\nu}$ (or equivalently $\tilde{\mathrm{F}}^{\mu\nu}\tilde{\mathrm{F}}_{\mu\nu}$) terms, we can write an additional *gauge and Lorentz invariant* term no higher than $\mathcal{O}(2)$ in $\mathrm{F}^{\mu\nu}$ to the action.
In 4D, such a θ term can be written for both abelian and non-abelian gauge theories and takes the form:

$$S_\theta = \frac{\theta}{16\pi^2}\int d^4x\,\mathrm{Tr}\Big\{\tilde{\mathrm{F}}^{\mu\nu}\,\mathrm{F}_{\mu\nu}\Big\} \tag{7.32}$$

with $\tilde{\mathrm{F}}^{\mu\nu} = \epsilon^{\mu\nu\rho\lambda}\,\mathrm{F}_{\rho\lambda}$, that is $\tilde{\mathrm{F}}$ is the dual stress tensor.
The existence of the dual stress tensor is a dimension dependent statement. For example - theta terms can only be written for theories in even dimensions.

The question we would like to address is whether simulating Yang-Mills in the presence of the θ-term makes sense on a Lefschetz thimble. The answer is yes. We should consider studying the θ-term in a thimble framework for the following possible reasons :

- The presence of the θ term in the Euclidean Yang-Mills actions leads to a *genuine* sign problem, because of the presence of the term representing the topological charge. The current state-of-the-art methods for studying the θ term [126, 127, 128] involve simulations at imaginary values of θ and their analytic continuation to real values of θ much in the same spirit as Imaginary μ_B simulations in QCD. If we solve the theory on a thimble, we would, in principle, be directly to simulate at real values of θ, without the need for analytic continuation.

- Further, in the usual formulations of computing the topological charge on the lattice, we are aware of a problem. Standard lattice simulations do not preserve topological charge, since topological boundaries lose their meaning on discrete and finite space-time. But this can theoretically be solved while simulating the topological charge on a thimble. There are two reasons for this: The first being that in order to perform a thimble simulation we have to start our simulation from a given critical point (orbit in the case of a gauge theory). Such an orbit only contains gauge configurations which are related to each other by a local gauge transformation, by definition of a gauge orbit. So starting the simulation from any point on the orbit would give the same value of the topological charge. The second point is the simulation along the thimble from any given point along the path of steepest ascent. This ascent can also be seen to preserve the topological charge because, once again, by definition and construction, a thimble *preserves the homotopy class* of the original domain of integration. And from the index theorems [129], such a change in geometry which preserves the homotopy class of a manifold - cannot change the topological charge.

Although implementing such a θ-term will be very computationally intensive to study on a lattice within the Lefschetz thimble framework, we believe it is a research direction which should be pursued.

Chapter 8

Conclusion

Knowledge of the QCD phase diagram remains a highly active field of research. Implications of the knowledge gained from the QCD phase diagram range from understanding the interior of compact stars to experiments involving heavy-ion collisions. The sign problem makes direct simulations hard, and methods of circumventing it should be further investigated. One of the methods that were proposed to minimise the sign problem a few years ago was the Lefschetz thimble approach. Although a very intuitive approach, its practical application beyond toy models is still both computationally (and conceptually for the non-abelian gauge theories) a tough challenge.

In this thesis, we have explored two potential methods of evading the sign problem. In the first part, we have systematically investigated singularities of the grand canonical partition function. In the second part, we focused on the Lefschetz thimble approach to solve the sign problem.

After introducing the general framework of the conjectured QCD phase diagram in Chapter 1, we moved on to discuss in detail the Padé approximation technique in Chapter 2. We started by motivating why rational approximations should be preferred over Taylor series expansions, especially when looking for non-analyticities in a function. We then showed a general framework for constructing such an approximation. We then motivated why we should look at multi-point Padé approximations. This was followed by showing through numerical experiments the scope of validity of our analysis. We also commented on the type of spurious singularities one can find in our analysis and how we were safe from them. In the next chapter, Chapter 3 we gave a general outline of phase transitions. This was followed by explaining in some details the two corners of the Columbia plot. We finally discussed the Roberge-Weiss(RW) plane and motivated our interest in the RW transition. Chapter 4 introduced the Lee-Yang theorems and edge singularities and showed their significance in hunting for critical points. We would like to mention that the subject of Lee-Yang and Fisher zeros is extremely rich with physics and some sophisticated mathematics. It should definitely be studied with enthusiasm. We finally moved on to the essence of this thesis, i.e., Chapter 5. Here we computed cumulants of the net baryon number density using lattice QCD simulations for two different temporal extents. These cumulants were approximated with Padé functions and their singularities studied. Signals for stable poles were found, which when fitted with the expected Lee-Yang scaling functions, were completely consistent with the known results (3d Z_2 for the RW transition.) We also showed the consistency of the single

pole found for the $36^3 \times 6$ lattices simulated at $T = 145$ MeV with the expected Lee-Yang edge singularity in the $O(2)$ universality class. We then concluded by showing some new results.

We finally moved to the second part of the thesis, where we focused on the sign problem and its possible solution via the Lefschetz thimble approach. In Chapter 6 we explained the many manifestations of the complex action problem, one of which is the sign problem. We then showed a few possible workarounds of the sign problem using re-weighting via phase and sign quenching. We then showed the success of a single thimble simulation using Taylor (but later Padé) series to bridge regions connected by single thimbles. We then applied the general framework of Lefschetz thimbles to Yang-Mills theories in Chapter 7 and showed how a naive application fails. We then showed some results from our code and left with some open questions. Finally, we concluded by giving the reader reasons to pursue simulating the θ-term using the Lefschetz thimble approach.

In the future, it would be interesting to study already existing cumulant data from lattice simulations by other groups who performed imaginary μ simulations and see if our multi-point Padé can find the appropriate signals for Lee-Yang singularities in them. It would also be very beneficial to go beyond numerical experiments and prove some theorems involving multi-point Padé approximants. Although we can say that we have "smoking gun" evidence of the RW transition via our approach, the same cannot be said about the Chiral transition point at the moment. We definitely need more data with higher statistics to perform a proper Lee-Yang scaling. More types of scalings are currently being explored by us in the framework of our 2D Ising model simulations, this time even involving Fisher zeros. Another important research direction is a systematic study of finite size effects on Lee-Yang edge singularities. Very special attention should also be paid when classifying singularities in various universality classes. We end this thesis by emphasizing that through our method of using Padé re-summation of the Taylor series expansion about zero and imaginary chemical potentials, we can obtain information about Lee Yang zeros of QCD. While the study is far from complete and currently ongoing, we hope that we have at the very least presented the reader with a convincing platform, where they can build from.

Appendix A

Useful relations between measured traces and cumulants

The goal of this appendix is to provide a map between the traces (of the fermion determinant) measured and the final form of the cumulants used, which have been plotted and used for Padé analysis in Chapter 5. This appendix is to a large extent very specific to the output of the Bielefeld GPU code [86], in the sense that the IDs given to the traces fo the fermion determinant are specific to their code. However, we first "unravel" those IDs in a readable form in terms of the traces. Then, proceeding section by section, we finally end up with the cumulants (up to the ones used by us) written in terms of the observable IDs obtained from the code. The primary goal of this appendix was to provide an easy to read crosscheck for the analysis of the cumulant data.

A.1 Relation between Traces measured and their observable ids :

The traces measured are : $obsid = 1, 2, 3, 4, 5, 6, 11, 12, 13, 14, 16, 17, 18, 61, 62, 63, 311, 312$
with $X_n = \frac{\partial^n M}{\partial \mu^n}$ and $X_0 = \mathbb{I}$

$$obsid = 1 \leftrightarrow \mathrm{Tr}\left(X_0 M^{-1}\right) = \mathrm{Tr}\left(M^{-1}\right)$$
$$obsid = 2 \leftrightarrow \mathrm{Tr}\left(X_1 M^{-1}\right) = \mathrm{Tr}\left(\frac{\partial M}{\partial \mu} M^{-1}\right)$$
$$obsid = 3 \leftrightarrow \mathrm{Tr}\left(X_2 M^{-1}\right) = \mathrm{Tr}\left(\frac{\partial^2 M}{\partial \mu^2} M^{-1}\right)$$
$$obsid = 4 \leftrightarrow \mathrm{Tr}\left(X_3 M^{-1}\right) = \mathrm{Tr}\left(\frac{\partial^3 M}{\partial \mu^3} M^{-1}\right)$$
$$obsid = 5 \leftrightarrow \mathrm{Tr}\left(X_4 M^{-1}\right) = \mathrm{Tr}\left(\frac{\partial^4 M}{\partial \mu^4} M^{-1}\right)$$
$$obsid = 6 \leftrightarrow \mathrm{Tr}\left(X_0 M^{-1} X_0 M^{-1}\right) = \mathrm{Tr}\left(M^{-1} M^{-1}\right)$$
$$obsid = 11 \leftrightarrow \mathrm{Tr}\left(X_1 M^{-1} X_0 M^{-1}\right) = \mathrm{Tr}\left(\frac{\partial M^{-1}}{\partial \mu} M^{-1} M^{-1}\right)$$

$$obsid = 12 \leftrightarrow \mathrm{Tr}\big(X_1 M^{-1} X_1 M^{-1}\big) = \mathrm{Tr}\left(\frac{\partial M^{-1}}{\partial \mu} M^{-1} \frac{\partial M^{-1}}{\partial \mu} M^{-1}\right)$$

$$obsid = 13 \leftrightarrow \mathrm{Tr}\big(X_1 M^{-1} X_2 M^{-1}\big) = \mathrm{Tr}\left(\frac{\partial M^{-1}}{\partial \mu} M^{-1} \frac{\partial^2 M^{-1}}{\partial \mu^2} M^{-1}\right)$$

$$obsid = 14 \leftrightarrow \mathrm{Tr}\big(X_1 M^{-1} X_3 M^{-1}\big) = \mathrm{Tr}\left(\frac{\partial M^{-1}}{\partial \mu} M^{-1} \frac{\partial^3 M^{-1}}{\partial \mu^3} M^{-1}\right)$$

$$obsid = 16 \leftrightarrow \mathrm{Tr}\big(X_2 M^{-1} X_0 M^{-1}\big) = \mathrm{Tr}\left(\frac{\partial^2 M^{-1}}{\partial \mu^2} M^{-1} M^{-1}\right)$$

$$obsid = 17 \leftrightarrow \mathrm{Tr}\big(X_2 M^{-1} X_1 M^{-1}\big) = \mathrm{Tr}\left(\frac{\partial^2 M^{-1}}{\partial \mu^2} M^{-1} \frac{\partial M^{-1}}{\partial \mu} M^{-1}\right)$$

$$obsid = 18 \leftrightarrow \mathrm{Tr}\big(X_2 M^{-1} X_2 M^{-1}\big) = \mathrm{Tr}\left(\frac{\partial^2 M^{-1}}{\partial \mu^2} M^{-1} \frac{\partial^2 M^{-1}}{\partial \mu^2} M^{-1}\right)$$

$$obsid = 61 \leftrightarrow \mathrm{Tr}\big(X_1 M^{-1} X_1 M^{-1} X_0 M^{-1}\big) = \mathrm{Tr}\left(\frac{\partial M^{-1}}{\partial \mu} M^{-1} \frac{\partial M^{-1}}{\partial \mu} M^{-1} M^{-1}\right)$$

$$obsid = 62 \leftrightarrow \mathrm{Tr}\big(X_1 M^{-1} X_1 M^{-1} X_1 M^{-1}\big) = \mathrm{Tr}\left(\frac{\partial M^{-1}}{\partial \mu} M^{-1} \frac{\partial M^{-1}}{\partial \mu} M^{-1} \frac{\partial M^{-1}}{\partial \mu} M^{-1}\right)$$

$$obsid = 63 \leftrightarrow \mathrm{Tr}\big(X_1 M^{-1} X_1 M^{-1} X_2 M^{-1}\big) = \mathrm{Tr}\left(\frac{\partial M^{-1}}{\partial \mu} M^{-1} \frac{\partial M^{-1}}{\partial \mu} M^{-1} \frac{\partial^2 M^{-1}}{\partial \mu^2} M^{-1}\right)$$

$$obsid = 311 \leftrightarrow \mathrm{Tr}\big(X_1 M^{-1} X_1 M^{-1} X_1 M^{-1} X_0 M^{-1}\big) = \mathrm{Tr}\left(\frac{\partial M^{-1}}{\partial \mu} M^{-1} \frac{\partial M^{-1}}{\partial \mu} M^{-1} \frac{\partial M^{-1}}{\partial \mu} M^{-1} M^{-1}\right)$$

$$obsid = 312 \leftrightarrow \mathrm{Tr}\big(X_1 M^{-1} X_1 M^{-1} X_1 M^{-1} X_1 M^{-1}\big) = \mathrm{Tr}\left(\frac{\partial M^{-1}}{\partial \mu} M^{-1} \frac{\partial M^{-1}}{\partial \mu} M^{-1} \frac{\partial M^{-1}}{\partial \mu} M^{-1} \frac{\partial M^{-1}}{\partial \mu} M^{-1}\right)$$

A.2 Relation between derivatives of $\ln\det M$ and the traces mentioned above :

$$\frac{\partial \ln\det M_f}{\partial \mu_f} = \mathrm{Tr}\left(\frac{\partial M}{\partial \mu} M^{-1}\right) \tag{A.1}$$

$$\frac{\partial^2 \ln\det M_f}{\partial \mu_f^2} = \mathrm{Tr}\left(M^{-1}\frac{\partial^2 M}{\partial \mu^2}\right) - \mathrm{Tr}\left(M^{-1}\frac{\partial M}{\partial \mu} M^{-1}\frac{\partial M}{\partial \mu}\right) \tag{A.2}$$

$$\begin{aligned}\frac{\partial^3 \ln\det M_f}{\partial \mu_f^3} &= \mathrm{Tr}\left(M^{-1}\frac{\partial^3 M}{\partial \mu^3}\right) - 3\,\mathrm{Tr}\left(M^{-1}\frac{\partial M}{\partial \mu} M^{-1}\frac{\partial^2 M}{\partial \mu^2}\right) \\ &\quad + 2\,\mathrm{Tr}\left(M^{-1}\frac{\partial M}{\partial \mu} M^{-1}\frac{\partial M}{\partial \mu} M^{-1}\frac{\partial M}{\partial \mu}\right)\end{aligned} \tag{A.3}$$

$$\begin{aligned}\frac{\partial^4 \ln\det M_f}{\partial \mu_f^4} &= \mathrm{Tr}\left(M^{-1}\frac{\partial^4 M}{\partial \mu^4}\right) - 4\,\mathrm{Tr}\left(M^{-1}\frac{\partial M}{\partial \mu} M^{-1}\frac{\partial^3 M}{\partial \mu^3}\right) \\ &\quad - 3\,\mathrm{Tr}\left(M^{-1}\frac{\partial^2 M}{\partial \mu^2} M^{-1}\frac{\partial^2 M}{\partial \mu^2}\right) + 12\,\mathrm{Tr}\left(M^{-1}\frac{\partial M}{\partial \mu} M^{-1}\frac{\partial M}{\partial \mu} M^{-1}\frac{\partial^2 M}{\partial \mu^2}\right) \\ &\quad - 6\,\mathrm{Tr}\left(M^{-1}\frac{\partial M}{\partial \mu} M^{-1}\frac{\partial M}{\partial \mu} M^{-1}\frac{\partial M}{\partial \mu} M^{-1}\frac{\partial M}{\partial \mu}\right)\end{aligned} \tag{A.4}$$

A.3 Relating the obsids to $\ln\det M$

With *obsid* $\leftrightarrow [N]_f$ with N$\in \{1,2,3,4,5,6,11,12,13,14,16,17,18,61,62,63,311,312\}$ and $f=\{u,d,s\}$

$$\frac{\partial \ln\det M_f}{\partial \mu_f} = [2]_f \tag{A.5}$$

$$\frac{\partial^2 \ln\det M_f}{\partial \mu_f^2} = [3]_f - [12]_f \tag{A.6}$$

$$\frac{\partial^3 \ln\det M_f}{\partial \mu_f^3} = [4]_f - 3\times[13]_f + 2\times[62]_f \tag{A.7}$$

$$\frac{\partial^4 \ln\det M_f}{\partial \mu_f^4} = [5]_f - 4\times[14]_f - 3\times[18]_f + 12\times[63]_f - 6\times[312]_f \tag{A.8}$$

A.4 Key observables in terms of obsids :

Starting with $A_{ijk} = \frac{1}{Z}\frac{\partial^i}{\partial\mu_u^i}\frac{\partial^j}{\partial\mu_d^j}\frac{\partial^k}{\partial\mu_s^k}Z = \langle a_i^u a_j^d a_k^s\rangle$ and hence

$$A_{001} = \frac{1}{Z}\frac{\partial Z}{\partial \mu_s} = \left\langle \frac{1}{4}\frac{\partial \ln\det M_s}{\partial \mu_s}\right\rangle = \left\langle \frac{1}{4}[2]_s\right\rangle \tag{A.9}$$

$$A_{010} = \left\langle \frac{1}{4}[2]_d\right\rangle \tag{A.10}$$

$$A_{100} = \left\langle \frac{1}{4}[2]_u\right\rangle \tag{A.11}$$

$$\begin{aligned} A_{002} &= \frac{1}{Z}\frac{\partial^2 Z}{\partial \mu_s^2} = \left\langle \left(\frac{1}{4}\frac{\partial \ln\det M_s}{\partial \mu_s}\right)^2 + \frac{1}{4}\frac{\partial^2 \ln\det M_s}{\partial \mu_s^2}\right\rangle \\ &= \left\langle \left(\frac{1}{4}[2]_s\right)^2 + \frac{1}{4}\left([3]_s - [12]_s\right)\right\rangle \end{aligned} \tag{A.12}$$

$$A_{020} = \left\langle \left(\frac{1}{4}[2]_d\right)^2 + \frac{1}{4}\left([3]_d - [12]_d\right)\right\rangle \tag{A.13}$$

$$A_{200} = \left\langle \left(\frac{1}{4}[2]_u\right)^2 + \frac{1}{4}\left([3]_u - [12]_u\right)\right\rangle \tag{A.14}$$

$$\begin{aligned} A_{011} &= \frac{1}{Z}\frac{\partial^2 Z}{\partial \mu_d \partial \mu_s} = \left\langle \frac{1}{4}\frac{\partial \ln\det M_d}{\partial \mu_d}\frac{1}{4}\frac{\partial \ln\det M_s}{\partial \mu_s}\right\rangle \\ &= \left\langle \frac{1}{4}[2]_d\frac{1}{4}[2]_s\right\rangle \end{aligned} \tag{A.15}$$

$$A_{101} = \left\langle \frac{1}{4}[2]_u\frac{1}{4}[2]_s\right\rangle \tag{A.16}$$

$$A_{110} = \left\langle \frac{1}{4}[2]_u\frac{1}{4}[2]_d\right\rangle \tag{A.17}$$

$$
\begin{aligned}
A_{003} &= \frac{1}{Z}\frac{\partial^3 Z}{\partial \mu_s^3} = \left\langle \frac{1}{4}\frac{\partial^3 \ln\det M_s}{\partial \mu_s^3} + \left(\frac{1}{4}\frac{\partial \ln\det M_s}{\partial \mu_s}\right)^3 \right\rangle \\
&\quad + 3\left\langle \frac{1}{4}\frac{\partial \ln\det M_s}{\partial \mu_s}\frac{1}{4}\frac{\partial^2 \ln\det M_s}{\partial \mu_s^2} \right\rangle \\
&= \left\langle \frac{1}{4}\left([4]_s - 3\times[13]_s + 2\times[62]_s\right) + \left(\frac{1}{4}[2]_s\right)^3 \right\rangle \\
&\quad + \left\langle \frac{1}{4}[2]_s \frac{1}{4}\left([3]_s - [12]_s\right) \right\rangle \qquad \text{(A.18)} \\
A_{030} &= \left\langle \frac{1}{4}\left([4]_d - 3\times[13]_d + 2\times[62]_d\right) + \left(\frac{1}{4}[2]_d\right)^3 \right\rangle \\
&\quad + \left\langle \frac{1}{4}[2]_d \frac{1}{4}\left([3]_d - [12]_d\right) \right\rangle \qquad \text{(A.19)} \\
A_{300} &= \left\langle \frac{1}{4}\left([4]_u - 3\times[13]_u + 2\times[62]_u\right) + \left(\frac{1}{4}[2]_u\right)^3 \right\rangle \\
&\quad + \left\langle \frac{1}{4}[2]_u \frac{1}{4}\left([3]_u - [12]_u\right) \right\rangle \qquad \text{(A.20)} \\
A_{111} &= \frac{1}{Z}\frac{\partial^3 Z}{\partial \mu_u \partial \mu_d \partial \mu_s} = \left\langle \frac{1}{4}\frac{\partial \ln\det M_u}{\partial \mu_u}\frac{1}{4}\frac{\partial \ln\det M_d}{\partial \mu_d}\frac{1}{4}\frac{\partial \ln\det M_s}{\partial \mu_s} \right\rangle \\
&= \left\langle \frac{1}{4}[2]_u \frac{1}{4}[2]_d \frac{1}{4}[2]_s \right\rangle \qquad \text{(A.21)} \\
A_{012} &= \frac{1}{Z}\frac{\partial^3 Z}{\partial \mu_d \partial \mu_s^2} = \left\langle \frac{1}{4}\frac{\partial \ln\det M_d}{\partial \mu_d}\left[\left(\frac{1}{4}\frac{\partial \ln\det M_s}{\partial \mu_s}\right)^2 + \frac{1}{4}\frac{\partial^2 \ln\det M_s}{\partial \mu_s^2}\right] \right\rangle \\
&= \left\langle \frac{1}{4}[2]_d \left[\left(\frac{1}{4}[2]_s\right)^2 + \frac{1}{4}\left([3]_s - [12]_s\right)\right] \right\rangle \qquad \text{(A.22)} \\
A_{021} &= \frac{1}{Z}\frac{\partial^3 Z}{\partial \mu_d^2 \partial \mu_s} = \left\langle \left[\left(\frac{1}{4}[2]_d\right)^2 + \frac{1}{4}\left([3]_d - [12]_d\right)\right]\frac{1}{4}[2]_s \right\rangle \qquad \text{(A.23)} \\
A_{120} &= \frac{1}{Z}\frac{\partial^3 Z}{\partial \mu_u \partial \mu_d^2} = \left\langle \frac{1}{4}[2]_u \left[\left(\frac{1}{4}[2]_d\right)^2 + \frac{1}{4}\left([3]_d - [12]_d\right)\right] \right\rangle \qquad \text{(A.24)} \\
A_{210} &= \frac{1}{Z}\frac{\partial^3 Z}{\partial \mu_u^2 \partial \mu_d} = \left\langle \left[\left(\frac{1}{4}[2]_u\right)^2 + \frac{1}{4}\left([3]_u - [12]_u\right)\right]\frac{1}{4}[2]_d \right\rangle \qquad \text{(A.25)} \\
A_{102} &= \frac{1}{Z}\frac{\partial^3 Z}{\partial \mu_u \partial \mu_s^2} = \left\langle \frac{1}{4}[2]_u \left[\left(\frac{1}{4}[2]_s\right)^2 + \frac{1}{4}\left([3]_s - [12]_s\right)\right] \right\rangle \qquad \text{(A.26)} \\
A_{201} &= \frac{1}{Z}\frac{\partial^3 Z}{\partial \mu_u^2 \partial \mu_s} = \left\langle \left[\left(\frac{1}{4}[2]_u\right)^2 + \frac{1}{4}\left([3]_u - [12]_u\right)\right]\frac{1}{4}[2]_s \right\rangle \qquad \text{(A.27)} \\
& \qquad \text{(A.28)}
\end{aligned}
$$

A.5 Writing X_{ijk}^{uds} in terms of the above observable IDs :

$$X_{001}^{uds} = A_{001} = \left\langle \frac{1}{4}[2]_s \right\rangle \tag{A.29}$$

$$\begin{aligned} X_{002}^{uds} &= -A_{001}^2 + A_{002} \\ &= -\left\langle \frac{1}{4}[2]_s \right\rangle^2 + \left\langle \left(\frac{1}{4}[2]_s\right)^2 + \frac{1}{4}\left([3]_s - [12]_s\right) \right\rangle \end{aligned} \tag{A.30}$$

$$\begin{aligned} X_{003}^{uds} &= 2A_{001}^3 - 3A_{001}A_{002} + A_{003} \\ &= 2\left\langle \frac{1}{4}[2]_s \right\rangle^3 - 3\left\langle \frac{1}{4}[2]_s \right\rangle \left\langle \left(\frac{1}{4}[2]_s\right)^2 + \frac{1}{4}\left([3]_s - [12]_s\right) \right\rangle \\ &+ \left\langle \frac{1}{4}\left([4]_s - 3\times[13]_s + 2\times[62]_s\right) + \left(\frac{1}{4}[2]_s\right)^3 \right\rangle \\ &+ \left\langle \frac{1}{4}[2]_s \frac{1}{4}\left([3]_s - [12]_s\right) \right\rangle \end{aligned} \tag{A.31}$$

$$X_{010}^{uds} = A_{010} = \left\langle \frac{1}{4}[2]_d \right\rangle \tag{A.32}$$

$$\begin{aligned} X_{011}^{uds} &= -A_{001}A_{010} + A_{011} \\ &= -\left\langle \frac{1}{4}[2]_s \right\rangle \left\langle \frac{1}{4}[2]_d \right\rangle + \left\langle \frac{1}{4}[2]_d \frac{1}{4}[2]_s \right\rangle \end{aligned} \tag{A.33}$$

$$\begin{aligned} X_{012}^{uds} &= -(-2A_{001}^2 + A_{002})A_{010} - 2A_{001}A_{011} + A_{012} \\ &= -\left(-2\left\langle \frac{1}{4}[2]_s \right\rangle^2 + \left\langle \left(\frac{1}{4}[2]_s\right)^2 + \frac{1}{4}\left([3]_s - [12]_s\right) \right\rangle\right) \left\langle \frac{1}{4}[2]_d \right\rangle \\ &- 2\left\langle \frac{1}{4}[2]_s \right\rangle \left\langle \frac{1}{4}[2]_d \frac{1}{4}[2]_s \right\rangle + \left\langle \frac{1}{4}[2]_d \left[\left(\frac{1}{4}[2]_s\right)^2 + \frac{1}{4}\left([3]_s - [12]_s\right)\right] \right\rangle \end{aligned} \tag{A.34}$$

$$\begin{aligned} X_{020}^{uds} &= -A_{010}^2 + A_{020} \\ &= -\left\langle \frac{1}{4}[2]_d \right\rangle^2 + \left\langle \left(\frac{1}{4}[2]_d\right)^2 + \frac{1}{4}\left([3]_d - [12]_d\right) \right\rangle \end{aligned} \tag{A.35}$$

$$\begin{aligned} X_{021}^{uds} &= -A_{020}A_{001} + 2A_{001}A_{010}^2 - 2A_{010}A_{011} + A_{021} \\ &= -\left\langle \left(\frac{1}{4}[2]_d\right)^2 + \frac{1}{4}\left([3]_d - [12]_d\right) \right\rangle \left\langle \frac{1}{4}[2]_s \right\rangle \\ &+ 2\left\langle \frac{1}{4}[2]_s \right\rangle \left\langle \frac{1}{4}[2]_d \right\rangle^2 - 2\left\langle \frac{1}{4}[2]_d \right\rangle \left\langle \frac{1}{4}[2]_d \frac{1}{4}[2]_s \right\rangle \\ &+ \left\langle \left[\left(\frac{1}{4}[2]_d\right)^2 + \frac{1}{4}\left([3]_d - [12]_d\right)\right] \frac{1}{4}[2]_s \right\rangle \end{aligned} \tag{A.36}$$

$$\begin{aligned} X_{030}^{uds} &= 2A_{010}^3 - 3A_{010}A_{020} + A_{030} \\ &= 2\left\langle \frac{1}{4}[2]_d \right\rangle^3 - 3\left\langle \frac{1}{4}[2]_d \right\rangle \left\langle \left(\frac{1}{4}[2]_d\right)^2 + \frac{1}{4}\left([3]_d - [12]_d\right) \right\rangle \end{aligned}$$

$$+\left\langle \frac{1}{4}\left([4]_d - 3\times[13]_d + 2\times[62]_d\right) + \left(\frac{1}{4}[2]_d\right)^3 \right\rangle$$
$$+\left\langle \frac{1}{4}[2]_d \frac{1}{4}\left([3]_d - [12]_d\right) \right\rangle \tag{A.37}$$

$$X^{uds}_{100} = A_{100} = \left\langle \frac{1}{4}[2]_u \right\rangle \tag{A.38}$$

$$\begin{aligned} X^{uds}_{101} &= -A_{001}A_{100} + A_{101} \\ &= -\left\langle \frac{1}{4}[2]_s \right\rangle \left\langle \frac{1}{4}[2]_u \right\rangle + \left\langle \frac{1}{4}[2]_u \frac{1}{4}[2]_s \right\rangle \end{aligned} \tag{A.39}$$

$$\begin{aligned} X^{uds}_{102} &= -(-2A^2_{001} + A_{002})A_{100} - 2A_{001}A_{101} + A_{102} \\ &= -\left(-2\left\langle \frac{1}{4}[2]_s \right\rangle^2 + \left\langle \left(\frac{1}{4}[2]_s\right)^2 + \frac{1}{4}\left([3]_s - [12]_s\right) \right\rangle\right) \left\langle \frac{1}{4}[2]_u \right\rangle \\ &\quad - 2\left\langle \frac{1}{4}[2]_s \right\rangle \left\langle \frac{1}{4}[2]_u \frac{1}{4}[2]_s \right\rangle + \left\langle \frac{1}{4}[2]_u \left[\left(\frac{1}{4}[2]_s\right)^2 + \frac{1}{4}\left([3]_s - [12]_s\right)\right] \right\rangle \end{aligned} \tag{A.40}$$

$$\begin{aligned} X^{uds}_{110} &= -A_{010}A_{100} + A_{110} \\ &= -\left\langle \frac{1}{4}[2]_d \right\rangle \left\langle \frac{1}{4}[2]_u \right\rangle + \left\langle \frac{1}{4}[2]_d \frac{1}{4}[2]_u \right\rangle \end{aligned} \tag{A.41}$$

$$\begin{aligned} X^{uds}_{111} &= 2A_{001}A_{010}A_{100} - A_{001}A_{110} - A_{010}A_{101} - A_{011}A_{100} + A_{111} \\ &= 2\left\langle \frac{1}{4}[2]_s \right\rangle \left\langle \frac{1}{4}[2]_d \right\rangle \left\langle \frac{1}{4}[2]_u \right\rangle - \left\langle \frac{1}{4}[2]_s \right\rangle \left\langle \frac{1}{4}[2]_d \frac{1}{4}[2]_u \right\rangle \\ &\quad - \left\langle \frac{1}{4}[2]_d \right\rangle \left\langle \frac{1}{4}[2]_s \frac{1}{4}[2]_u \right\rangle - \left\langle \frac{1}{4}[2]_u \right\rangle \left\langle \frac{1}{4}[2]_d \frac{1}{4}[2]_s \right\rangle \\ &\quad + \left\langle \frac{1}{4}[2]_u \frac{1}{4}[2]_d \frac{1}{4}[2]_s \right\rangle \end{aligned} \tag{A.42}$$

$$\begin{aligned} X^{uds}_{120} &= -(-2A^2_{010} + A_{020})A_{100} - 2A_{010}A_{110} + A_{120} \\ &= -\left(-2\left\langle \frac{1}{4}[2]_d \right\rangle^2 + \left\langle \left(\frac{1}{4}[2]_d\right)^2 + \frac{1}{4}\left([3]_d - [12]_d\right) \right\rangle\right) \left\langle \frac{1}{4}[2]_u \right\rangle \\ &\quad - 2\left\langle \frac{1}{4}[2]_d \right\rangle \left\langle \frac{1}{4}[2]_u \frac{1}{4}[2]_d \right\rangle \\ &\quad + \left\langle \frac{1}{4}[2]_u \left[\left(\frac{1}{4}[2]_d\right)^2 + \frac{1}{4}\left([3]_d - [12]_d\right)\right] \right\rangle \end{aligned} \tag{A.43}$$

$$\begin{aligned} X^{uds}_{200} &= -A^2_{100} + A_{200} \\ &= -\left\langle \frac{1}{4}[2]_u \right\rangle^2 + \left\langle \left(\frac{1}{4}[2]_u\right)^2 + \frac{1}{4}\left([3]_u - [12]_u\right) \right\rangle \end{aligned} \tag{A.44}$$

$$\begin{aligned} X^{uds}_{201} &= -A_{200}A_{001} + 2A_{001}A^2_{100} - 2A_{100}A_{101} + A_{201} \\ &= -\left\langle \left(\frac{1}{4}[2]_u\right)^2 + \frac{1}{4}\left([3]_u - [12]_u\right) \right\rangle \left\langle \frac{1}{4}[2]_s \right\rangle \\ &\quad + 2\left\langle \frac{1}{4}[2]_s \right\rangle \left\langle \frac{1}{4}[2]_u \right\rangle^2 - 2\left\langle \frac{1}{4}[2]_u \right\rangle \left\langle \frac{1}{4}[2]_u \frac{1}{4}[2]_s \right\rangle \end{aligned}$$

$$+\left\langle\left[\left(\frac{1}{4}[2]_u\right)^2+\frac{1}{4}\left([3]_u-[12]_u\right)\right]\frac{1}{4}[2]_s\right\rangle \tag{A.45}$$

$$\begin{aligned}X^{uds}_{210} &= -A_{200}A_{010}+2A_{010}A^2_{100}-2A_{100}A_{110}+A_{210}\\ &= -\left\langle\left(\frac{1}{4}[2]_u\right)^2+\frac{1}{4}\left([3]_u-[12]_u\right)\right\rangle\left\langle\frac{1}{4}[2]_d\right\rangle\\ &+2\left\langle\frac{1}{4}[2]_d\right\rangle\left\langle\frac{1}{4}[2]_u\right\rangle^2-2\left\langle\frac{1}{4}[2]_u\right\rangle\left\langle\frac{1}{4}[2]_u\frac{1}{4}[2]_d\right\rangle\\ &+\left\langle\left[\left(\frac{1}{4}[2]_u\right)^2+\frac{1}{4}\left([3]_u-[12]_u\right)\right]\frac{1}{4}[2]_d\right\rangle\end{aligned} \tag{A.46}$$

$$\begin{aligned}X^{uds}_{300} &= 2A^3_{100}-3A_{100}A_{200}+A_{300}\\ &= 2\left\langle\frac{1}{4}[2]_u\right\rangle^3-3\left\langle\frac{1}{4}[2]_u\right\rangle\left\langle\left(\frac{1}{4}[2]_u\right)^2+\frac{1}{4}\left([3]_u-[12]_u\right)\right\rangle\\ &+\left\langle\frac{1}{4}\left([4]_u-3\times[13]_u+2\times[62]_u\right)+\left(\frac{1}{4}[2]_u\right)^3\right\rangle\\ &+\left\langle\frac{1}{4}[2]_u\frac{1}{4}\left([3]_u-[12]_u\right)\right\rangle\end{aligned} \tag{A.47}$$

A.6 Some χ^{BQS}_{ijk} (cumulants of conserved charges) in terms of the measured quantities

The cumulants (χ^{uds}_{ijk}) are related to the expectation values with a pre-factor : $\chi^{uds}_{ijk} = \frac{1}{VT^3}X^{uds}_{ijk}$.
Now the conserved charges are easy to read from the values of {i,j,k} in χ^{BQS}_{ijk}.For example,

$$\begin{aligned}\chi^{BQS}_{100} &= \chi^B_1 = \frac{1}{VT^3}\frac{\partial}{\partial\mu_B}\ln Z\\ \chi^{BQS}_{200} &= \chi^B_2 = \frac{1}{VT^3}\frac{\partial^2}{\partial\mu^2_B}\ln Z\\ \chi^{BQS}_{010} &= \chi^Q_1 = \frac{1}{VT^3}\frac{\partial}{\partial\mu_Q}\ln Z\\ \chi^{BQS}_{110} &= \frac{\partial\chi^Q_1}{\partial\mu_B} = \frac{1}{VT^3}\frac{\partial^2}{\partial\mu_Q\partial\mu_B}\ln Z\\ &\&....\end{aligned}$$

Finally writing the desired cumulants directly in terms of the measured observables. Do not forget to put the factors of $(1/VT^3)$ that relate X's to χ's:

$$\chi^{BQS}_{001} = -\chi^{uds}_{001} = -\left(\frac{1}{VT^3}\right)\left\langle\frac{1}{4}[2]_s\right\rangle \tag{A.48}$$

$$\chi^{BQS}_{002} = \chi^{uds}_{002}$$

$$= \left(\frac{1}{VT^3}\right)\left(-\left\langle\frac{1}{4}[2]_s\right\rangle^2 + \left\langle\left(\frac{1}{4}[2]_s\right)^2 + \frac{1}{4}\left([3]_s - [12]_s\right)\right\rangle\right) \tag{A.49}$$

$$\begin{aligned}\chi_{003}^{BQS} &= -\chi_{003}^{uds} \\ &= -\left(\frac{1}{VT^3}\right)\left(2\left\langle\frac{1}{4}[2]_s\right\rangle^3 - 3\left\langle\frac{1}{4}[2]_s\right\rangle\left\langle\left(\frac{1}{4}[2]_s\right)^2 + \frac{1}{4}\left([3]_s - [12]_s\right)\right\rangle\right. \\ &+ \left\langle\frac{1}{4}\left([4]_s - 3\times[13]_s + 2\times[62]_s\right) + \left(\frac{1}{4}[2]_s\right)^3\right\rangle \\ &+ \left.\left\langle\frac{1}{4}[2]_s\frac{1}{4}\left([3]_s - [12]_s\right)\right\rangle\right)\end{aligned} \tag{A.50}$$

$$\begin{aligned}\chi_{010}^{BQS} &= \left(-\chi_{010}^{uds} - \chi_{001}^{uds} + 2\chi_{100}^{uds}\right)/3 \\ &= \left(\frac{1}{3}\frac{1}{VT^3}\right)\left(-\left\langle\frac{1}{4}[2]_d\right\rangle - \left\langle\frac{1}{4}[2]_s\right\rangle + 2\left\langle\frac{1}{4}[2]_u\right\rangle\right)\end{aligned} \tag{A.51}$$

$$\begin{aligned}\chi_{011}^{BQS} &= \left(\chi_{002}^{uds} + \chi_{011}^{uds} - 2\chi_{101}^{uds}\right)/3 \\ &= \left(\frac{1}{3}\frac{1}{VT^3}\right)\left(-\left\langle\frac{1}{4}[2]_s\right\rangle^2 + \left\langle\left(\frac{1}{4}[2]_s\right)^2 + \frac{1}{4}\left([3]_s - [12]_s\right)\right\rangle\right. \\ &- \left.\left\langle\frac{1}{4}[2]_s\right\rangle\left\langle\frac{1}{4}[2]_d\right\rangle + \left\langle\frac{1}{4}[2]_d\frac{1}{4}[2]_s\right\rangle + 2\left\langle\frac{1}{4}[2]_s\right\rangle\left\langle\frac{1}{4}[2]_u\right\rangle - 2\left\langle\frac{1}{4}[2]_u\frac{1}{4}[2]_s\right\rangle\right)\end{aligned} \tag{A.52}$$

$$\begin{aligned}\chi_{012}^{BQS} &= \left(-\chi_{003}^{uds} - \chi_{012}^{uds} + 2\chi_{102}^{uds}\right)/3 \\ &= \left(\frac{1}{3}\frac{1}{VT^3}\right)\left(-2\left\langle\frac{1}{4}[2]_s\right\rangle^3 + 3\left\langle\frac{1}{4}[2]_s\right\rangle\left\langle\left(\frac{1}{4}[2]_s\right)^2 + \frac{1}{4}\left([3]_s - [12]_s\right)\right\rangle\right. \\ &- \left\langle\frac{1}{4}\left([4]_s - 3\times[13]_s + 2\times[62]_s\right) + \left(\frac{1}{4}[2]_s\right)^3\right\rangle - \left\langle\frac{1}{4}[2]_s\frac{1}{4}\left([3]_s - [12]_s\right)\right\rangle \\ &+ \left[-2\left\langle\frac{1}{4}[2]_s\right\rangle^2 + \left\langle\left(\frac{1}{4}[2]_s\right)^2 + \frac{1}{4}\left([3]_s - [12]_s\right)\right\rangle\right]\left\langle\frac{1}{4}[2]_d\right\rangle \\ &+ 2\left\langle\frac{1}{4}[2]_s\right\rangle\left\langle\frac{1}{4}[2]_d\frac{1}{4}[2]_s\right\rangle - \left\langle\frac{1}{4}[2]_d\left[\left(\frac{1}{4}[2]_s\right)^2 + \frac{1}{4}\left([3]_s - [12]_s\right)\right]\right\rangle \\ &- 2\left[-2\left\langle\frac{1}{4}[2]_s\right\rangle^2 + \left\langle\left(\frac{1}{4}[2]_s\right)^2 + \frac{1}{4}\left([3]_s - [12]_s\right)\right\rangle\right]\left\langle\frac{1}{4}[2]_u\right\rangle \\ &- 4\left\langle\frac{1}{4}[2]_s\right\rangle\left\langle\frac{1}{4}[2]_u\frac{1}{4}[2]_s\right\rangle + 2\left\langle\frac{1}{4}[2]_u\left[\left(\frac{1}{4}[2]_s\right)^2 + \frac{1}{4}\left([3]_s - [12]_s\right)\right]\right\rangle\Bigg)\end{aligned} \tag{A.53}$$

$$\begin{aligned}\chi_{020}^{BQS} &= \left(\chi_{020}^{uds} + \chi_{002}^{uds} + 4\chi_{200}^{uds} - 4\chi_{110}^{uds} - 4\chi_{101}^{uds} + 2\chi_{011}^{uds}\right)/9 \\ &= \left(\frac{1}{9}\frac{1}{VT^3}\right)\left(-\left\langle\frac{1}{4}[2]_d\right\rangle^2 + \left\langle\left(\frac{1}{4}[2]_d\right)^2 + \frac{1}{4}\left([3]_d - [12]_d\right)\right\rangle\right. \\ &- \left.\left\langle\frac{1}{4}[2]_s\right\rangle^2 + \left\langle\left(\frac{1}{4}[2]_s\right)^2 + \frac{1}{4}\left([3]_s - [12]_s\right)\right\rangle\right.\end{aligned}$$

$$
\begin{aligned}
&-4\left\langle\frac{1}{4}[2]_u\right\rangle^2+4\left\langle\left(\frac{1}{4}[2]_u\right)^2+\frac{1}{4}\left([3]_u-[12]_u\right)\right\rangle\\
&+4\left\langle\frac{1}{4}[2]_d\right\rangle\left\langle\frac{1}{4}[2]_u\right\rangle-4\left\langle\frac{1}{4}[2]_d\frac{1}{4}[2]_u\right\rangle\\
&+4\left\langle\frac{1}{4}[2]_s\right\rangle\left\langle\frac{1}{4}[2]_u\right\rangle-4\left\langle\frac{1}{4}[2]_u\frac{1}{4}[2]_s\right\rangle\Big)\\
&-2\left\langle\frac{1}{4}[2]_s\right\rangle\left\langle\frac{1}{4}[2]_d\right\rangle+2\left\langle\frac{1}{4}[2]_d\frac{1}{4}[2]_s\right\rangle\Big) \qquad \text{(A.54)}\\
\chi_{021}^{BQS}&=\left(-\chi_{003}^{uds}-\chi_{021}^{uds}-4\chi_{201}^{uds}-2\chi_{012}^{uds}+4\chi_{102}^{uds}+4\chi_{111}^{uds}\right)/9\\
&=\left(\frac{1}{9}\frac{1}{VT^3}\right)\left(-2\left\langle\frac{1}{4}[2]_s\right\rangle^3+3\left\langle\frac{1}{4}[2]_s\right\rangle\left\langle\left(\frac{1}{4}[2]_s\right)^2+\frac{1}{4}\left([3]_s-[12]_s\right)\right\rangle\right.\\
&-\left\langle\frac{1}{4}\left([4]_s-3\times[13]_s+2\times[62]_s\right)+\left(\frac{1}{4}[2]_s\right)^3\right\rangle\\
&-\left\langle\frac{1}{4}[2]_s\frac{1}{4}\left([3]_s-[12]_s\right)\right\rangle\\
&+\left\langle\left(\frac{1}{4}[2]_d\right)^2+\frac{1}{4}\left([3]_d-[12]_d\right)\right\rangle\left\langle\frac{1}{4}[2]_s\right\rangle\\
&-2\left\langle\frac{1}{4}[2]_s\right\rangle\left\langle\frac{1}{4}[2]_d\right\rangle^2+2\left\langle\frac{1}{4}[2]_d\right\rangle\left\langle\frac{1}{4}[2]_d\frac{1}{4}[2]_s\right\rangle\\
&-\left\langle\left[\left(\frac{1}{4}[2]_d\right)^2+\frac{1}{4}\left([3]_d-[12]_d\right)\right]\frac{1}{4}[2]_s\right\rangle\\
&+4\left\langle\left(\frac{1}{4}[2]_u\right)^2+\frac{1}{4}\left([3]_u-[12]_u\right)\right\rangle\left\langle\frac{1}{4}[2]_s\right\rangle\\
&-8\left\langle\frac{1}{4}[2]_s\right\rangle\left\langle\frac{1}{4}[2]_u\right\rangle^2-2\left\langle\frac{1}{4}[2]_u\right\rangle\left\langle\frac{1}{4}[2]_u\frac{1}{4}[2]_s\right\rangle\\
&-4\left\langle\left[\left(\frac{1}{4}[2]_u\right)^2+\frac{1}{4}\left([3]_u-[12]_u\right)\right]\frac{1}{4}[2]_s\right\rangle\Big)\\
&+2\left(-2\left\langle\frac{1}{4}[2]_s\right\rangle^2+\left\langle\left(\frac{1}{4}[2]_s\right)^2+\frac{1}{4}\left([3]_s-[12]_s\right)\right\rangle\right)\left\langle\frac{1}{4}[2]_d\right\rangle\\
&+4\left\langle\frac{1}{4}[2]_s\right\rangle\left\langle\frac{1}{4}[2]_d\frac{1}{4}[2]_s\right\rangle-2\left\langle\frac{1}{4}[2]_d\left[\left(\frac{1}{4}[2]_s\right)^2+\frac{1}{4}\left([3]_s-[12]_s\right)\right]\right\rangle\\
&-4\left(-2\left\langle\frac{1}{4}[2]_s\right\rangle^2+\left\langle\left(\frac{1}{4}[2]_s\right)^2+\frac{1}{4}\left([3]_s-[12]_s\right)\right\rangle\right)\left\langle\frac{1}{4}[2]_u\right\rangle\\
&-8\left\langle\frac{1}{4}[2]_s\right\rangle\left\langle\frac{1}{4}[2]_u\frac{1}{4}[2]_s\right\rangle+4\left\langle\frac{1}{4}[2]_u\left[\left(\frac{1}{4}[2]_s\right)^2+\frac{1}{4}\left([3]_s-[12]_s\right)\right]\right\rangle\\
&+8\left\langle\frac{1}{4}[2]_s\right\rangle\left\langle\frac{1}{4}[2]_d\right\rangle\left\langle\frac{1}{4}[2]_u\right\rangle-4\left\langle\frac{1}{4}[2]_s\right\rangle\left\langle\frac{1}{4}[2]_d\frac{1}{4}[2]_u\right\rangle
\end{aligned}
$$

$$
\begin{aligned}
&-4\left\langle\frac{1}{4}[2]_d\right\rangle\left\langle\frac{1}{4}[2]_s\frac{1}{4}[2]_u\right\rangle-4\left\langle\frac{1}{4}[2]_u\right\rangle\left\langle\frac{1}{4}[2]_d\frac{1}{4}[2]_s\right\rangle\\
&+4\left\langle\frac{1}{4}[2]_u\frac{1}{4}[2]_d\frac{1}{4}[2]_s\right\rangle\Bigg) \qquad \text{(A.55)}\\
\chi_{030}^{BQS}&=\left(-\chi_{030}^{uds}-\chi_{003}^{uds}+8\chi_{300}^{uds}-12\chi_{210}^{uds}-12\chi_{201}^{uds}-3\chi_{012}^{uds}-3\chi_{021}^{uds}\right.\\
&\left.+6\chi_{120}^{uds}+6\chi_{102}^{uds}+12\chi_{111}^{uds}\right)/27 \qquad \text{(A.56)}\\
\chi_{101}^{BQS}&=\left(-\chi_{002}^{uds}-\chi_{011}^{uds}-\chi_{101}^{uds}\right)/3\\
&=\left(\frac{1}{3}\frac{1}{VT^3}\right)\left(\left\langle\frac{1}{4}[2]_s\right\rangle^2-\left\langle\left(\frac{1}{4}[2]_s\right)^2+\frac{1}{4}\left([3]_s-[12]_s\right)\right\rangle\right.\\
&\left.+\left\langle\frac{1}{4}[2]_s\right\rangle\left\langle\frac{1}{4}[2]_d\right\rangle-\left\langle\frac{1}{4}[2]_d\frac{1}{4}[2]_s\right\rangle+\left\langle\frac{1}{4}[2]_s\right\rangle\left\langle\frac{1}{4}[2]_u\right\rangle-\left\langle\frac{1}{4}[2]_u\frac{1}{4}[2]_s\right\rangle\right) \qquad \text{(A.57)}\\
\chi_{102}^{BQS}&=\left(\chi_{003}^{uds}+\chi_{012}^{uds}+\chi_{102}^{uds}\right)/3\\
&=\left(\frac{1}{3}\frac{1}{VT^3}\right)\left(2\left\langle\frac{1}{4}[2]_s\right\rangle^3-3\left\langle\frac{1}{4}[2]_s\right\rangle\left\langle\left(\frac{1}{4}[2]_s\right)^2+\frac{1}{4}\left([3]_s-[12]_s\right)\right\rangle\right.\\
&+\left\langle\frac{1}{4}\left([4]_s-3\times[13]_s+2\times[62]_s\right)+\left(\frac{1}{4}[2]_s\right)^3\right\rangle\\
&+\left\langle\frac{1}{4}[2]_s\frac{1}{4}\left([3]_s-[12]_s\right)\right\rangle\\
&-\left[-2\left\langle\frac{1}{4}[2]_s\right\rangle^2+\left\langle\left(\frac{1}{4}[2]_s\right)^2+\frac{1}{4}\left([3]_s-[12]_s\right)\right\rangle\right]\left\langle\frac{1}{4}[2]_d\right\rangle\\
&-2\left\langle\frac{1}{4}[2]_s\right\rangle\left\langle\frac{1}{4}[2]_d\frac{1}{4}[2]_s\right\rangle+\left\langle\frac{1}{4}[2]_d\left[\left(\frac{1}{4}[2]_s\right)^2+\frac{1}{4}\left([3]_s-[12]_s\right)\right]\right\rangle\\
&-\left[-2\left\langle\frac{1}{4}[2]_s\right\rangle^2+\left\langle\left(\frac{1}{4}[2]_s\right)^2+\frac{1}{4}\left([3]_s-[12]_s\right)\right\rangle\right]\left\langle\frac{1}{4}[2]_u\right\rangle\\
&\left.-2\left\langle\frac{1}{4}[2]_s\right\rangle\left\langle\frac{1}{4}[2]_u\frac{1}{4}[2]_s\right\rangle+\left\langle\frac{1}{4}[2]_u\left[\left(\frac{1}{4}[2]_s\right)^2+\frac{1}{4}\left([3]_s-[12]_s\right)\right]\right\rangle\right) \qquad \text{(A.58)}\\
\chi_{110}^{BQS}&=\left(-\chi_{020}^{uds}-\chi_{002}^{uds}+2\chi_{200}^{uds}+\chi_{110}^{uds}+\chi_{101}^{uds}-2\chi_{011}^{uds}\right)/9\\
&=\left(\frac{1}{9}\frac{1}{VT^3}\right)\left(\left\langle\frac{1}{4}[2]_d\right\rangle^2-\left\langle\left(\frac{1}{4}[2]_d\right)^2+\frac{1}{4}\left([3]_d-[12]_d\right)\right\rangle\right.\\
&+\left\langle\frac{1}{4}[2]_s\right\rangle^2-\left\langle\left(\frac{1}{4}[2]_s\right)^2+\frac{1}{4}\left([3]_s-[12]_s\right)\right\rangle\\
&-2\left\langle\frac{1}{4}[2]_u\right\rangle^2+2\left\langle\left(\frac{1}{4}[2]_u\right)^2+\frac{1}{4}\left([3]_u-[12]_u\right)\right\rangle\\
&\left.-\left\langle\frac{1}{4}[2]_d\right\rangle\left\langle\frac{1}{4}[2]_u\right\rangle+\left\langle\frac{1}{4}[2]_d\frac{1}{4}[2]_u\right\rangle\right.
\end{aligned}
$$

$$
\begin{aligned}
&- \left\langle \frac{1}{4}[2]_s \right\rangle \left\langle \frac{1}{4}[2]_u \right\rangle + \left\langle \frac{1}{4}[2]_u \frac{1}{4}[2]_s \right\rangle \\
&+2 \left\langle \frac{1}{4}[2]_s \right\rangle \left\langle \frac{1}{4}[2]_d \right\rangle - 2 \left\langle \frac{1}{4}[2]_d \frac{1}{4}[2]_s \right\rangle \Big)
\end{aligned} \tag{A.59}
$$

Appendix B

Data Measured for Cumulants of conserved charges

In this appendix we present the results of our analysis for the cumulants measured. The first two tables B.1 and B.2 are the data already published in [16]. Finally, in tables B.3 and B.4 we show the first two cumulants fo the net baryon and net charge densities.
The gauge fields have been generated with a rational hybrid Monte Carlo algorithm (RHMC). In Tables B.1 and B.2 we list results from calculation on the $24^3 \times 4$ and $36^3 \times 6$ lattices, respectively. Also listed are the number of configurations on which we have measured the observables and which are separated by 10 RHMC trajectories of length 0.5-1.0.

	Im $[\chi_1^B]$	Re $[\chi_2^B]$	Im $[\chi_3^B]$	#conf.		Im $[\chi_1^B]$	Re $[\chi_2^B]$	Im $[\chi_3^B]$	#conf.
$T = 201.4$ [MeV]					$T = 176.6$ [MeV]				
0.000	-0.00002(18)	0.26421(52)	0.0009(21)	4800	0.000	0.00062(28)	0.2288(10)	-0.0018(43)	1600
0.393	0.10319(17)	0.26066(46)	0.0155(27)	4800	0.209	0.04840(25)	0.22800(83)	0.01876(43)	1600
0.785	0.20388(21)	0.25134(72)	0.0367(30)	4800	0.419	0.09556(42)	0.22487(11)	0.0279(52)	1600
1.178	0.29940(27)	0.2344(11)	0.0478(47)	4800	0.628	0.14253(36)	0.2178(10)	0.0305(74)	1600
1.571	0.38637(20)	0.2107(11)	0.0762(68)	4800	0.838	0.18703(38)	0.2084(15)	0.0420(93)	1600
1.963	0.46004(44)	0.1675(22)	0.132(15)	5400	1.047	0.22836(50)	0.1951(18)	0.0706(87)	1600
2.356	0.51602(51)	0.1049(28)	0.224(22)	5400	1.257	0.26744(63)	0.1761(23)	0.092(14)	1600
2.749	0.53076(91)	-0.0589(73)	0.72(13)	5400	1.466	030325(65)	0.1599(29)	0096(20)	1600
2.880	0.52279(99)	-0.1291(79)	1.00(11)	10800	1.676	0.33369(37)	0.1253(17)	0.201(16)	1600
3.011	0.4851(21)	-0.516(34)	5.39(79)	10800	1.885	0.35465(57)	0.0961(35)	0.175(18)	1600
3.105	0.3859(78)	-2.92(54)	141(48)	11000	2.094	0.36401(57)	0.0147(62)	0.360(72)	1600
$T = 186.3$ [MeV]					2.304	0.3594(11)	-0.086(13)	0.73(12)	1600
0.000	0.00025(12)	0.24537(35)	0.0021(20)	4100	2.513	0.32881(51)	-0.235(18)	1.06(42)	1600
0.286	0.06986(20)	0.24361(51)	0.0062(17)	4100	2.723	0.2608(24)	-0.482(17)	1.40(44)	1600
0.571	0.13876(20)	0.23687(52)	0.0127(23)	4100	2.932	0.1454(32)	-0.567(29)	0.31(55)	1600
0.857	0.20486(26)	0.22681(75)	0.0181(29)	4100	3.142	0.0055(30)	-0.626(33)	-0.58(53)	1600
1.142	0.26792(27)	0.21248(91)	0.0271(46)	4100	$T = 167.4$ [MeV]				
1.428	0.32485(30)	0.1850(16)	0.0796(97)	4100	0.000	-0.00029(23)	0.21093(75)	-0.0070(53)	6000
1.714	0.37469(41)	0.1588(15)	0.068(12)	4100	0.393	0.08176(27)	0.2059(13)	0.0283(67)	6000
1.999	0.41448(59)	0.1088(38)	0.140(22)	4100	0.785	0.15952(31)	0.1860(12)	0.0668(70)	6000
2.285	0.43543(90)	0.0350(73)	0.271(48)	4100	1.178	0.22720(45)	0.1551(21)	0.1017(85)	6000
2.570	0.4213(15)	-0.145(11)	0.88(15)	4100	1.571	0.27782(81)	0.0982(36)	0.181(33)	6000
2.713	0.3918(24)	-0.349(25)	2.21(49)	4000	1.963	0.29885(84)	-0.0083(59)	0.372(68)	6000
2.856	0.3262(34)	-0.757(61)	5.3(1.2)	4100	2.356	0.2630(16)	-0.179(15)	0.57(12)	12000
2.999	0.2020(41)	-1.061(54)	2.9(1.6)	4000	2.749	0.1554(16)	-0.343(19)	0.23(25)	12000
3.142	-0.0069(61)	-1.40(12)	-0.0(3.2)	4100	3.142	-0.0015(16)	-0.421(13)	0.07(27)	12000
$T = 160.4$ [MeV]					$T = 160.4$ [MeV]				
0.000	-0.00027(25)	0.1919(12)	-0.0000(82)	5550	1.571	0.23653(81)	0.0584(60)	0.190(39)	5550
0.393	0.07427(36)	0.1865(14)	0.0287(84)	5550	1.963	0.2391(13)	-0.0476(83)	0.262(89)	5550
0.785	0.14273(32)	0.1637(18)	0.071(14)	5550	2.356	0.1990(16)	-0.1580(88)	0.16(16)	5550
1.178	0.20104(40)	0.1262(27)	0.109(17)	5550	2.749	0.1061(13)	-0.271(17)	0.13(23)	5550

Table B.1: Mean values and statistical errors of net baryon number cumulants from $24^3 \times 4$ lattices. Also indicated is the number of measured configurations.

	Im $[\chi_1^B]$	Re $[\chi_2^B]$	Im $[\chi_3^B]$	#conf.		Im $[\chi_1^B]$	Re $[\chi_2^B]$	Im $[\chi_3^B]$	#conf.
$T = 145.1$ (MeV)					$T = 145.1$ (MeV)				
0.000	0.00024(51)	0.0579(24)	0.001(20)	5280	1.963	0.05578(61)	-0.0217(39)	0.074(36)	5280
0.393	0.02276(42)	0.0526(27)	0.026(24)	5280	2.356	0.04384(73)	-0.0467(49)	0.099(46)	5280
0.785	0.04142(56)	0.0426(22)	0.057(19)	5280	2.749	0.02391(81)	-0.0569(44)	0.024(37)	5280
1.178	0.05436(54)	0.0176(27)	0.055(27)	5280	2.945	0.01315(95)	-0.0663(47)	0.008(46)	5280
1.571	0.05995(76)	-0.0042(24)	0.075(25)	5280	3.142	0.00024(80)	-0.0538(41)	0.071(39)	5280

Table B.2: Mean values and statistical errors of net baryon number cumulants from $36^3 \times 6$ lattices. Also indicated is the number of measured configurations.

$\hat{\mu}_B^I$	Im $\left[\chi_1^B\right]$	Re $\left[\chi_2^B\right]$	#conf.
$T = 190$ [MeV]			
0	0.00004(23)	0.21723(77)	
0.393	0.08453(38)	0.2140(11)	
0.785	0.16715(39)	0.1992(14)	
1.178	0.24091(55)	0.1783(20)	
1.571	0.30577(67)	0.1491(19)	
1.963	0.3549(13)	0.0908(71)	
2.356	0.3713(12)	-0.0177(70)	
2.749	0.3083(24)	-0.417(44)	
2.945	0.1931(42)	-0.712(51)	
3.141	0.0042(40)	-0.942(70)	
3.141	0.0038(25)	−0.484(27)	
$T = 185$ [MeV]			
0	0.00011(25)	0.20524(90)	
0.393	0.08045(26)	0.2008(11)	
0.785	0.15823(25)	0.1908(11)	
1.178	0.22713(56)	0.1652(20)	
1.571	0.28627(63)	0.1321(21)	
1.963	0.3260(10)	0.0664(43)	
2.356	0.3244(17)	−0.0873(83)	
2.749	0.2304(19)	−0.463(33)	
2.945	0.1278(38)	−0.627(50)	
3.141	0.0043(32)	−0.720(42)	
$T = 179$ [MeV]			
0	−0.00008(29)	0.1912(10)	
0.393	0.07481(33)	0.1865(11)	
0.785	0.14535(41)	0.1730(12)	
1.178	0.20806(47)	0.1463(16)	
1.571	0.25758(64)	0.1004(36)	
1.963	0.28318(86)	0.0412(48)	
2.356	0.2652(15)	−0.125(11)	
2.749	0.1656(15)	−0.350(16)	
2.945	0.0882(24)	−0.498(30)	

Table B.3: Mean values and statistical errors of net baryon number cumulants from $36^3 \times 6$ lattices at new values of temperatures $T \in \{179.5, 185, 190\}$ MeV. Also indicated is the number of measured configurations.

$\hat{\mu}_B^I$	Im $\left[\chi_1^Q\right]$	Re $\left[\chi_{11}^{QB}\right]$	#conf.
$T = 190$ [MeV]			
0	0.000053(45)	0.02479(11)	
0.39276	0.009701(48)	0.02477(17)	
0.78534	0.019448(67)	0.02431(17)	
1.1781	0.028965(58)	0.02435(24)	
1.5709	0.038456(76)	0.02375(24)	
1.9634	0.047198(87)	0.02006(54)	
2.3562	0.05324(12)	0.00819(63)	
2.749	0.04804(36)	−0.0538(62)	
2.9452	0.03119(65)	−0.1111(76)	
3.1415	0.00069(65)	−0.155(12)	
$T = 185$ [MeV]			
0	−0.000026(47)	0.02640(14)	
0.39276	0.010349(47)	0.02622(21)	
0.78534	0.020859(53)	0.02640(20)	
1.1781	0.030889(73)	0.02507(28)	
1.5709	0.040614(80)	0.02331(23)	
1.9634	0.048770(89)	0.01717(47)	
2.3562	0.05185(19)	−0.0046(10)	
2.749	0.03923(34)	−0.0730(51)	
2.9452	0.02218(64)	−0.1063(81)	
3.1415	0.00067(55)	−0.1250(68)	
$T = 179.5$ [MeV]			
0	0.000014(58)	0.02878(18)	
0.39276	0.011216(58)	0.02852(17)	
0.78534	0.022122(53)	0.02767(24)	
1.1781	0.032704(74)	0.02577(22)	
1.5709	0.041847(93)	0.02076(50)	
1.9634	0.04811(11)	0.01230(76)	
2.3562	0.04742(24)	−0.0168(18)	
2.749	0.03071(26)	−0.0631(28)	
2.9452	0.01657(44)	−0.0917(52)	
3.1415	0.00073(44)	−0.0898(48)	

Table B.4: Mean values and statistical errors of net charge cumulants from $36^3 \times 6$ lattices at new values of temperatures $T \in \{179.5, 185, 190\}$ MeV. Also indicated is the number of measured configurations.

Appendix C

2D Ising model simulation data

C.1 Simulation details :

We used a cluster algorithm to perform Monte Carlo simulations for the 2D Ising model with ferromagnetic couplings with only nearest neighbour interactions. We use the following Hamiltonian,

$$\mathcal{H}_{2D} = -J \sum_{\langle i,j \rangle} s_i.s_j - h. \sum_i s_i \ , \tag{C.1}$$

where we will fix for our simulations $J = 1$, an array of values for the external magnetic field h will be sampled along along with an array of temperature values.

The values of βh simulated are given in the following Table :

βh	0
0.01	0.025
0.05	0.1
0.15	0.2
0.25	0.4
0.6	0.8
1.0	1.2
1.4	1.6
1.8	2.0

From these we constructed the M vs H data. Notice that we only simulated the positive values for βh, since we know the symmetry properties of the data. But we also explicitly performed simulations at negative βh values for smaller lattices and confirmed the symmetry properties. Shown below are for two lattices sizes L=30 and L=80

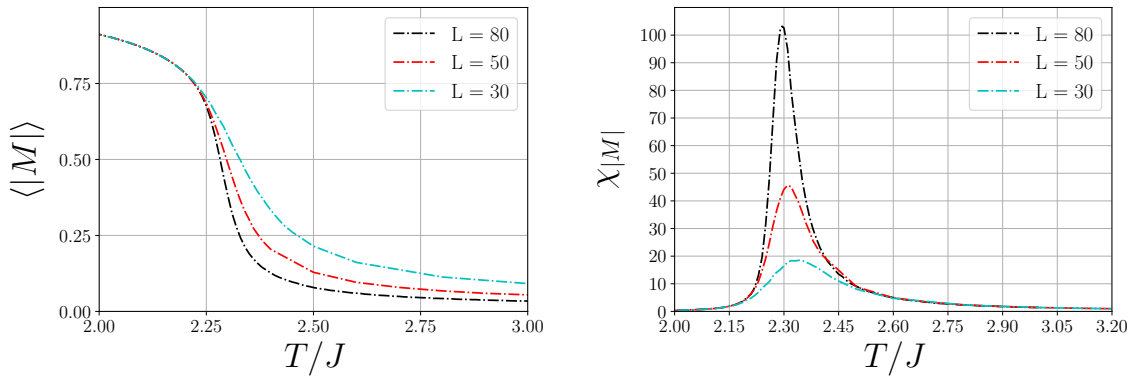

Figure C.1: Magnetisation and the peaks of susceptibility for the three lattices simulated L=30,50,80.

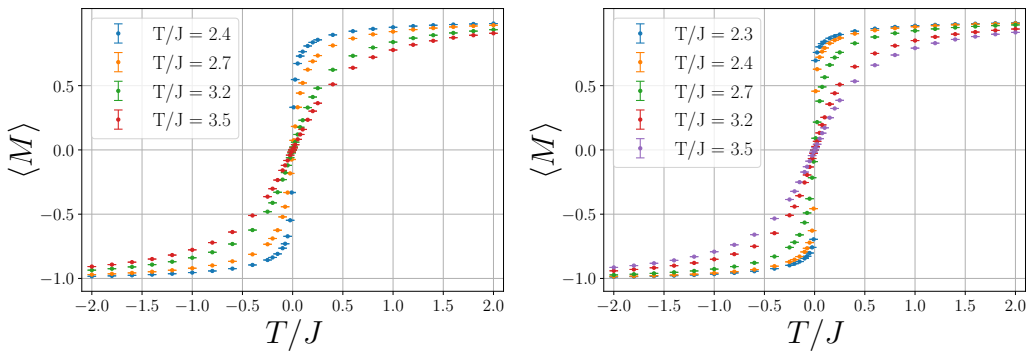

Figure C.2: Magnetization as a function of the external magnetic field displayed for a few selected temperatures shown in the legends. (Left) : L=30, (Right) : L=80

Appendix D

Yang Mills with theta term

This appendix is organised as follows: In Section D.1 we show why cannot write down a theta term for SU(N) in 2D and hence cannot use the Yang Mills 2D exact results to test our ideas. In Section D.2 we show how the theta term in is complexified, that being our first step in the thimble regularisation procedure. In Section D.3 we show via two different ways that the topological charge, now defined using complexified gauge fields can still be written as a total derivative term and hence it is still a topological term. Finally, in Section D.4 we will show the lattice version of the θ term we have implemented in our code.

D.1 θ-term in 1+1 D

In 1+1 D, the volume form $\epsilon^{\mu\nu}$ contains only two indices , and since the field tensor $\mathrm{F}^{\mu\nu}$ also contains only two indices, the dual tensor is actually a scalar (a 0-form):

$$\tilde{\mathrm{F}} = \epsilon^{\mu\nu}\,\mathrm{F}_{\mu\nu} \tag{D.1}$$

Hence there exists no combination of $\mathrm{F}_{\mu\nu}$ and $\tilde{\mathrm{F}}$ at $\mathcal{O}(2)$ in $\mathrm{F}^{\mu\nu}$ that can be used to form a Lorentz scalar!
In Abelian theories , this is not a problem as we can add a *linear* θ term:

$$S_{1+1D,U(1)} = \int d^2x \left(\frac{1}{2g^2}\,\mathrm{F}^{\mu\nu}\,\mathrm{F}_{\mu\nu} + \frac{\theta}{2\pi}\epsilon^{\mu\nu}\,\mathrm{F}_{\mu\nu}\right) \tag{D.2}$$

The problem occurs when we go to non-abelian theories because $\mathrm{F}^{\mu\nu}$ transforms non trivially under gauge transformations, the Lorentz invariant term $\epsilon^{\mu\nu}\,\mathrm{F}_{\mu\nu a}\,T^a$ is not sufficient - since it is not gauge invariant, since F transforms as $\mathrm{F}^{\mu\nu} \to \Omega(x)\,\mathrm{F}^{\mu\nu}\,\Omega^{-1}(x)$. Moreover, taking a trace will make the term zero : $\mathrm{Tr}\{(\epsilon^{\mu\nu}\,\mathrm{F}_{\mu\nu a}\,T^a)\} = 0$!

So it seems that 2D SU(N) does not have a theta term, in the usual sense when discussing the 4D theory [1].

D.2 θ term in 4D SU(N) (complexified)

In this section we proceed to start with our thimble construction by first complexifying the θ term. Our goal is to split the action in real and imaginary parts. This

[1] It is however possible to write a particular θ-term also for the group $\mathbb{CP}$. More details at [130]

is because we know that, by construction, the imaginary part of the action remains fixed while ascenting on the thimble. Therefore, we would like to identify what remains constant on a thimble. As will be apparent, we do complexification on the continuum theory.

We start with the usual YM Euclidean action in the presence of the θ term defined as,

$$\mathcal{L}_\theta(x) = \frac{1}{4}F^a_{\mu\nu}(x)\,F^a_{\mu\nu}(x) - \iota\theta\frac{g^2}{64\pi^2}\epsilon_{\mu\nu\rho\sigma}F^a_{\mu\nu}(x)\,F^a_{\rho\sigma}(x)$$
$$S = \int d^4x\mathcal{L}_\theta = \int d^4x\left(\frac{1}{4}F^a_{\mu\nu}(x)\,F^a_{\mu\nu}(x) - \iota\theta\frac{g^2}{64\pi^2}\epsilon_{\mu\nu\rho\sigma}F^a_{\mu\nu}(x)\,F^a_{\rho\sigma}(x)\right)$$

with,

$$\begin{aligned}F^a_{\mu\nu}(x) &= \partial_\mu A^a_\nu(x) - \partial_\nu A^a_\mu(x) - \iota g\left[A_\mu, A_\nu\right]^a \\ &= \partial_\mu A^a_\nu(x) - \partial_\nu A^a_\mu(x) + g f^{abc}A^b_\mu(x)\,A^c_\nu(x)\end{aligned}$$

Complexifying the field degrees of freedom : $A^a_\nu \to A^a_\nu + \iota\tilde{A}^a_\nu$, we get

$$\begin{aligned}\mathcal{S} &= S_{YM}\left[A + \iota\tilde{A}\right] - \iota S_\theta\left[A + \iota\tilde{A}\right] \\ \mathcal{S} &= S_{YM} + \iota\tilde{S}_{YM} - \iota S_\theta + \tilde{S}_\theta\end{aligned}$$

So the part that remains constabt is $\mathcal{S}_I = \tilde{S}_{YM} - S_\theta$. In terms of $F^a_{\mu\nu}$ and A^a_μ, the complexification looks like:

$$\begin{aligned}F^a_{\mu\nu} &\to \partial_\mu\left(A^a_\nu + i\tilde{A}^a_\nu\right) - \partial_\nu\left(A^a_\mu + i\tilde{A}^a_\mu\right) - \iota g\left[A_\mu + i\tilde{A}_\mu, A_\nu + i\tilde{A}_\nu\right]^a \\ &= \partial_\mu A^a_\mu - \partial_\nu A^a_\mu - \iota g\left[A_\mu, A_\nu\right]^a + \iota\partial_\mu\tilde{A}^a_\mu - \iota\partial_\nu\tilde{A}^a_\mu - \iota g\left[\iota\tilde{A}_\mu, \iota\tilde{A}_\nu\right]^a - \iota g\left[A_\mu, \tilde{A}_\nu\right] - \iota g\left[\tilde{A}_\mu, A_\nu\right] \\ &= F^a_{\mu\nu}[A] + F^a_{\mu\nu}[\iota\tilde{A}] - \iota g\left[A_\mu, \iota\tilde{A}_\nu\right] - \iota g\left[\iota\tilde{A}_\mu, A_\nu\right]\end{aligned}$$

So $F^a_{\mu\nu}F^a_{\mu\nu}$ becomes (still incomplete) :

$$F^a_{\mu\nu}F^a_{\mu\nu} \to \left(F^a_{\mu\nu}[A]\right)^2 + \left(F^a_{\mu\nu}[\iota\tilde{A}]\right)^2 + cross\,terms$$

And $i\epsilon_{\mu\nu\rho\sigma}F^a_{\mu\nu}F^a_{\rho\sigma}$ becomes (it is easier to write this in compact form because of the $\epsilon_{\mu\nu\rho\sigma}$).

$$\begin{aligned}\iota\epsilon_{\mu\nu\rho\sigma}F^a_{\mu\nu}F^a_{\rho\sigma} \to &\iota\epsilon_{\mu\nu\rho\sigma}\,\mathrm{Tr}\left[\left(\partial_\mu Z_\nu - \partial_\nu Z_\mu - \iota g\left[Z_\mu, Z_\nu\right]\right)\left(\partial_\rho Z_\sigma - \partial_\sigma Z_\rho - \iota g\left[Z_\rho, Z_\sigma\right]\right)\right] \\ &= 4\epsilon_{\mu\nu\rho\sigma}\,\mathrm{Tr}\left[\left(\partial_\mu Z_\nu - \iota g Z_\mu Z_\nu\right)\left(\partial_\rho Z_\sigma - \iota g Z_\rho Z_\sigma\right)\right]\end{aligned}$$

With $Z^a_\mu T^a = (A^a_\mu + \iota\tilde{A}^a_\mu)T^a$.

We can further simplfy the above to get rid of the term with $ZZZZ$, to get:

$$\iota\epsilon_{\mu\nu\rho\sigma}F^a_{\mu\nu}F^a_{\rho\sigma} \to 4\epsilon_{\mu\nu\rho\sigma}\,\mathrm{Tr}\left(\partial_\mu Z_\nu\partial_\rho Z_\sigma - \iota g Z_\mu Z_\nu\partial_\rho Z_\sigma - \iota g(\partial_\mu Z_\nu)Z_\rho Z_\sigma\right)$$

$$
\begin{aligned}
&= 4\epsilon_{\mu\nu\rho\sigma}\,\mathrm{Tr}\,(\partial_\mu Z_\nu \partial_\rho Z_\sigma - 2\iota g Z_\mu Z_\nu \partial_\rho Z_\sigma) \\
&= 4\epsilon_{\mu\nu\rho\sigma}\,\mathrm{Tr}\,\Big(\partial_\mu(A_\nu + \iota\tilde{A}_\nu)\partial_\rho(A_\sigma + \iota\tilde{A}_\sigma) \\
&-2\iota g(A_\mu + \iota\tilde{A}_\mu)(A_\nu + \iota\tilde{A}_\nu)\partial_\rho(A_\sigma + \iota\tilde{A}_\sigma)\Big)
\end{aligned}
$$

However, because of all the cross terms present, we couldn't conclude what relevance (if any) the net imaginary term being fixed on a thimble has. As can be guessed, we hoped that only the topological term would survive. We then moved onto try a different exercise - hoe see if after the complexification of the algebra the topological charge would still remain a total derivative term.

D.3 To show that $\epsilon_{\mu\nu\rho\sigma}\,\mathrm{Tr}\{F_{\mu\nu}F_{\rho\sigma}\} = \partial_\mu K^\mu$ for complex potentials : $A + \iota\tilde{A}$

We know that the theta-term of Yang-Mills can be written as a total derivative in the action, *i.e.*

$$
\epsilon_{\mu\nu\rho\sigma}\,\mathrm{Tr}\{F_{\mu\nu}F_{\rho\sigma}\} = \partial_\mu K^\mu \tag{D.3}
$$

where K^μ is known as the Chern-Simons term and is given by

$$
K^\mu = \epsilon_{\mu\nu\rho\sigma}\left(A^a_\nu F^a_{\rho\sigma} \pm \frac{g}{3} f^{abc} A^a_\nu A^b_\rho A^c_\sigma\right) \tag{D.4}
$$

Note that the sign $\pm$ depends on conventions. We now want to show that this relation also holds for complexified stress tensor. We complexify the potential as follows

$$
F^a_{\mu\nu} \to \partial_\mu\left(A^a_\nu + i\tilde{A}^a_\nu\right) - \partial_\nu\left(A^a_\mu + i\tilde{A}^a_\mu\right) - \iota g\left[A_\mu + i\tilde{A}_\mu, A_\nu + i\tilde{A}_\nu\right]^a \tag{D.5}
$$

and thus define the corresponding complexified stress-energy tensor as

$$
K^a_{\mu\nu}(x) = \partial_\mu Z^a_\nu(x) - \partial_\nu Z^a_\mu(x) - \iota g\left[Z_\mu, Z_\nu\right]^a \tag{D.6}
$$

with $Z_\mu = A_\mu + \iota\tilde{A}_\mu$.

Going through the algebra it can readily be seen that the topological term with a complexified stress-tensor can also be written as a total derivative term

$$
\begin{aligned}
\epsilon_{\mu\nu\rho\sigma}\,\mathrm{Tr}\,K_{\mu\nu}K_{\rho\sigma} &= \epsilon_{\mu\nu\rho\sigma}\,\mathrm{Tr}\left[\left(\partial_\mu Z_\nu - \partial_\nu Z_\mu - \iota g\left[Z_\mu, Z_\nu\right]\right)\left(\partial_\rho Z_\sigma - \partial_\sigma Z_\rho - \iota g\left[Z_\rho, Z_\sigma\right]\right)\right] \\
&= 4\epsilon_{\mu\nu\rho\sigma}\,\mathrm{Tr}\left[\left(\partial_\mu Z_\nu - \iota g Z_\mu Z_\nu\right)\left(\partial_\rho Z_\sigma - \iota g Z_\rho Z_\sigma\right)\right] \\
&= 4\epsilon_{\mu\nu\rho\sigma}\,\mathrm{Tr}\left[\left(\partial_\mu Z_\nu - \iota g Z_\mu Z_\nu\right)\left(\partial_\rho Z_\sigma - \iota g Z_\rho Z_\sigma\right)\right] \\
&= 4\epsilon_{\mu\nu\rho\sigma}\,\mathrm{Tr}\left(\partial_\mu Z_\nu \partial_\rho Z_\sigma - \iota g Z_\mu Z_\nu \partial_\rho Z_\sigma - \iota g(\partial_\mu Z_\nu) Z_\rho Z_\sigma\right) \\
&- 4g^2\cancel{\epsilon_{\mu\nu\rho\sigma}\,\mathrm{Tr}\left(Z_\mu Z_\nu Z_\rho Z_\sigma\right)} \\
&= 4\epsilon_{\mu\nu\rho\sigma}\,\mathrm{Tr}\left(\partial_\mu Z_\nu \partial_\rho Z_\sigma - \iota g Z_\mu Z_\nu \partial_\rho Z_\sigma - \iota g(\partial_\mu Z_\nu) Z_\rho Z_\sigma\right) \\
&= 4\epsilon_{\mu\nu\rho\sigma}\,\mathrm{Tr}\left(\partial_\mu Z_\nu \partial_\rho Z_\sigma - 2\iota g Z_\mu Z_\nu \partial_\rho Z_\sigma\right) \\
&= 4\epsilon_{\mu\nu\rho\sigma}\,\mathrm{Tr}\left(\partial_\mu\left(Z_\nu \partial_\rho Z_\sigma\right) - Z_\nu \partial_\mu \partial_\rho Z_\sigma - 2\iota g Z_\mu Z_\nu \partial_\rho Z_\sigma\right) \\
&= 4\epsilon_{\mu\nu\rho\sigma}\,\mathrm{Tr}\left[\partial_\mu\left(Z_\nu \partial_\rho Z_\sigma\right) - 2\iota g Z_\mu Z_\nu \partial_\rho Z_\sigma\right] - \cancel{4\epsilon_{\mu\nu\rho\sigma}\,\mathrm{Tr}\,Z_\nu \partial_\mu \partial_\rho Z_\sigma}
\end{aligned}
$$

$$= 4\epsilon_{\mu\nu\rho\sigma}\,\mathrm{Tr}\left[\partial_\mu\left(Z_\nu\partial_\rho Z_\sigma\right) - \frac{2}{3}\iota g\partial_\mu\left(Z_\nu Z_\rho Z_\sigma\right)\right]$$
$$= 4\partial_\mu\left(\epsilon_{\mu\nu\rho\sigma}\,\mathrm{Tr}\left[Z_\nu\partial_\rho Z_\sigma - \frac{2}{3}\iota g Z_\nu Z_\rho Z_\sigma\right]\right)$$

It is interesting to note that the Chern-Simons term in this scenario is the obvious generalization of Eq. D.4. Nonetheless, it is not yet clear what the corresponding winding number would mean for such gauge group $\mathrm{SL}\left(n, C\right)$ and we leave such interesting matter for further work.

D.4 Action on the lattice

In the Euclidean QCD lagrangian (with the θ-term), the action becomes complex for real values of θ. Hence, direct MC simulations become impossible. So the idea is to continue $\theta \to -i\theta_i$, with θ_i real and then carry out the MC simulations and continue the results back to real θ.

The θ term in the continuum is given by:

$$q(x) = i\theta\frac{g^2}{64\pi^2}\epsilon_{\mu\nu\rho\sigma}F^a_{\mu\nu}\left(x\right)F^a_{\rho\sigma}\left(x\right) \tag{D.7}$$

On the lattice this becomes $\theta_L \mathrm{Q}_L$, with:

$$Q_L = \sum_n q_L(n) \tag{D.8}$$

$$q_L(n) = \frac{-1}{2^4 32\pi^2}\sum_{\mu\nu\rho\sigma=\pm1}^{\pm4}\tilde{\epsilon}_{\mu\nu\rho\sigma}\,\mathrm{Tr}\{[\Pi_{\mu\nu}\left(n\right)\Pi_{\rho\sigma}\left(n\right)]\} \tag{D.9}$$

with $\tilde{\epsilon}_{\mu\nu\rho\sigma} = \epsilon_{\mu\nu\rho\sigma}$ for positive directions and $\tilde{\epsilon}_{(-\mu)\nu\rho\sigma}$ = -$\epsilon_{\mu\nu\rho\sigma}$ for every negative direction. And the plaquttes being,

$$\Pi_{\mu\nu}(n) = U_\mu(n)U_\nu(n+\hat{\mu})U^\dagger_\mu(n+\hat{\nu})U^\dagger_\nu(n)$$
$$\Pi_{\rho\sigma}(n) = U_\rho(n)U_\sigma(n+\hat{\rho})U^\dagger_\rho(n+\hat{\sigma})U^\dagger_\sigma(n)$$

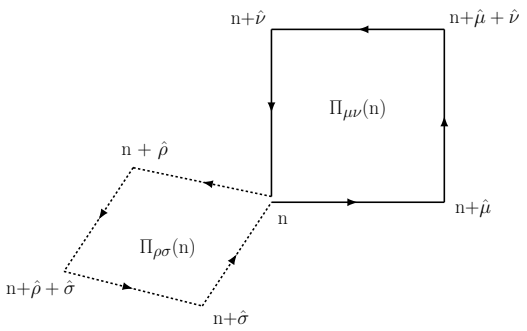

Figure D.1: The loop associated to theta term (not the only diagram relevant on the lattice with positive directions)

Since our code is made for only positive directions - we need to split sums for μ,ν,ρ and σ for positive and negative directions. We can split the sum in Eqn(5) and convert all directions to positive in order to get the diagrams relevant to our code.

What happens to the plaquettes under $\hat{\mu} \to -\hat{\mu}$, $\hat{\nu} \to -\hat{\nu}$, $\hat{\rho} \to -\hat{\rho}$ and $\hat{\sigma} \to -\hat{\sigma}$?

Using $U_{-\mu}(n) \equiv U_{\mu}^{\dagger}(n - \hat{\mu})$, we get:

$$\begin{aligned}
\Pi_{(-\mu)\nu}(n) &= U_{-\mu}(n)U_{\nu}(n-\hat{\mu})U_{-\mu}^{\dagger}(n+\hat{\nu})U_{\nu}^{\dagger}(n) \\
&= U_{\mu}^{\dagger}(n-\hat{\mu})U_{\nu}(n-\hat{\mu})U_{\mu}(n+\hat{\nu}-\hat{\mu})U_{\nu}^{\dagger}(n) \\
&\neq \left[U_{\nu}(n-\hat{\mu})U_{\mu}(n+\hat{\nu}-\hat{\mu})U_{\nu}^{\dagger}(n)U_{\mu}^{\dagger}(n-\hat{\mu}) = \Pi_{\mu\nu}^{\dagger}(n-\hat{\mu})\right]
\end{aligned}$$

$$\begin{aligned}
\Pi_{\mu(-\nu)}(n) &= U_{\mu}(n)U_{-\nu}(n+\hat{\mu})U_{\mu}^{\dagger}(n-\hat{\nu})U_{-\nu}^{\dagger}(n) \\
&= U_{\mu}(n)U_{\nu}^{\dagger}(n+\hat{\mu}-\hat{\nu})U_{\mu}^{\dagger}(n-\hat{\nu})U_{\nu}(n-\hat{\nu}) \neq \Pi_{\mu\nu}^{\dagger}(n-\hat{\nu}) \\
\Pi_{(-\mu)(-\nu)}(n) &= U_{-\mu}(n)U_{-\nu}(n-\hat{\mu})U_{-\mu}^{\dagger}(n-\hat{\nu})U_{-\nu}^{\dagger}(n) \\
&= U_{\mu}^{\dagger}(n-\hat{\mu})U_{\nu}^{\dagger}(n-\hat{\nu}-\hat{\mu})U_{\mu}(n-\hat{\mu}-\hat{\nu})U_{\nu}(n-\hat{\nu}) \neq \Pi_{\mu\nu}(n-\hat{\mu}-\hat{\nu})
\end{aligned}$$

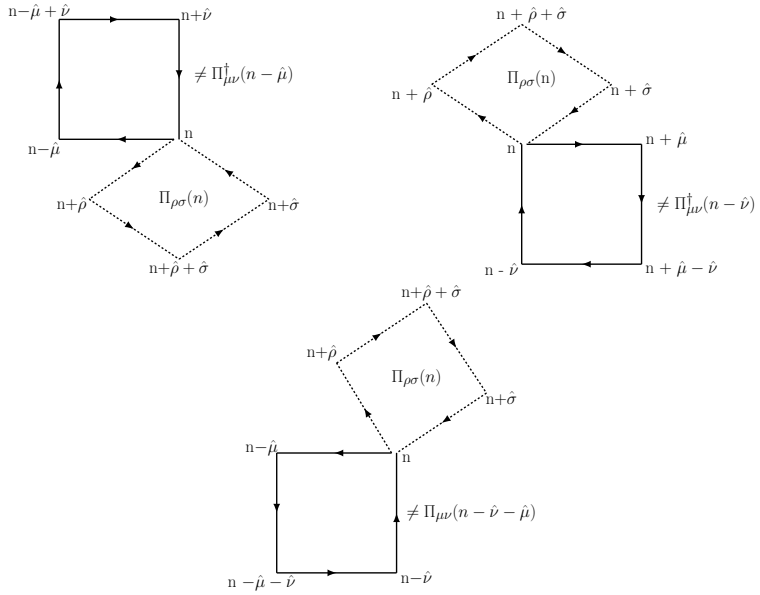

Figure D.2: The loop associated to theta term in (Top Left) $-\hat{\mu}$, (Top Right) $-\hat{\nu}$ and (Bottom) $(-\hat{\mu} - \hat{\nu})$ direction

The inequality represents the fact that we cannot use trace cyclibility to move the links in $\Pi_{\mu\nu}$ without commuting over $\Pi_{\rho\sigma}$.

But these four diagrams do not exhaust all the terms in the diagrams possible. All the sixteen terms appearing in the "positive" direction sum are:

$$\begin{aligned}
q_L(n) = \frac{-1}{2^4 32\pi^2} \sum_{\mu\nu\rho\sigma=1}^{4} \epsilon_{\mu\nu\rho\sigma} \operatorname{Tr}\Big(&\left[\Pi_{\mu\nu}(n) - \Pi_{(-\mu)\nu}(n) - \Pi_{\mu(-\nu)}(n) + \Pi_{-\mu-\nu}(n)\right] \times \\
&\left[\Pi_{\rho\sigma}(n) - \Pi_{(-\rho)\sigma}(n) - \Pi_{\rho(-\sigma)}(n) + \Pi_{-\rho-\sigma}(n)\right]\Big)
\end{aligned}$$

Bibliography

[1] C. R. Allton et al. "The QCD thermal phase transition in the presence of a small chemical potential". In: *Phys. Rev. D* 66 (2002), p. 074507. DOI: 10.1103/PhysRevD.66.074507. arXiv: hep-lat/0204010.

[2] Philippe de Forcrand and Owe Philipsen. "The QCD phase diagram for small densities from imaginary chemical potential". In: *Nuclear Physics B* 642.1 (2002), pp. 290–306. ISSN: 0550-3213. DOI: https://doi.org/10.1016/S0550-3213(02)00626-0. URL: https://www.sciencedirect.com/science/article/pii/S0550321302006260.

[3] Marco Cristoforetti, Francesco Di Renzo, and Luigi Scorzato. "New approach to the sign problem in quantum field theories: High density QCD on a Lefschetz thimble". In: *Phys. Rev. D* 86 (7 Oct. 2012), p. 074506. DOI: 10.1103/PhysRevD.86.074506. URL: https://link.aps.org/doi/10.1103/PhysRevD.86.074506.

[4] Zoltan Fodor and Sandor D Katz. "Lattice determination of the critical point of QCD at finiteiT/iand ". In: *Journal of High Energy Physics* 2002.03 (Mar. 2002), pp. 014–014. DOI: 10.1088/1126-6708/2002/03/014. URL: https://doi.org/10.1088/1126-6708/2002/03/014.

[5] Y. Aoki et al. "The Order of the quantum chromodynamics transition predicted by the standard model of particle physics". In: *Nature* 443 (2006), pp. 675–678. DOI: 10.1038/nature05120. arXiv: hep-lat/0611014.

[6] M. A. Halasz et al. "Phase diagram of QCD". In: *Phys. Rev. D* 58 (9 Sept. 1998), p. 096007. DOI: 10.1103/PhysRevD.58.096007. URL: https://link.aps.org/doi/10.1103/PhysRevD.58.096007.

[7] Simon Hands. "Lattice matter". In: *Nuclear Physics B - Proceedings Supplements* 106-107 (2002). LATTICE 2001 Proceedings of the XIXth International Symposium on Lattice Field Theory, pp. 142–150. ISSN: 0920-5632. DOI: https://doi.org/10.1016/S0920-5632(01)01653-X. URL: https://www.sciencedirect.com/science/article/pii/S092056320101653X.

[8] Mikhail A. Stephanov. "QCD phase diagram and the critical point". In: *Prog. Theor. Phys. Suppl.* 153 (2004). Ed. by Berndt Muller and C. I. Tan, pp. 139–156. DOI: 10.1142/S0217751X05027965. arXiv: hep-ph/0402115.

[9] Jana N. Guenther. "An overview of the QCD phase diagram at finite T and μ". In: *38th International Symposium on Lattice Field Theory*. Jan. 2022. arXiv: 2201.02072 [hep-lat].

[10] Andre Roberge and Nathan Weiss. "Gauge Theories With Imaginary Chemical Potential and the Phases of QCD". In: *Nucl. Phys. B* 275 (1986), pp. 734–745. DOI: 10.1016/0550-3213(86)90582-1.

[11] C. N. Yang and T. D. Lee. "Statistical Theory of Equations of State and Phase Transitions. I. Theory of Condensation". In: *Phys. Rev.* 87 (3 Aug. 1952), pp. 404–409. DOI: 10.1103/PhysRev.87.404. URL: https://link.aps.org/doi/10.1103/PhysRev.87.404.

[12] T. D. Lee and C. N. Yang. "Statistical Theory of Equations of State and Phase Transitions. II. Lattice Gas and Ising Model". In: *Phys. Rev.* 87 (3 Aug. 1952), pp. 410–419. DOI: 10.1103/PhysRev.87.410. URL: https://link.aps.org/doi/10.1103/PhysRev.87.410.

[13] M. E. Fisher. "Yang-Lee Edge Singularity and phi**3 Field Theory". In: *Phys. Rev. Lett.* 40 (1978), pp. 1610–1613. DOI: 10.1103/PhysRevLett.40.1610.

[14] MIT virtual lattice conference. URL: https://mit.zoom.us/rec/share/O1KqkaIw0cZnSKFoDeOaL5eKI_HQHJvF7MN56PYj0IFysG5bf1DDW2hF3jpjT5oH.uqqrsu459WatbcDt.

[15] Marco Cristoforetti, Francesco Di Renzo, and Luigi Scorzato. "New approach to the sign problem in quantum field theories: High density QCD on a Lefschetz thimble". In: *Phys. Rev. D* 86 (2012), p. 074506. DOI: 10.1103/PhysRevD.86.074506. arXiv: 1205.3996 [hep-lat].

[16] P. Dimopoulos et al. "Contribution to understanding the phase structure of strong interaction matter: Lee-Yang edge singularities from lattice QCD". In: *Phys. Rev. D* 105.3 (2022), p. 034513. DOI: 10.1103/PhysRevD.105.034513. arXiv: 2110.15933 [hep-lat].

[17] A.D. Kennedy. "Approximation theory for matrices". In: *Nuclear Physics B - Proceedings Supplements* 128 (2004). Proceedings of the 2nd Cairns Topical Workshop on Lattice Hadron Physics, pp. 107–116. ISSN: 0920-5632. DOI: https://doi.org/10.1016/S0920-5632(03)02466-6. URL: https://www.sciencedirect.com/science/article/pii/S0920563203024666.

[18] William Fraser and J. F. Hart. "On the computation of rational approximations to continuous functions". In: *Commun. ACM* 5 (1962), pp. 401–403.

[19] E.Ya Remez. "Fundamentals of numerical methods for Chebyshev approximations". In: *Naukova Dumka* (1969).

[20] V.T. Gavrilyuk. "Generalization of the first polynomial algorithm of E.Ya.Remez for the problem of constructing rational-fractional Chebyshev approximations". In: *Ukr. Mat. Zh. 16* 575-585 (1961).

[21] George A. Jr. Baker. *Essentials of Padé Approximants*. Cambridge, Massachusetts: Academic Press, 1975.

[22] Michael E. Fisher. *The nature of critical points*. 1965.

[23] Massimo D'Elia and Maria-Paola Lombardo. "Imaginary chemical potential in QCD at finite temperature". In: *Workshop on Quark Gluon Plasma and Relativistic Heavy Ions*. May 2002. DOI: 10.1142/9789812776532_0026. arXiv: hep-lat/0205022.

[24] MATLAB. *version 9.7.0.1190202 (R2019b - academic use)*. Natick, Massachusetts: The MathWorks Inc., 2019.

[25] Thomas Kluyver et al. "Jupyter Notebooks – a publishing format for reproducible computational workflows". In: *Positioning and Power in Academic Publishing: Players, Agents and Agendas*. Ed. by F. Loizides and B. Schmidt. IOS Press. 2016, pp. 87–90.

[26] Gert Aarts and Ion-Olimpiu Stamatescu. "Stochastic quantization at finite chemical potential". In: *Journal of High Energy Physics* 2008.09 (Sept. 2008), pp. 018–018. DOI: 10.1088/1126-6708/2008/09/018. URL: https://doi.org/10.1088/1126-6708/2008/09/018.

[27] Jan M. Pawlowski, Ion-Olimpiu Stamatescu, and Christian Zielinski. "Simple QED- and QCD-like models at finite density". In: *Phys. Rev. D* 92 (1 July 2015), p. 014508. DOI: 10.1103/PhysRevD.92.014508. URL: https://link.aps.org/doi/10.1103/PhysRevD.92.014508.

[28] Walter E Thirring. "A soluble relativistic field theory". In: *Annals of Physics* 3.1 (1958), pp. 91–112. ISSN: 0003-4916. DOI: https://doi.org/10.1016/0003-4916(58)90015-0. URL: https://www.sciencedirect.com/science/article/pii/0003491658900150.

[29] Hiroaki S. Yamada and Kensuke S. Ikeda. "A Numerical Test of Pade Approximation for Some Functions with singularity". In: (2014). arXiv: 1308.4453 [math-ph].

[30] Andrei Alexandru, Gökçe Basar, and Paulo Bedaque. "Monte Carlo algorithm for simulating fermions on Lefschetz thimbles". In: *Phys. Rev. D* 93.1 (2016), p. 014504. DOI: 10.1103/PhysRevD.93.014504. arXiv: 1510.03258 [hep-lat].

[31] F. Di Renzo, S. Singh, and K. Zambello. "Taylor expansions on Lefschetz thimbles". In: *Phys. Rev. D* 103 (3 Feb. 2021), p. 034513. DOI: 10.1103/PhysRevD.103.034513. URL: https://link.aps.org/doi/10.1103/PhysRevD.103.034513.

[32] Francesco Di Renzo and Kevin Zambello. "Solution of the Thirring model in thimble regularization". In: *Phys. Rev. D* 105.5 (2022), p. 054501. DOI: 10.1103/PhysRevD.105.054501. arXiv: 2109.02511 [hep-lat].

[33] Andrei Alexandru et al. "Sign problem and Monte Carlo calculations beyond Lefschetz thimbles". In: *JHEP* 05 (2016), p. 053. DOI: 10.1007/JHEP05(2016)053. arXiv: 1512.08764 [hep-lat].

[34] "Chapter 2. Stieltjes functions". In: *Bernstein Functions: Theory and Applications*. De Gruyter, 2012, pp. 16–20. DOI: doi:10.1515/9783110269338.16. URL: https://doi.org/10.1515/9783110269338.16.

[35] I. Momoniat. "A de Montessue de Ballore Theorem for Best Rational Approximation over the Whole Plane". In: *J. Approx. Theory* 54.2 (Aug. 1988), pp. 123–138. ISSN: 0021-9045. DOI: 10.1016/0021-9045(88)90012-3. URL: https://doi.org/10.1016/0021-9045(88)90012-3.

[36] J Nuttall. "The convergence of Padé approximants of meromorphic functions". In: *Journal of Mathematical Analysis and Applications* 31.1 (1970), pp. 147–153. ISSN: 0022-247X. DOI: https://doi.org/10.1016/0022-247X(70)90126-5. URL: https://www.sciencedirect.com/science/article/pii/0022247X70901265.

[37] Ch Pommerenke. "Padé approximants and convergence in capacity". In: *Journal of Mathematical Analysis and Applications* 41.3 (1973), pp. 775–780. ISSN: 0022-247X. DOI: https://doi.org/10.1016/0022-247X(73)90248-5. URL: https://www.sciencedirect.com/science/article/pii/0022247X73902485.

[38] J. Nuttall. "The convergence of padé approximants and their generalizations". In: *The Riemann Problem, Complete Integrability and Arithmetic Applications*. Ed. by David V. Chudnovsky and Gregory V. Chudnovsky. Berlin, Heidelberg: Springer Berlin Heidelberg, 1982, pp. 246–257. ISBN: 978-3-540-39152-4.

[39] A. Cuyt, K. Driver, and D.S. Lubinsky. "Nuttall-Pommerenke theorems for homogeneous Padé approximants". In: *Journal of Computational and Applied Mathematics* 67.1 (1996), pp. 141–146. ISSN: 0377-0427. DOI: https://doi.org/10.1016/0377-0427(94)00115-4. URL: https://www.sciencedirect.com/science/article/pii/0377042794001154.

[40] Pere Masjuan. "Hunting resonance poles with Rational Approximants". In: (Dec. 2010). arXiv: 1012.2806 [hep-ph].

[41] Pere Masjuan. *Rational Approximations in Quantum Chromodynamics*. 2010. DOI: 10.48550/ARXIV.1005.5683. URL: https://arxiv.org/abs/1005.5683.

[42] A. Bazavov et al. "Chiral crossover in QCD at zero and non-zero chemical potentials". In: *Physics Letters B* 795 (2019), pp. 15–21. ISSN: 0370-2693. DOI: https://doi.org/10.1016/j.physletb.2019.05.013. URL: https://www.sciencedirect.com/science/article/pii/S0370269319303223.

[43] E Ising. "Beitrag zur Theorie des Ferromagnetismus". In: *Z. Phys.* 31 (1925), pp. 253–258. URL: http://cds.cern.ch/record/429052.

[44] Frank R. Brown et al. "On the existence of a phase transition for QCD with three light quarks". In: *Phys. Rev. Lett.* 65 (20 Nov. 1990), pp. 2491–2494. DOI: 10.1103/PhysRevLett.65.2491. URL: https://link.aps.org/doi/10.1103/PhysRevLett.65.2491.

[45] Claudia Ratti and Rene Bellwied. *The Deconfinement Transition of QCD*. Lecture Notes in Physics, Vol 981. Springer, 2021. ISBN: 978.3.030-67234-8.

[46] Christof Gattringer and Christian B Lang. *Quantum chromodynamics on the lattice. An introductory presentation*. July 2010. DOI: 10.1007/978-3-642-01850-3.

[47] Gert Aarts. "Introductory lectures on lattice QCD at nonzero baryon number". In: *Journal of Physics: Conference Series* 706 (Apr. 2016), p. 022004. DOI: 10.1088/1742-6596/706/2/022004. URL: https://doi.org/10.1088/1742-6596/706/2/022004.

[48] Philippe de Forcrand and Owe Philipsen. "Constraining the QCD Phase Diagram by Tricritical Lines at Imaginary Chemical Potential". In: *Phys. Rev. Lett.* 105 (15 Oct. 2010), p. 152001. DOI: 10.1103/PhysRevLett.105.152001. URL: https://link.aps.org/doi/10.1103/PhysRevLett.105.152001.

[49] G. 't Hooft. "On the phase transition towards permanent quark confinement". In: *Nuclear Physics B* 138.1 (1978), pp. 1–25. ISSN: 0550-3213. DOI: https://doi.org/10.1016/0550-3213(78)90153-0. URL: https://www.sciencedirect.com/science/article/pii/0550321378901530.

[50] Robert D. Pisarski. "Quark-gluon plasma as a condensate of $Z(3)$ Wilson lines". In: *Phys. Rev. D* 62 (11 Nov. 2000), p. 111501. DOI: 10.1103/PhysRevD.62.111501. URL: https://link.aps.org/doi/10.1103/PhysRevD.62.111501.

[51] R.D. Pisarski. "Tests of the Polyakov loops model". In: *Nuclear Physics A* 702.1 (2002). International Symposium on Statistical QCD, pp. 151–158. ISSN: 0375-9474. DOI: https://doi.org/10.1016/S0375-9474(02)00699-1. URL: https://www.sciencedirect.com/science/article/pii/S0375947402006991.

[52] J Engels and T Scheideler. "The pseudo specific heat in SU(2) gauge theory: finite size dependence and finite temperature effects". In: *Physics Letters B* 394.1 (1997), pp. 147–151. ISSN: 0370-2693. DOI: https://doi.org/10.1016/S0370-2693(96)01681-4. URL: https://www.sciencedirect.com/science/article/pii/S0370269396016814.

[53] Robert D. Pisarski and Frank Wilczek. "Remarks on the chiral phase transition in chromodynamics". In: *Phys. Rev. D* 29 (2 Jan. 1984), pp. 338–341. DOI: 10.1103/PhysRevD.29.338. URL: https://link.aps.org/doi/10.1103/PhysRevD.29.338.

[54] A. Bazavov et al. "Chiral phase structure of three flavor QCD at vanishing baryon number density". In: *Phys. Rev. D* 95 (7 Apr. 2017), p. 074505. DOI: 10.1103/PhysRevD.95.074505. URL: https://link.aps.org/doi/10.1103/PhysRevD.95.074505.

[55] P. Hasenfratz and F. Karsch. "Chemical potential on the lattice". In: *Physics Letters B* 125.4 (1983), pp. 308–310. ISSN: 0370-2693. DOI: https://doi.org/10.1016/0370-2693(83)91290-X. URL: https://www.sciencedirect.com/science/article/pii/037026938391290X.

[56] Owe Philipsen. "Constraining the phase diagram of QCD at finite temperature and density". In: *PoS* LATTICE2019 (2019), p. 273. DOI: 10.22323/1.363.0273. arXiv: 1912.04827 [hep-lat].

[57] Philippe de Forcrand and Owe Philipsen. "The QCD phase diagram for small densities from imaginary chemical potential". In: *Nucl. Phys. B* 642 (2002), pp. 290–306. DOI: 10.1016/S0550-3213(02)00626-0. arXiv: hep-lat/0205016.

[58] Christopher Czaban et al. "Roberge-Weiss transition in $N_f = 2$ QCD with Wilson fermions and $N_\tau = 6$". In: *Phys. Rev. D* 93 (5 Mar. 2016), p. 054507. DOI: 10.1103/PhysRevD.93.054507. URL: https://link.aps.org/doi/10.1103/PhysRevD.93.054507.

[59] F. Cuteri et al. “Towards the chiral phase transition in the Roberge-Weiss plane”. In: (May 2022). arXiv: 2205.12707 [hep-lat].

[60] Philippe de Forcrand and Massimo D’Elia. “Continuum limit and universality of the Columbia plot”. In: *PoS* LATTICE2016 (Feb. 2017). 7 pages, 5 figures, talk presented at the 34th annual International Symposium on Lattice Field Theory (Lattice2016), 24-30 July 2016, University of Southampton, UK, 081. 7 p. DOI: 10.22323/1.256.0081. arXiv: 1702.00330. URL: https://cds.cern.ch/record/2257659.

[61] Claudio Bonati et al. “Curvature of the pseudocritical line in QCD: Taylor expansion matches analytic continuation”. In: *Phys. Rev. D* 98.5 (2018), p. 054510. DOI: 10.1103/PhysRevD.98.054510. arXiv: 1805.02960 [hep-lat].

[62] Asakawa Masayuki and Yazaki Koichi. “Chiral restoration at finite density and temperature”. In: *Nuclear Physics A* 504.4 (1989), pp. 668–684. ISSN: 0375-9474. DOI: https://doi.org/10.1016/0375-9474(89)90002-X. URL: https://www.sciencedirect.com/science/article/pii/037594748990002X.

[63] A. Barducci et al. “Chiral phases of QCD at finite density and temperature”. In: *Phys. Rev. D* 49 (1 Jan. 1994), pp. 426–436. DOI: 10.1103/PhysRevD.49.426. URL: https://link.aps.org/doi/10.1103/PhysRevD.49.426.

[64] N.G. Antoniou, F.K. Diakonos, and A.S. Kapoyannis. “The critical endpoint of bootstrap and lattice QCD matter”. In: *Nuclear Physics A* 759.3 (2005), pp. 417–438. ISSN: 0375-9474. DOI: https://doi.org/10.1016/j.nuclphysa.2005.05.156. URL: https://www.sciencedirect.com/science/article/pii/S0375947405008559.

[65] Mark Alford, Krishna Rajagopal, and Frank Wilczek. “Color-flavor locking and chiral symmetry breaking in high density QCD”. In: *Nuclear Physics B* 537.1 (1999), pp. 443–458. ISSN: 0550-3213. DOI: https://doi.org/10.1016/S0550-3213(98)00668-3. URL: https://www.sciencedirect.com/science/article/pii/S0550321398006683.

[66] Heng-Tong Ding et al. “The chiral phase transition temperature in (2+1)-flavor QCD”. In: *18th International Conference on Hadron Spectroscopy and Structure*. 2020, pp. 672–677. DOI: 10.1142/9789811219313_0115.

[67] Chiho Nonaka and Masayuki Asakawa. “Hydrodynamical evolution near the QCD critical end point”. In: *Phys. Rev. C* 71 (2005), p. 044904. DOI: 10.1103/PhysRevC.71.044904. arXiv: nucl-th/0410078.

[68] Rajeev S. Bhalerao. “Relativistic heavy-ion collisions”. In: (2014). DOI: 10.48550/ARXIV.1404.3294. URL: https://arxiv.org/abs/1404.3294.

[69] M. Giordano and A. Pásztor. “Reliable estimation of the radius of convergence in finite density QCD”. In: *Physical Review D* 99 (June 2019). DOI: 10.1103/PhysRevD.99.114510.

[70] Eduardo Ibarra-Garcıa-Padilla, Carlos Gerardo Malanche-Flores, and Freddy Jackson Poveda-Cuevas. “The hobbyhorse of magnetic systems: the Ising model”. In: *European Journal of Physics* 37.6 (Sept. 2016), p. 065103. DOI: 10.1088/0143-0807/37/6/065103. URL: https://doi.org/10.1088/0143-0807/37/6/065103.

[71] IOANA BENA, MICHEL DROZ, and ADAM LIPOWSKI. "STATISTICAL MECHANICS OF EQUILIBRIUM AND NONEQUILIBRIUM PHASE TRANSITIONS: THE YANG–LEE FORMALISM". In: *International Journal of Modern Physics B* 19.29 (2005), pp. 4269–4329. DOI: 10.1142/S0217979205032759. eprint: https://doi.org/10.1142/S0217979205032759. URL: https://doi.org/10.1142/S0217979205032759.

[72] Elton Yechao Zhu. *Lee Yang theorem*. URL: http://web.mit.edu/8.334/www/grades/projects/projects14/EltonZhu_Lee%20Yang%20singularity.pdf. (accessed: 01.03.2022).

[73] Mehran Kardar. *Statistical Physics of Fields*. Cambridge University Press, 2007. DOI: 10.1017/CBO9780511815881.

[74] Ch. Binek. "Density of Zeros on the Lee-Yang Circle Obtained from Magnetization Data of a Two-Dimensional Ising Ferromagnet". In: *Phys. Rev. Lett.* 81 (25 Dec. 1998), pp. 5644–5647. DOI: 10.1103/PhysRevLett.81.5644. URL: https://link.aps.org/doi/10.1103/PhysRevLett.81.5644.

[75] Aydin Deger and Christian Flindt. "Determination of universal critical exponents using Lee-Yang theory". In: *Phys. Rev. Research* 1 (2 Sept. 2019), p. 023004. DOI: 10.1103/PhysRevResearch.1.023004. URL: https://link.aps.org/doi/10.1103/PhysRevResearch.1.023004.

[76] Christian Flindt and Juan P. Garrahan. "Trajectory Phase Transitions, Lee-Yang Zeros, and High-Order Cumulants in Full Counting Statistics". In: *Phys. Rev. Lett.* 110 (5 Jan. 2013), p. 050601. DOI: 10.1103/PhysRevLett.110.050601. URL: https://link.aps.org/doi/10.1103/PhysRevLett.110.050601.

[77] Xin An, David Mesterházy, and Mikhail A. Stephanov. "Functional renormalization group approach to the Yang-Lee edge singularity". In: *JHEP* 07 (2016), p. 041. DOI: 10.1007/JHEP07(2016)041. arXiv: 1605.06039 [hep-th].

[78] Andrew Connelly et al. "Universal Location of the Yang-Lee Edge Singularity in O(N) Theories". In: *Phys. Rev. Lett.* 125 (19 Nov. 2020), p. 191602. DOI: 10.1103/PhysRevLett.125.191602. URL: https://link.aps.org/doi/10.1103/PhysRevLett.125.191602.

[79] Lars Onsager. "Crystal Statistics. I. A Two-Dimensional Model with an Order-Disorder Transition". In: *Phys. Rev.* 65 (3-4 Feb. 1944), pp. 117–149. DOI: 10.1103/PhysRev.65.117. URL: https://link.aps.org/doi/10.1103/PhysRev.65.117.

[80] M. A. Stephanov. "QCD critical point and complex chemical potential singularities". In: *Phys. Rev. D* 73 (9 May 2006), p. 094508. DOI: 10.1103/PhysRevD.73.094508. URL: https://link.aps.org/doi/10.1103/PhysRevD.73.094508.

[81] Gök çe Ba şar. "Universality, Lee-Yang Singularities, and Series Expansions". In: *Phys. Rev. Lett.* 127 (17 Oct. 2021), p. 171603. DOI: 10.1103/PhysRevLett.127.171603. URL: https://link.aps.org/doi/10.1103/PhysRevLett.127.171603.

[82] Szabolcs Borsanyi et al. "Higher order fluctuations and correlations of conserved charges from lattice QCD". In: *Journal of High Energy Physics* 10 (2018), p. 205. DOI: 10.1007/JHEP10(2018)205. URL: https://doi.org/10.1007/JHEP10(2018)205.

[83] Attila Pásztor, Zsolt Szép, and Gergely Markó. "Apparent convergence of Padé approximants for the crossover line in finite density QCD". In: *Phys. Rev. D* 103 (3 Feb. 2021), p. 034511. DOI: 10.1103/PhysRevD.103.034511. URL: https://link.aps.org/doi/10.1103/PhysRevD.103.034511.

[84] J. M. Karthein et al. "Strangeness-neutral equation of state for QCD with a critical point". In: *Eur. Phys. J. Plus* 136.6 (2021), p. 621. DOI: 10.1140/epjp/s13360-021-01615-5. arXiv: 2103.08146 [hep-ph].

[85] Sourav Mondal, Swagato Mukherjee, and Prasad Hegde. "Lattice QCD Equation of State for Nonvanishing Chemical Potential by Resumming Taylor Expansions". In: *Phys. Rev. Lett.* 128 (2 Jan. 2022), p. 022001. DOI: 10.1103/PhysRevLett.128.022001. URL: https://link.aps.org/doi/10.1103/PhysRevLett.128.022001.

[86] Dennis Bollweg et al. "HotQCD on multi-GPU Systems". In: *PoS* LATTICE2021 (2022), p. 196. DOI: 10.22323/1.396.0196.

[87] M. A. Clark and A. D. Kennedy. "Accelerating Dynamical-Fermion Computations Using the Rational Hybrid Monte Carlo Algorithm with Multiple Pseudofermion Fields". In: *Phys. Rev. Lett.* 98 (5 Jan. 2007), p. 051601. DOI: 10.1103/PhysRevLett.98.051601. URL: https://link.aps.org/doi/10.1103/PhysRevLett.98.051601.

[88] A. Bazavov et al. "Chiral and deconfinement aspects of the QCD transition". In: *Phys. Rev. D* 85 (5 Mar. 2012), p. 054503. DOI: 10.1103/PhysRevD.85.054503. URL: https://link.aps.org/doi/10.1103/PhysRevD.85.054503.

[89] A. Bazavov et al. "Equation of state in $(2+1)$-flavor QCD". In: *Phys. Rev. D* 90 (9 Nov. 2014), p. 094503. DOI: 10.1103/PhysRevD.90.094503. URL: https://link.aps.org/doi/10.1103/PhysRevD.90.094503.

[90] D. Bollweg et al. "Second order cumulants of conserved charge fluctuations revisited: Vanishing chemical potentials". In: *Phys. Rev. D* 104 (7 Oct. 2021), p. 074512. DOI: 10.1103/PhysRevD.104.074512. URL: https://link.aps.org/doi/10.1103/PhysRevD.104.074512.

[91] Jishnu Goswami et al. "QCD phase diagram for finite imaginary chemical potential with HISQ fermions". In: *PoS* LATTICE2018 (2019), p. 162. DOI: 10.22323/1.334.0162.

[92] V. Skokov, K. Morita, and B. Friman. "Mapping the phase diagram of strongly interacting matter". In: *Phys. Rev. D* 83 (2011), p. 071502. DOI: 10.1103/PhysRevD.83.071502. arXiv: 1008.4549 [hep-ph].

[93] Ovidiu Costin and Gerald V. Dunne. "Conformal and Uniformizing Maps in Borel Analysis". In: *Eur. Phys. J. ST* 230 (2021), pp. 2679–2690. DOI: 10.1140/epjs/s11734-021-00267-x. arXiv: 2108.01145 [hep-th].

[94] Claudio Bonati et al. "Roberge-Weiss endpoint at the physical point of $N_f = 2 + 1$ QCD". In: *Phys. Rev. D* 93 (7 Apr. 2016), p. 074504. DOI: 10.1103/PhysRevD.93.074504. URL: https://link.aps.org/doi/10.1103/PhysRevD.93.074504.

[95] A. Bazavov et al. "Chiral crossover in QCD at zero and non-zero chemical potentials". In: *Phys. Lett. B* 795 (2019), pp. 15–21. DOI: 10.1016/j.physletb.2019.05.013. arXiv: 1812.08235 [hep-lat].

[96] H.T. Ding et al. "Chiral Phase Transition Temperature in (2+1)-Flavor QCD". In: *Phys. Rev. Lett.* 123.6 (2019), p. 062002. DOI: 10.1103/PhysRevLett.123.062002. arXiv: 1903.04801 [hep-lat].

[97] Szabolcs Borsanyi et al. "QCD Crossover at Finite Chemical Potential from Lattice Simulations". In: *Phys. Rev. Lett.* 125.5 (2020), p. 052001. DOI: 10.1103/PhysRevLett.125.052001. arXiv: 2002.02821 [hep-lat].

[98] Swagato Mukherjee and Vladimir Skokov. "Universality driven analytic structure of the QCD crossover: Radius of convergence in the baryon chemical potential". In: *Phys. Rev. D* 103 (7 Apr. 2021), p. L071501. DOI: 10.1103/PhysRevD.103.L071501. URL: https://link.aps.org/doi/10.1103/PhysRevD.103.L071501.

[99] M. A. Stephanov. "QCD critical point and complex chemical potential singularities". In: *Phys. Rev. D* 73 (9 May 2006), p. 094508. DOI: 10.1103/PhysRevD.73.094508. URL: https://link.aps.org/doi/10.1103/PhysRevD.73.094508.

[100] Ian M. Barbour et al. "Results on finite density QCD". In: *Nuclear Physics B - Proceedings Supplements* 60.1 (1998), pp. 220–233. ISSN: 0920-5632. DOI: https://doi.org/10.1016/S0920-5632(97)00484-2. URL: https://www.sciencedirect.com/science/article/pii/S0920563297004842.

[101] M. Giordano et al. "Effect of stout smearing on the phase diagram from multiparameter reweighting in lattice QCD". In: *Phys. Rev. D* 102 (3 Aug. 2020), p. 034503. DOI: 10.1103/PhysRevD.102.034503. URL: https://link.aps.org/doi/10.1103/PhysRevD.102.034503.

[102] J.C. Osborn, K. Splittorff, and J.J.M. Verbaarschot. "Statistical QCD with Non-positive Measure". In: *Continuous Advances in QCD 2008*. WORLD SCIENTIFIC, Dec. 2008. DOI: 10.1142/9789812838667_0012. URL: https://doi.org/10.1142%2F9789812838667_0012.

[103] Philippe de Forcrand. "Simulating QCD at finite density". In: (2010). DOI: 10.48550/ARXIV.1005.0539. URL: https://arxiv.org/abs/1005.0539.

[104] Masanori Hanada, Yoshinori Matsuo, and Naoki Yamamoto. "Sign problem and phase quenching in finite-density QCD: Models, holography, and lattice". In: *Phys. Rev. D* 86 (7 Oct. 2012), p. 074510. DOI: 10.1103/PhysRevD.86.074510. URL: https://link.aps.org/doi/10.1103/PhysRevD.86.074510.

[105] Zoltan Fodor, Sandor D Katz, and Christian Schmidt. "The density of states method at non-zero chemical potential". In: *Journal of High Energy Physics* 2007.03 (Mar. 2007), pp. 121–121. DOI: 10.1088/1126-6708/2007/03/121. URL: https://doi.org/10.1088/1126-6708/2007/03/121.

[106] G. Endr ődi et al. “Applying constrained simulations for low temperature lattice QCD at finite baryon chemical potential”. In: *Phys. Rev. D* 98 (7 Oct. 2018), p. 074508. DOI: 10.1103/PhysRevD.98.074508. URL: https://link.aps.org/doi/10.1103/PhysRevD.98.074508.

[107] Szabolcs Borsanyi et al. “Lattice simulations of the QCD chiral transition at real baryon density”. In: *Phys. Rev. D* 105.5 (2022), p. L051506. DOI: 10.1103/PhysRevD.105.L051506. arXiv: 2108.09213 [hep-lat].

[108] Ph. de Forcrand, S. Kim, and T. Takaishi. “QCD simulations at small chemical potential”. In: *Nuclear Physics B - Proceedings Supplements* 119 (2003). Proceedings of the XXth International Symposium on Lattice Field Theory, pp. 541–543. ISSN: 0920-5632. DOI: https://doi.org/10.1016/S0920-5632(03)80451-6. URL: https://www.sciencedirect.com/science/article/pii/S0920563203804516.

[109] STEPHEN D. H. HSU and DAVID REEB. “ON THE SIGN PROBLEM IN DENSE QCD”. In: *International Journal of Modern Physics A* 25.01 (2010), pp. 53–67. DOI: 10.1142/S0217751X10047968. eprint: https://doi.org/10.1142/S0217751X10047968. URL: https://doi.org/10.1142/S0217751X10047968.

[110] Andrei Alexandru et al. “Lattice QCD at finite density via a new canonical approach”. In: *Phys. Rev. D* 72 (11 Dec. 2005), p. 114513. DOI: 10.1103/PhysRevD.72.114513. URL: https://link.aps.org/doi/10.1103/PhysRevD.72.114513.

[111] Edward Witten. “Analytic Continuation Of Chern-Simons Theory”. In: *AMS/IP Stud. Adv. Math.* 50 (2011). Ed. by Joergen E. Andersen et al., pp. 347–446. arXiv: 1001.2933 [hep-th].

[112] Hirotsugu Fujii, Syo Kamata, and Yoshio Kikukawa. “Monte Carlo study of Lefschetz thimble structure in one-dimensional Thirring model at finite density”. In: *JHEP* 12 (2015). [Erratum: JHEP 09, 172 (2016)], p. 125. DOI: 10.1007/JHEP12(2015)125. arXiv: 1509.09141 [hep-lat].

[113] Hirotsugu Fujii, Syo Kamata, and Yoshio Kikukawa. “Lefschetz thimble structure in one-dimensional lattice Thirring model at finite density”. In: *JHEP* 11 (2015). [Erratum: JHEP 02, 036 (2016)], p. 078. DOI: 10.1007/JHEP02(2016)036. arXiv: 1509.08176 [hep-lat].

[114] Marco Cristoforetti, Francesco Di Renzo, and Luigi Scorzato. “New approach to the sign problem in quantum field theories: High density QCD on a Lefschetz thimble”. In: *Phys. Rev. D* 86 (7 Oct. 2012), p. 074506. DOI: 10.1103/PhysRevD.86.074506. URL: https://link.aps.org/doi/10.1103/PhysRevD.86.074506.

[115] Martin Luscher. “Trivializing maps, the Wilson flow and the HMC algorithm”. In: *Commun. Math. Phys.* 293 (2010), pp. 899–919. DOI: 10.1007/s00220-009-0953-7. arXiv: 0907.5491 [hep-lat].

[116] Martin Lüscher. “Properties and uses of the Wilson flow in lattice QCD”. In: *JHEP* 08 (2010). [Erratum: JHEP 03, 092 (2014)], p. 071. DOI: 10.1007/JHEP08(2010)071. arXiv: 1006.4518 [hep-lat].

[117] Giovanni Eruzzi. "Regolarizzazione di teorie quantistiche di campo su ditali di Lefschetz come soluzione del problema del segno". In: (2017).

[118] G. 't Hooft. "A property of electric and magnetic flux in non-Abelian gauge theories". In: *Nuclear Physics B* 153 (1979), pp. 141–160. ISSN: 0550-3213. DOI: https://doi.org/10.1016/0550-3213(79)90595-9. URL: https://www.sciencedirect.com/science/article/pii/0550321379905959.

[119] J Groeneveld, J Jurkiewicz, and C P Korthals Altes. "Twist as a Probe for Phase Structure". In: *Physica Scripta* 23.5B (May 1981), pp. 1022–1031. DOI: 10.1088/0031-8949/23/5b/022. URL: https://doi.org/10.1088/0031-8949/23/5b/022.

[120] Martin Luscher, Peter Weisz, and Ulli Wolff. "A Numerical method to compute the running coupling in asymptotically free theories". In: *Nucl. Phys. B* 359 (1991), pp. 221–243. DOI: 10.1016/0550-3213(91)90298-C.

[121] Antonio Gonzalez-Arroyo, J. Jurkiewicz, and C. P. Korthals-Altes. "GROUND STATE METAMORPHOSIS FOR YANG-MILLS FIELDS ON A FINITE PERIODIC LATTICE". In: Dec. 1981.

[122] F. Di Renzo and G. Eruzzi. "Thimble regularization at work: From toy models to chiral random matrix theories". In: *Phys. Rev. D* 92 (8 Oct. 2015), p. 085030. DOI: 10.1103/PhysRevD.92.085030. URL: https://link.aps.org/doi/10.1103/PhysRevD.92.085030.

[123] Marco Cè et al. "Testing the Witten-Veneziano mechanism with the Yang-Mills gradient flow on the lattice". In: (2014). DOI: 10.48550/ARXIV.1410.8358. URL: https://arxiv.org/abs/1410.8358.

[124] Edward Witten. "Two dimensional gauge theories revisited". In: *Journal of Geometry and Physics* 9.4 (1992), pp. 303–368. ISSN: 0393-0440. DOI: https://doi.org/10.1016/0393-0440(92)90034-X. URL: https://www.sciencedirect.com/science/article/pii/039304409290034X.

[125] A. A. Migdal. "Phase transitions in gauge and spin-lattice systems". In: *Soviet Journal of Experimental and Theoretical Physics* 42 (Oct. 1975), p. 743.

[126] V. Azcoiti et al. "New Proposal for Numerical Simulations of θ-Vacuum-like Systems". In: *Phys. Rev. Lett.* 89 (14 Sept. 2002), p. 141601. DOI: 10.1103/PhysRevLett.89.141601. URL: https://link.aps.org/doi/10.1103/PhysRevLett.89.141601.

[127] H. Panagopoulos and E. Vicari. "The 4D SU(3) gauge theory with an imaginary θ term". In: *Journal of High Energy Physics* 2011 (11 Nov. 2011). DOI: 10.1007/JHEP11(2011)119. URL: https://doi.org/10.1007/JHEP11(2011)119.

[128] Massimo D'Elia and Francesco Negro. "θ Dependence of the Deconfinement Temperature in Yang-Mills Theories". In: *Phys. Rev. Lett.* 109 (7 Aug. 2012), p. 072001. DOI: 10.1103/PhysRevLett.109.072001. URL: https://link.aps.org/doi/10.1103/PhysRevLett.109.072001.

[129] M. F. Atiyah and I. M. Singer. "The index of elliptic operators on compact manifolds". In: *Bulletin of the American Mathematical Society* 69.3 (1963), pp. 422–433. DOI: bams/1183525276. URL: https://doi.org/.

[130] David Tong. *David Tong: Lectures on Gauge Theory*. URL: https://www.damtp.cam.ac.uk/user/tong/gaugetheory.html. (accessed: 10.05.2022).